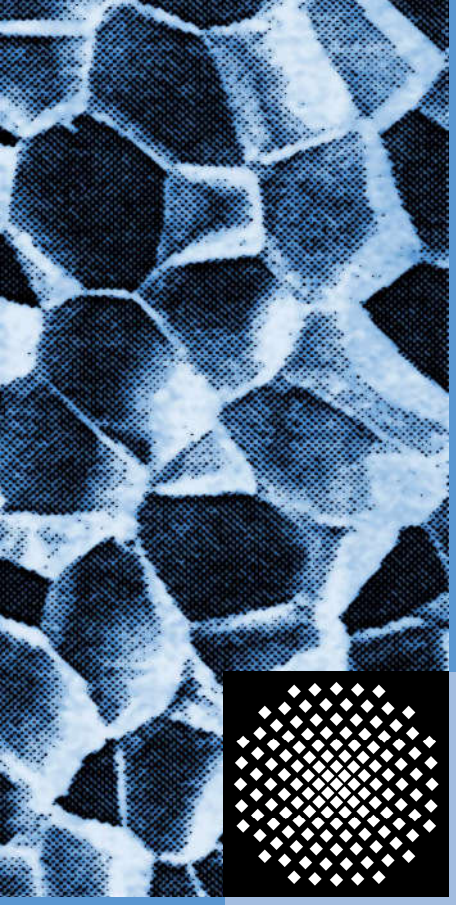

Universität Stuttgart
Germany

Institut für Mechanik (Bauwesen)
Lehrstuhl für Kontinuumsmechanik
Prof. Dr.-Ing. Dr. h. c. W. Ehlers

From Particle Mechanics to Micromorphic Continua

Sami Bidier

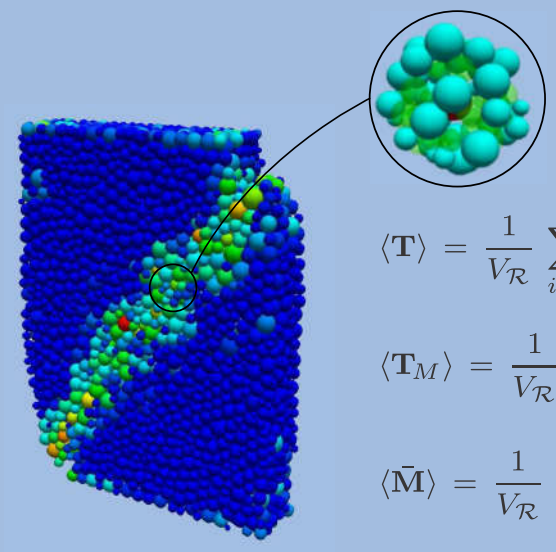

$$\langle \mathbf{T} \rangle = \frac{1}{V_{\mathcal{R}}} \sum_{i=1}^{B} (\mathbf{f}_{ex}^{(i)} \otimes \mathbf{x}_{M}^{(i)})$$

$$\langle \mathbf{T}_M \rangle = \frac{1}{V_{\mathcal{R}}} \sum_{i=1}^{B} (\mathbf{f}_{M}^{(i)} \otimes \mathbf{x}_{M}^{(i)})$$

$$\langle \bar{\mathbf{M}} \rangle = \frac{1}{V_{\mathcal{R}}} \sum_{i=1}^{B} (\bar{\mathbf{m}}_{ex}^{(i)} \otimes \mathbf{x}_{M}^{(i)})$$

Report No.: II-36 (2019)

From Particle Mechanics to Micromorphic Continua

Von der Fakultät Bau- und Umweltingenieurwissenschaften und
dem Stuttgart Research Centre for Simulation Technology
der Universität Stuttgart zur Erlangung der Würde
eines Doktor-Ingenieurs (Dr.-Ing.)
genehmigte Abhandlung

von

Dipl.-Ing. Sami Bidier

aus
Filderstadt

Hauptberichter:	Prof. Dr.-Ing. Dr. h. c. Wolfgang Ehlers
1. Mitberichter:	Prof. Dr.-Ing. Rolf Mahnken
2. Mitberichter:	Prof. Dr. Samuel Forest

Tag der mündlichen Prüfung: 3. Mai 2019

Institut für Mechanik (Bauwesen) der Universität Stuttgart
Lehrstuhl für Kontinuumsmechanik
Prof. Dr.-Ing. Dr. h. c. W. Ehlers

2019

Report No. II-36
Institut für Mechanik (Bauwesen)
Lehrstuhl für Kontinuumsmechanik
Universität Stuttgart, Germany, 2019

Editor:
Prof. Dr.-Ing. Dr. h. c. W. Ehlers

Institut für Mechanik (Bauwesen)
Lehrstuhl für Kontinuumsmechanik
Universität Stuttgart
Pfaffenwaldring 7
70569 Stuttgart, Germany

ISBN 3 – 937399 – 36 – 2
(D 93 – Dissertation, Universität Stuttgart)

Acknowledgements

The work presented in this doctoral thesis was developed during my time as a research assistant at the Institute of Applied Mechanics (Civil Engineering), Chair of Continuum Mechanics, at the University of Stuttgart. I want to thank numerous people who contributed in many ways to the realisation of this work.

First of all, I would like to express my deepest appreciation to Professor Wolfgang Ehlers for giving me the opportunity to prepare my thesis under his supervision and the many challenging scientific discussions over the years. I am also particularly grateful to Professor Rolf Mahnken for taking the first co-chair in my dissertation procedure and the conversations at meetings and conferences. Furthermore, I want to thank Professor Samuel Forest for taking on the function of the second co-chair. I would also like to thank Professor Peter Eberhard, Dr. Florian Fleissner and Dr. Fabian Spreng from the Institute of Engineering and Computational Mechanics for their support and the discussions surrounding my work with Pasimodo.

The atmosphere during my time at the Institute of Applied Mechanics was outstanding, scientific and personal conversations always had their equal and open spaces. For this, I would like to thank my colleagues and friends Ekin Altan, Dr. Lukas Böger, Christian Bleiler, Lukas Eurich, Dr. Felix Fritzen, Davina Fink, Dr. Ehsan Ghobadi, Dr. Kai Häberle, Dr. Thomas Heidlauf, Andreas Hessenthaler, Dr. Said Jamai, Nadine Kijanski, Dr. David Koch, Oliver Kunc, Dr. Chenyi Luo, Mylena Mordhorst, Matthias Ruf, Malte Sauerwein, Dr. Maik Schenke, Patrick Schmidt, Patrick Schröder, Alixa Sonntag, Dr. Michael Sprenger, Stephan Teichtmeister and Dr. Arndt Wagner. I really enjoyed the time I spent with all of you. Beyond that I owe thanks to Dr. Okan Avci for firstly introducing me to the continuum-mechanical world during his time at the institute and for the competitive tennis matches.

Finally, I want to thank my family, especially my parents on whom I can always rely on and Faris for his careful proof-reading. My deepest gratitude go to Katrin, Franka and Kuno for their patience and for their incomparable way of reminding me of the essential things in life.

Stuttgart, June 2019 Sami Bidier

Contents

Deutschsprachige Zusammenfassung

In der Natur, aber auch in klassischen Bauteilversuchen, kann mit dem bloßen Auge nur das makroskopische Verhalten von Strukturen und Materialien beobachtet werden. Die Materialantwort auf eine äußere Belastung ergibt sich jedoch stets aus der Zusammensetzung und der Interaktion des Materials auf verschiedenen Längen- und Zeitskalen. In den letzten Jahrzehnten war das Verständnis verschiedener Prozesse und Wechselwirkungen zwischen den Skalen ein maßgeblicher Bestandteil der Forschung. Dies trifft besonders auf den Bereich der Materialmodellierung zu, bei dem skalenabhängig unterschiedliche physikalische Prinzipien angewandt werden, was wiederum zu der Verwendung unterschiedlicher Berechnungsmethoden führt.

Die mechanische Beschreibung granularer Materialien bleibt eine wissenschaftlich sehr anspruchsvolle Aufgabe, in der viele Phänomene noch nicht vollständig verstanden sind. Dies erklärt sich primär durch das unterschiedliche Verhalten von Granulaten unter verschiedenen Bedingungen. In loser Zusammensetzung ähnelt ihr Verhalten dem von Flüssigkeiten. Im Gegensatz dazu können verfestigte oder unter Druck stehende Granulate Schubspannungen übertragen und zeigen daher festkörperähnliches Materialverhalten. Ferner versagen granulare Materialien oftmals lokal durch Scherbandbildung, welche beispielsweise bei Erdrutschen aber auch experimentell in Biaxial- und Triaxialversuchen beobachtet werden kann. Im Rahmen einer mathematisch-physikalisch basierten Modellierung granularer Medien kann eine partikelbasierte Beschreibung gewählt werden. Dabei wird die Bewegung der Partikel direkt beschrieben und somit die Komplexität des Materials basierend auf der tatsächlichen Mikrostruktur so exakt wie möglich abgebildet. Die Diskrete-Elemente-Methode stellt hierbei ein geeignetes numerisches Verfahren dar, um mit einer großen Anzahl als starr angenommener Partikel umzugehen. Sie wird häufig im Bereich der Geomaterialien sowie in Pulver- und Partikelverfahrenstechnologien angewandt. Trotz rasch wachsender Rechenleistung kann diese Methode jedoch nicht mit klassischen kontinuumsbasierten Ansätzen, insbesondere in Kombination mit der weit verbreiteten Finite-Elemente-Technologie konkurrieren, da mit diesem Ansatz nahezu alle Arten groß- und kleinskaliger Ingenieursprobleme berechnet werden können.

Die klassischen kontinuumsmechanischen Ansätze basieren jedoch auf der Annahme, dass der Gesamtkörper die Manigfaltigkeit unendlich kleiner materieller Punkte ist, welchen wiederum die physikalischen Eigenschaften zugewiesen werden. Die diskrete Charakteristik der Mikrostruktur des Materials wird daher als homogen verteilt angenommen, sodass sie nur in einem effektiven Sinne in die Modellierung einfließen muss. Im Bereich granularer Medien zeigen experimentelle Beobachtungen der letzten Jahrzehnte jedoch deutlich, dass beispielsweise lokale Rotationen der einzelnen Körner auf der Mikroebene eine signifikante Rolle bei der Scherbandbildung spielen. Die Gruppe der kinematisch erweiterten Mikrokontinuumstheorien ist eine Möglichkeit diese Mikrostruktureffekte in eine kontinuumsbasierte Modellierungsstrategie einzubeziehen. Dabei wird die makroskopische Bewegung an einem materiellen Punkt durch eine Mikrobewegung ergänzt, die möglichst so formuliert ist, dass alle relevanten mikroskopischen Deformationsmechanismen berücksichtigt

sind. Gleichzeitig ergibt sich dadurch die Möglichkeit, größenabhängige Phänomene abzubilden, da die Annahme der Infinitesimalität des materiellen Punktes aufgehoben werden muss, und damit inhärent eine Längenskala in die Modellierung einbezogen wird. In dieser Arbeit spielen insbesondere mikromorphe und mikropolare Kontinuumsformulierungen eine zentrale Rolle. Der Unterschied liegt dabei in der Annahme, ob das eingebettete Mikrokontinuum starr (mikropolare Formulierung) oder homogen deformierbar (mikromorphe Fomrulierung) ist. Trotz der Erweiterung sind beide Formulierungen jedoch weiterhin rein makroskopische Ansätze, da beispielsweise der Mikro- und der Makrodeformationsgradient immer noch als gemittelte Größen aufgefasst werden müssen und damit auf ein phänomenologisches Modell führen. Bei der Anwendung derartiger Formulierungen stellt sich allerdings die Frage, ob die in diesem Zusammenhang eingeführten zusätzlichen Spannungs- und Verformungsgrößen tatsächlich makroskopisch in Erscheinung treten und daher auch eine physikalische Notwendigkeit besitzen. Diese Fragestellung kann durch die Anwendung geeigneter Homogenisierungsverfahren, welche mikrostrukturelle Informationen durch Mittelungsverfahren auf eine höherwertige Skala übertragen, beantwortet werden. Dabei wird im Idealfall ohne Berücksichtigung makroskopischer Annahmen eine Verbindung zwischen mikro- und makroskopischen Größen hergestellt.

Die methodische Entwicklung einer solchen Homogenisierungsmethode im Bereich granularer Medien ist das wesentliche Ziel der vorliegenden Monografie. Dabei werden, wie oben erwähnt, partikelbasierte Informationen der Mikroskala mit makroskopischen Größen mikromorphen und mikropolaren Charakters verknüpft. Die Arbeit stellt dabei insbesondere mikromorphe Kontinuumsmodelle im Anwendungsbereich granularer Materialien mit deformierbaren Konstituierenden in den Fokus, da existierende Homogenisierungsmethoden bereits detailliert den Zusammenhang zwischen Mikrostrukuren, die aus starren Partikeln bestehen, und mikropolaren Kontinuumsansätzen hergestellt haben.

Zunächst ist jedoch ein Verständnis der erweiterten kontinuumsmechanischen Formulierungen notwendig. Im Anschluss an die Einleitung in Kapitel 1, welche eine ausführliche Motivation der Arbeit und eine Zusammenstellung des wesentlichen Stands der Forschung in den behandelten Bereichen umfasst, wird daher in Kapitel 2 eine systematische Einführung in die Thematik der Mikrokontinuumstheorien gegeben. Dazu werden die grundlegenden Beziehungen für die kinematische Beschreibung, den Spannungszustand und die beschreibenden Bilanzgleichungen strukturiert abgeleitet. Ausgangspunkt ist eine kurze Einführr ung in die Standardbeschreibung des Cauchy-Kontinuums, gefolgt von der mikropolaren Erweiterung und einer detailliertere Ausarbeitung der mikromorphen Kontinuumsformulierung.

Kapitel 3 behandelt das eigentliche Homogenisierungsverfahren. Dieses basiert im Wesentlichen auf der Ausnutzung des sogenannten Mikro-meso-makro Prinzips. Dabei wird für die Formulierung einer mikromorphen Homogenisierung ein Ensemble homogen deformierbarer Partikel als Repräsentatives Elementarvolumen (REV) auf einer zusätzlich eingeführten Mesoskala definiert. Die mesoskopische Skala ist in ihrer Größenordnung klar von der räumlich niedrigeren Mikroskala der einzelnen Partikel und der darüber liegenden makroskopischen Skala des Gesamtkörpers getrennt. Die Anwendung dieser Skalentrennung zwischen den drei betrachteten Skalen vereinfacht die Gleichgewichtsbeziehungen, sowohl für in den Gesamtkörper eingebettete REV, als auch für in das REV eingebet-

tete Einzelpartikel. Dies führt letztendlich zu der Möglichkeit, Gleichungen für die volumenspezifische Mittelung herzuleiten, welche die direkte Übertragung der mikroskopischen Informationen auf mikromorphe Größen erlaubt. Dadurch wird die physikalische Verbindung zwischen der granularen Mikrostruktur und dem makroskopischen Kontinuum in Form von Kontaktkräften und Spannungen auf der Partikelskala und den erweiterten Spannungstensoren der mikromorphen Makroformulierung hergestellt. Die Spannungshomogenisierung basiert auf dem Vergleich zweier unterschiedlicher Spannungsdefinitionen bezüglich des REV. In der ersten Beschreibung wird der Spannungstensor aus dem Kräftegleichgewicht am REV bestimmt, er ist dadurch nicht explizit von lokalen Partikeldeformationen abhängig. In der zweiten Beschreibung wird ein weiteres Spannungsmaß als volumetrisches Mittel der Partikelspannungen bestimmt, demnach ist es explizit von möglichen lokalen Deformationen der einzelnen Partikel im REV abhängig. Die Verknüpfung der beiden Spannungsgrößen führt auf eine Spannungsdifferenz, die hier als wesentlicher Indikator für mikromorphes Materialverhalten angesehen wird. Eine weitere Verbindung zwischen partikelbasierten und mikromorphen Größen besteht außerdem zwischen den lokalen Partikeldeformationen, den Partikelverschiebungen und -rotationen auf der einen Seite und den Deformations- und Verzerrungstensoren der Kontinuumsbeschreibung auf der anderen Seite.

Um die eingeführte Homogenisierungsmethodik zu verifizieren, sind partikelbasierte Simulationen von Materialversagen in granularen Materialien erforderlich. Die dadurch berechneten Mikrostrukturinformationen werden dann in Richtung der REV Skala verarbeitet. Dazu werden in Kapitel 4 die notwendigen Grundlagen der Diskrete-Elemente-Methode vorgestellt. Für die Simulationen wird eine vereinfachende Repräsentation des Granulats mittels starrer kugelförmiger Partikel gewählt. Das Materialverhalten wird durch konstitutive Kontaktformulierungen festgelegt. Diese werden getrennt für den Normalkontakt, den Tangentialkontakt und zusätzlich in rotatorischer Richtung definiert. Das dadurch definierte Modell ist geeignet, um nach der Homogenisierung mikropolare Größen zu identifizieren. Um zusätzlich mikromorphe Eigenschaften zu erfassen, wird das Model durch verformbares Binde- oder Matrixmaterial erweitert. Diese werden über verformbare Balkenelemente, die benachbarte Partikel verbinden, zusätzlich in die Modellierung einbezogen. Das vollständige idealisierte Modell ermöglicht den Übergang der kontinuierlich formulierten Mittelungsgleichungen auf eine diskrete Form, in welcher nur noch eine finite Anzahl von Partikeln ausgewertet werden.

Da mikropolare Effekte unabdingbar bei der Lokalisierung granularer Materialien sind, liegt der Schwerpunkt der darauf folgenden Simulationen in Kapitel 5 auf der Modellierung von Scherbandphänomenen. Als beispielhafte Materialien werden ein reiner Quarzsand und ein mittels Bindermaterial gebundener Quarzsand gewählt. Letzterer ist hierbei ein häufig verwendetes Material für Sandgußverfahren in Metallgussanwendungen. In beiden Fällen kann die Initiierung und die vollständige Ausbildung von Scherbändern erfolgreich simuliert werden. Dazu werden kleinskalige Simulationen uniaxialer Druck- und Zugversuche sowie biaxialer Druckversuche durchgeführt.

Die Anwendung der Homogenisierungsstrategie auf die Ergebnisse der Diskrete-Elemente-Simulationen sind in Kapitel 6 zusammengestellt. Dabei ergeben sich die folgenden Kernaussagen: Wie im mikropolaren Fall sind die erweiterten Spannungs- und Defor-

mationsgrößen der mikromorphen Theorie überwiegend in lokalisierten Zonen konzentriert. Die Größe des gewählten REV ist der wesentliche kritische Faktor, um mikromorphe Effekte auf der makroskopischen Skala identifizieren zu können und korreliert daher mit der intrinsischen Längenskala der Kontinuumsformulierung. In diesem Zusammenhang zeigt eine Variation der REV-Größe den Verlust der mikrostrukturellen Informationen mit zunehmender REV-Größe im mikromorphen und im mikropolaren Fall. Mit Hilfe der Bilanz der mechanischen Leistung eines REV können außerdem die arbeitskonjugierten Paare von gemittelten Spannungs- und Verformungsgrößen identifiziert werden. Die Evaluierung der geleisteten Arbeit von REV in der Scherzone liefert einen zusätzlichen wichtigen Einblick in die Notwendigkeit, Mikrokontinuumserweiterungen bei der Wahl eines makroskopischen Modellierungsansatzes zu berücksichtigen. Während die mikropolaren Anteile signifikant zur gesamten mechanischen Arbeit beitragen, trifft dies, zumindest für die in dieser Arbeit exemplarisch gewählten Materialien, nicht für die zusätzlichen mikromorphen Anteile der Beschreibung zu.

Die vorliegende Arbeit wird durch eine Zusammenfassung und einen kritischen Ausblick in Kapitel 7 abgeschlossen.

English summary

In classical material tests, but also in nature, the macroscopic behaviour of structures and materials is observed. However, the material response to an external loading always results from the composition and the interaction of the material at different time and length scales. In recent decades, the understanding of different processes and interactions between scales has been a major topic of research. This is especially true in the field of material modelling, where often different physical principles are applied depending on the chosen scale, which in turn leads to the use of different computational methods.

The mechanical description of granular materials remains a scientifically demanding task, in which many phenomena are yet not fully understood. This is primarily due to the different behaviour of granules under different conditions. In loose composition, their behaviour resembles that of fluids. In contrast, solidified or pressurised granulates can transmit shear stresses and therefore exhibit solid-like material behaviour. Furthermore, granular materials often fail locally by shear banding, which can be observed, for example, in landslides but also experimentally in biaxial and triaxial experiments. Within the scope of a modelling of granular media, a particle-based description can be chosen, describing the movement of the particles in a direct way. Thus, the material's complexity is accounted for as accurately as possible based on the actual microstructural composition. The Discrete-Element Method is a suitable numerical method for dealing with a large number of rigidly assumed particles. It is widely used in the field of geomaterials as well as in powder and particle-process technologies. However, despite rapidly increasing computational power, this method can not compete with classical continuum-based approaches, especially when they are applied in combination with the widely used Finite-Element technology, since this approach allows the computation of almost all types of large- and small-scale engineering problems.

However, classical continuum-mechanical approaches are based on the assumption that the overall body is the manifold of infinitesimally small material points to which the physical properties are assigned. The discrete characteristic of the microstructure of the material is therefore assumed to be distributed homogeneously, such that it only needs to be incorporated into the modelling in an effective sense. In the field of granular media, however, experimental observations from recent decades clearly show that, for example, local rotations of the individual grains at the micro-level play a significant role in shear band formations. The group of kinematically extended microcontinuum theories is one way of incorporating these microstructural effects into a continuum-based modelling strategy, in which the macroscopic motion at a material point is extended by a micromotion that should consider all relevant microscopic deformation mechanisms. At the same time, this results in the possibility of modelling size-dependent material behaviour, since the assumption of the infinitesimality of the material point is abandoned, and thus a length scale is inherently included into the description. Especially micromorphic and micropolar continuum formulations play a central role in this work. The difference lies in the assumption whether the embedded microcontinuum is rigid (micropolar formulation) or

homogeneously deformable (micromorphic formulation). However, despite the kinematic extensions, both formulations continue to be purely macroscopic approaches, since, for example, the micro- and macrodeformation gradients still have to be understood as averaged quantities and the overall approach remains a phenomenological one. The application of such formulations, however, arises the question whether the additional stresses and deformations introduced in this context actually emerge macroscopically and therefore exhibit a physical necessity. This question can be answered by applying suitable homogenisation methods, which transfer microstructural information to a spatially higher scale via volumetric averaging techniques. Ideally, a connection is thereby established between the microscopic and the macroscopic scale without taking into any assumptions concerning the macroscopic material behaviour into account.

The methodical development of such a homogenisation method in the field of granular media is the main aim of this monograph. As mentioned above, particle-based information from the microscale is thereby linked to macroscopic quantities of micromorphic and micropolar character. A particular emphasis is on micromorphic continuum models in the application field of granular materials with deformable constituents, since existing homogenisation methods already clearly show the relationship between microstructures consisting of rigid particles and micropolar continuum formulations.

First, however, an understanding of the extended continuum-mechanical formulations is necessary. Following the introduction in Chapter 1, which provides a more detailed motivation for the work and a short revision of the state of the art in the treated areas, Chapter 2 gives a systematic introduction to the topic of microcontinuum theories. For this purpose, the basic relationships for the kinematic description, the stress state and the governing balance relations are derived in a structured manner. The starting point is a short introduction to the standard description of the Cauchy continuum, followed by the micropolar extension and a more detailed elaboration of the micromorphic continuum formulation.

Chapter 3 deals with the actual homogenisation strategy. It is based on the exploitation of the so-called micro-meso-macro principle. For the formulation of a micromorphic homogenisation, an ensemble of homogeneously deformable particles is therefore defined as a Representative Elementary Volume (REV) on an additionally introduced mesoscale. The mesoscopic scale is clearly separated from the spatially lower microscale of the individual particles and the spatially higher macroscopic scale of the continuum body. The application of this scale separation between the three considered scales simplifies the equilibrium relationships, both for REV embedded in the overall body and for single particles embedded in the REV. This ultimately leads to the possibility of deriving volume-specific averaging formalisms, which allow the direct transfer of microscopic information towards micromorphic quantities on the REV level.

This establishes the physical connection between the granular microstructure and the micromorphic continuum. The relationship exists between contact forces and stresses on the particle scale and the extended stress tensors of the micromorphic formulation. The stress homogenisation is based on the comparison of two different stress averaging procedures with respect to the REV. In the first description, the stress tensor is determined from the equilibrium of the external forces at the REV level, and is therefore not explicitly

dependent on local particle deformations. In the second description, a microstress average tensor is determined as the volume average of the microscale particle stresses. It is thus explicitly dependent on possible local deformations of the individual particles in the REV. The combination of the two balance relations incorporating the two stress measures leads to a micromorphic stress difference, which is here considered to be an essential indicator for micromorphic material behaviour. A further link between particle-based information and micromorphic continua is derived between the local particle deformation, the particle displacement and rotation on the one side, and the deformation and curvature tensors of the extended continuum description on the other side.

To verify the established homogenisation methodology, particle-based simulations of material failure in granular materials are required, supplying the necessary microstructural information, which is then processed towards the REV scale. For this purpose, the fundamentals of the applied Discrete-Element Method are presented in Chapter 4. For the simulations, a simplifying spherical discrete element representation of the granular material is chosen. The material behaviour is assigned to constitutive contact formulations. These are defined separately for the normal contact, the tangential contact and additionally for the relative rotational direction between two interacting particles, introducing a rolling resistance model to tackle the grain-shape simplification. The thereby obtained model is suitable for identifying micropolar effects after homogenisation. In order to additionally detect micromorphic properties, the model is extended by deformable binder or matrix material, which is phenomenologically included into the model via deformable beam elements connecting neighbouring particles. The complete idealised model allows for the transition of the continuously formulated averaging formalisms towards discrete forms in which only a finite number of particles are evaluated for the computation of the stress and strain quantities on the REV level.

Since micropolar effects are known to be active in localised zones of granular materials, the focus of the subsequent simulations in Chapter 5 is on the modelling of shear band phenomena, using as exemplary materials an unbonded and an initially bonded quartz sand. The latter is a frequently used material for sand-based moulds for metal casting applications. In both cases, the initiation and the complete evolution of primary shear bands is successfully simulated in uniaxial compression and tension tests as well as biaxial compression tests.

The application of the homogenisation strategy to the results of Discrete-Element simulations is summarised in Chapter 6. The investigation reveals the following key points: As in the micropolar case, the extended stress and deformation measures of the micromorphic theory are predominantly concentrated in localised zones. The chosen size of the REV is the major critical factor for identifying micromorphic effects on the REV scale, and thus correlates with the intrinsic length scale of the continuum formulation. In this context, a variation in the REV size shows the loss of microstructural information with increasing REV size in the micromorphic and in the micropolar case. The balance of mechanical power of an REV is furthermore used to identify the work-conjugated pairs of averaged stress and strain quantities. The evaluation of the internal mechanical work of an REV in the shear zone then provides additional important insight into the need to consider microcontinuum extensions when choosing a macroscopic modelling approach. While the

micropolar extension contributes significantly to the overall mechanical work, this is not true for the additional micromorphic part of the extensions, at least for the materials exemplarily modelled in this work.

The monograph concludes with a summary and a critical outlook in Chapter 7.

Nomenclature

The nomenclature and notation of modern tensor calculus, generally used in continuum mechanics, is adopted for the present monograph. The principle style follows the notation given in Ehlers [59]. Specific conventions and symbols are given in the following, excluding additional symbols and notations used in the Appendices.

Conventions

General conventions

$(\bullet)$			placeholder for arbitrary quantities
$a, b, \ldots$	or	$\alpha, \beta, \ldots$	scalars (zero-order tensors)
$\mathbf{a}, \mathbf{b}, \ldots$	or	$\boldsymbol{\alpha}, \boldsymbol{\beta}, \ldots$	vectors (first-order tensors)
$\mathbf{A}, \mathbf{B}, \ldots$			tensors of second order
$\overset{n}{\mathbf{A}}, \overset{n}{\mathbf{B}}, \ldots$			tensors of n-th order

Index and suffix conventions

$i, j, k, n, \ldots$	indices (control variables) as super- or subscripts
$(\bullet)_{\mathcal{B}}$	stress or deformation quantity at the body scale following from homogenisation
$(\bullet)_m$	quantities at the microcontinuum/particle scale
$(\bullet)^{(i)}$	quantities in a setting with a distinct number of particles
$(\bullet)_0$	initial values of non-kinematical quantities with respect to the referential configuration
$\dot{(\bullet)} = \mathrm{d}(\bullet)/\mathrm{d}t$	total time derivative
$\overset{\Delta}{(\bullet)} / \overset{\nabla}{(\bullet)}$	upper/lower Oldroyd time derivative
$\mathrm{d}(\bullet)$	differential operator
$\partial(\bullet)$	partial derivative operator
$\langle(\bullet)\rangle$	volume-specific average
$\langle(\bullet)\rangle_A$	surface-specific average

Symbols

Greek letters

Symbol	Unit	Description
α_c	[-]	compressive strength factor of the bond-element formulation
α_s	[-]	shear coefficient of the Timoshenko-beam formulation
δ	[m]	characteristic size of the microscale
δ_i^j		Kronecker symbol or Kronecker delta
$\delta^{(ij)}$	[m]	particle indentation
Δt	[s]	time increment
ϵ	[-]	scale parameter between micro- and mesoscale
ε	[J/kg]	mass-specific internal energy
$\bar{\theta}$	[rad]	angle, defining the active contact are at $\mathcal{S}_c$ of the rotational resistance model
μ_s	[-]	sticking (static) friction coefficient
μ_d	[-]	sliding (dynamic) friction coefficient
ν	[-]	Poison's ratio
ρ	[kg/m^3]	density
ς	[$\cdot$/m^3]	volume-specific supply term of scalar-valued mechanical quantities
σ_V	[N/m^2]	von Mises equivalent stress
σ_y	[N/m^2]	stress-threshold value
φ	[rad]	rotation angle
$\bar{\varphi}$	[rad]	total rotation angle
Ψ	[$\cdot$/m^3]	volume-specific density of scalar mechanical quantities
$\hat{\Psi}$	[$\cdot$/m^3]	volume-specific production term of scalar mechanical quantities
$\boldsymbol{\zeta}$ / $\boldsymbol{Z}$		actual/referential normal vector to the material surface of the microccontinuum
$\boldsymbol{\xi}$ / $\boldsymbol{\Xi}$		actual/referential director
$\boldsymbol{\varsigma}$	[$\cdot$/m^3]	volume-specific supply term of vector-valued mechanical quantities
$\boldsymbol{\varphi}$	[rad]	rotation vector
$\boldsymbol{\varphi}^{(ij)}$	[rad]	relative rotation between two particles
$\bar{\boldsymbol{\varphi}}^{(ij)}$	[-]	normalised relative rotation between two particles
$\boldsymbol{\varphi}_r^{(ij)}$	[rad]	rolling part of $\boldsymbol{\varphi}^{(ij)}$
$\boldsymbol{\varphi}_t^{(ij)}$	[rad]	twisting part of $\boldsymbol{\varphi}^{(ij)}$
$\boldsymbol{\chi}$ / $\boldsymbol{\chi}^{-1}$		motion/inverse motion function

$\boldsymbol{\Psi}$	$[\cdot/\mathrm{m}^3]$	volume-specific densities of vector-valued mechanical quantities
$\hat{\boldsymbol{\Psi}}$	$[\cdot/\mathrm{m}^3]$	volume-specific production term of vector-valued mechanical quantities
$\boldsymbol{\phi}$	$[\cdot/\mathrm{m}^2]$	vector-valued surface-specific efflux term of mechanical quantities
$\boldsymbol{\omega}$	$[\cdot/\mathrm{s}]$	angular velocity
$\boldsymbol{\Delta}$	$[\cdot/\mathrm{s}]$	deformation velocity tensor
$\bar{\boldsymbol{\Delta}}$	$[\cdot/\mathrm{s}]$	micropolar deformation velocity tensor
$\bar{\boldsymbol{\varepsilon}}$	[-]	geometrically linearised micropolar or micromorphic strain tensor
$\boldsymbol{\theta}$	$[\mathrm{kg\,m}^2]$	mass-moment-of-inertia tensor of a microcontinuum
$\bar{\boldsymbol{\Theta}}$	$[\mathrm{kg\,m}^2]$	micropolar mass-moment-of-inertia tensor
$\boldsymbol{\Theta}_{\mathcal{M}}$	$[\mathrm{kg\,m}^2]$	mass-moment-of-inertia tensor of a rigid particle $\mathcal{P}$ with respect to $\mathcal{M}$
$\bar{\boldsymbol{\kappa}}$	$[1/\mathrm{m}]$	geometrically linearised curvature tensor
$\overset{3}{\bar{\boldsymbol{\kappa}}}$	$[1/\mathrm{m}]$	geometrically linearised third-order curvature tensor
$\boldsymbol{\lambda}$	$[\mathrm{m\,m/s}^2]$	micromorphic spin-inertia tensor
$\bar{\boldsymbol{\mu}}$	$[\mathrm{Nm/m}^2]$	geometrically linearised couple stress tensor
$\overset{3}{\bar{\boldsymbol{\mu}}}^d$	$[\mathrm{Nm/m}^2]$	geometrically linearised dyadic stress moment tensor
$\boldsymbol{\varepsilon}$	[-]	geometrically linearised strain tensor
$\bar{\boldsymbol{\varepsilon}}$	[-]	geometrically linearised micropolar or micromorphic strain tensor
$\boldsymbol{\varepsilon}_b$	[-]	geometrically linearised bond strain tensor
$\boldsymbol{\varepsilon}_M$	[-]	geometrically linearised REV mircrostrain tensor
$\boldsymbol{\sigma}$	$[\mathrm{N/m}^2]$	geometrically linearised stress tensor
$\boldsymbol{\sigma}_b$	$[\mathrm{N/m}^2]$	geometrically linearised bond stress tensor
$\boldsymbol{\sigma}_M$	$[\mathrm{N/m}^2]$	geometrically linearised microstress average
$\boldsymbol{\tau}$	$[\mathrm{N/m}^2]$	Kirchhoff stress tensor
$\boldsymbol{\Phi}$	$[\cdot/\mathrm{m}^2]$	surface-specific efflux term of mechanical quantities
$\boldsymbol{\Omega}$	$[\cdot/\mathrm{s}]$	skew-symmetric gyration tensor
$\bar{\boldsymbol{\Omega}}$	$[\cdot/\mathrm{s}]$	skew-symmetric micropolar gyration tensor
$\boldsymbol{\Omega}_M$	$[\cdot/\mathrm{s}]$	skew-symmetric gyration tensor of an embedded particle in an REV

Latin letters

Symbol	Unit	Description
A		number of particles in an REV
B		number of REV-boundary particles
c		contact point between two interacting particles
c_s	[-]	shape parameter of the rolling resistance model
d	[m]	characteristic size of the mesoscale
d_{50}	[m]	mean particle size of a grain size distribution
d_n	[Ns/m^3]	local damping coefficient in contact normal direction at $\mathcal{S}_c$
$d_{\mathcal{R}}$	[m]	REV diameter
D	[m]	characteristic size of the macroscale
D_n	[Ns/m]	damping coefficient in contact normal direction
D_t	[Ns/m]	damping coefficient in relative tangential contact direction
D_φ	[Nms]	damping coefficient in relative rotational contact direction
$\mathrm{d}m$	[kg]	local mass element
$\mathrm{d}v \,/\, \mathrm{d}V$	[m^3]	actual/referential volume element
E	[N/m^2]	Young's modulus
J	[-]	Jacobian determinant of $\mathbf{F}$
k_n	[N/m^3]	local contact stiffness in contact normal direction at $\mathcal{S}_c$
K_n	[N/m^2]	Hertzian contact stiffness in contact normal direction
K_n^{lin}	[N/m]	linear contact stiffness in contact normal direction
K_t	[N/m]	contact stiffness in relative tangential contact direction
K_φ	[Nm]	contact stiffness in relative rotational contact direction
m	[kg]	mass
M		number of bond contacts
N		number of direct point contacts
P		material point
r	[m]	radius of a particle
$r^{(ij)}$	[m]	common radius (harmonic mean of the radii of two particles)
R	[m]	radius of the contact surface $\mathcal{S}_c$
t	[s]	time
V	[m^3]	volume
w_i	[Nm/(kg s)]	mass-specific internal stress power
W_i	[Nm]	internal mechanical work
$\mathbf{a}$	[m/s^2]	acceleration vector
$\mathbf{b}$	[m/s^2]	mass-specific body force vector
$\mathbf{c}$	[m^2/s^2]	mass-specific body couple

$\mathrm{d}\mathbf{a}\,/\,\mathrm{d}\mathbf{A}$	$[\,\mathrm{m}^2\,]$	actual/referential area element
$\mathrm{d}\mathbf{x}\,/\,\mathrm{d}\mathbf{X}$	$[\,\mathrm{m}\,]$	actual/referential line element
$\mathbf{e}_i$	$[\,\text{-}\,]$	(Cartesian) basis of orthonormal vectors
$\mathbf{e}$	$[\,\text{-}\,]$	central axis of the rotation vector $\boldsymbol{\varphi}$
$\bar{\mathbf{e}}$	$[\,\text{-}\,]$	central axis of the total rotation vector $\bar{\boldsymbol{\varphi}}$
$\mathbf{f}$	$[\,\mathrm{N}\,]$	volume force vector acting on P from a distance
$\mathbf{f}_b$	$[\,\mathrm{N}\,]$	resulting force from the stress distribution of a bond
$\mathbf{f}_c$	$[\,\mathrm{N}\,]$	contact force at c
$\mathbf{f}_{c,n}$	$[\,\mathrm{N}\,]$	normal part of the contact force
$\mathbf{f}_{c,t}$	$[\,\mathrm{N}\,]$	tangential part of the contact force
$\mathbf{f}_{ex}$	$[\,\mathrm{N}\,]$	resulting discrete force vector at $\mathcal{M}$, corresponding to $\mathbf{t}$
$\mathbf{f}_M$	$[\,\mathrm{N}\,]$	resulting discrete force vector at $\mathcal{M}$, corresponding to $\mathbf{t}_M$
$\mathbf{g}$	$[\,\mathrm{m/s}^2\,]$	constant gravitation vector
$\mathbf{h}_{\mathcal{O}}$	$[\,\mathrm{kg/m\,s}\,]$	local angular momentum with respect to $\mathcal{O}$
$\mathbf{h}_{\mathcal{M}}$	$[\,\mathrm{kg/m\,s}\,]$	local angular momentum with respect to $\mathcal{M}$
$\mathbf{k}$	$[\,\mathrm{N}\,]$	total force from contact and volume-specific forces
$\mathbf{l}$	$[\,\mathrm{kg/m}^2\,\mathrm{s}\,]$	local linear momentum vector
$\mathbf{l}_b$	$[\,\mathrm{m}\,]$	branch vector to the contact surface $\mathcal{S}_c$
$\mathbf{l}_c$	$[\,\mathrm{m}\,]$	branch vector to the contact point c
$\bar{\mathbf{m}}$	$[\,\mathrm{Nm/m}^2\,]$	couple stress vector in relation to $\bar{\mathbf{M}}$
$\mathbf{m}_b$	$[\,\mathrm{Nm}\,]$	resulting moment from the stress distribution of a bond
$\mathbf{m}_c$	$[\,\mathrm{Nm}\,]$	contact moment
$\mathbf{m}_d$	$[\,\mathrm{Nm}\,]$	viscous contact moment
$\mathbf{m}_{\mathcal{M}}$	$[\,\mathrm{Nm}\,]$	resulting moment with respect to $\mathcal{M}$
$\bar{\mathbf{m}}_c$	$[\,\text{-}\,]$	normalised contact moment
$\bar{\mathbf{m}}_{ex}$	$[\,\mathrm{Nm}\,]$	resulting discrete moment at $\mathcal{M}$, corresponding to $\bar{\mathbf{m}}$
$\mathbf{m}_{\mathcal{O}}$	$[\,\mathrm{Nm}\,]$	resulting moment with respect to $\mathcal{O}$
$\bar{\mathbf{m}}_M$	$[\,\mathrm{Nm/m}^2\,]$	couple stress vector in relation to $\bar{\mathbf{M}}_M$
$\mathbf{n}$	$[\,\text{-}\,]$	outward-oriented unit surface normal vector
$\mathbf{n}_c$	$[\,\text{-}\,]$	outward-oriented contact normal at c
$\mathbf{t}$	$[\,\mathrm{N/m}^2\,]$	surface traction vector in relation to the stress tensor $\mathbf{T}$
$\mathbf{t}_b$	$[\,\mathrm{N/m}^2\,]$	surface traction vector in relation to the bond stress tensor $\mathbf{T}_b$
$\mathbf{t}_M$	$[\,\mathrm{N/m}^2\,]$	surface traction vector in relation to the stress tensor $\mathbf{T}_M$
$\mathbf{u}$	$[\,\mathrm{m}\,]$	displacement vector
$\mathbf{u}_b$	$[\,\mathrm{m}\,]$	local displacement vector of a bond
$\mathbf{u}_c^{(ij)}$	$[\,\mathrm{m}\,]$	relative contact displacement vector at c
$\mathbf{u}_{c,t}^{(ij)}$	$[\,\mathrm{m}\,]$	tangential part of $\mathbf{u}_c^{(ij)}$

$\mathbf{u}_r^{(ij)}$	[m]	relative displacement vector between the mass centres of two bonded particles
$\mathbf{v}$	[m/s]	velocity vector
$\mathbf{v}_c$	[m/s]	absolute particle velocity vector at c
$\mathbf{v}_c^{(ij)}$	[m/s]	relative contact velocity at c
$\mathbf{v}_{c,t}^{(ij)}$	[m/s]	tangential part of $\mathbf{v}_c^{(ij)}$
$\mathbf{v}_{\mathcal{M}}$	[m/s]	velocity vector at the mass centre $\mathcal{M}$
$\mathbf{x}\,/\,\mathbf{X}$	[m]	absolute actual/referential position vector to a material point P
$\mathbf{x}_c$	[m]	absolute position vector to the contact point c
$\bar{\mathbf{x}}_c$	[m]	relative position vector to c with respect to $\mathcal{M}$
$\mathbf{x}_M\,/\,\mathbf{X}_M$	[m]	actual/referential relative position vector of $\mathcal{M}$
$\mathbf{x}_{\mathcal{M}}\,/\,\mathbf{X}_{\mathcal{M}}$	[m]	actual/referential absolute position vector of $\mathcal{M}$
$\mathbf{A}$	[-]	contravariant Almansian strain tensor
$\bar{\mathbf{A}}$	[-]	micropolar or micromorphic Almansian strain tensor
$\mathbf{B}$	[-]	covariant left Cauchy-Green deformation tensor
$\mathbf{C}$	[-]	contravariant right Cauchy-Green deformation tensor
$\bar{\mathbf{C}}\,/\,{}^R\bar{\mathbf{C}}$	[1/m]	actual/referential second-order curvature tensor
$\overset{3}{\bar{\mathbf{C}}}\,/\,{}^R\overset{3}{\bar{\mathbf{C}}}$	[1/m]	actual/referential third-order curvature tensor
$\mathbf{D}$	[1/s]	symmetric deformation velocity tensor
$\overset{3}{\mathbf{E}}$	[-]	Ricci permutation tensor (third-order fundamental tensor)
$\mathbf{E}$	[-]	contravariant Green-Lagrangean strain tensor
$\bar{\mathbf{E}}$	[-]	micropolar or micromorphic Green-Lagrangean strain tensor
$\mathbf{F}$	[-]	deformation gradient
$\bar{\mathbf{F}}$	[-]	micromorphic director motion
$\mathbf{F}_M$	[-]	deformation gradient of an embedded particle in a REV
$\mathbf{I}$	[-]	identity tensor (second-order fundamental tensor)
$\mathbf{K}\,/\,{}^R\mathbf{K}$	[-]	actual/referential covariant Karni-Reiner strain tensor
$\mathbf{L}$	[1/s]	spatial velocity gradient
$\bar{\mathbf{L}}$	[1/s]	spatial velocity gradient of the micromorphic director motion
$\mathbf{L}_M$	[1/s]	spatial velocity gradient of an embedded particle in an REV
$\mathbf{M}$	[Nm/m^2]	Cauchy stress moment tensor
$\bar{\mathbf{M}}$	[Nm/m^2]	couple stress tensor
$\bar{\mathbf{M}}_M$	[Nm/m^2]	couple stress average tensor
$\bar{\mathbf{M}}^d$	[Nm/m^2]	surface-specific dyadic stress moment tensor at $\partial\mathcal{B}$
$\bar{\mathbf{M}}_M^d$	[Nm/m^2]	surface-specific dyadic stress moment tensor at $\partial\mathcal{R}$

$\overset{3}{\tilde{\mathbf{M}}}$	$[\mathrm{Nm/m^2}]$	third-order micromorphic dyadic stress moment tensor
$\overset{3}{\mathbf{M}}^d$	$[\mathrm{Nm/m^2}]$	third-order dyadic stress moment tensor to $\mathbf{T}$
$\overset{3}{\mathbf{M}}{}^d_M$	$[\mathrm{Nm/m^2}]$	third-order dyadic stress moment tensor to $\mathbf{T}_M$
$\overset{3}{\bar{\mathbf{M}}}{}^d_M$	$[\mathrm{Nm/m^2}]$	third-order dyadic stress moment tensor to $\bar{\mathbf{M}}^d_M$
$\mathbf{P}$	$[\mathrm{N/m^2}]$	first Piola-Kirchhoff or nominal stress tensors
$\mathbf{R}$	[-]	proper orthogonal rotation tensor of the polar decomp. of $\mathbf{F}$
$\bar{\mathbf{R}}$	[-]	micropolar director motion
$\mathbf{S}$	$[\mathrm{N/m^2}]$	second Piola-Kirchhoff stress tensor
$\mathbf{T}$	$[\mathrm{N/m^2}]$	Cauchy (true) stress tensor
$\mathbf{T}_b$	$[\mathrm{N/m^2}]$	bond stress tensor
$\mathbf{T}_M$	$[\mathrm{N/m^2}]$	microstress average
$\mathbf{U}\,/\,\mathbf{V}$	[-]	right/left stretch tensors of the polar decomposition of $\mathbf{F}$
$\bar{\mathbf{U}}\,/\,\bar{\mathbf{V}}$	[-]	right/left micropolar or micromorphic stretch tensors
$\mathbf{W}$	$[1/\mathrm{s}]$	skew-symmetric spin tensor

Calligraphic letters

Symbol	Unit	Description
$\mathcal{B}$		macroscopic body
$\partial\mathcal{B}$		surface of the macroscopic body
$\mathcal{E}$	$[\mathrm{Nm}]$	internal energy
$\mathcal{K}$	$[\mathrm{Nm}]$	kinetic energy
$\mathcal{L}_a$	$[\mathrm{Nm/s}]$	external mechanical power
$\mathcal{L}_i$	$[\mathrm{Nm/s}]$	internal mechanical power
$\mathcal{M}$		mass centre of a particle $\mathcal{P}$
$\mathcal{O}$		spatial origin
$\mathcal{P}$		particle
$\partial\mathcal{P}$		particle surface
$\mathcal{Q}_a$	$[\mathrm{Nm/s}]$	external non-mechanical power
$\mathcal{R}$		REV
$\partial\mathcal{R}$		REV surface
$\mathcal{S}_c$	$[\mathrm{m^2}]$	contact surface
$\boldsymbol{\mathcal{C}}$	$[\mathrm{m^2/s^2}]$	second-order body couples
$\bar{\boldsymbol{\mathcal{M}}}$	$[\mathrm{Nm/m^2}]$	weighted couple stress tensor

Selected acronyms

Symbol	Description
2-d	two-dimensional
3-d	three-dimensional
DE(M)	Discrete-Element (Method)
DIC	digital image correlation
DNS	direct numerical simulation
DOF	degree of freedom
FE(M)	Finite-Element (Method)
(I)BVP	(initial-)boundary-value problem
MMM	micro-meso-macro
Pasimodo	particle simulation and molecular dynamics in an object oriented fashion
PIV	particle image velocimetry
REV	representative elementary volume

Chapter 1:
Introduction and overview

1.1 Motivation

When we look at natural and engineering materials with the naked eye, we see their macroscopic behaviour. The material response, however, stems from the composition and interaction of the material on various length and time scales. Understanding the different processes on and the interactions between the scales has been one of the main driving forces in research over the last decades, calling for cooperative work between natural, computational, material and engineering sciences. This is especially true for the field of material modelling, where, depending on the scale, different physical principles are applied, leading to the use of different computational methods. One could even go as far as to state that the academic education of the individual researcher often determines the methodological approach. Engineers commonly regard an effective material behaviour or an overall structural response at the macroscale and therefore tend to apply methods such as the Finite-Element Method (FEM). Physicists often start from a quantum-mechanical point of view, while chemists investigate the bonding mechanisms between molecular structures. Both hence apply atomistic or molecular dynamic modelling techniques. Figure 1.1 gives an overview over the different length scales. In the present work, materials with a granular microstructure play an important role. Consequently, the microscale is assumed as the grain scale of such materials in the millimetre region. The macroscopic scale is given as the structural engineering or application scale.

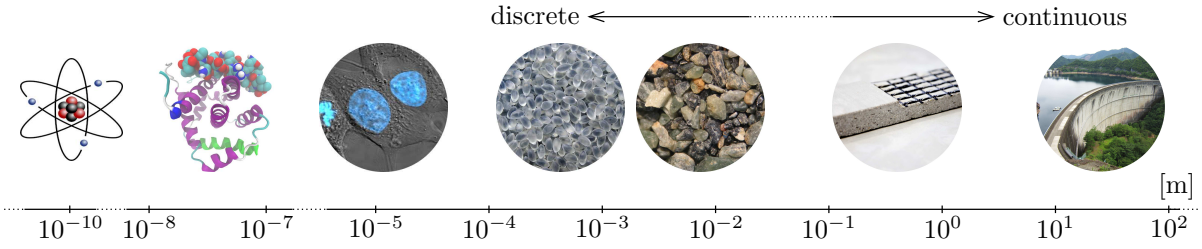

Figure 1.1: *Scales, from the atomic to the macroscopic application scale*[1].

Media with a granular character on the microscale occur in many natural circumstances as well as in engineered processes. The solid skeleton of soils generally exhibits a granular microstructure, which is frequently classified through a hydrometer or sieve analysis, showing the characteristic lognormal grain size distributions of sedimented sands as given

[1]Images, from left to right: Atom by Indolences / CCBY 3.0, BAX protein by Ayacop / public domain, HeLA cells by TenOfAllTrades / public domain, granule of thermoplastic urethane by Luigi Chiesa / CCBY 3.0, Sand grains / public domain, Carbon Concrete by Stipriaan /CCBY 3.0 and Ikehara Dam by Qurren / CCBY 3.0.

in Figure 1.2. Granulates also play an important role in pharmaceutical engineering, where pulverised medicinal products are agglomerated as particles, before being filled into pills. In plastics industry, the base materials for manufacturing processes are generally transported as granules. Despite years of scientific research, the mechanical description of granular materials is still a very challenging task and many phenomena are still not fully understood. This mainly originates from the fact that granular material behaviour is fundamentally different under varying conditions: Exemplarily, grain ensembles tend to segregate according to size, shape or density, especially when loose granulates flow in fluid-like behaviour out of silos or through pipelines or when they are exposed to cyclic loading. In contrast, wet sands show a solid-like behaviour, allowing for the construction of sand castles as the cohesion between particles is increased. Granulates not only behave like solids when they are in a fluid-saturated state, but also when they are stabilised, e. g. by an externally applied pressure. Under extensive loading, such granular solids fail through a localisation of deformation in a very narrow zone, commonly denoted as the shear zone. The transition from a mechanically stable to a mechanically unstable point in granular systems is thereby often referred to as jamming. On a large scale, localisation effects can cause severe damage to natural and human-made structures, e. g. through landslide catastrophes, while in an experimental setting, the localisation phenomena can be captured e. g. in bi- and triaxial compression tests.

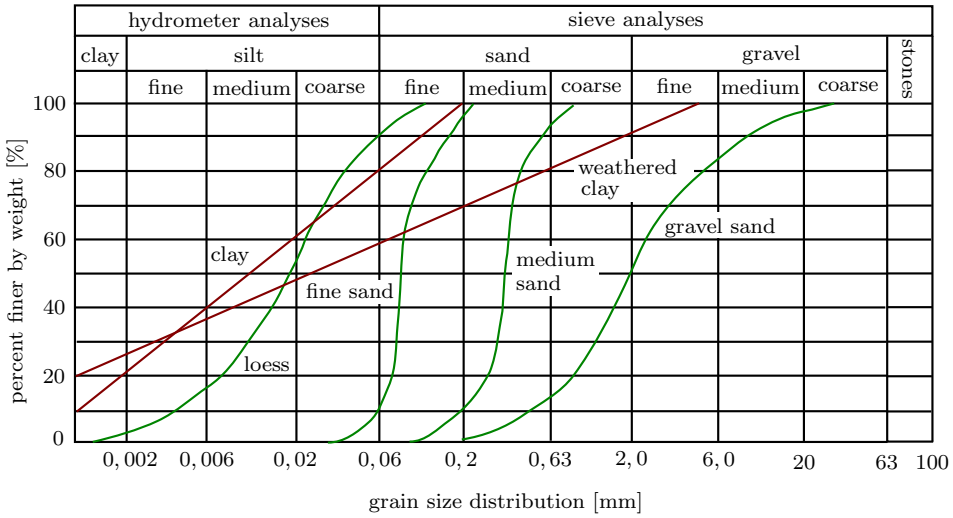

Figure 1.2: *Classification of natural soils by grain size distributions.*

Concerning the mathematical modelling, it is intuitive to choose a particle-based description for the mechanical characterisation of granular material, thereby describing the motion of each individual particle. In the case of rigid particles, this follows by the combination of Newton's equation of translational motion and Euler's equation of rotational motion for rigid bodies. The Discrete-Element Method (DEM) is the numerical computation tool to handle large numbers of such rigid particles and is frequently used in the field of geomaterials as well as in powder and particle process technologies. However, despite rapidly growing computing power, it can still not compete with classical continuum-based approaches in combination with e. g. FE tools, which allow for the computation of nearly all kinds of engineering problems. Here, in comparison to the capabilities of the

DEM, large periods of time are of interest, and additionally, when dissolved into the microstructural particles, tens of millions of discrete elements would be necessary. Classical continuum-mechanical approaches, however, are based on the principle assumption that the overall body is the manifold of infinitely small material points carrying the physical quantities and that the discrete nature of the materials micro- or atomistic structure is neglected. Although the failure of a material is clearly observed at the macroscopic engineering scale, it is yet always a result of effects at the microscale, the nanoscale or even the atomistic scale. In the case of granular media, experimental observations over the last decades clearly show that the combination of individual grain displacement and rotation play an important role in the shear band initiation and its evolution. It is therefore reasonable and common practise to regard the scale of the grains, following Figure 1.1, on the microscopic level as the smallest scale that needs consideration, at least as long as no grain crushing occurs. Microcontinuum concepts, mainly developed and introduced by A. C. Eringen and his co-workers, are one possibility to include these microstructural effects in a top-down continuum-based modelling strategy. In doing so, the motion at a material point is enriched by a micromotion that carries the deformation arising from possible deformation modes at the microscale. The envisaged consideration of microstructural deformation should foster the characterisation of the embedded micromotion in the continuum description. In particular, concerning granular media, it is well established that grain rotations are linked to a purely rotational micromotion, which leads to the micropolar or Cosserat continuum. Thus, it serves as a well suited, physically based, continuum modelling approach for granular bodies. If further microdeformational modes, for example local deformation of binder or matrix material in bonded granular material, are present, the question arises if and how the micromotion within microcontinuum approaches should be extended.

The combination of microstructural particle-based modelling with appropriate homogenisation strategies is a very promising way to answer this question. This approach directly links microstructural information to continuum theories in a bottom-up approach and is at the centre of this thesis. The process of homogenisation is, furthermore, also used in coupled multiscale simulation strategies, where it describes the transfer of stresses, strains and the material tangent from a nested microscopic Boundary-Value Problem (BVP) to a material point of the continuum description.

1.2 State of the art

Experimental background: The modelling of localisation phenomena in granular media is one key aspect of the presented thesis. In particular, a main focus is on the grain-scale simulations of shear banding in unbonded and bonded granular matter, which are needed to obtain particle-based information to be processed within the developed homogenisation scheme. In this regard, huge developments in the field of experimental mechanics over the last decades have supplied a deep insight into the mechanical behaviour of granulates and offer a new perspective for the theoretical treatment and the description of granulates. For many years, stereophotogrammetry has been used to supply deformation measures on strain localisation in sand, see e. g. Finno *et al.* [77] or the

overview given in Desrues & Viggiani [48]. After that it has become possible to determine the shear band width and its orientation in an experimental set-up. A large step forward from these full-field measurements is the usage of three-dimensional (3-d) imaging techniques, as presented in Al-Raoush [4] and Fonseca *et al.* [83], and digital microscopy (Alshibli *et al.* [6]), as they offer the possibility of accurately capturing the microstructural arrangement of grains and the geometric properties of individual grains. Thereby they furthermore allow for the clear classification of granular microstructure and its evolution during localisation (Alshibli *et al.* [6, 7], Oda *et al.* [174], Viggiani *et al.* [210]). The usage of x-ray microtomography or high resolution digital imaging techniques and the 'in situ' conduction of material tests, followed by a successive application of Digital Image Correlation (DIC), Particle Image Velocimetry (PIV) or grain tracking methods finally lead the way to the direct observation of the grain kinematics up until the microscale of the individual grain. In this regard, Niedostatkiewicz *et al.* [167] and Wolf *et al.* [220] investigated shear zone patterning in non-cohesive sand using PIV, while Adam *et al.* [1] used PIV to study mechanisms in tectonic faulting through scaled sandbox experiments. Rechenmacher [178] presented local displacement measures on the grain scale based on DIC of various experimental test set-ups. A combination of DIC and computer tomography was given by Hall *et al.* [104], where not only the displacement of individual grains was accounted for. Additionally, grain rotations were directly measured throughout the onset and the complete evolution of the localisation. Lenoir *et al.* [139] used the same combination to study localised deformation in argillaceous rocks. A combination of x-ray microtomogrophy with grain tracking methods, as presented in Andò *et al.* [11] or Gupta *et al.* [103], finally allowed the identification of the kinematics of nearly all grains during a material test based on their individual geometry. Using this so-called ID-tracking method, Desrues & Andò [46] presented summarising findings based on small-scale triaxial tests containing around 50 000 grains on three different sands. An angular-shaped Hostun quartz sand, a sub-rounded Ottawa sand and a round-grained Caicos sand. These results are of particular interest for the present thesis, as the experimental results show a single shear band on the specimen scale for all three materials with the highest shear strain concentration, meaning the smallest shear band width, for the case of rounded grains. A clear concentration of polarised grain rotations in all shear bands was observed. Most recently, the integration of the data obtained from image-based methods into simulation technologies has become a major topic in order to allow data-driven computational engineering, cf. for example Kawamoto *et al.* [132], Lim *et al.* [143] or Schneider *et al.* [186].

The aforementioned works focused on experiments on unbonded granular material, mostly sand, where the grain kinematics are of great importance, as the macroscopically observed deformation stems from particle displacement and rotation and not from particle deformation itself. If one is interested in bonded granular material, such as cemented sand (Schnaid *et al.* [185]) or sand-based moulds for metal casting (Boenisch & Lotz [25]), the mechanics of the bonding component play an equivalent role. Exemplarily, the microstructure of sand moulds used in the so-called cold box technology (Janis [123], Shriver *et al.* [195]) is an artificially generated structure of bonded quartz sand, where thin films of polyurethane-based moulding material enclose each grain, and binder bridges connect the grains at their contact areas, cf. Iden *et al.* [117]. On a microscopic scale, material failure

is frequently due to failure of these binder bridges (Boenisch & Lotz [26]), which can result in macroscopically observed shear bands (Caylak & Mahnken [28]). In this context, it is reasonable to assume that the sand particles are rigid in comparison to the deformation of the binder material, which originates from relative displacement of connected grains.

A strong need for experimental data arises from the material modelling on the microscale. When using Discrete-Element (DE) techniques, the defining material characteristics enter the constitutive contact formulation in the sense of contact modelling parameters. Attempts to directly determine these material parameters are, for example, based on impact velocity measurements for artificial spherical particles (Foerster *et al.* [82], Labous *et al.* [136], Lorenz *et al.* [146]) or single particle breakage measurements (Tavares & King [200]). However, it is generally extremely difficult to experimentally determine the elastic material constants of the natural grain material under consideration. Promising results for natural sand grains were obtained examplarily by Daphalapurkar *et al.* [45], where a nanoindentation technique was used to determine the Young's modulus and the fracture toughness of sand grains. With regard to Quartz sand material, Senetakis *et al.* [190] and Senetakis & Sandeep [191] performed a series of micromechanical shearing tests to identify the inter-particle friction coefficients. Furthermore, the experimental identification of the grain-level normal and tangential behaviour was studied in detail in Nardelli *et al.* [162] and Sandeep & Senetakis [184], including propositions of contact stiffness and friction parameters to be used in DE simulations.

Alternatively to this direct determination of the material parameters, the set of introduced modelling parameters can be calibrated by means of a parameter identification, known from respective continuum-mechanical settings, compare Mahnken & Stein [153] or Ehlers & Scholz [65]. In this context, Wang & Tonon [214] proposed an inverse calibration technique applied to DE models of rock until peak strength, while Cheng *et al.* [33] probabilistically calibrated a DE model to experimental data using a Monte-Carlo filter method.

Particle-based modelling of granular media: When taking a microscopic point of view, each grain in a granular system needs direct consideration within a particle-based modelling approach. This approach leads to the DEM as a numerical tool, firstly introduced by Cundall and Strack in the late 1970's (Cundall & Strack [42]). Although the first applications of the DEM were mostly in the field of geomechanics (Cundall [40], Cundall & Strack [42], Hart *et al.* [106]), it is nowadays, also due to commercial applications, in large parts used to model particle flow in process engineering and agriculture, see, for example, Cleary [36], Fleissner *et al.* [80, 81], Li *et al.* [141] or Tijskens *et al.* [202]. For further insight into the possibilities of the DEM, their theoretical background and application fields, the interested reader is referred to the review articles by Zhu *et al.* [224, 225]. Concerning granular solids, as they are of primary interest in this monograph, the research in the field of the DEM is mainly driven by the wish to accurately capture the granular microstructure under consideration. Two ways can be followed in this context: On the one hand, one may disregard the actual shape of the particles through the simplified use of spherical particles and consequently account for shape and frictional effects by use of enriched constitutive contact formulations between interacting particles, cf. e. g. Ai *et al.*

[2], Hertz [110], Iwashita & Oda [118], Jiang *et al.* [126] or Luding [149, 150]. On the other hand, the contact force computation is kept simple and one seeks to describe the shape of the natural grains as closely as possible, reaching from sphere clusters (Ferellec & McDowell [76], Salot *et al.* [183]), superellipsoids (Wellmann *et al.* [215]), polyhedra (Cundall [40], Hart *et al.* [106]), sphero-polyhedra (Galindo-Torres & Pedroso [93]) to the description of grains by nurbs formulations (Andrade *et al.* [14]) and level set methods (Kawamoto *et al.* [131]). Recent combinations of FE analysis for local deformation of individual particles and DE computations of the global motion furthermore lead the way to more complex granular motion and deformation scenarios (Stühler *et al.* [199]).

One of the first applications of the DEM to localisation phenomena was given by Cundall [41], already comparing two-dimensional (2-d) numerical experiments from unbonded DE simulations to a continuum-based approach. Bardet & Proubet [19], Herrmann *et al.* [109] and Iwashita & Oda [118, 119] pointed out the importance of flexible boundary conditions when simulating, for example, biaxial material tests and reported the activation of rolling modes in the shear band under 2-d conditions. Further applications to the modelling of shear zones in unbonded granular media are given in Åström *et al.* [16], D'Addetta & Ramm [44], Hu & Molinari [114] or Widuliński *et al.* [218]. Bonds between particles, e. g. in order to capture material behaviour of solids like rock, cf. e. g. Behraftar *et al.* [22], Ergenzinger *et al.* [68], Galindo-Torres *et al.* [94] or Potyondy & Cundall [177] furthermore extend the possibilities of the DEM. In this regard, Jiang *et al.* [125] and Wang & Leung [213] studied shear bands in cemented sand under 2-d conditions, while Utili & Nova [205] studied soil failure using a Mohr-Coulomb-type bond formulation and a transition towards unbonded contacts between particles.

Continuum-based modelling of granular media: Instead of considering each particle on its own, the description of the overall body as a continuum implies the assumption of a homogenised microstructure at each material point, allowing for the description of the kinematics of the continuous body and the axiomatic introduction of global balance relations. The continuum mechanical problem is closed by constitutive material formulations and allows, for example, through the consideration of plasticity, for the modelling of non-linear material behaviour and strain localisation. The usage of the FEM to solve the governing equations allows for the treatment of realistic Initial-Boundary-Value Problems (IBVP) on the application scale. The utilisation of this approach to geomaterials and granular material and their respective failure mechanisms has been of great interest over the last decades, cf. e. g. Anand & Gu [9], Andrade & Borja [13], de Borst [27], Diebels & Ehlers [50], Ehlers & Avci [60], Ehlers *et al.* [63], Leroy & Ortiz [140], Neff [164], Nübel & Huang [169] or, most recently, Yamakawa *et al.* [221].

A special role in this regard belongs to kinematically extended continuum theories, in particular the micropolar or Cosserat continuum (Cosserat & Cosserat [37]), as it allows for an independent free rotation that can be associated to rotational fields active in localising granulates on the microstructural scale, cf. Mühlhaus & Vardoulakis [160]. In a micropolar description, the rotational field is accounted for by rigid directors attached to each material point of the continuum body, resulting furthermore in the additional consideration of corresponding countervailing couple stresses. The micropolar continuum is a suitable

approach in the field of localisation modelling in granular materials. Exemplarily, Ehlers [56] and Ehlers & Volk [66, 67] applied it in combination with the Theory of Porous Media to model localisation in liquid-saturated and empty porous solids, while Tordesillas *et al.* [203, 204] derived micromechanically based constitutive laws for a micropolar continuum description of shear banding, incorporating results from DE simulations. Recently, Stefanou *et al.* [197] summarised the possibilities and advantages of the Cosserat continuum with regard to the modelling of localisation in geomaterials. The main micropolar feature in this context is the regularisation of the localisation problem occurring due to the loss of ellipticity of the governing set of equations when an elasto-plastic material description is chosen, cf. de Borst [27], Cramer *et al.* [39] or Dietsche *et al.* [52]. In the case of granular material, the internal length is additionally linked to the shear band width, see Ehlers & Scholz [65], in which a calibration of the internal length with respect to the shear band width via parameter calibration was successfully performed.

Microcontinuum theories: The micropolar continuum belongs to the group of microcontinuum theories introduced by A. C. Eringen and, for example, summarised in Eringen [71]. Microcontinuum formulations offer a macroscopic way to include deformation mechanisms due to an underlying heterogeneous microstructure. Thereby, a microcontinuum is attached to each material point of the macroscopic continuum body, adding degrees of freedom to the material point. Depending on the restriction on the microdeformation, different microcontinuum theories have been introduced and can be categorised as proposed in Forest [87]. A homogeneous microdeformation leads to the micromorphic continuum of grade one (Eringen & Suhubi [72], Eringen [71]), a restriction to a microrotation yields the previously mentioned micropolar theory (Kafadar & Eringen [130]), while a homogeneous stretching of the microcontinuum leads to the microstrain formulation (Forest & Sievert [91], Hütter [115]). If the microstrain is additionally restricted to a dilatant volumetric stretch and microrotations are suppressed, the formulation is termed microdilatational, compare also Forest & Sievert [91]. A combination of the micropolar and the microdilatational formulations yields the so-called microstretch continuum, first introduced in Eringen [70]. Leismann & Mahnken [138] compared constitutive modelling for microcontinuum models and proposed an additive micromorphic formulation based on micropolar and microstrain material descriptions. The thermodynamically consistent formulation of microcontinuum theories and their application, especially to microstructural-induced material behaviour, has been of great interest. Among others, Forest & Sievert [90, 91] presented elasto-viscoplastic formulations for micromorphic, micropolar and microdilatational formulations, while, in a series of papers, Grammenoudis & Tsakmakis [99] and Grammenoudis *et al.* [100, 101] gave consistent approaches for micromorphic continua, including a geometrical derivation of deformation measures and applications to plasticity and damage. Vernerey *et al.* [208, 209] developed a hierarchical three-scale elasto-plastic micromorphic material description to tackle localisation and failure of heterogeneous materials. Regueiro [180] formulated a finite strain micromorphic elastoplasticity theory and Forest [86] gave a general framework how to use the micromorphic approach to obtain several classes of continuum descriptions that include extended effects, such as gradient elasticity and damage. The most frequently used microcontinuum formulation is without doubt the micropolar continuum with applications, apart from the already mentioned ap-

plications in the field of geomaterials and localisation, in the field of cellular solids, (Lakes [137], Onck [176], Diebels & Steeb [51], Rueger & Lakes [182]), magnetic powders (Kotera *et al.* [133]), crystal plasticity (Neff [164], Mayeur *et al.* [155], Mayeur & McDowell [154]) or ductile damage (Steinmann [198]). Furthermore, Forest *et al.* [88] and Hütter [115] studied the ability of modelling size-dependent material behaviour with micropolar and microstrain formulations, respectively. Thereby, the finite size of the microcontinuum intrinsically provides the continuum description with an internal length scale. Diebels & Steeb [51] and Tekoğlu & Onck [201] extended the size-effect investigation by including comparative studies with averaged results from microscopic models.

Although they are often termed 'continua with microstructure', microcontinua are still purely macroscopic theories and their formulation presents two major drawbacks. At first, a physical interpretation and justification of the additional degrees of freedom is crucial and secondly, it is vital to identify and, in particular, calibrate the additional material parameters within the constitutive material description. Generally, the identification of parameters for inelastic material descriptions in continuum mechanics is treated with respect to data from material tests. Thereby, an inverse formulation in combination with numerical optimisation techniques and the FEM, cf. e. g. Mahnken & Stein [153], is generally applied. With an increasing number of unknown material parameters (an isotropic, linear-elastic micromorphic material description is in need of 18 material constants compared to the two Lamé constants of a standard formulation), this task becomes nearly impossible to solve. A way to overcome this drawback is the application of computational homogenisation within multiscale techniques, where the constitutive material laws are substituted by a BVP on a lower scale and appropriate homogenisation or projection rules link the results from the lower scale with extended continuum descriptions on the macroscale. The subscale BVP, in this framework either the microscale of one element of the microstructure or a mesoscale structure containing several microstructural elements, enables, at least to some extent, a geometrical representation of the microstructure. Furthermore, it can generally be treated as a standard Cauchy continuum. In multiscale FE technologies, commonly called FE^2 methods, compare Schröder [189], the subscale BVP is nested at each integration point of the respective finite element leading to a so-called concurrent or hierarchical multiscale approach. The difficulties, especially in the context of microcontinua, then lie, at first, in the consistent prolongation of the macroscopic deformation onto the subscale BVP, generally as boundary conditions, and secondly, after solution of the subscale BVP in the consistent transfer of the microscopic information to the macroscale, a process generally referred to as homogenisation. In this regard, Forest & Sab [89] and Jänicke & Steeb [122] substituted a micropolar model on the macroscale with cellular or layered structures of microscopic Cauchy-type material, Ebinger *et al.* [55] developed a multiscale technique linking a micropolar continuum approach with a Timoshenko beam model on the microscale, while Jänicke *et al.* [120] and Biswas & Poh [24] presented appropriate two-scale modelling approaches for micromorphic media in the sense of the FE^2 method. Finally, Jänicke & Steeb [121] gave the minimal loading conditions for the subscale model in the framework of micromorphic homogenisation strategies, while Hütter [116] and Forest [85] determined consistent homogenisation theories for micromorphic continua based on a microscale Cauchy continuum description.

Multiscale and homogenisation strategies for granular media: The most intuitive approach to include particle-based models into continuum approaches is the direct combination of the DEM as a microscale method with the continuum-scale model, numerically treated within the FEM. In this framework, Miehe & Dettmar [156] and Miehe *et al.* [157] gave a computational homogenisation procedure and coupled two-scale simulations using periodic Representative Elementary Volumes (REV). The focus is thereby on the consistent formulation of the subscale boundary conditions and the homogenisation procedure based on the equivalence of micro- and macroscopic virtual work, i. e. the so-called Hill-Mandel macrohomogeneity condition. Guo & Zhao [102], Ma *et al.* [152] and Nguyen *et al.* [166] used a coupled DEM-FEM formulation to model strain localisation in cohesive and cohesionless granular material, respectively, the first work furthermore demonstrated the large possibilities of parallel computing by extending their work to geotechnical BVP and liquefaction during cyclic loading. In Andrade *et al.* [12], the internal variables of a plasticity law on the macroscale were found by DE simulations on the microscale in combination with experimental data from DIC and computer tomography. This idea was followed up in Lim *et al.* [143] using grain-morphology from imaging techniques to construct unit cells within a coupled FE-DE method based on the exact representation of the grain morphology by the so-called Level-Set-Discrete-Element Method (LS-DEM). Instead of nesting a DE simulation directly into an FE computation, a method that is generally referred to as the combined Finite-Discrete-Element Method (FDEM, FEM $\times$ DEM), compare Argilaga *et al.* [15], Munjiza [161] and Shahin *et al.* [192], it is also possible to combine DE and FE techniques in a spatial way. Exemplarily, Sorg & Bischoff [196], Wellmann & Wriggers [216] and Yan *et al.* [222] used the DEM in regions of large deformation and an FE calculation in regions with small deformation, coupled via overlaying domains, as proposed in Bauman *et al.* [21]. The mentioned coupled strategies, however, are based on the assumption of a Cauchy-type continuum description. Thereby, they ignore the well established relation between the additional stress and curvature contributions of micropolar continua and granular media physics, as e. g. stated in Oda & Iwashita [173], Luding *et al.* [151], Zhu & Yu [223], Kruyt [134], Ehlers *et al.* [64], D'Addetta *et al.* [43], Froiio *et al.* [92], Walsh *et al.* [212], Goldhirsch [98] or Li *et al.* [142]. Furthermore, as also pointed out in Guo & Zhao [102], due to the standard formulation on the macroscale, the coupled strategies lack a size-independent description within FE discretisation schemes. Pursuing the development of consistent multiscale techniques incorporating microcontinuum formulations in the framework of granular media is therefore still an open and challenging task.

In this context, the main goal of the presented work is the formulation of a homogenisation strategy for microcontinuum stress and deformation quantities based on the evaluation of a microstructural particle model. The formulation is an extension of the established homogenisation from particle mechanics to micropolar continua given in Ehlers *et al.* [64] using a particle-centre-based REV definition. The main focus thereby lies on the micromorphic case, while the micropolar case is directly included in a downwardly compatible way. Direct applications of the homogenisation strategy to DE-simulations of strain localisation thereby offer a new insight into the detection and the evaluation of extended micromorphic and micropolar effects in granular materials.

Brief applications of homogenisation techniques, linking granular material to the micromorphic continuum were already given in Goddard [96, 97]. The hierarchical upscaling technique in Regueiro *et al.* [179] shows many similarities with the presented formulations, as they are both based on the determination of extended micromorphic relations in the sense of Eringen & Suhubi [72] for ensembles of particles. Furthermore, similarities are found in the works of Chen & Lee [30, 31] and Zimmerman *et al.* [226], where atomistic molecular dynamics models have been linked to micromorphic continua through statistical ensemble averaging. Moreover, Chen *et al.* [32] presented the micromorphic theory as a successful top-down approach that can also be derived by averaging of atomic-scale quantities. This is due to the fact that both particle mechanics and molecular dynamics are, apart from the size and the scale difference, strongly related mathematical techniques to capture particle-based material behaviour and, therefore, averaging over ensembles of particles leads to comparable continuum quantities.

1.3 Scope, aims and outline of the thesis

The presented work aims at providing a justification of micromorphic continuum models in the field of granular media based on a sound homogenisation technique applied to DE simulations of IBVP. Existing strategies in this field are mostly restricted to microstructures consisting of mesostructural ensembles of rigid particles, which then yield micropolar continuum-type quantities at the higher spatial scale. In the present work, an additional micromorphic character is investigated, that results from the assumption that parts of the microstructure are assumed as deformable, such as e. g. binding or matrix material enclosing or connecting neighbouring grains in the material.

In order to foster the understanding of micromorphic media, Chapter 2 gives a short introduction to the fundamentals of Cauchy continuum mechanics, followed by the micropolar and the micromorphic extensions. Thereby, the influence of the kinematically extended formulations concerning the overall kinematic description, the stress states and the balance relations is given. The subsequent Chapter 3 emphasises on the physical link between the particle dynamical framework on the microscale and micromorphic, respectively micropolar, quantities on the mesoscopic REV scale. In particular, it is assumed that the micromorphic microstructure is built by rigid grains with attached deformable binder material, theoretically described by an ensemble of homogeneously deformable particles, thus representing the basis of grade-one micromorphic continua, cf. Eringen [71]. In this regard, the homogeneous particle deformation can generally be composed of a rotational and a stretching contribution both assigned to the deformation of any local position vector with respect to the particle's centre of mass. The crucial assumption in the present approach is the use of the particle-centre-based definition of an REV as it was introduced in Ehlers *et al.* [64], where contact forces of unbonded granular media were linked to Cosserat-type continuum stresses. In the present work, single particles are taken as microscopic REV for the computation of average particle stresses and strains, while an ensemble of particles is additionally taken as a mesoscopic REV for the computation of the macroscopic stress, strain and curvature measures. A geometrically linear point of view is taken, which simplifies the derived kinematic deformation measures such that an

additive decomposition into standard and extended contributions is possible.

After a transition of the obtained averaging formalisms towards discrete particle ensembles, the applied particle model in the sense of a DE model is presented in Chapter 4. The grains are thereby represented by spherical discrete elements in order to construct IBVP of granular systems that exhibit the onset and the full evolution of localisation, both in unbonded (micropolar setting) and bonded granular media (micromorphic setting). Suitable constitutive formulations are chosen within a so-called soft-contact approach to account for local compression at particle contacts, sticking and sliding friction between particles and, furthermore, rotational resistance between interacting particles resulting from the obvious simplification of the natural grain shape. The formulation is extended by beam formulations in order to phenomenologically include binding material. Overall, the thereby obtained model serves as a microstructure-based environment that accurately captures macroscopically observable shear bands. Numerical examples of different IBVP are therefore presented in Chapter 5. They are set up in the particle-simulation environment Pasimodo[2], a commercial and research code developed at the neighbouring Institute of Engineering and Computational Mechanics at the University of Stuttgart in cooperation with Inpartik[3]. As the activation of micropolar characteristics in shear bands is well known, the numerical examples are chosen with the goal to capture a single, dominating shear band. In this regard, small-scale simulations of uniaxial compression and tension tests on initially bonded material and of biaxial compression tests on initially bonded and unbonded granular specimen proved to be suitable numerical experiments.

With the complete solutions of the DE simulations at hand, Chapter 6 finally evaluates and interprets the application of the proposed homogenisation strategy with emphasis on the activation of the extended stress and deformation states in the region of shear bands.

Finally, a summary and an outlook of the work is given in Chapter 7, thereby also reflecting the obtained results. Moreover, appendices A, B and C give additional information on frequently used vector and tensor calculus, as well as additional detailed derivations of several continuum and particle-mechanical quantities.

[2] Particle Simulation and Molecular Dynamics in an Object oriented fashion, cf. Fleissner [78] and http://www.itm.uni-stuttgart.de/research/pasimodo/pasimodo_de.php.

[3] http://www.inpartik.de

Chapter 2:
Fundamentals of microcontinuum theories

This chapter presents the basic principles of microcontinuum theories. Therefore, at first an overview of extended continuum mechanics is given in order to establish a classification of the investigated microcontinuum theories. Before taking a closer look into the kinematics and the balance relations of the two microcontinuum formulations that are of importance to this monograph, the micromorphic and the micropolar continuum, the respective relations for the standard Cauchy continuum are given, laying the ground for the subsequent deviations from this classical approach.

2.1 Overview and classification

The terminology used in the literature in order to classify the characteristics of microcontinuum theories is sometimes not consistent, reaching from statements concerning the *nonlocality*, the *grade* or the *order* of micromorphic continua to the general term *continua with microstructure* when referring to microcontinuum formulations. In contrast, Forest [87] gives an adequate classification for microcontinuum theories in the sense of rational thermodynamics, which is adapted here. Thereby, at first, the analysed theories are restricted by assuming that the mechanical state at a material point is dependent on the state of variables at that point, following the principle of local action (Noll [168]). As a consequence, continuum descriptions including non-local actions are not considered. However, a non-locality can still be incorporated into continuum-mechanical descriptions. This can be achieved either through gradient-based extensions (Aifantis [3], Mindlin [158]) or through the consideration of deformable microcontinua with a small but finite size attached at the material points. The microcontinuum deformation then leads to additional degrees of freedom (DOF) at each material point. If no such extension to include nonlocality is incorporated, the standard Cauchy or Cauchy-Boltzmann continuum is retrieved, where the DOF are given by the displacement field. An assumed restriction of the microcontinuum deformation leads to a further characterisation of microcontinuum approaches: If the micromotion at a material point is assumed to lead to a homogeneous microdeformation, the micromorphic continuum of order one, or simply micromorphic continuum, is obtained. Eringen [71] names this formulation micromorphic continuum of *grade one*, a term not used here, in order to avoid confusion with gradient theories. The linearisation of the microdeformation is justified, as the material points are still considered to be very small compared to the macroscopic scale. Consequently, the additional DOF are given by a deformation tensor of second order. This furthermore allows to dissolve the contradiction between the infinite number of material points in the considered body and their finite size by replacing the deformable material point with a geometrical point and an attached deformable director to which the microdeformation is assigned. If the microdeformation is characterised by a symmetric deformation tensor, e. g. of Green-Lagrangean type, the

microstrain formulation is retained (Forest & Sievert [91]). A consideration of a stretching of the directors only in their referential direction is named the microdilatational case, while in the case where the directors are assumed to be rigid, the micromotion becomes a pure rotation and leads to the micropolar continuum, also named Cosserat continuum after the brothers Eugène and François Cosserat, who firstly introduced the concept of an additional free rotational field (Cosserat & Cosserat [37]). Combining the micropolar with the microdilatational micromotion leads to the so-called microstretch continuum. In conclusion, Figure 2.1 gives an overview of the formulations and the respective DOF.

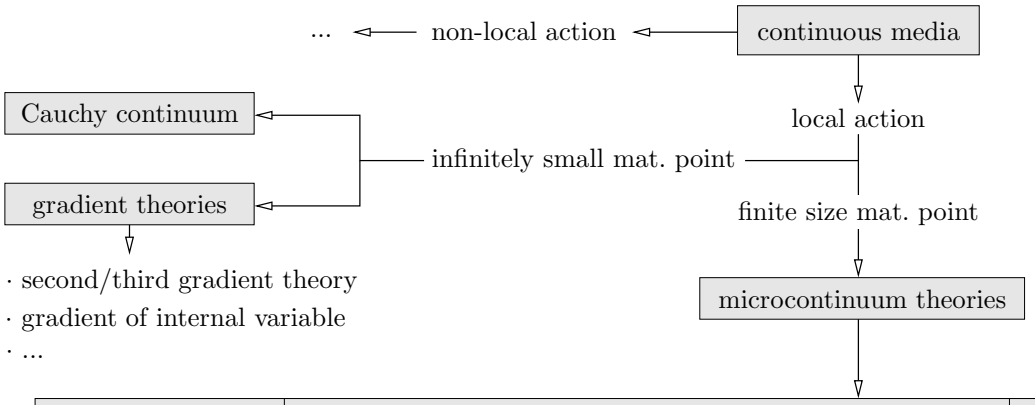

denotation	DOF at the material point	No. of DOF
micromorph	displacement field & microdeformation tensor	12
microstrain	displacement field & symmetric microdeformation tensor	9
microstretch	displacement field, scalar stretch & micro rotation tensor	7
micropolar	displacement field & micro rotation tensor	6
microdilatational	displacement field & scalar stretch	4

Figure 2.1: *Classification of microcontinuum formulations in the framework of generalised continua after Forest [87].*

The following sections extend the standard Cauchy continuum formulation stepwise towards the micropolar and the micromorphic descriptions in the sense of Eringen's introduction within the theory of microcontinua. For each formulation, the emphasis is laid on the kinematical setting and the governing balance equations. These relations are necessary to understand and evaluate whether micropolar and micromorphic characteristics are detectable based on a particle-mechanical investigation of granular material with and without deformable components. This is at the centre of the subsequent Chapter 3. No attempts to close the continuum-mechanical problem and to formulate macroscopic continuum mechanical models are made. In this regard, it should again be noted that micropolar and micromorphic models are in need of a large number of additional modelling/material parameters that need identification and calibration, compare Neff [163]. While this is possible for micropolar applications through inverse parameter optimisation (Ehlers & Scholz [65]) or through direct experimental determination of the additional

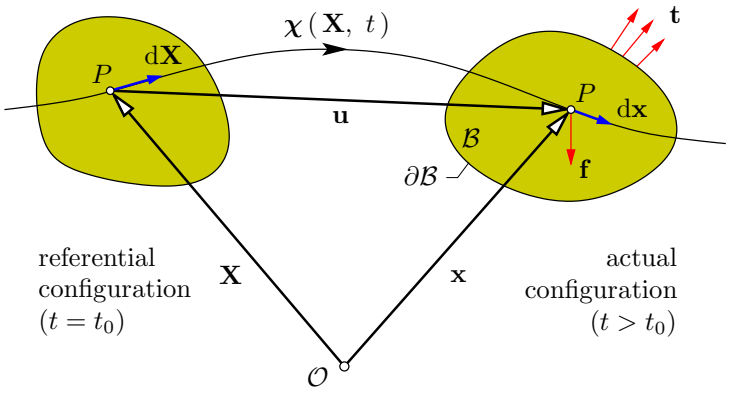

Figure 2.2: *Physical picture of Cauchy continuum kinematics.*

micropolar material constants (Rueger & Lakes [182]), the calibration of micromorphic material models, especially in the non-linear regime, is still an open task, cf. Ju & Mahnken [129].

2.2 The Cauchy continuum

In this section, a short review of the classical approach to single-component continuum mechanics is given, which leads to the Cauchy-type description.

2.2.1 Kinematical relations

Motion and configurations: In general, continuum mechanics describes the motion and deformation of a macroscopic body $\mathcal{B}$ assuming that it can be divided infinitely into material points P, which carry the physical variables. In order to account for the motion and the deformation of a continuous deformable body $\mathcal{B}$, a unique and uniquely invertible placement function $\boldsymbol{\chi}(P,\, t)$ is introduced, which captures the motion $\mathbf{x}$ of P at any time t. With $\mathbf{X} = \boldsymbol{\chi}(P,\, t_0)$ being the referential position of P at time t_0, the material description, expressing the motion with respect to the referential configuration, is given by

$$\mathbf{x} \;=\; \boldsymbol{\chi}\,(\,\mathbf{X},\, t\,)\,. \tag{2.1}$$

Consequently, the velocity field $\mathbf{v}$ and the acceleration field $\mathbf{a}$ in the material description follow as

$$\begin{aligned} \mathbf{v} \;&:=\; \dot{\mathbf{x}} \;=\; \frac{\mathrm{d}}{\mathrm{d}t}\,\boldsymbol{\chi}\,(\,\mathbf{X},\, t\,) \;=\; \dot{\mathbf{x}}\,(\,\mathbf{X},\, t\,) \qquad \text{and} \\ \mathbf{a} \;&:=\; \dot{\mathbf{v}} \;=\; \ddot{\mathbf{x}} \;=\; \frac{\mathrm{d}^2}{\mathrm{d}t^2}\,\boldsymbol{\chi}\,(\,\mathbf{X},\, t\,) \;=\; \ddot{\mathbf{x}}\,(\,\mathbf{X},\, t\,)\,, \end{aligned} \tag{2.2}$$

respectively. Thereby, the time derivative $\dot{(\,\cdot\,)}$ denotes the (total) material time derivative of an arbitrary field quantity, represented by the abstract placeholder $(\,\cdot\,)$. As the material

point is dimensionless and non-deformable, the deformation of the body $\mathcal{B}$ results from a relative displacement of the material points, making it therefore suitable to introduce the displacement vector

$$\mathbf{u} = \mathbf{x} - \mathbf{X}\,, \tag{2.3}$$

which points from the referential position to the actual position of the material point, cf. Figure 2.2.

Deformation and strain measures: The deformation gradient $\mathbf{F}$ and the inverse deformation gradient $\mathbf{F}^{-1}$ are introduced as the partial derivatives of the motion (2.1) with respect to $\mathbf{X}$ and $\mathbf{x}$, respectively. By use of (2.3), $\mathbf{F}$ and $\mathbf{F}^{-1}$ follow as

$$\begin{aligned} \mathbf{F}\,(\,\mathbf{X},\,t\,) &= \frac{\partial\,\boldsymbol{\chi}\,(\,\mathbf{X}\,,t\,)}{\partial\mathbf{X}} =: \operatorname{Grad}\mathbf{x} = \mathbf{I} + \operatorname{Grad}\mathbf{u} \\ \text{and}\quad \mathbf{F}^{-1}\,(\,\mathbf{x},\,t\,) &= \frac{\partial\,\boldsymbol{\chi}^{-1}\,(\,\mathbf{x}\,,t\,)}{\partial\mathbf{x}} =: \operatorname{grad}\mathbf{X} = \mathbf{I} - \operatorname{grad}\mathbf{u}\,, \end{aligned} \tag{2.4}$$

where $\mathbf{I}$ denotes the second-order identity tensor and the gradient operators $\operatorname{grad}(\,\cdot\,) = \partial(\,\cdot\,)/\partial\mathbf{x}$ and $\operatorname{Grad}(\,\cdot\,) = \partial(\,\cdot\,)/\partial\mathbf{X}$ denote the spatial derivatives with respect to the actual and the referential position vectors, respectively. Note that the postulation of the existence of $\mathbf{F}^{-1}$ demands that the functional determinant, the so-called Jacobian $J = \det\mathbf{F}$ of the deformation gradient, is non-zero. Furthermore, by evaluating $\mathbf{F}(t_0) = \mathbf{I}$ at the initial state, physically admissible deformation restricts $J > 0$, as $\det\mathbf{I} = 1$. The theorem of the polar decomposition expresses $\mathbf{F}$ uniquely through a proper orthogonal rotation tensor $\mathbf{R}$ and a symmetric, positive-definite right or left stretch tensor $\mathbf{U}$ or $\mathbf{V}$, respectively, viz.:

$$\mathbf{F} = \mathbf{R}\,\mathbf{U} = \mathbf{V}\,\mathbf{R} \quad \text{with} \quad \mathbf{R}^{-1} = \mathbf{R}^{T}\,,\ \det\mathbf{R} = 1\,,\ \mathbf{U} = \mathbf{U}^{T} \text{ and } \mathbf{V} = \mathbf{V}^{T}\,. \tag{2.5}$$

Note that $\mathbf{U}$ represents a stretch tensor purely expressed in the reference configuration, while $\mathbf{V}$ is its corresponding counterpart with respect to the actual configuration. Hence, the two field character of $\mathbf{F}$ is only present in $\mathbf{R}$, which can also be seen directly from a reformulation of (2.5) revealing the push-forward operation of $\mathbf{U}$ towards $\mathbf{V}$ or the respective pull-back operation via $\mathbf{R}$ and $\mathbf{R}^{T}$, viz.:

$$\mathbf{V} = \mathbf{R}\,\mathbf{U}\,\mathbf{R}^{T} \quad \longleftrightarrow \quad \mathbf{U} = \mathbf{R}^{T}\,\mathbf{V}\,\mathbf{R}\,. \tag{2.6}$$

The continuum rotation $\mathbf{R}$ can, for example, be expressed in the Euler-Rodrigues notation as

$$\mathbf{R} = \mathbf{e}\otimes\mathbf{e} + (\,\mathbf{I} - \mathbf{e}\otimes\mathbf{e}\,)\cos\varphi + (\,\mathbf{e}\times\mathbf{I}\,)\sin\varphi\,, \tag{2.7}$$

Therein, φ is the value of the continuum rotation vector $\boldsymbol{\varphi}$ around the central axis of rotation $\mathbf{e}$. Furthermore note that $\mathbf{F}$ transports the referential line element $\mathrm{d}\mathbf{X}$ to its image $\mathrm{d}\mathbf{x}$ in the actual configuration, viz.:

$$\mathrm{d}\mathbf{x} = \mathbf{F}\,\mathrm{d}\mathbf{X} \quad \longleftrightarrow \quad \mathrm{d}\mathbf{X} = \mathbf{F}^{-1}\,\mathrm{d}\mathbf{x}\,. \tag{2.8}$$

Additionally, the transport mechanisms for the surface element $\mathrm{d}\mathbf{A}$ and the volume element $\mathrm{d}V$ can be identified as

$$\mathrm{d}\mathbf{a} = (\,\det\mathbf{F}\,)\,\mathbf{F}^{T-1}\,\mathrm{d}\mathbf{A} \quad \text{and} \quad \mathrm{d}v = \det\mathbf{F}\,\mathrm{d}V\,. \tag{2.9}$$

Given the polar decompositions (2.5), it follows that the line element $\mathrm{d}\mathbf{X}$ is either deformed by $\mathbf{U}$ in the referential configuration and then rotated forward to the actual configuration by $\mathbf{R}$ yielding $\mathrm{d}\mathbf{x}$ or it is firstly rotated by $\mathbf{R}$ and then deformed by $\mathbf{V}$ in the actual configuration, again resulting in $\mathrm{d}\mathbf{x}$. By use of (2.8), the computation of the square of the line element leads to the definition of the right and left Cauchy-Green deformation tensors,

$$\mathrm{d}\mathbf{x} \cdot \mathrm{d}\mathbf{x} = \mathrm{d}\mathbf{X} \cdot \mathbf{C}\,\mathrm{d}\mathbf{X} \quad \text{with} \quad \mathbf{C} := \mathbf{F}^T\mathbf{F} = \mathbf{U}\,\mathbf{U} \tag{2.10}$$

and

$$\mathrm{d}\mathbf{X} \cdot \mathrm{d}\mathbf{X} = \mathrm{d}\mathbf{x} \cdot \mathbf{B}^{-1}\,\mathrm{d}\mathbf{x} \quad \text{with} \quad \mathbf{B} := \mathbf{F}\,\mathbf{F}^T = \mathbf{V}\,\mathbf{V}\,, \tag{2.11}$$

respectively. Finally, a comparison of the squares of the line elements in the referential and the actual configuration allows for the definition of the Green-Lagrange strain tensor $\mathbf{E}$ and the Almansi strain tensor $\mathbf{A}$[1] as

$$\mathbf{E} := \tfrac{1}{2}(\,\mathbf{C} - \mathbf{I}\,) \quad \text{and} \quad \mathbf{A} := \tfrac{1}{2}(\,\mathbf{I} - \mathbf{B}^{-1}\,)\,, \quad \text{where} \quad \mathbf{A} = \mathbf{F}^{T-1}\,\mathbf{E}\,\mathbf{F}^{-1}\,. \tag{2.12}$$

Deformation and strain rates: The computation of the temporal changes of the deformation quantities follows from the total time derivative of the line element $\mathrm{d}\mathbf{x}$, compare (2.8), which reads

$$(\,\mathrm{d}\mathbf{x}\,)^{\cdot} = \frac{\mathrm{d}}{\mathrm{d}t}(\,\mathbf{F}\,\mathrm{d}\mathbf{X}\,) = \dot{\mathbf{F}}\,\mathrm{d}\mathbf{X} = \dot{\mathbf{F}}\,\mathbf{F}^{-1}\,\mathrm{d}\mathbf{x}\,, \tag{2.13}$$

where $\dot{\mathbf{F}} = \mathrm{Grad}\,\dot{\mathbf{x}}$ is the material velocity gradient. The spatial velocity gradient $\mathbf{L}$ is hence defined as

$$\mathbf{L} := \dot{\mathbf{F}}\,\mathbf{F}^{-1} = \mathrm{grad}\,\dot{\mathbf{x}}\,. \tag{2.14}$$

Two additive splits of the spatial velocity gradient are common for applications: On the one hand, a split into symmetric and skew-symmetric parts is possible, leading to the deformation velocity tensor $\mathbf{D}$ and the rate of rotation tensor $\mathbf{W}$. On the other hand, proceeding from the polar decomposition of $\mathbf{F}$ leads to a split into a non-symmetric deformation rate tensor $\boldsymbol{\Delta}$ and a skew-symmetric gyration tensor $\boldsymbol{\Omega}$. Summarising, one obtains

$$\mathbf{L} = \mathbf{D} + \mathbf{W} \quad \text{with} \quad \begin{cases} \mathbf{D} = \tfrac{1}{2}(\,\mathbf{L} + \mathbf{L}^T\,) & \rightarrow \quad \mathbf{D} = \mathbf{D}^T \\ \mathbf{W} = \tfrac{1}{2}(\,\mathbf{L} - \mathbf{L}^T\,) & \rightarrow \quad \mathbf{W} = -\,\mathbf{W}^T \end{cases} \tag{2.15}$$

and

$$\mathbf{L} = \boldsymbol{\Delta} + \boldsymbol{\Omega} \quad \text{with} \quad \begin{cases} \boldsymbol{\Delta} = \mathbf{R}\,\dot{\mathbf{U}}\,\mathbf{U}^{-1}\,\mathbf{R}^T & \rightarrow \quad \boldsymbol{\Delta} \neq \boldsymbol{\Delta}^T \\ \boldsymbol{\Omega} = \dot{\mathbf{R}}\,\mathbf{R}^T & \rightarrow \quad \boldsymbol{\Omega} = -\,\boldsymbol{\Omega}^T\,, \end{cases} \tag{2.16}$$

[1] Further strain tensors can be defined, in particular the so-called Karni-Reiner strains $\mathbf{K}$ and ${}^R\mathbf{K}$ with respect to the actual and the referential frame, respectively, reading $\mathbf{K} := \frac{1}{2}(\,\mathbf{B} - \mathbf{I}\,)$ and ${}^R\mathbf{K} := \frac{1}{2}(\,\mathbf{I} - \mathbf{C}^{-1}\,)$.

respectively. A natural basis representation of $\mathbf{D}$, see Appendix B.1.1, shows the special property of admitting a representation of $\mathbf{D}$ with respect to convective co- and contravariant basis systems, where the time derivative acts only on the coefficient metric. Concerning the rates of the respective strain tensors, a formal computation of the material time derivative $\dot{\mathbf{E}}$ of the Green-Lagrange strain tensor $\mathbf{E}$ results in

$$\dot{\mathbf{E}} = \tfrac{1}{2}\dot{\mathbf{C}} \quad \text{with} \quad \dot{\mathbf{C}} = (\mathbf{F}^T\mathbf{F})^{\cdot} = \mathbf{F}^T(\mathbf{L}^T + \mathbf{L})\mathbf{F} = 2\mathbf{F}^T\mathbf{D}\mathbf{F}, \tag{2.17}$$

with $\dot{\mathbf{C}}$ as the material time derivative of the right Cauchy-Green deformation tensor. Formulating the material time derivative $\dot{\mathbf{A}}$ of the Almansi strain tensor $\mathbf{A}$ analogously yields the rate $\dot{\mathbf{B}}^{-1}$ of the inverted left Cauchy-Green tensor $\mathbf{B}^{-1}$, viz.:

$$\dot{\mathbf{A}} = -\tfrac{1}{2}(\mathbf{B}^{-1})^{\cdot} \quad \text{with} \quad (\mathbf{B}^{-1})^{\cdot} = (\mathbf{F}^{T-1}\mathbf{F}^{-1})^{\cdot} = -\mathbf{L}^T\mathbf{B}^{-1} - \mathbf{B}^{-1}\mathbf{L}, \tag{2.18}$$

cf. Ehlers [58]. An identification of the relative time derivative with respect to a convective basis system of the spatial quantity $\mathbf{A}$ can be achieved through the computation of the material time derivative of the difference of the squared line elements in the actual and the referential configuration. This yields, by use of the material time derivative of line elements (2.13),

$$\begin{aligned}(\mathrm{d}\mathbf{x}\cdot\mathrm{d}\mathbf{x} - \mathrm{d}\mathbf{X}\cdot\mathrm{d}\mathbf{X})^{\cdot} &= (\mathrm{d}\mathbf{X}\cdot 2\mathbf{E}\,\mathrm{d}\mathbf{X})^{\cdot} = \mathrm{d}\mathbf{X}\cdot\dot{\mathbf{E}}\,\mathrm{d}\mathbf{X} \\ &= (\mathrm{d}\mathbf{x}\cdot 2\mathbf{A}\,\mathrm{d}\mathbf{x})^{\cdot} = \mathrm{d}\mathbf{x}\cdot 2(\dot{\mathbf{A}} + \mathbf{L}^T\mathbf{A} + \mathbf{A}\mathbf{L})\,\mathrm{d}\mathbf{x} \\ &:= \mathrm{d}\mathbf{x}\cdot 2\overset{\Delta}{\mathbf{A}}\,\mathrm{d}\mathbf{x}.\end{aligned} \tag{2.19}$$

Therein, $\overset{\Delta}{(\cdot)}$ denotes the upper (contravariant) Lie/Oldroyd derivative, where, formally, the basis system of the tensor is held constant and the time differentiation only acts on its coefficient metric[2]:

$$\overset{\Delta}{(\cdot)} = \dot{(\cdot)} + \mathbf{L}^T(\cdot) + (\cdot)\mathbf{L}. \tag{2.20}$$

Inserting the definition of the Almansian strain tensor (2.12) into (2.19) allows by comparison with (2.18) for the conclusion that the Oldroyd rate of $\mathbf{A}$ yields the contravariant representation of $\mathbf{D}$ and is therefore also equivalent to the contravariant transport of the Green-Lagrangean strain velocity tensor $\dot{\mathbf{E}}$, viz.:

$$\overset{\Delta}{\mathbf{A}} = \tfrac{1}{2}(\mathbf{L} + \mathbf{L}^T) = \mathbf{D} = \mathbf{F}^{T-1}\dot{\mathbf{E}}\mathbf{F}^{-1}. \tag{2.21}$$

[2] A corresponding lower (covariant) Oldyroyd derivative $\overset{\nabla}{(\cdot)}$ with

$$\overset{\nabla}{(\cdot)} := \dot{(\cdot)} - \mathbf{L}(\cdot) - (\cdot)\mathbf{L}^T,$$

can also be derived for the respective relative time derivative of the Karni-Reiner strain tensor $\mathbf{K}$ and reads

$$\overset{\nabla}{\mathbf{K}} := \dot{\mathbf{K}} - \mathbf{L}\mathbf{K} - \mathbf{K}\mathbf{L}^T = \mathbf{F}\,{}^R\mathbf{K}\,\mathbf{F}^T = \mathbf{D}.$$

This yields the covariant representation of $\mathbf{D}$.

2.2.2 Stress concept

The deformation process of a continuum body is a consequence of the load the body exhibits. In general, the overall body $\mathcal{B}$ can sustain volumetric forces $\mathbf{f}$ acting on all material points P of $\mathcal{B}$ and direct contact forces $\mathbf{t}$ acting at the vicinity, i. e. on all those material points composing the surface $\partial\mathcal{B}$ of $\mathcal{B}$. An integration over the domain of the body results in the total force $\mathbf{k}$ acting on the body $\mathcal{B}$ as

$$\mathbf{k}(\mathcal{B},\, t) = \int_{\mathcal{B}} \mathbf{f}\,\mathrm{d}v + \int_{\partial\mathcal{B}} \mathbf{t}\,\mathrm{d}a \quad \text{with} \quad \mathbf{f} = \rho\,\mathbf{b}\,, \tag{2.22}$$

where $\mathbf{b}$ is a gravitational volume force per unit mass, generally interpreted as the gravitation $\mathbf{g}$. The surface force $\mathbf{t} = \mathbf{t}(\mathbf{x},\, t,\, \mathbf{n})$ is a function of the actual position $\mathbf{x}$, the time t and the outward-oriented normal unit vector $\mathbf{n}$. The last dependence on $\mathbf{n}$ poses a disadvantageous property for an objective stress measure. Therefore, by use of Cauchy's lemma,

$$\mathbf{t} = \mathbf{t}(\mathbf{x},\, t,\, \mathbf{n}) = -\,\mathbf{t}(\mathbf{x},\, t,\, -\mathbf{n})\,, \tag{2.23}$$

a tensor-valued stress measure $\mathbf{T}$ is determined from the equilibrium of an infinitesimal volume surrounding the material point P at $\mathbf{x}$. Thereby, the volumetric forces acting at P are neglected in comparison to the surface-specific loading. Cauchy's theorem finally connects the stress tensor $\mathbf{T}$ to the stress vector $\mathbf{t}$ via

$$\mathbf{t}(\mathbf{x},\, t,\, \mathbf{n}) = [\,\mathbf{T}(\mathbf{x},\, t\,)\,]\,\mathbf{n}\,. \tag{2.24}$$

The so-called Cauchy stress tensor $\mathbf{T}$ is also denoted the true stress, as it relates the actual surface force element $\mathbf{t}\,\mathrm{d}a$ to the area element $\mathrm{d}\mathbf{a}$ of the actual frame via

$$\mathbf{t}\,\mathrm{d}a = \mathbf{T}\,\mathbf{n}\,\mathrm{d}a = \mathbf{T}\,\mathrm{d}\mathbf{a}\,. \tag{2.25}$$

Using the transport of a surface element (2.9), the so-called Kirchhoff stress $\boldsymbol{\tau}$, relating the force element to a weighted area element $\mathrm{d}\bar{\mathbf{a}} = (\mathrm{d}V/\mathrm{d}v)\,\mathrm{d}\mathbf{a}$ of the actual configuration as well as the first Piola-Kirchhoff (engineering) stress $\mathbf{P}$, relating the force element to a referential area element $\mathrm{d}\mathbf{A}$ are found. Furthermore, a complete map of $\mathbf{P}$ towards the actual frame yields the second Piola-Kirchhoff stress tensor $\mathbf{S}$. Summarising, the relations

$$\boldsymbol{\tau} = \det\mathbf{F}\,\mathbf{T}\,, \quad \mathbf{P} = \boldsymbol{\tau}\,\mathbf{F}^{T-1} = \det\mathbf{F}\,\mathbf{T}\,\mathbf{F}^{T-1}\,, \quad \mathbf{S} = \mathbf{F}^{-1}\,\mathbf{P} = \mathbf{F}^{-1}\,\boldsymbol{\tau}\,\mathbf{F}^{T-1} \tag{2.26}$$

are obtained.

2.2.3 Balance relations

General balance structure: Balance relations evaluate the temporal change of physical quantities in a body $\mathcal{B}$ resulting from effluxes at the surface $\partial\mathcal{B}$ of $\mathcal{B}$ (actions at the vicinity), supply terms (actions from a distance) or possible production terms, as they are commonly introduced within multi-component theories due to coupling of individual

constituents with each other, cf. Ehlers [56]. The conservation of a scalar or vector-valued mechanical quantity Ψ or $\boldsymbol{\Psi}$ is generally given by

$$\begin{aligned} \frac{\mathrm{d}}{\mathrm{d}t}\int_{\mathcal{B}} \Psi \,\mathrm{d}v &= \int_{\partial\mathcal{B}} (\,\boldsymbol{\phi}\cdot\mathbf{n}\,)\,\mathrm{d}a + \int_{\mathcal{B}} \varsigma \,\mathrm{d}v + \int_{\mathcal{B}} \hat{\Psi}\,\mathrm{d}v\,, \\ \frac{\mathrm{d}}{\mathrm{d}t}\int_{\mathcal{B}} \boldsymbol{\Psi} \,\mathrm{d}v &= \int_{\partial\mathcal{B}} (\,\boldsymbol{\Phi}\,\mathbf{n}\,)\,\mathrm{d}a + \int_{\mathcal{B}} \boldsymbol{\varsigma} \,\mathrm{d}v + \int_{\mathcal{B}} \hat{\boldsymbol{\Psi}}\,\mathrm{d}v\,, \end{aligned} \tag{2.27}$$

wherein $\boldsymbol{\phi}$, $\boldsymbol{\Phi}$ are the vector- and tensor-valued effluxes at the boundary, described by the outward-oriented surface normal $\mathbf{n}$, and ς, $\boldsymbol{\varsigma}$ are the scalar- and vector-valued supply terms, respectively. $\hat{\Psi}$, $\hat{\boldsymbol{\Psi}}$ are the scalar- and vector-valued production terms of the respective quantity inside the domain of $\mathcal{B}$. Assuming steadiness and steady differentiability of the field quantities, a transformation of the surface integrals into volumetric contributions via the Gaussian integral theorem yields a local representation of the general balance relations, valid for each material point P of $\mathcal{B}$, which reads

$$\begin{aligned} \dot{\Psi} + \Psi \operatorname{div}\dot{\mathbf{x}} &= \operatorname{div}\phi + \varsigma + \hat{\Psi}\,, \\ \dot{\boldsymbol{\Psi}} + \boldsymbol{\Psi} \operatorname{div}\dot{\mathbf{x}} &= \operatorname{div}\boldsymbol{\Phi} + \boldsymbol{\varsigma} + \hat{\boldsymbol{\Psi}}. \end{aligned} \tag{2.28}$$

In a general thermodynamic description, balanced quantities are given for the mass density, the linear momentum, the angular momentum, the total energy and the entropy. They are introduced in an axiomatic manner. In the following, the balance of entropy is not discussed, as, although it plays a major role in the framework of constitutive material modelling for continua, it is not needed for the contents of this monograph. Furthermore, the balance of energy is reduced to the balance of mechanical power, assuming the absence of non-mechanical power, i. e. assuming adiabatic conditions. Thereby, it looses its axiomatic character and can, in the frame of a Cauchy-continuum formulation, also be derived from the balance of linear momentum through a scalar multiplication with the velocity field and appropriate modifications.

Balance of mass: The axiom of mass conservation states that the total mass m of a body $\mathcal{B}$ is constant. Equivalently, it is possible to state that the body is in a closed system, in which the mass is not able to leave or enter the domain. This implies

$$m = \int_{\mathcal{B}} \rho \,\mathrm{d}v = \int_{\mathcal{B}} \mathrm{d}m = \text{const.} \quad \rightarrow \quad \frac{\mathrm{d}}{\mathrm{d}t}\, m = 0\,, \tag{2.29}$$

identifying the mass density ρ as the scalar-valued physical quantity Ψ. A comparison with $(2.27)_1$ furthermore identifies

$$\boldsymbol{\phi} \rightarrow \mathbf{0}\,, \quad \varsigma \rightarrow 0\,, \quad \hat{\Psi} \rightarrow 0\,. \tag{2.30}$$

Hence, the local form of the balance of mass is given by

$$\dot{\rho} + \rho \operatorname{div}\dot{\mathbf{x}} = 0\,. \tag{2.31}$$

Moreover, a combination of $(2.29)_1$ and (2.9) leads to the referential mass density ρ_0, given as

$$\rho_0 = \det\mathbf{F}\,\rho\,. \tag{2.32}$$

Balance of linear momentum: It is axiomatically stated that the total temporal change in linear momentum

$$\mathbf{l}(\mathcal{B},t) = \int_{\mathcal{B}} \rho\,\dot{\mathbf{x}}\,\mathrm{d}v \tag{2.33}$$

of the body $\mathcal{B}$ equals the sum of surface and volumetric forces $\mathbf{k}$ applied on $\mathcal{B}$, as specified in (2.22). Consequently, the global form of the balance of linear momentum is given as

$$\frac{\mathrm{d}}{\mathrm{d}t}\mathbf{l}(\mathcal{B},t) = \mathbf{k}(\mathcal{B},\,t) \quad \longleftrightarrow \quad \frac{\mathrm{d}}{\mathrm{d}t}\int_{\mathcal{B}} \rho\,\dot{\mathbf{x}}\,\mathrm{d}v = \int_{\partial\mathcal{B}} \mathbf{t}\,\mathrm{d}a + \int_{\mathcal{B}} \rho\,\mathbf{b}\,\mathrm{d}v\,. \tag{2.34}$$

A comparison with the global form of the vector-valued general balance formulation $(2.27)_2$ allows for the identifications

$$\boldsymbol{\Psi} \;\to\; \rho\,\dot{\mathbf{x}}\,, \quad \boldsymbol{\Phi}\,\mathbf{n} \;\to\; \mathbf{T}\,\mathbf{n} = \mathbf{t}, \quad \boldsymbol{\varsigma} \;\to\; \rho\,\mathbf{b}\,, \quad \hat{\boldsymbol{\Psi}} \;\to\; \mathbf{0}\,. \tag{2.35}$$

The hierarchical structure of the balance relations enables the formulation of the local form of the linear momentum balance by use of the mass balance (2.31) as

$$\rho\,\ddot{\mathbf{x}} = \operatorname{div}\mathbf{T} + \rho\,\mathbf{b}\,. \tag{2.36}$$

Balance of angular momentum: The angular momentum of a body naturally needs to be formulated with respect to an arbitrary fixed point. With the spatial origin $\mathcal{O}$ of an inertial system as the point of reference, the angular momentum $\mathbf{h}_{\mathcal{O}}(\mathcal{B},t)$ of the body $\mathcal{B}$ is computed as the first moment of the linear momentum

$$\mathbf{h}_{\mathcal{O}}(\mathcal{B},t) = \int_{\mathcal{B}} \mathbf{x}\times[\,\mathbf{l}(\mathcal{B},t)\,]\,\mathrm{d}v = \int_{\mathcal{B}} \mathbf{x}\times(\,\rho\,\dot{\mathbf{x}}\,)\,\mathrm{d}v\,. \tag{2.37}$$

The axiomatic statement concerns the temporal change in angular momentum, which is postulated to equal the resultant moment $\mathbf{m}_{\mathcal{O}}(\mathcal{B},\,t)$ of all forces applied on $\mathcal{B}$. With $\mathbf{m}_{\mathcal{O}}(\mathcal{B},\,t)$ computed with respect to $\mathcal{O}$, viz.

$$\mathbf{m}_{\mathcal{O}}(\mathcal{B},\,t) = \int_{\partial\mathcal{B}} \mathbf{x}\times\mathbf{t}\,\mathrm{d}a + \int_{\mathcal{B}} \mathbf{x}\times(\,\rho\,\mathbf{b}\,)\,\mathrm{d}v\,, \tag{2.38}$$

the balance of angular momentum reads

$$\begin{aligned} &\frac{\mathrm{d}}{\mathrm{d}t}\mathbf{h}_{\mathcal{O}}(\mathcal{B},t) = \mathbf{m}_{\mathcal{O}}(\mathcal{B},\,t) \\ \longleftrightarrow \quad &\frac{\mathrm{d}}{\mathrm{d}t}\int_{\mathcal{B}} \mathbf{x}\times(\,\rho\,\dot{\mathbf{x}}\,)\,\mathrm{d}v = \int_{\partial\mathcal{B}} \mathbf{x}\times\mathbf{t}\,\mathrm{d}a + \int_{\mathcal{B}} \mathbf{x}\times(\,\rho\,\mathbf{b}\,)\,\mathrm{d}v\,. \end{aligned} \tag{2.39}$$

A comparison with $(2.27)_2$ identifies the relevant physical quantities as

$$\boldsymbol{\Psi} \;\to\; \mathbf{x}\times(\,\rho\,\dot{\mathbf{x}}\,), \quad \boldsymbol{\Phi}\,\mathbf{n} \;\to\; (\,\mathbf{x}\times\mathbf{T}\,)\,\mathbf{n} = \mathbf{x}\times\mathbf{t}\,, \quad \boldsymbol{\varsigma} \;\to\; \mathbf{x}\times(\,\rho\,\mathbf{b}\,), \quad \hat{\boldsymbol{\Psi}} \;\to\; \mathbf{0}\,. \tag{2.40}$$

With the balance of mass (2.31) and the balance of linear momentum (2.36), the local statement of the balance of angular momentum (2.39) reduces to

$$\mathbf{0} = \mathbf{I} \times \mathbf{T} \,. \tag{2.41}$$

Bearing in mind the computation of the axial vector, which accounts for the skew-symmetric contributions of a second-order tensor, cf. (A.15), (2.41) shows the symmetry of the stress tensor $\mathbf{T} = \mathbf{T}^T$ for Cauchy continua.

Balance of total energy: The total energy of a body $\mathcal{B}$ is composed of the internal energy $\mathcal{E}(\mathcal{B},\, t)$ and the kinetic energy $\mathcal{K}(\mathcal{B},\, t)$, which are given as

$$\mathcal{E}\,(\,\mathcal{B},t\,) \,=\, \int_{\mathcal{B}} \rho\, \varepsilon\,(\,\mathbf{x},\, t\,)\,\mathrm{d}v \quad \text{and} \quad \mathcal{K}\,(\,\mathcal{B},t\,) \,=\, \int_{\mathcal{B}} \tfrac{1}{2}\,\dot{\mathbf{x}} \,\cdot\, \dot{\mathbf{x}}\,\rho\,\mathrm{d}v\,, \tag{2.42}$$

respectively. Therein, ε is the specific internal energy per mass element $\rho\,\mathrm{d}v$. The axiom of total energy conservation, also known as the first law of thermodynamics, postulates the balance between the temporal change of the total energy of the body $\mathcal{B}$ and the external mechanical and non-mechanical power $\mathcal{L}_a(\mathcal{B},\, t)$ and $\mathcal{Q}_a(\mathcal{B},\, t)$, respectively. The global form of the total energy balance is thus given in the form

$$\frac{\mathrm{d}}{\mathrm{d}t}\,[\,\mathcal{E}\,(\,\mathcal{B},t\,) \,+\, \mathcal{K}\,(\,\mathcal{B},t\,)\,] \,=\, \mathcal{L}_a\,(\,\mathcal{B},t\,) \,+\, \mathcal{Q}_a\,(\,\mathcal{B},t\,)\,. \tag{2.43}$$

The non-mechanical power $\mathcal{Q}_a(\mathcal{B},\, t)$ includes heat influx through contact and heat supply through radiation from the vicinity. As no temperature-dependent problem settings are investigated within this monograph, the balance of total energy is not further discussed at this point. However, its reduced form as the non-axiomatic balance of mechanical power offers the possibility to identify work-conjugated pairs of stresses and strains for Cauchy and extended continuum formulations and is therefore discussed in the following.

Balance of mechanical power: The balance of mechanical power of a Cauchy continuum can be derived in two ways. Either from an evaluation of the balance of total energy under adiabatic conditions or from a scalar multiplication of the balance of momentum with the velocity field. Following the first approach, one recognises that the mechanical power stemming from the power of the external forces $\mathbf{k}$ acting on $\mathcal{B}$, cf. (2.22), reads

$$\mathcal{L}_a\,(\,\mathcal{B},t\,) \,=\, \int_{\partial\mathcal{B}} \dot{\mathbf{x}} \,\cdot\, \mathbf{t}\,\mathrm{d}a \,+\, \int_{\mathcal{B}} \dot{\mathbf{x}} \,\cdot\, \rho\,\mathbf{b}\,\mathrm{d}v\,. \tag{2.44}$$

Under this consideration, the balance of the total energy reduces to

$$\frac{\mathrm{d}}{\mathrm{d}t}\,[\int_{\mathcal{B}} \rho\,(\,\varepsilon \,+\, \tfrac{1}{2}\,\dot{\mathbf{x}} \,\cdot\, \dot{\mathbf{x}}\,)\,\mathrm{d}v\,] \,=\, \int_{\partial\mathcal{B}} \dot{\mathbf{x}} \,\cdot\, \mathbf{t}\,\mathrm{d}a \,+\, \int_{\mathcal{B}} \dot{\mathbf{x}} \,\cdot\, \rho\,\mathbf{b}\,\mathrm{d}v\,. \tag{2.45}$$

Comparing to the general balance $(2.27)_1$ reveals by use of Cauchy's theorem (2.24) that

$$\Psi \,\rightarrow\, \rho\,(\,\varepsilon + \tfrac{1}{2}\,\dot{\mathbf{x}}\cdot\dot{\mathbf{x}}\,)\,, \quad \boldsymbol{\phi}\cdot\mathbf{n} \,\rightarrow\, (\,\mathbf{T}^T\,\dot{\mathbf{x}}\,)\cdot\mathbf{n} \,=\, \dot{\mathbf{x}}\cdot\mathbf{t}\,, \quad \varsigma \,\rightarrow\, \rho\,\dot{\mathbf{x}}\cdot\mathbf{b}\,, \quad \hat{\Psi} \,\rightarrow\, 0\,. \tag{2.46}$$

With the results of the hierarchically lower balance relations and the identity (A.27), the local form of the balance of energy follows after (2.28) by use of (2.15) and $\mathbf{T} \cdot \mathbf{W} = 0$ as

$$\rho\,\dot{\varepsilon} \;=\; \mathbf{T} \cdot \mathbf{L} \;=\; \mathbf{T} \cdot \mathbf{D} \;:=\; \rho\, w_i\,(\,\mathbf{x}\,,\;t\,)\,. \tag{2.47}$$

Therein, $w_i(\mathbf{x},\,t) = \frac{1}{\rho}\mathbf{T} \cdot \mathbf{D}$ defines the specific internal stress power per unit volume of the actual configuration. As a consequence, the balance of total energy incorporates only mechanical contributions and reduces to the balance of mechanical power. Through the introduction of the internal stress power $\mathcal{L}_i(\mathcal{B},\,t)$ as

$$\mathcal{L}_i\,(\,\mathcal{B},t\,) \;=\; \int_{\mathcal{B}} \rho\, w_i\,(\,\mathbf{x}\,,\;t\,)\;\mathrm{d}v \;=\; \int_{\mathcal{B}} \mathbf{T} \cdot \mathbf{D}\,\mathrm{d}v \;=\; \int_{\mathcal{B}} \boldsymbol{\tau} \cdot \mathbf{D}\,\mathrm{d}V \tag{2.48}$$

by use of (2.9), the balance of mechanical power is finally expressed as

$$\frac{\mathrm{d}}{\mathrm{d}t}\,\mathcal{K}\,(\,\mathcal{B},t\,) \;+\; \mathcal{L}_i\,(\,\mathcal{B},t\,) \;=\; \mathcal{L}_a\,(\,\mathcal{B},t\,)\,. \tag{2.49}$$

Moreover, the specific internal stress power w_i incorporates the conjugated pairs of stresses and strain rates, because the scalar products between the respective tensors result in invariant representations of w_i computed on different configurations. With the result of the mass balance (2.32) as well as the transport mechanisms for stresses and strains (2.12) and (2.26), respectively, $w_i(\mathbf{x},\,t)$ is given by

$$w_i\,(\,\mathbf{x}\,,\;t\,) \;=\; \frac{1}{\rho}\,\mathbf{T} \cdot \overset{\triangle}{\mathbf{A}} \;=\; \frac{1}{\rho_0}\,\boldsymbol{\tau} \cdot \overset{\triangle}{\mathbf{A}} \;=\; \frac{1}{\rho_0}\,\mathbf{S} \cdot \dot{\mathbf{E}}\,, \quad \text{where} \quad \overset{\triangle}{\mathbf{A}} \;=\; \mathbf{D}\,. \tag{2.50}$$

As a direct consequence, the work-conjugated stress and strain pairs, defining the mechanical work generated in a body, are

$$\{\,\frac{1}{\rho}\,\mathbf{T}\,,\;\mathbf{A}\,\}\,, \quad \{\,\frac{1}{\rho_0}\,\boldsymbol{\tau}\,,\;\mathbf{A}\,\} \quad \text{or} \quad \{\,\frac{1}{\rho_0}\,\mathbf{S}\,,\;\mathbf{E}\,\}\,. \tag{2.51}$$

2.3 The micropolar continuum

A first extension of the Cauchy continuum is the micropolar or Cosserat continuum (Cosserat & Cosserat [37]), where the assumption of an infinitely small material point is dropped. Instead, it is assumed that the material point occupies a small but finite domain. This microcontinuum is assumed to be rigid and exhibits an additional free rotational motion. As a consequence, the additional kinematical relations need to be derived. Furthermore, couple stresses countervail the rotational motion, thus extending the stress concept towards the existence of boundary couple-stress vectors and corresponding couple-stress tensors. Moreover, the balance of angular momentum does not result in the symmetry of the stress tensor, but rather serves as the governing equation to determine the rotational motion. For a more complete insight into this approach, compared to the subsequent short introduction, the reader is referred to Altenbach & Eremeyev [8], Diebels [49], Ehlers [56], Ehlers & Bidier [61] or Forest [84].

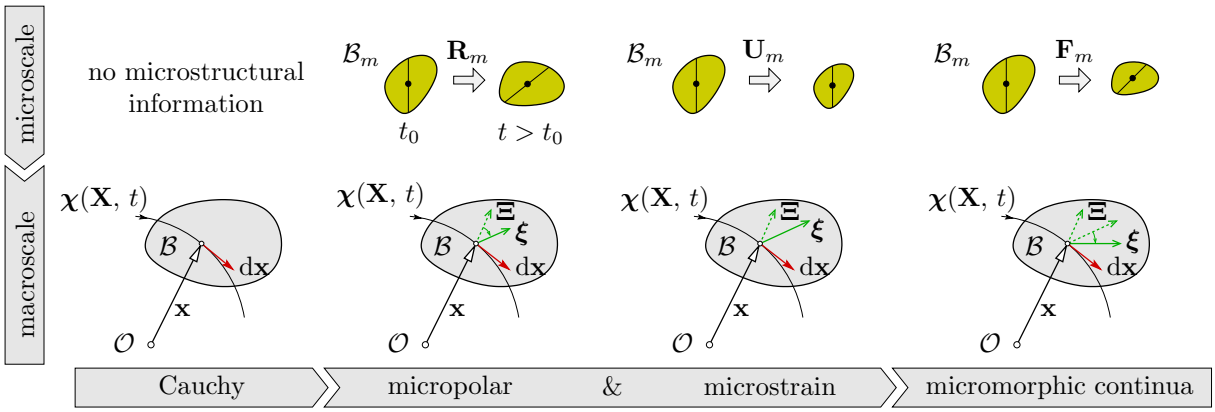

Figure 2.3: *Principle sketch of Cauchy, micropolar, microstrain and micromorphic deformation.*

2.3.1 Kinematical relations

The director motion: In order to allow for the consideration of the independent rotational motion $\boldsymbol{\varphi}_m$ of the rigid microcontinuum, a rigid director is attached to each material point of the overall body, compare Figure 2.3. The micromotion of the director is a proper orthogonal rotation $\bar{\mathbf{R}}$ that transports directors $\boldsymbol{\Xi}$ from their referential orientation to their image $\boldsymbol{\xi}$ in the actual configuration and vice versa:

$$\boldsymbol{\xi} = \bar{\mathbf{R}}(\mathbf{X}, t)\,\boldsymbol{\Xi} \quad \longleftrightarrow \quad \boldsymbol{\Xi} = \bar{\mathbf{R}}^T(\mathbf{X}, t)\,\boldsymbol{\xi}\,. \tag{2.52}$$

Note that here and in the following the notation $\bar{(\cdot)}$ refers to quantities that incorporate the respective micromotion. Moreover, $\bar{\mathbf{R}}$ can be expressed in the Euler-Rodrigues representation as a function of the complete rotation $\bar{\boldsymbol{\varphi}}$, in equivalence to the continuum rotation tensor $\mathbf{R}$, compare (2.7). The complete rotation $\bar{\boldsymbol{\varphi}}$ itself results from the additional free micropolar rotation $(\boldsymbol{\varphi}_m)_{\mathcal{B}}$ combined with the continuum rotation $\boldsymbol{\varphi}$, all three expressed with respect to a rotation around a corresponding central rotation axis, compare also Figure 2.5.

Micropolar deformation, strain and curvature tensors: With the introduced director's micromotion, two alternative multiplicative micropolar decompositions of the deformation gradient $\mathbf{F}$ are possible. Both lead to deformation and strain tensors that combine the macro- and the micromotion. On the one hand, a decomposition is given proceeding from the right polar decomposition of $\mathbf{F}$, which leads to

$$\mathbf{F} = \mathbf{R}\,\mathbf{U} = \bar{\mathbf{R}}\,\bar{\mathbf{U}} \quad \text{together with} \quad \bar{\mathbf{R}} = \mathbf{R}\,(\mathbf{R}_m)_{\mathcal{B}} \quad \text{and} \quad \bar{\mathbf{U}} = (\mathbf{R}_m)_{\mathcal{B}}^T\,\mathbf{U}\,, \tag{2.53}$$

where $(\mathbf{R}_m)_{\mathcal{B}}$ now represents the rotation tensor to the free rotation in an averaged sense on the scale of the macroscopic body $\mathcal{B}$ and $\bar{\mathbf{U}}$ as the right micropolar deformation tensor. On the other hand, the corresponding formulation proceeding from the left polar decomposition of $\mathbf{F}$ reads

$$\mathbf{F} = \mathbf{V}\,\mathbf{R} = \bar{\mathbf{V}}\,\bar{\mathbf{R}} \quad \text{together with} \quad \bar{\mathbf{R}} = (\mathbf{R}_m)_{\mathcal{B}}\,\mathbf{R} \quad \text{and} \quad \bar{\mathbf{V}} = \mathbf{V}\,(\mathbf{R}_m)_{\mathcal{B}}^T\,, \tag{2.54}$$

with $\bar{\mathbf{V}}$ as the left micropolar deformation tensor. A geometric derivation of $\bar{\mathbf{U}}$ and $\bar{\mathbf{V}}$ follows from the scalar product of directors $\boldsymbol{\xi}$, $\boldsymbol{\Xi}$ and line elements $\mathrm{d}\mathbf{x}$, $\mathrm{d}\mathbf{X}$ by used of (2.8) and (2.52), viz.:

$$\boldsymbol{\xi} \cdot \mathrm{d}\mathbf{x} = \boldsymbol{\Xi} \cdot \bar{\mathbf{U}}\,\mathrm{d}\mathbf{X} \quad \text{together with (2.53)} \tag{2.55}$$

and

$$\boldsymbol{\Xi} \cdot \mathrm{d}\mathbf{X} = \boldsymbol{\xi} \cdot \bar{\mathbf{V}}^{-1}\,\mathrm{d}\mathbf{x} \quad \text{together with (2.54)}\,. \tag{2.56}$$

In equivalence to Green-Lagrangean and Almansian strain measures of the standard formulation, two Cosserat strains are defined as

$$\bar{\mathbf{E}} := \bar{\mathbf{U}} - \mathbf{I} \quad \text{and} \quad \bar{\mathbf{A}} = \mathbf{I} - \bar{\mathbf{V}}^{-1} \quad \text{with} \quad \bar{\mathbf{A}} := \bar{\mathbf{R}}\,\bar{\mathbf{E}}\,\mathbf{F}^{-1}\,. \tag{2.57}$$

Compared to the transport of strain measures of a standard continuum approach, the micromotion, i. e. the rotation of the director frame (2.52) instead of the macroscopic deformation tensor $\mathbf{F}$ exemplarily transports the first basis system of $\bar{\mathbf{E}}$ and $\bar{\mathbf{A}}$[3]. In addition to the micropolar deformation tensors, the spatial change of the micromotion needs to be accounted for in order to complete the kinematic setting. Therefore, the gradient $\mathrm{Grad}\,\bar{\mathbf{R}}$ of $\bar{\mathbf{R}}$ is considered. To obtain a curvature measure ${}^{R}\overset{3}{\bar{\mathbf{C}}}$ of the referential configuration, a pull-back of the two-field tensor $\mathrm{Grad}\,\bar{\mathbf{R}}$ by $\bar{\mathbf{R}}^T$ towards the referential frame is performed. Accordingly, a curvature tensor $\overset{3}{\bar{\mathbf{C}}}$ of the actual configuration can be constructed from the gradient $\mathrm{grad}\,\bar{\mathbf{R}}$ and an appropriate forward rotation. After reformulation, the third-order curvature tensors read

$$\begin{aligned} {}^{R}\overset{3}{\bar{\mathbf{C}}} = (\,\bar{\mathbf{R}}^T\,\mathrm{Grad}\,\bar{\mathbf{R}}\,)^{\underline{3}} \quad \text{and} \quad \overset{3}{\bar{\mathbf{C}}} = -\,(\,\bar{\mathbf{R}}\,\mathrm{grad}\,\bar{\mathbf{R}}^T\,)^{\underline{3}} \\ \text{with} \quad \overset{3}{\bar{\mathbf{C}}} = [\,\bar{\mathbf{R}}\,(\,{}^{R}\overset{3}{\bar{\mathbf{C}}}{}^{\underline{23}T}\,\bar{\mathbf{R}}^T\,)^{\underline{3}\underline{23}T}\,\mathbf{F}^{-1}\,]^{\underline{3}}. \end{aligned} \tag{2.58}$$

Furthermore, the consideration of the identity $\mathrm{Grad}\,(\bar{\mathbf{R}}^T\bar{\mathbf{R}}) = \mathbf{0}$ leads to the skew-symmetry condition of the curvature tensor with respect to its first two basis vectors,

$${}^{R}\overset{3}{\bar{\mathbf{C}}} = -\,({}^{R}\overset{3}{\bar{\mathbf{C}}})^{\underline{12}T} \quad \text{as well as} \quad \overset{3}{\bar{\mathbf{C}}} = -\,(\overset{3}{\bar{\mathbf{C}}})^{\underline{12}T}\,. \tag{2.59}$$

Therefore, in analogy to the computation of axial vectors of skew-symmetric tensors of second order, a compaction of the third-order towards associated second-order curvature tensors is possible. Without loss of information, this leads to

$${}^{R}\bar{\mathbf{C}} = -\tfrac{1}{2}\,(\,\overset{3}{\mathbf{E}}\,{}^{R}\overset{3}{\bar{\mathbf{C}}}{}^{\underline{12}T}\,)^{\underline{2}} \quad \text{and} \quad \bar{\mathbf{C}} = -\tfrac{1}{2}\,(\,\overset{3}{\mathbf{E}}\,\overset{3}{\bar{\mathbf{C}}}{}^{\underline{12}T}\,)^{\underline{2}}, \quad \text{where} \quad \bar{\mathbf{C}} = \bar{\mathbf{R}}\,{}^{R}\bar{\mathbf{C}}\,\mathbf{F}^{-1}\,. \tag{2.60}$$

[3]This originates in the fact that $\bar{\mathbf{E}}$ and $\bar{\mathbf{A}}$ can physically be identified by the differences of the scalar product of directors $\boldsymbol{\xi}$ and line elements $\mathrm{d}\mathbf{x}$ via

$$\boldsymbol{\xi} \cdot \mathrm{d}\mathbf{x} - \boldsymbol{\Xi} \cdot \mathrm{d}\mathbf{X} = \boldsymbol{\Xi} \cdot \bar{\mathbf{E}}\,\mathrm{d}\mathbf{X} = \boldsymbol{\xi} \cdot \bar{\mathbf{A}}\,\mathrm{d}\mathbf{x}\,.$$

Therein, $\overset{3}{\mathbf{E}}$ is the third-order Ricci-permutation tensor, cf. (A.13).

Deformation, strain and curvature rates: A computation of the material time derivative of the director motion (2.52) reveals the skew-symmetric micropolar gyration tensor $\bar{\boldsymbol{\Omega}} = -\bar{\boldsymbol{\Omega}}^T$ as the tensor-valued operator relating the director frame rate $\dot{\boldsymbol{\xi}}$ to $\boldsymbol{\xi}$. Specifically, this yields

$$\dot{\boldsymbol{\xi}} = \dot{\bar{\mathbf{R}}}\,\bar{\mathbf{R}}^T := \bar{\boldsymbol{\Omega}}\,\boldsymbol{\xi} \quad \text{with} \quad \bar{\boldsymbol{\Omega}} = \dot{\bar{\mathbf{R}}}\,\bar{\mathbf{R}}^T = -\overset{3}{\mathbf{E}}\,\bar{\boldsymbol{\omega}} \quad \text{and} \quad \bar{\boldsymbol{\omega}} = \tfrac{1}{2}\overset{3}{\mathbf{E}}\,\bar{\boldsymbol{\Omega}}^T\,, \tag{2.61}$$

where $\bar{\boldsymbol{\omega}} = \dot{\bar{\boldsymbol{\varphi}}}$ is the rotational velocity of the director frame. Proceeding from the spatial velocity gradient $\mathbf{L}$, specified in (2.16) for the standard Cauchy formulation, an alternative micropolar split of $\mathbf{L}$ follows by use of (2.61) as

$$\mathbf{L} = \mathbf{D} + \mathbf{W} = \bar{\boldsymbol{\Omega}} + \bar{\boldsymbol{\Delta}} \quad \text{with} \quad \bar{\boldsymbol{\Delta}} = \bar{\mathbf{R}}\,\dot{\bar{\mathbf{U}}}\,\bar{\mathbf{U}}^{-1}\,\bar{\mathbf{R}}^T\,. \tag{2.62}$$

Therein, $\bar{\boldsymbol{\Delta}} \neq \bar{\boldsymbol{\Delta}}^T$ denotes the non-symmetric micropolar deformation velocity tensor. Due to the alternative introduction of the strain tensors and their covariant transport mechanism for the micropolar formulation, the objective upper Oldroyd derivative $\overset{\Delta}{\mathbf{A}}$ of the strain tensor $\mathbf{A}$ takes the modified form

$$\overset{\Delta}{\bar{\mathbf{A}}} = \bar{\mathbf{R}}\,\dot{\bar{\mathbf{E}}}\,\mathbf{F}^{-1} = \bar{\boldsymbol{\Omega}}^T\,\bar{\mathbf{A}} + \dot{\bar{\mathbf{A}}} + \mathbf{A}\,\mathbf{L} = \mathbf{L} - \bar{\boldsymbol{\Omega}} = \bar{\boldsymbol{\Delta}}\,, \tag{2.63}$$

compare, for example, Volk [211]. The corresponding rate of the curvature tensor follows from the material time derivative of the referential third-order curvature and the appropriate push forward transport, as specified in (2.58). In particular, one obtains by additionally making use of the skew-symmetry of $\bar{\boldsymbol{\Omega}}$,

$$(\overset{3}{\bar{\mathbf{C}}})^{\Delta} = [\,\bar{\mathbf{R}}\,(\,{}^{R}\dot{\overset{3}{\bar{\mathbf{C}}}}^{T}\,\bar{\mathbf{R}}^T\,)^{\underline{3}\,\underline{23}\,T}\,\mathbf{F}^{-1}\,]^{\underline{3}} = \operatorname{grad}\bar{\boldsymbol{\Omega}} = (\,\overset{3}{\mathbf{E}}\operatorname{grad}\bar{\boldsymbol{\omega}}\,)^{\underline{3}}\,. \tag{2.64}$$

By computation of the corresponding axial tensor to (2.64), the Oldroyd rate of the second-order curvature tensor $\bar{\mathbf{C}}$ is finally given by

$$\overset{\Delta}{\bar{\mathbf{C}}} = \bar{\mathbf{R}}\,{}^{R}\dot{\bar{\mathbf{C}}}\,\mathbf{F}^{-1} = \operatorname{grad}\bar{\boldsymbol{\omega}}\,. \tag{2.65}$$

2.3.2 Stress concept

In a micropolar continuum formulation, the interaction between micro-particles is governed by stresses and additional couple or moment stresses. Therefore, the macroscopic point at $\mathbf{x}$ can support couple and stress vectors, $\bar{\mathbf{m}}$ and $\mathbf{t}$, respectively, when the body is virtually separated at a cut with the outward-oriented surface normal vector $\mathbf{n}$. Cauchy's lemma of classical continuum mechanics is therefore extended, such that

$$\mathbf{t}\,(\,\mathbf{x},\,\mathbf{n},\,t\,) = -\,\mathbf{t}\,(\,\mathbf{x},\,-\mathbf{n},\,t\,) \quad \text{and} \quad \bar{\mathbf{m}}\,(\,\mathbf{x},\,\mathbf{n},\,t\,) = -\,\bar{\mathbf{m}}\,(\,\mathbf{x},\,-\mathbf{n},\,t\,)\,. \tag{2.66}$$

Thus, in addition to the stress tensor $\mathbf{T}$, a couple stress tensor $\bar{\mathbf{M}}$ is introduced. Both are connected to the corresponding surface vectors through the extended Cauchy theorem

$$\mathbf{t}\,(\,\mathbf{x},\,\mathbf{n},\,t\,) = [\,\mathbf{T}\,(\,\mathbf{x},\,t\,)\,]\,\mathbf{n} \quad \text{and} \quad \bar{\mathbf{m}}\,(\,\mathbf{x},\,\mathbf{n},\,t\,) = [\,\bar{\mathbf{M}}\,(\,\mathbf{x},\,t\,)\,]\,\mathbf{n}\,. \tag{2.67}$$

2.3.3 Balance relations

The above considerations concerning the kinematic extension through a free rotational field and the existence of couple stresses need to be accounted for in the balances of angular momentum as well as the balance of total energy. The balances of mass and linear momentum remain unchanged and are thus not recapitulated at this point; the statements given in (2.29) – (2.36) remain valid.

Balance of angular momentum: The angular momentum vector $\mathbf{h}_{\mathcal{O}}(\mathcal{B},\, t)$ needs to be extended by the additional contributions stemming from the rotational motion. Furthermore, the acting moments $\mathbf{m}_{\mathcal{O}}(\mathcal{B},\, t)$ on the body exhibit couple stresses $\bar{\mathbf{m}}$ and possible volume-specific body couples $\mathbf{c}$. As a consequence, the axiomatic global balance of angular momentum (2.39) extends towards

$$\frac{\mathrm{d}}{\mathrm{d}t}\int_{\mathcal{B}}[\,\mathbf{x}\times(\,\rho\,\dot{\mathbf{x}}\,)+\rho\,\bar{\boldsymbol{\Theta}}\,\bar{\boldsymbol{\omega}}\,]\,\mathrm{d}v \;=\; \int_{\partial\mathcal{B}}(\,\mathbf{x}\times\mathbf{t}+\bar{\mathbf{m}}\,)\,\mathrm{d}a+\int_{\mathcal{B}}[\,\mathbf{x}\times(\,\rho\,\mathbf{b}\,)+\rho\,\mathbf{c}\,]\,\mathrm{d}v\,, \tag{2.68}$$

where $\bar{\boldsymbol{\Theta}}$ defines the mass-moment-of-inertia tensor. Not that, due to the assumed rigidity of the underlying microcontinuum, the coefficients of $\bar{\boldsymbol{\Theta}}$ are constant in a local co-rotating frame fixed to the microcontinuum. This can be seen from the computation of the vanishing time derivative with respect to the co-rotating frame, the so-called Green-Naghdi derivative, which reads $\overset{\diamondsuit}{\bar{\boldsymbol{\Theta}}} = \dot{\bar{\boldsymbol{\Theta}}} - \bar{\boldsymbol{\Omega}}\bar{\boldsymbol{\Theta}} - \bar{\boldsymbol{\Theta}}\bar{\boldsymbol{\Omega}}^{T} = \mathbf{0}$, cf. Diebels [49] or Ehlers [56]. In comparison with the vector-valued general balance $(2.27)_2$, one identifies by use of (2.67)

$$\begin{aligned}&\boldsymbol{\Psi} \;\to\; \mathbf{x}\times(\,\rho\,\dot{\mathbf{x}}\,)+\rho\,\bar{\boldsymbol{\Theta}}\,\bar{\boldsymbol{\omega}}\,,\quad \boldsymbol{\Phi}\,\mathbf{n} \;\to\; (\,\mathbf{x}\times\mathbf{T}\,)\,\mathbf{n}+\bar{\mathbf{M}}\,\mathbf{n}\,,\\ &\boldsymbol{\varsigma} \;\to\; \mathbf{x}\times(\,\rho\,\mathbf{b}\,)+\rho\,\mathbf{c}\,,\quad \hat{\boldsymbol{\Psi}} \;\to\; \mathbf{0}\,.\end{aligned} \tag{2.69}$$

The local form of the angular momentum balance of a micropolar medium follows by use of the mass balance and the linear momentum balance as

$$\rho\,\bar{\boldsymbol{\Theta}}\,\dot{\bar{\boldsymbol{\omega}}} \;=\; \mathbf{I}\,\times\,\mathbf{T}\,+\,\operatorname{div}\bar{\mathbf{M}}\,+\,\rho\,\mathbf{c}\,, \tag{2.70}$$

where the divergence identity (A.24) is applied. Note that the term $\mathbf{I}\times\mathbf{T} = \overset{3}{\mathbf{E}}\mathbf{T}^{T} = 2\overset{A}{\mathbf{t}}$ in (2.70) again incorporates the skew-symmetric contributions of $\mathbf{T}$, with $\overset{A}{\mathbf{t}}$ as the axial vector to $\mathbf{T}$, cf. (A.13). Hence, (2.70) implies that the stress state $\mathbf{T}\neq\mathbf{T}^{T}$ is non-symmetric for a micropolar continuum.

Balance of mechanical power: In comparison to the standard formulation, the kinetic part of the body's total energy is extended, again to account for the contributions stemming from the rotational director motion, such that

$$\mathcal{K}\,(\,\mathcal{B},\;t\,) \;=\; \int_{\mathcal{B}}[\,\tfrac{1}{2}\,\rho\,\dot{\mathbf{x}}\,\cdot\,\dot{\mathbf{x}}\,+\,\tfrac{1}{2}\,\bar{\boldsymbol{\omega}}\,\cdot\,(\,\rho\,\bar{\boldsymbol{\Theta}}\,\bar{\boldsymbol{\omega}}\,)\,]\,\mathrm{d}v\,. \tag{2.71}$$

Furthermore, the external mechanical power needs to include the power generated by surface couples at the boundary and by volume-specific couples in the interior of the

body. This yields in extension to the mechanical power of a Cauchy continuum (2.44),

$$\mathcal{L}_a(\mathcal{B},\,t) = \int_{\partial\mathcal{B}} (\,\dot{\mathbf{x}}\cdot\mathbf{t} + \bar{\boldsymbol{\omega}}\cdot\bar{\mathbf{m}}\,)\,\mathrm{d}a + \int_{\mathcal{B}} (\,\dot{\mathbf{x}}\cdot\rho\,\mathbf{b} + \bar{\boldsymbol{\omega}}\cdot\rho\,\mathbf{c}\,)\,\mathrm{d}v\,. \tag{2.72}$$

In the absence of non-mechanical external power and assuming adiabatic conditions, one recognises in comparison to the scalar-valued general balance structure $(2.27)_1$ that

$$\begin{aligned} &\Psi \;\to\; \rho\,[\,\varepsilon + \tfrac{1}{2}\,\dot{\mathbf{x}}\cdot\dot{\mathbf{x}} + \tfrac{1}{2}\,\bar{\boldsymbol{\omega}}\cdot(\,\bar{\boldsymbol{\Theta}}\,\bar{\boldsymbol{\omega}}\,)\,]\,, \quad \boldsymbol{\phi}\cdot\mathbf{n} \;\to\; (\,\mathbf{T}^T\dot{\mathbf{x}} + \bar{\mathbf{M}}^T\bar{\boldsymbol{\omega}}\,)\cdot\mathbf{n}\,, \\ &\varsigma \;\to\; \rho\,(\,\dot{\mathbf{x}}\cdot\mathbf{b} + \bar{\boldsymbol{\omega}}\cdot\mathbf{c}\,), \quad \hat{\Psi} \;\to\; 0\,. \end{aligned} \tag{2.73}$$

The balance of total energy again reduces to the balance of mechanical power, which now takes the local form

$$\rho\,\dot{\varepsilon} = \mathbf{T}\cdot\bar{\boldsymbol{\Delta}} + \bar{\mathbf{M}}\cdot\operatorname{grad}\bar{\boldsymbol{\omega}} =: \rho\,w_i\,(\,\mathbf{x}\,,\;\boldsymbol{\xi}\,,\;t\,)\,. \tag{2.74}$$

Thereby use is made of the hierarchically lower balance relations and of the identity $(\mathbf{I}\times\mathbf{T})\cdot\bar{\boldsymbol{\omega}} = \mathbf{T}\cdot\bar{\boldsymbol{\Omega}}$ in combination with the micropolar split of the deformation velocity gradient (2.62). It is evident that the kinematic alteration from the Cauchy continuum also effects the generated mechanical stress power w_i. Now, the non-symmetric stress $\mathbf{T}$ is energetically conjugated to the Oldroyd rate $\overset{\vartriangle}{\mathbf{A}} = \bar{\boldsymbol{\Delta}}$ leading to the term $\mathbf{T}\cdot\bar{\boldsymbol{\Delta}}$, while the couple stress $\bar{\mathbf{M}}$ naturally extends the internal stress power in combination with the gradient $\operatorname{grad}\bar{\boldsymbol{\omega}}$ of the director's rotational velocity field $\bar{\boldsymbol{\omega}}$. For the overall body $\mathcal{B}$, internal mechanical stress power $\mathcal{L}_i(\mathcal{B},\,t)$ is thus generated by

$$\mathcal{L}_i(\mathcal{B},\,t) = \int_{\mathcal{B}} (\,\mathbf{T}\cdot\bar{\boldsymbol{\Delta}} + \bar{\mathbf{M}}\cdot\operatorname{grad}\bar{\boldsymbol{\omega}}\,)\,\mathrm{d}v = \int_{\mathcal{B}} (\,\boldsymbol{\tau}\cdot\bar{\boldsymbol{\Delta}} + \bar{\boldsymbol{\mathcal{M}}}\cdot\operatorname{grad}\bar{\boldsymbol{\omega}}\,)\,\mathrm{d}V\,. \tag{2.75}$$

Therein, $\bar{\boldsymbol{\mathcal{M}}} = (\det\mathbf{F})\bar{\mathbf{M}}$ denotes the weighted couple stress tensor following from relating the couple stress vector $\bar{\mathbf{m}}$ to a weighted area element of the actual configuration analogously to the Kirchhoff stress $\boldsymbol{\tau}$. In extension to the mechanical stress power w_i of the Cauchy continuum formulation (2.50), equivalent expressions of w_i in the case of a micropolar extension are thus given by

$$\begin{aligned} w_i = \frac{1}{\rho}\,(\,\mathbf{T}\cdot\overset{\vartriangle}{\bar{\mathbf{A}}} + \bar{\mathbf{M}}\cdot\overset{\vartriangle}{\bar{\mathbf{C}}}\,) = \frac{1}{\rho_0}\,(\,\boldsymbol{\tau}\cdot\overset{\vartriangle}{\bar{\mathbf{A}}} + \bar{\boldsymbol{\mathcal{M}}}\cdot\overset{\vartriangle}{\bar{\mathbf{C}}}\,) \\ \text{with}\quad \overset{\vartriangle}{\bar{\mathbf{A}}} = \bar{\boldsymbol{\Delta}} \quad\text{and}\quad \overset{\vartriangle}{\bar{\mathbf{C}}} = \operatorname{grad}\bar{\boldsymbol{\omega}}\,, \end{aligned} \tag{2.76}$$

according to (2.63) and (2.65), respectively. Finally, two work-conjugated sets of pairs between the micropolar stresses and the micropolar deformation quantities follow as

$$\{\,\frac{1}{\rho}\,\mathbf{T}\,,\;\bar{\mathbf{A}}\,\} \quad\text{and}\quad \{\,\frac{1}{\rho}\,\bar{\mathbf{M}}\,,\;\bar{\mathbf{C}}\,\} \quad\text{or}\quad \{\,\frac{1}{\rho_0}\,\boldsymbol{\tau}\,,\;\bar{\mathbf{A}}\,\} \quad\text{and}\quad \{\,\frac{1}{\rho_0}\,\bar{\boldsymbol{\mathcal{M}}}\,,\;\bar{\mathbf{C}}\,\}\,. \tag{2.77}$$

2.4 The micromorphic continuum

The micromorphic approach is a further extension of the micropolar continuum, in which the finite-size material point is regarded as an embedded microcontinuum with a homogeneous deformation, cf. Figure 2.3. The attached director is thus no longer assumed to be rigid, but is also able to deform.

2.4.1 Micromorphic director motion

The physical picture of an embedded microcontinuum: In order to derive the micromorphic director motion, a macroscopic body $\mathcal{B}$ with an attached Cauchy-type microcontinuum $\mathcal{B}_m$ of finite size at the underlying microscale is considered, cf. Figure 2.4. In this setting, the position $\mathbf{x}$, pointing at any material point of $\mathcal{B}_m$, reads

$$\mathbf{x} \,=\, \mathbf{x}_{\mathcal{M}}\,(\,\mathbf{X}_{\mathcal{M}},\; t\,) \,+\, \mathbf{x}_m\,(\,\mathbf{X}_{\mathcal{M}},\; \mathbf{X}_m,\; t\,)\,, \tag{2.78}$$

where $\mathbf{x}_{\mathcal{M}}$ points at the centroid of the underlying microcontinuum and $\mathbf{x}_m$ is a local position vector, both with their respective placements $\mathbf{X}_{\mathcal{M}}$ and $\mathbf{X}_m$ in the referential state. The macroscopic motion function $\boldsymbol{\chi}(\mathbf{X}_{\mathcal{M}},\, t)$ is assumed to be accompanied by an independent micromotion $\boldsymbol{\chi}_m(\mathbf{X}_{\mathcal{M}},\, \mathbf{X}_m,\, t)$, such that

$$\mathbf{x} \,=\, \boldsymbol{\chi}\,(\,\mathbf{X}_{\mathcal{M}}\,,\; t\,) \quad \text{and} \quad \mathbf{x}_m \,=\, \boldsymbol{\chi}_m\,(\,\mathbf{X}_{\mathcal{M}}\,,\; \mathbf{X}_m\,,\; t\,)\,. \tag{2.79}$$

As a result, the deformation of the micromorphic material point is taken into consideration, however, as a homogeneous deformation, following a linearisation of $(2.79)_2$ around $\mathbf{X}_m = \mathbf{0}$, viz.:

$$\mathbf{x}_m \,=\, \boldsymbol{\chi}_m\,(\,\mathbf{X},\; t\,) \,=\, \boldsymbol{\chi}_m\,\Big|_{\mathbf{X}_m\,=\,\mathbf{0}} \,+\, \frac{\partial \boldsymbol{\chi}_m}{\partial \mathbf{X}_m}\,\Big|_{\mathbf{X}_m\,=\,\mathbf{0}}\,\mathbf{X}_m\,. \tag{2.80}$$

As a result, $(2.79)_2$ reduces to

$$\mathbf{x}_m \,=\, \mathbf{F}_m\,(\,\mathbf{X}_{\mathcal{M}},\, t\,)\,\mathbf{X}_m\,, \tag{2.81}$$

where $\mathbf{F}_m := \partial \boldsymbol{\chi}_m / \partial \mathbf{X}_m$ is the deformation gradient of the micromotion that can be split into

$$\mathbf{F}_m \,=\, \mathbf{R}_m\,\mathbf{U}_m \,=\, \mathbf{V}_m\,\mathbf{R}_m \quad \text{with} \begin{cases} \mathbf{U}_m \,=\, \mathbf{I}\,,\; \mathbf{V}_m \,=\, \mathbf{I} & : \text{the micropolar case} \\ \mathbf{R}_m \,=\, \mathbf{I} & : \text{the microstrain case.} \end{cases} \tag{2.82}$$

Therein, $\mathbf{U}_m$ and $\mathbf{V}_m$ are the respective right and left stretch tensors of the microdeformation and $\mathbf{R}_m$ is the rotation tensor to the free microrotation $\boldsymbol{\varphi}_m$, cf. (2.53). Assuming

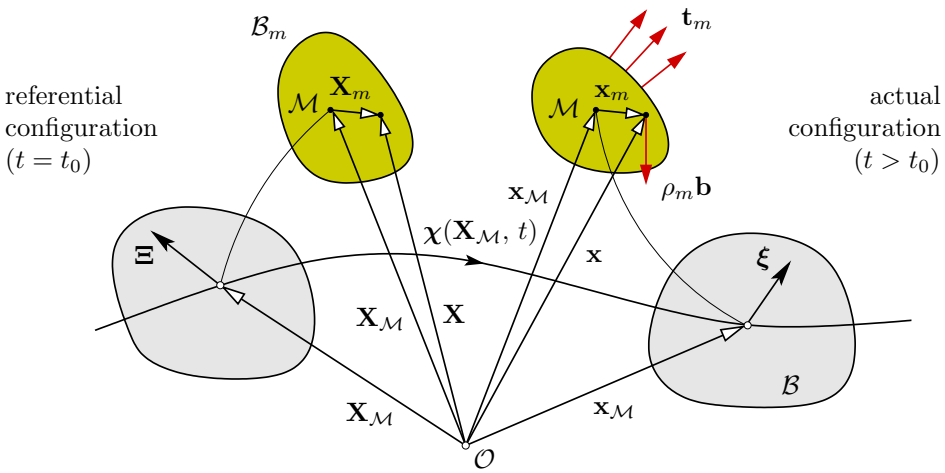

Figure 2.4: *Kinematics of the micromorphic continuum.*

a homogeneous density distribution in the domain of $\mathcal{B}_m$ additionally implies that the geometrical centre at $\mathbf{x}_\mathcal{M}$ always coincides with the microcontinuum's centre of mass $\mathcal{M}$. The material time derivative of (2.81) leads to

$$\dot{\mathbf{x}}_m \,=\, \mathbf{L}_m\,\mathbf{x}_m\,, \quad \ddot{\mathbf{x}}_m \,=\, (\,\dot{\mathbf{L}}_m \,+\, \mathbf{L}_m\,\mathbf{L}_m\,)\,\mathbf{x}_m\,, \tag{2.83}$$

where $\mathbf{L}_m := \dot{\mathbf{F}}_m\mathbf{F}_m^{-1}$ defines the microscopic spatial velocity gradient. In accordance to (2.15) and (2.16), $\mathbf{L}_m$ can again be additively split into microscopic versions of the deformation velocity tensor $\mathbf{D}_m$ and the spin tensor $\mathbf{W}_m$ or into the deformation velocity tensor $\boldsymbol{\Delta}_m$ and the gyration tensor $\boldsymbol{\Omega}_m$. As a direct consequence of (2.81) and (2.83), the relations

$$\int_{\mathcal{B}_m} \mathbf{x}_m\,\mathrm{d}m \,=\, \mathbf{0} \quad\rightarrow\quad \int_{\mathcal{B}_m} \dot{\mathbf{x}}_m\,\mathrm{d}m \,=\, \mathbf{0} \quad\rightarrow\quad \int_{\mathcal{B}_m} \ddot{\mathbf{x}}_m\,\mathrm{d}m \,=\, \mathbf{0} \tag{2.84}$$

hold due to the homogeneity of $\mathbf{F}_m$ and $\mathbf{L}_m$ in the domain of $\mathcal{B}_m$. Note that, to obtain $(2.84)_{2/3}$, the time derivative of $(2.84)_1$ is computed using the consequences of the mass balance of a Cauchy continuum, compare (2.29).

Extended micromotion: Given micromorphic material, a combination of micro- and macromotions yields a micromorphic director motion $\bar{\mathbf{F}}$ in substitution of the micropolar motion $\bar{\mathbf{R}}$, cf. (2.52), where

$$\boldsymbol{\xi}\,(\,\mathbf{X},\,t\,) \,=\, \bar{\mathbf{F}}\,(\,\mathbf{X},\,t\,)\,\boldsymbol{\Xi} \quad\longleftrightarrow\quad \boldsymbol{\Xi}\,(\,\mathbf{X},\,t_0\,) \,=\, \bar{\mathbf{F}}^{-1}\,(\,\mathbf{X},\,t\,)\,\boldsymbol{\xi}\,, \tag{2.85}$$

compare Neff & Forest [165]. Two combinations for the micromotion are then possible and enable the micromorphic motion to be downwardly compatible to the aforementioned micropolar formulation. These are

$$\bar{\mathbf{F}} \,=\, \begin{cases} \mathbf{R}\,(\mathbf{F}_m)_\mathcal{B} \,=\, \bar{\mathbf{R}}\,(\mathbf{U}_m)_\mathcal{B} & \text{together with } (2.82)_1 \text{ and } (2.53)\,, \\ (\mathbf{F}_m)_\mathcal{B}\,\mathbf{R} \,=\, (\mathbf{V}_m)_\mathcal{B}\,\bar{\mathbf{R}} & \text{together with } (2.82)_2 \text{ and } (2.54)\,, \end{cases} \tag{2.86}$$

where $(\mathbf{F}_m)_\mathcal{B}$, $(\mathbf{U}_m)_\mathcal{B}$ and $(\mathbf{V}_m)_\mathcal{B}$ define the averaged macroscopic counterparts to the microscale quantities $\mathbf{F}_m$, $\mathbf{U}_m$ and $\mathbf{V}_m$, respectively. It is evident that for the case of a vanishing microstretch $(\mathbf{U}_m)_\mathcal{B}$, $\bar{\mathbf{F}}$ falls back to the combined micropolar director rotation $\bar{\mathbf{R}}$, compare (2.52). Regarding the motion of the director from its referential to its actual position, exemplarily with $(2.86)_1$, it can be seen that it is composed of a microstretch $(\mathbf{U}_m)_\mathcal{B}$, followed by the total rotation, which itself is composed of the free microrotation $(\mathbf{R}_m)_\mathcal{B}$ and the continuum rotation $\mathbf{R}$, as illustrated in Figure 2.5.

2.4.2 Kinematical relations

Deformation, strain and curvature tensors: With the two combinations (2.86) of the director motion, two corresponding micromorphic deformation tensors can be defined by applying a multiplicative split of the macroscopic deformation gradient $\mathbf{F}$. Proceeding again either from the right or from the left polar decomposition, results in

$$\mathbf{F} \,=\, \begin{cases} \mathbf{R}\,\mathbf{U} \,=\, \bar{\mathbf{F}}\,\bar{\mathbf{U}} & \text{togehter with } (2.86)_1 \text{ and } \quad \bar{\mathbf{U}} \,=\, \bar{\mathbf{F}}^{-1}\,\mathbf{F} \,=\, (\mathbf{F}_m)_\mathcal{B}^{-1}\,\mathbf{U} \\ \mathbf{V}\,\mathbf{R} \,=\, \bar{\mathbf{V}}\,\bar{\mathbf{F}} & \text{togehter with } (2.86)_2 \text{ and } \quad \bar{\mathbf{V}} \,=\, \mathbf{F}\,\bar{\mathbf{F}}^{-1} \,=\, \mathbf{V}\,(\mathbf{F}_m)_\mathcal{B}^{-1}\,. \end{cases} \tag{2.87}$$

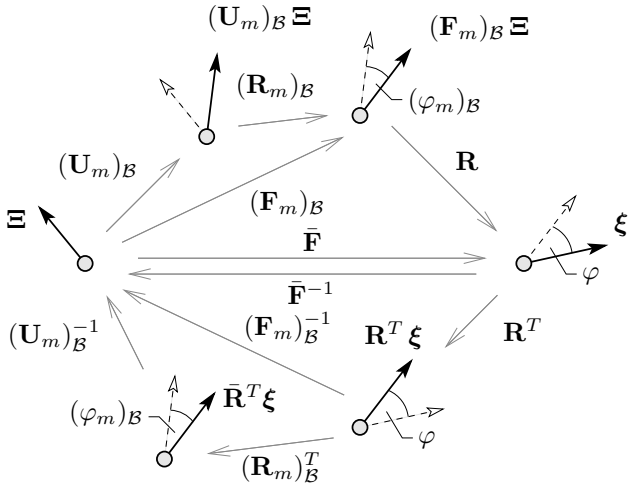

Figure 2.5: *Complete combined motion of the micromorphic director.*

Thereby the micromorphic right and left stretch tensors $\bar{\mathbf{U}}$ and $\bar{\mathbf{V}}$, respectively, substitute their micropolar counterparts given in (2.53) and (2.54). Note that neither the micromorphic stretch tensors $\bar{\mathbf{U}}$ and $\bar{\mathbf{V}}$ nor the micromotion tensor $\bar{\mathbf{F}}$ show symmetry or orthogonality conditions. Furthermore note that in contrast to the polar decomposition of $\mathbf{F}$, the multiplicative splits given by $\mathbf{F} = \bar{\mathbf{F}}\bar{\mathbf{U}} = \bar{\mathbf{V}}\bar{\mathbf{F}}$ are not unique. Thus, additional governing equations are required for the solution of the microdeformation in order to determine the full deformational process given by (2.87). In the micropolar case, where the microdeformation is a pure rotation, the remaining axiomatic part of the balance of angular momentum, cf. (2.70), supplies the governing equations for the determination of the unknown microrotation. In the micromorphic case, the balance of angular momentum is generalised to include the homogeneous microdeformation and consequently serves as the governing equation for the determination of $(\mathbf{F}_m)_{\mathcal{B}}$, cf. the subsequent Section 2.4.3.

The micromorphic strain tensors of Green-Lagrangean and Almansian-type are formally identical to the micropolar strain tensors (2.57), but differ by the definition $\bar{\mathbf{U}}$ and $\bar{\mathbf{V}}$, viz.:

$$\bar{\mathbf{E}} := \bar{\mathbf{U}} - \mathbf{I} \quad \text{and} \quad \bar{\mathbf{A}} := \mathbf{I} - \bar{\mathbf{V}}^{-1}, \quad \text{where} \quad \bar{\mathbf{A}} = \bar{\mathbf{F}}\,\bar{\mathbf{E}}\,\mathbf{F}^{-1}. \tag{2.88}$$

Note that $\bar{\mathbf{E}}$ and $\bar{\mathbf{A}}$ are not geometrically obtained by comparison of scalar measures stemming from the combination of macroscopic line elements and directors, as this is the case in the micropolar formulation. This originates from the fact that both, director and macroscopic line element, have a covariant character and a corresponding covariant transport mechanism, while $\bar{\mathbf{E}}$ and $\bar{\mathbf{A}}$ from (2.88) both have one covariant and one contravariant basis system, compare the derivation of Cauchy and micromorphic strain measures by means of a natural basis representation given in Appendix B.1. Only in the case of a proper orthogonal director motion, as given in the micropolar case, the co- and contravariant transports are formally identical[4].

[4] The suitable quantity to geometrically derive the micromorphic versions of $\bar{\mathbf{U}}$ and $\bar{\mathbf{V}}$ is the contravariant element $\boldsymbol{\zeta}$, with its image $\mathbf{Z}$ in the referential state, which can be thought of as the normal to the material surface of the embedded microcontinuum, cf. Grammenoudis & Tsakmakis [99]. In analogy to an oriented continuum surface element, its transport from referential to actual configuration and vice

While $\bar{\mathbf{U}}$ and $\bar{\mathbf{V}}$ (or $\bar{\mathbf{E}}$ and $\bar{\mathbf{A}}$, respectively) are relative strain measures that account for the deviation between micro- and macrodeformation, the deformation of the microcontinuum itself is measured through comparison of the scalar products of the directors in actual and referential states, viz.:

$$\boldsymbol{\xi} \cdot \boldsymbol{\xi} - \boldsymbol{\Xi} \cdot \boldsymbol{\Xi} = \boldsymbol{\Xi} \cdot 2\,(\mathbf{E}_m)_{\mathcal{B}}\,\boldsymbol{\Xi} = \boldsymbol{\xi} \cdot 2\,(\mathbf{A}_m)_{\mathcal{B}}\,\boldsymbol{\xi}\,, \tag{2.89}$$

with the Green-Lagrangean microstrain $(\mathbf{E}_m)_{\mathcal{B}}$ and the Almansian microstrain $(\mathbf{A}_m)_{\mathcal{B}}$ defined as

$$(\mathbf{E}_m)_{\mathcal{B}} := \tfrac{1}{2}\,(\,\bar{\mathbf{F}}^T\,\bar{\mathbf{F}} - \mathbf{I}\,) = \tfrac{1}{2}\,[\,(\mathbf{F}_m)_{\mathcal{B}}^T\,(\mathbf{F}_m)_{\mathcal{B}} - \mathbf{I}\,] \tag{2.90}$$

by use of $(2.82)_1$ and $(2.86)_1$ and

$$(\mathbf{A}_m)_{\mathcal{B}} := \tfrac{1}{2}\,[\,\mathbf{I} - (\,\bar{\mathbf{F}}\,\bar{\mathbf{F}}^T\,)^{-1}\,] = \tfrac{1}{2}\big(\,\mathbf{I} - [\,(\mathbf{F}_m)_{\mathcal{B}}\,(\mathbf{F}_m)_{\mathcal{B}}^T\,]^{-1}\,\big) \tag{2.91}$$

by use of $(2.82)_2$ and $(2.86)_2$, respectively. Consequently, the transformation relation between $(\mathbf{A}_m)_{\mathcal{B}}$ and $(\mathbf{E}_m)_{\mathcal{B}}$ follows as

$$(\mathbf{A}_m)_{\mathcal{B}} = \bar{\mathbf{F}}^{T-1}\,(\mathbf{E}_m)_{\mathcal{B}}\,\bar{\mathbf{F}}^{-1}\,. \tag{2.92}$$

The set of kinematic variables is again completed with the introduction of a third-order curvature tensor, which apart from the change in the director motion from $\bar{\mathbf{R}}$ to $\bar{\mathbf{F}}$ remains unchanged in comparison to the micropolar curvature tensor, viz.:

$${}^{R}\overset{3}{\bar{\mathbf{C}}} = (\,\bar{\mathbf{F}}^{-1}\,\mathrm{Grad}\,\bar{\mathbf{F}}\,)^{\underline{3}} \quad \text{and} \quad \overset{3}{\bar{\mathbf{C}}} = [\,(\,\mathrm{grad}\,\bar{\mathbf{F}})^{\overset{23}{T}}\,\bar{\mathbf{F}}^{-1}\,]^{\underline{\underline{3}}\overset{23}{T}}\,, \tag{2.93}$$

with the corresponding transport from the referential to the actual frame reading

$$\overset{3}{\bar{\mathbf{C}}} = \big(\,[\,\bar{\mathbf{F}}\,(\,{}^{R}\overset{3}{\bar{\mathbf{C}}}\overset{23}{T}\,\bar{\mathbf{F}}^{-1}\,)^{\underline{\underline{3}}\overset{23}{T}}\,]^{\underline{3}}\,\mathbf{F}^{-1}\,\big)^{\underline{3}}\,. \tag{2.94}$$

However, in comparison to the micropolar curvature, a reduction of the tensorial order of the curvature tensor is no longer possible without loss of information, as the symmetry condition (2.59) does not hold for the micromorphic case.

Material time derivatives: The material time derivative of the director motion (2.85) reads

$$\dot{\boldsymbol{\xi}} = \dot{\bar{\mathbf{F}}}\,\bar{\mathbf{F}}^{-1}\,\boldsymbol{\xi} =: \bar{\mathbf{L}}\,\boldsymbol{\xi}\,, \tag{2.95}$$

with $\bar{\mathbf{L}} = \dot{\bar{\mathbf{F}}}\bar{\mathbf{F}}^{-1}$ defined as the micromorphic spatial velocity gradient relating the director rate $\dot{\boldsymbol{\xi}}$ to $\boldsymbol{\xi}$. Again, objective upper Oldroyd derivatives can be defined for the

versa are contravariant operations reading

$$\boldsymbol{\zeta} = \bar{\mathbf{F}}^{T-1}\,\mathbf{Z} \quad \longleftrightarrow \quad \mathbf{Z} = \bar{\mathbf{F}}^{T}\,\boldsymbol{\zeta}\,.$$

Consequently, the micromorphic right and left deformation tensors $\bar{\mathbf{U}}$ and $\bar{\mathbf{V}}$ then follow from

$$\boldsymbol{\zeta} \cdot \mathrm{d}\mathbf{x} = \mathbf{Z} \cdot \bar{\mathbf{U}}\,\mathrm{d}\mathbf{X} \quad \text{and} \quad \mathbf{Z} \cdot \mathrm{d}\mathbf{X} = \boldsymbol{\zeta} \cdot \bar{\mathbf{V}}^{-1}\,\mathrm{d}\mathbf{x}\,,$$

together with $\bar{\mathbf{F}}$ from (2.87), while the strain tensors $\bar{\mathbf{E}}$ and $\bar{\mathbf{A}}$ result from the corresponding comparison of the scalar measures (4) in referential and actual configuration.

micromorphic rates of deformation and curvature. In particular, the following modified set of Oldroyd rates is obtained for the micromorphic microstrain $\mathbf{A}_M$, the micromorphic strain $\bar{\mathbf{A}}$ and the curvature $\overset{3}{\bar{\mathbf{C}}}$:

$$\begin{aligned}
(\overset{\Delta}{\bar{\mathbf{A}}}_m)_{\mathcal{B}} &= \bar{\mathbf{F}}^{T-1}\,(\dot{\mathbf{E}}_m)_{\mathcal{B}}\,\bar{\mathbf{F}}^{-1} = \bar{\mathbf{L}}^T\,(\mathbf{A}_m)_{\mathcal{B}} + (\dot{\mathbf{A}}_m)_{\mathcal{B}} + (\mathbf{A})_{\mathcal{B}}\,\bar{\mathbf{L}} \\
&= \tfrac{1}{2}\,(\,\bar{\mathbf{L}} + \bar{\mathbf{L}}^T) = \bar{\mathbf{L}}_{\mathrm{sym}} \\
\overset{\diamondsuit}{\bar{\mathbf{A}}} &= \bar{\mathbf{F}}\,\dot{\bar{\mathbf{E}}}\,\mathbf{F}^{-1} = -\,\bar{\mathbf{L}}\,\bar{\mathbf{A}} + \dot{\bar{\mathbf{A}}} + \bar{\mathbf{A}}\,\mathbf{L} = \mathbf{L} - \bar{\mathbf{L}}\,, \\
(\overset{3}{\bar{\mathbf{C}}})^{\diamondsuit} &= \big(\bar{\mathbf{F}}\,[\,(\,{}^{R}\overset{3}{\bar{\mathbf{C}}}{}^{\underline{23}}{}^{T})^{\cdot}\,\bar{\mathbf{F}}^{-1}\,]^{\underline{3}\underline{23}T}\,\mathbf{F}_{\mathcal{B}}^{-1}\big)^{\underline{3}} = \operatorname{grad}\bar{\mathbf{L}} \\
&= (\overset{3}{\bar{\mathbf{C}}})^{\cdot} - (\,\bar{\mathbf{L}}\overset{3}{\bar{\mathbf{C}}}\,)^{\underline{3}} + (\,\overset{3}{\bar{\mathbf{C}}}{}^{\underline{23}}{}^{T}\,\bar{\mathbf{L}}\,)^{\underline{3}\underline{23}T} + (\,\overset{3}{\bar{\mathbf{C}}}\,\mathbf{L})^{\underline{3}}.
\end{aligned} \tag{2.96}$$

Thereby, the symbol $(\,\cdot\,)^{\diamondsuit}$ is used for mixed-mode terms, where the Oldroyd derivatives of $\bar{\mathbf{A}}$ and $\overset{3}{\bar{\mathbf{C}}}$ exhibit, in the natural-basis formulation, the first basis in the covariant frame of the tangential space and the second and third bases in the contravariant frame of the cotangential space.

Relations for the microstrain continuum: From the director motion (2.86) it is clear that the micromorphic continuum not only encompasses the micropolar continuum for $(\mathbf{U}_m)_{\mathcal{B}} = \mathbf{I}$, but also the microstrain continua for $(\mathbf{R}_m)_{\mathcal{B}} = \mathbf{I}$. Then, the relations for the microstrain continuum kinematics are given for the case, where the microdeformation gradient becomes a stretch tensor. In this case (2.87) is substituted by

$$\mathbf{F} = \begin{cases} \bar{\mathbf{F}}\,\bar{\mathbf{U}} & \text{with} \quad \bar{\mathbf{F}} = \mathbf{R}\,(\mathbf{U}_m)_{\mathcal{B}} \quad \text{and} \quad \bar{\mathbf{U}} = \bar{\mathbf{F}}^{-1}\,\mathbf{F} = (\mathbf{U}_m)_{\mathcal{B}}^{-1}\,\mathbf{U} \\ \bar{\mathbf{V}}\,\bar{\mathbf{F}} & \text{with} \quad \bar{\mathbf{F}} = (\mathbf{V}_m)_{\mathcal{B}}\,\mathbf{R} \quad \text{and} \quad \bar{\mathbf{V}} = \mathbf{F}\,\bar{\mathbf{F}}^{-1} = \mathbf{V}\,(\mathbf{V}_m)_{\mathcal{B}}^{-1}\,, \end{cases} \tag{2.97}$$

Therein, $\bar{\mathbf{U}}$ and $\bar{\mathbf{V}}$ are now given as symmetric right and left stretch tensors, measuring only a relative deformation between the macroscopic and the microscopic continuum stretches.

2.4.3 Balance relations

The first derivation of the balance equations for micromorphic continua goes back to Eringen & Suhubi [72] and Eringen [69], where the governing equations of the macroscopic micromorphic body are derived based on volume- and surface-specific averages of resulting quantities of an underlying Cauchy-type microcontinuum. Hence, in the following, the previously established physical picture of an embedded microcontinuum is further investigated, laying the ground for the extended balance relations of micromorphic continua, which are recapitulated in the line of Eringen & Suhubi [72].

Volume- and surface-specific averages: In order to define macroscopic field quantities as a result of microcontinuum counterparts, two different averaging formalisms are used.

On the one hand, a volume-specific average $\langle(\,\cdot\,)\rangle$ is given based on Hill's homogenisation theorem (Hill [111]) yielding

$$\langle(\,\cdot\,)\rangle \;:=\; \frac{1}{V}\int_V (\,\cdot\,)\,\mathrm{d}v\,, \tag{2.98}$$

where V is the volumetric homogenisation domain of interest. On the other hand, a surface-specific average $\langle(\,\cdot\,)\rangle_A$ is defined as

$$\langle(\,\cdot\,)\rangle_A \;:=\; \frac{1}{A}\int_A (\,\cdot\,)\,\mathrm{d}a\,, \tag{2.99}$$

where A is the areic homogenisation domain of interest, cf. Hassanizadeh & Gray [108]. Following Eringen & Suhubi [72], this average differentiation allows to distinguish between extrinsic and intrinsic stress measures for the micromorphic continuum, where the first stems from a surface-specific average of the microcontinuum stress vector $\mathbf{t}_m$ with respect to the external boundary of the macroscopic body and the latter stems from the volume average of the microcontinuum stress $\mathbf{T}_m$. All macroscopic field quantities, including the above mentioned stress definitions, will be introduced by defining averages according to (2.98) and (2.99) in the course of deriving the governing balance relations for the micromorphic continuum.

Balance of mass: Mass conservation is assumed to hold for the microcontinuum, such that, according to (2.32), the microscopic mass density ρ_m relates to its referential quantity ρ_{m0} via

$$\rho_{m0} \;=\; \rho_m \det\mathbf{F}_m\,. \tag{2.100}$$

Note that due to the homogeneity of the microcontiuum deformation, the overall microcontinuum volume $V_{\mathcal{B}_m}$ computes to

$$V_{\mathcal{B}_m} = \det\mathbf{F}_m\, V_{\mathcal{B}_{m0}} \quad \text{with} \quad V_{\mathcal{B}_m} \;=\; \int_{\mathcal{B}_m} \mathrm{d}v_m \quad \text{and} \quad V_{\mathcal{B}_{m0}} \;=\; \int_{\mathcal{B}_m} \mathrm{d}V_{m0}\,, \tag{2.101}$$

where $V_{\mathcal{B}_{m0}}$ is the referential volume of $\mathcal{B}_m$ and $\mathrm{d}v_m$, $\mathrm{d}V_{m0}$ are the actual and referential volume elements at the microcontinuum scale, respectively. As a consequence, $V_{\mathcal{B}_m}$ and $V_{\mathcal{B}_{m0}}$ define the local volume elements at the material point of the higher spatial scale (Hassanizadeh & Gray [108]), viz.:

$$\mathrm{d}v \;:=\; V_{\mathcal{B}_m} \quad \text{and} \quad \mathrm{d}V \;:=\; V_{\mathcal{B}_{m0}}\,. \tag{2.102}$$

The referential macroscopic mass density ρ_0 is thus defined as the volume average of its microcontinuum counterpart and reads

$$\rho_0 \;:=\; \langle\rho_{m0}\rangle \;:=\; \frac{1}{V_{\mathcal{B}_{m0}}}\int_{\mathcal{B}_{m0}} \rho_{m0}\,\mathrm{d}V_{m0}\,. \tag{2.103}$$

As the macroscopic mass density ρ must also be conserved, the relation from the macroscopic mass balance is valid and ρ computes by use of (2.101) and (2.103) to

$$\rho \;=\; \rho_0\,(\det\mathbf{F}\,)^{-1} \;=\; \frac{1}{V_{\mathcal{B}_m}}\int_{\mathcal{B}_m} \rho_m\,\mathrm{d}v_m \;=:\; \langle\rho_m\rangle\,. \tag{2.104}$$

Consequently, ρ also follows from the volume average $\langle \rho_m \rangle$ of ρ_m over $V_{\mathcal{B}_m}$. Note that, following (2.98), the referential and actual volumes $V_{\mathcal{B}_{m0}}$ and $V_{\mathcal{B}_m}$ in (2.103) and (2.104) are taken as the volumetric homogenisation domains of interest.

Balance of linear momentum: The local form of the balance of linear momentum of a Cauchy continuum (2.36) applies to the embedded microcontinuum, leading to the statement

$$\rho_m \, \ddot{\mathbf{x}} \;=\; \operatorname{div} \mathbf{T}_m \;+\; \rho_m \, \mathbf{b} \,, \tag{2.105}$$

where $\mathbf{T}_m$ is the Cauchy stress at the microcontinuum scale. The respective global balance of linear momentum for $\mathcal{B}_m$ with respect to the deformed configuration can be obtained by integration of (2.105) over the domain of $\mathcal{B}_m$. By use of (2.78) in combination with (2.84), one obtains

$$\int_{\mathcal{B}_m} \rho_m \, \ddot{\mathbf{x}}_{\mathcal{M}} \, \mathrm{d}v_m \;=\; \int_{\partial \mathcal{B}_m} \mathbf{t}_m \, \mathrm{d}a_m \;+\; \int_{\mathcal{B}_m} \rho_m \, \mathbf{b} \, \mathrm{d}v_m \,, \tag{2.106}$$

with $\mathbf{t}_m = \mathbf{T}_m \mathbf{n}$ as the microstress vector acting at $\partial \mathcal{B}_m$ and $\mathrm{d}a_m$ as the microcontinuum surface element. It thus determines the motion of the mass centre of the microcontinuum. The corresponding macroscopic balance of linear momentum for the micromorphic body is identified by averaging of the quantities contained in (2.105). The volumetric average $\langle \rho_m \, \ddot{\mathbf{x}}_{\mathcal{M}} \rangle$ defines the macroscopic change in linear momentum $\rho \, \ddot{\mathbf{x}}_{\mathcal{M}}$ and the average $\langle \rho_m \mathbf{b} \rangle$ defines the values of the macroscopic body force $\rho \, \mathbf{b}$, viz.:

$$\begin{aligned} \rho \, \ddot{\mathbf{x}}_{\mathcal{M}} \;&:=\; \langle \rho_m \, \ddot{\mathbf{x}}_{\mathcal{M}} \rangle \;:=\; \frac{1}{V_{\mathcal{B}_m}} \int_{\mathcal{B}_m} \rho_m \, \ddot{\mathbf{x}}_{\mathcal{M}} \, \mathrm{d}v_m \\ \text{and} \quad \rho \, \mathbf{b} \;&:=\; \langle \rho_m \, \mathbf{b} \rangle \;:=\; \frac{1}{V_{\mathcal{B}_m}} \int_{\mathcal{B}_m} \rho_m \, \mathbf{b} \, \mathrm{d}v_m \,. \end{aligned} \tag{2.107}$$

The surface-specific average $\langle \mathbf{t}_m \rangle_A$, taken as an average of $\mathbf{t}_m$ over the external boundary $A_{\mathcal{B}_m^{ex}}$, which constitutes the macroscopic boundary $\partial \mathcal{B}$, cf. Figure 2.6, yields the macroscopic boundary stress vector $\mathbf{t}$ as

$$\mathbf{t} \;:=\; \langle \mathbf{t}_m \rangle_A \;:=\; \frac{1}{A_{\mathcal{B}_m^{ex}}} \int_{\partial \mathcal{B}_m^{ex}} \mathbf{t}_m \, \mathrm{d}a_m \,. \tag{2.108}$$

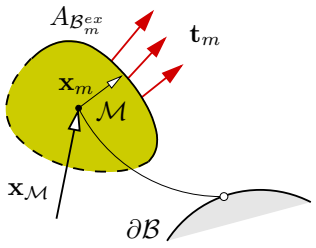

Figure 2.6: Microcontinuum setting at $\partial \mathcal{B}$.

Note that in contrast to (2.103), (2.104) and (2.107), $A_{\mathcal{B}_m^{ex}}$ is taken as the areic averaging domain of interest following the definition of a surface-specific average (2.99) and defines the infinitesimal surface element $\mathrm{d}a := A_{\mathcal{B}_m^{ex}}$ at the macroscopic boundary $\partial \mathcal{B}$.
The macroscopic balance of linear momentum for the micromorphic body thus reads

$$\int_{\mathcal{B}} \rho \, \ddot{\mathbf{x}}_{\mathcal{M}} \, \mathrm{d}v \;=\; \int_{\partial \mathcal{B}} \mathbf{t} \, \mathrm{d}a \;+\; \int_{\mathcal{B}} \rho \, \mathbf{b} \, \mathrm{d}v \;=\; \int_{\partial \mathcal{B}} (\, \mathbf{T} \, \mathbf{n} \,) \, \mathrm{d}a \;+\; \int_{\mathcal{B}} \rho \, \mathbf{b} \, \mathrm{d}v \,, \tag{2.109}$$

where the Cauchy stress $\mathbf{T}$, cf. (2.24), is retrieved. Evidently, (2.109) is formally identical to the balance of linear momentum of a standard Cauchy continuum as given in Section

2.2.3.

The extended micromorphic balance of angular momentum: Within numerical treatments of continuum-mechanical problems, (2.109) is used to solve for the unknown displacement field. For the case of a micromorphic continuum, the number of these unknowns is increased by the nine components of the microdeformation gradient, compare Figure 2.1. The so-called extended or generalised balance of moment of momentum (Eringen [71], Eringen & Suhubi [72], Grammenoudis & Tsakmakis [99]) provides an appropriate equation for the direct determination of the microdeformation or the respective director motion. It can be derived by weighting the balance of linear momentum, as given in (2.105), with the position vector $\mathbf{x}$ in terms of a dyadic multiplication before applying an integration over the domain of $\mathcal{B}_m$. This procedure yields

$$\int_{\mathcal{B}_m} [\, \mathbf{x} \otimes (\, \rho_m \ddot{\mathbf{x}}\,) \,-\, \mathbf{x} \otimes \operatorname{div} \mathbf{T}_m \,-\mathbf{x} \otimes (\, \rho_m \mathbf{b}\,)\,] \, \mathrm{d}v_m \,=\, \mathbf{0}\,. \tag{2.110}$$

This approach generalises the Cauchy and the micropolar continuum formulations, where the balance of angular momentum is derived following from a vector-valued cross product of the position vector $\mathbf{x}$ with the balance of linear momentum. For the Cauchy continuum, the angular momentum balance results in the symmetry condition of the stress tensor $\mathbf{T}$, cf. (2.41). In the micropolar formulation, the procedure results in a new axiomatic statement for the balance of angular momentum, where, as a consequence, $\mathbf{T}$ is non-symmetric, cf. (2.70). Bearing in mind the association between the skew-symmetric part of the dyadic product of two vectors and the vector product, cf. (A.13), allows to state two consequences for the derivations based on (2.110). Firstly, the symmetry condition of $\mathbf{T}$ will not be recovered due to the generalisation of the procedure and, secondly, the micropolar formulation will be included in the skew-symmetric contributions of the results, when they are expressed using the axial vector computation of the second-order tensorial quantities. By use of the divergence identity (A.25), the additive composition of $\mathbf{x}$ stated in (2.78) and taking notice of $\operatorname{grad} \mathbf{x}_{\mathcal{M}} \approx \operatorname{grad} \mathbf{x} = \mathbf{I}$, (2.110) reformulates to

$$\begin{aligned} \mathbf{x}_{\mathcal{M}} \otimes \int_{\mathcal{B}_m} \rho_m \ddot{\mathbf{x}}_{\mathcal{M}} \, \mathrm{d}v_m \,-\, \mathbf{x}_{\mathcal{M}} \otimes \int_{\mathcal{B}_m} \rho_m \mathbf{b} \, \mathrm{d}v_m \,+\, \int_{\mathcal{B}_m} [\, \mathbf{x}_m \otimes (\, \rho_m \ddot{\mathbf{x}}_m\,) \,+\, \mathbf{T}_m^T\,] \, \mathrm{d}v_m \,- \\ - \int_{\mathcal{B}_m} \mathbf{x}_m \otimes (\, \rho_m \mathbf{b}\,) \, \mathrm{d}v_m \,=\, \mathbf{x}_{\mathcal{M}} \otimes \int_{\partial \mathcal{B}_m} \mathbf{t}_m \, \mathrm{d}a_m \,+\, \int_{\partial \mathcal{B}_m} \mathbf{x}_m \otimes \mathbf{t}_m \, \mathrm{d}a_m \,. \end{aligned} \tag{2.111}$$

Based on (2.111) and in order to formulate the respective balance for the microcontinuum body, the following further field quantities of the macroscopic point are defined as volumetric averages over the microcontinuum domain in addition to (2.107): At first, the so-called microstress average $(\mathbf{T}_m)_{\mathcal{B}}$ is defined via

$$(\mathbf{T}_m)_{\mathcal{B}} \,:=\, \langle \mathbf{T}_m^T \rangle \,:=\, \frac{1}{V_{\mathcal{B}_m}} \int_{\mathcal{B}_m} \mathbf{T}_m^T \, \mathrm{d}v_m \,, \tag{2.112}$$

where the transposition $(\,\cdot\,)^T$ could also be dropped when accounting for the symmetry of $\mathbf{T}_m$, as it can be derived from the balance of angular momentum of the underlying

Cauchy continuum. Next, the mass-specific second-order tensor $\boldsymbol{\lambda}$ is defined, where the volume averaging procedure yields the definition

$$\rho\,\boldsymbol{\lambda} := \langle \rho_m\,\mathbf{x}_m \otimes \ddot{\mathbf{x}}_m \rangle := \frac{1}{V_{\mathcal{B}_m}} \int_{\mathcal{B}_m} \rho_m\,(\,\mathbf{x}_m \otimes \ddot{\mathbf{x}}_m\,)\,\mathrm{d}v_m\,. \tag{2.113}$$

Due to the homogeneity of the microdeformation, this so-called specific spin inertia tensor is related to the non-constant microinertia tensor $\boldsymbol{\theta} := \frac{1}{\rho V_{\mathcal{B}_m}} \int_{\mathcal{B}_m} \rho_m(\mathbf{x}_m \otimes \mathbf{x}_m)\mathrm{d}v_m = \boldsymbol{\theta}^T$ via $\boldsymbol{\lambda} = (\dot{\mathbf{L}}_m + \mathbf{L}_m\mathbf{L}_m)\boldsymbol{\theta}$ by use of (2.83), cf. Grammenoudis & Tsakmakis [99]. Finally, possible mass-specific second-order body couples $\boldsymbol{\mathcal{C}}$ exist, with

$$\rho\,\boldsymbol{\mathcal{C}} := \langle \mathbf{x}_m \otimes \rho_m\,\mathbf{b} \rangle = \frac{1}{V_{\mathcal{B}_m}} \int_{\mathcal{B}_m} \mathbf{x}_m \otimes (\,\rho_m\,\mathbf{b}\,)\,\mathrm{d}v_m\,. \tag{2.114}$$

For the formulation of the external stresses acting at the macroscopic boundary $\partial\mathcal{B}$, one recognises from the right-hand side of (2.111) that, in addition to the resulting boundary stress vector $\mathbf{t}$, a dyadic stress moment $\bar{\mathbf{M}}^d$ completes the boundary stresses of the micromorphic continuum. By use of a surface-specific average, $\bar{\mathbf{M}}^d$ defines the resulting dyadic moment at $\partial\mathcal{B}$ due to the microstress $\mathbf{t}_m$ acting again at the external boundary $A_{\mathcal{B}_m^{ex}}$ of the microcontinuum, viz.:

$$\bar{\mathbf{M}}^d := \langle \mathbf{x}_m \otimes \mathbf{t}_m \rangle_A := \frac{1}{A_{\mathcal{B}_m^{ex}}} \int_{\partial\mathcal{B}_m^{ex}} \mathbf{x}_m \otimes \mathbf{t}_m\,\mathrm{d}a_m\,. \tag{2.115}$$

With the averages (2.107), (2.108) and (2.112) – (2.115), all field quantities of the extended material point of the macroscopic micromorphic body are defined. Thus, a subsequent insertion of these definitions into (2.111) followed by an integration over the macroscopic domain of $\mathcal{B}$ yields the respective relations on the body scale as

$$\int_{\mathcal{B}} [\,(\,\rho\,\boldsymbol{\lambda} + \mathbf{x}_{\mathcal{M}} \otimes (\rho\,\ddot{\mathbf{x}}_{\mathcal{M}}\,) + \mathbf{T}_M^T - \mathbf{x}_{\mathcal{M}} \otimes (\rho\,\mathbf{b}\,) - \rho\,\boldsymbol{\mathcal{C}}\,]\,\mathrm{d}v = \int_{\partial\mathcal{B}} (\,\mathbf{x}_{\mathcal{M}} \otimes \mathbf{t} + \bar{\mathbf{M}}^d\,)\,\mathrm{d}a\,. \tag{2.116}$$

By application of the Gaussian integral theorem and the divergence theorem (A.25), (2.116) can be divided into two statements, where the first vanishes with the local form of the macroscopic balance of linear momentum (2.109). The second statement is frequently referred to as the generalised, extended or first moment of momentum balance (Chen [29], Eringen [71], Grammenoudis & Tsakmakis [99]). The two statements read

$$\begin{aligned} \int_{\mathcal{B}} \mathbf{x}_{\mathcal{M}} \otimes (\,\rho\,\ddot{\mathbf{x}}_{\mathcal{M}} - \operatorname{div}\mathbf{T} - \rho\,\mathbf{b}\,)\,\mathrm{d}v &= \mathbf{0} \quad \text{and} \\ \int_{\mathcal{B}} [\,\rho\,\boldsymbol{\lambda} - \operatorname{div}\overset{3}{\bar{\mathbf{M}}}{}^d + [\,(\mathbf{T}_m)_{\mathcal{B}}^T - \mathbf{T}^T\,] - \rho\,\boldsymbol{\mathcal{C}}\,]\,\mathrm{d}v &= \mathbf{0}\,, \end{aligned} \tag{2.117}$$

where $\overset{3}{\bar{\mathbf{M}}}{}^d$ is the third-order dyadic stress tensor with $\bar{\mathbf{M}}^d = \overset{3}{\bar{\mathbf{M}}}{}^d\mathbf{n}$. In general micromorphic continuum theories, $(2.117)_2$ is interpreted as a governing equation to solve for the unknown director motion included in $\boldsymbol{\lambda}$. It obeys the structure of a balance relation and

represents the remaining axiomatic part of the generalised balance, where the stress state $\mathbf{T} \neq \mathbf{T}^T$ remains non-symmetric.
It is of interest to note that by defining the macroscopic surface stresses $\mathbf{t}$ and $\bar{\mathbf{M}}^d$, the microstresses acting on the boundary of the microcontinuum are reduced to its centre of mass $\mathcal{M}$. Thereby, a resulting external moment $\bar{\mathbf{m}}$ with

$$\bar{\mathbf{m}} := \langle \mathbf{x}_m \times \mathbf{t}_m \rangle_A := \frac{1}{A_{\mathcal{B}_m^{ex}}} \int_{\partial \mathcal{B}_m^{ex}} (\mathbf{x}_m \times \mathbf{t}_m) \, \mathrm{d}a_m \tag{2.118}$$

is incorporated in the skew-symmetric contributions of $\bar{\mathbf{M}}^d$. In particular, with the axial vector as defined in $(\mathrm{A.13})_3$, $\bar{\mathbf{m}}$ represents twice the negative axial vector to $\bar{\mathbf{M}}^d$, viz.:

$$\bar{\mathbf{m}} = \overset{3}{\mathbf{E}} (\bar{\mathbf{M}}^d_{\mathrm{skw}}) = -2 \operatorname{axl} \bar{\mathbf{M}}^d . \tag{2.119}$$

The resulting moment $\bar{\mathbf{m}}$ is clearly identified as the boundary couple stress vector of the micropolar continuum formulation, cf. (2.66) of Section 2.3.2, now obtained by means of an averaging formalism. The relation given in (2.119) also holds for the further quantities in (2.116), such that a consistent identification of the micropolar quantities is possible for the case of a rigid microcontinuum. Note in passing that the local microdeformation is then given as a rigid rotation with

$$\mathbf{x}_m = \mathbf{R}_m \mathbf{X}_m \quad \text{and} \quad \dot{\mathbf{x}}_m = \boldsymbol{\Omega}_m \mathbf{x}_m \tag{2.120}$$

in substitution of (2.82) and (2.83) due to $\mathbf{U}_m = \mathbf{I}$. As a consequence, the micropolar balance of angular momentum (2.68) is contained in the skew-symmetric part of the extended micromorphic balance, when these are reduced to vector-valued quantities by means of the axial vector representation. Note that the definitions of $\mathbf{t}$ and $\bar{\mathbf{m}}$ exactly correspond to the external boundary stresses introduced in Ehlers *et al.* [64] for a transition of particle interaction forces towards micropolar stresses by means of an equivalent shifting of the external contact stresses of an REV towards the mass centres of the REV-boundary particles. An extension towards the present micromorphic setting is given in the subsequent Chapter 3.

Balance of mechanical power: In order to consistently derive the extensions stemming from the additional microcontinuum deformation, the embedded microcontinuum is again revisited. Its kinetic energy and its external stress power are given by

$$\begin{aligned} \mathcal{K} (\mathcal{B}_m, t) &= \int_{\mathcal{B}_m} \tfrac{1}{2} \rho_m \, \dot{\mathbf{x}} \cdot \dot{\mathbf{x}} \, \mathrm{d}v_m \\ \text{and} \quad \mathcal{L}_a (\mathcal{B}_m, t) &= \int_{\partial \mathcal{B}_m} \dot{\mathbf{x}} \cdot \mathbf{t}_m \, \mathrm{d}a_m + \int_{\mathcal{B}_m} \dot{\mathbf{x}} \cdot (\rho_m \, \mathbf{b}) \, \mathrm{d}v_m , \end{aligned} \tag{2.121}$$

where the consideration of the additive character of $\mathbf{x}$ given in (2.78) in combination with

(2.83), (A.4) and (A.6) yields the microscopic balance of mechanical power in the form

$$\begin{aligned}
&\underbrace{\dot{\mathbf{x}}_{\mathcal{M}} \cdot \int_{\mathcal{B}_m} \rho_m \, \ddot{\mathbf{x}}_{\mathcal{M}} \, \mathrm{d}v_m \, + \, \mathbf{L}_m^T \cdot \int_{\mathcal{B}_m} \rho_m \, (\, \mathbf{x}_m \otimes \ddot{\mathbf{x}}_m \,) \, \mathrm{d}v_m}_{\dfrac{\mathrm{d}}{\mathrm{d}t} \mathcal{K} \, (\, \mathcal{B}_m, \, t \,)} + \underbrace{\int_{\mathcal{B}_m} \rho_m \, \dot{\varepsilon}_m \, \mathrm{d}v_m}_{\dfrac{\mathrm{d}}{\mathrm{d}t} \mathcal{E} \, (\, \mathcal{B}_m, \, t \,)} \\
&= \dot{\mathbf{x}}_{\mathcal{M}} \cdot \Big(\int_{\partial \mathcal{B}_m} \mathbf{t}_m \, \mathrm{d}a_m \, + \, \int_{\mathcal{B}_m} \rho_m \, \mathbf{b} \, \mathrm{d}v_m \, \Big) \\
&\qquad \underbrace{+ \mathbf{L}_m^T \cdot \Big[\int_{\partial \mathcal{B}_m} (\, \mathbf{x}_m \otimes \mathbf{t}_m \,) \, \mathrm{d}a_m \, + \, \int_{\mathcal{B}} \mathbf{x}_m \otimes (\, \rho_m \, \mathbf{b} \,) \, \mathrm{d}v_m \Big]}_{\mathcal{L}_a \, (\mathcal{B}_m, \, t \,)} .
\end{aligned} \tag{2.122}$$

Therein, ε_m is the microcontinuum's mass-specific internal energy. Obviously, the first term in the expression of the rate of kinetic energy and first term in the expression of the external mechanical power stem from the translational motion of the macroscopic point by means of the velocity field $\dot{\mathbf{x}}_{\mathcal{M}}$. The second term in the rate of kinetic energy and the second and third terms in the external mechanical power represent the extended contributions stemming from the microcontinuum deformation. In comparison to the before identified field quantities of the micromorphic continuum body, it is concluded that the second term in the rate of kinetic energy includes the averaged spin inertia tensor $\boldsymbol{\lambda}$, while the second term in the external stress power incorporates the dyadic boundary stress moment $\bar{\mathbf{M}}^d$, when the external surface $A_{\mathcal{B}_m^{ex}}$ is again taken as the averaging domain. Furthermore, the last term in (2.122) is in relation to the averaged volumetric body couple $\rho \boldsymbol{\mathcal{C}}$. All three extended contributions are scalerly multiplied with the transposed microscopic spatial velocity gradient $\mathbf{L}_m^T$ of the independent microcontinuum deformation. Taking the micromorphic director motion (2.85) into account, which substitutes $\mathbf{L}_m$ by the micromorphic spatial velocity gradient $\bar{\mathbf{L}}$ for the macroscopic point, yields, that the balance of mechanical energy of the micromorphic body can be derived based on a scalar multiplication of the local statements of the balance of linear momentum (2.109) with the velocity field $\dot{\mathbf{x}}_{\mathcal{M}}$ and of the extended balance of angular momentum $(2.117)_2$ with the transposed micromophic velocity gradient $\bar{\mathbf{L}}^T$, viz.:

$$\begin{aligned}
\rho \, \ddot{\mathbf{x}}_{\mathcal{M}} \cdot \dot{\mathbf{x}}_{\mathcal{M}} \, &= \, \mathrm{div} \, \mathbf{T} \cdot \dot{\mathbf{x}}_{\mathcal{M}} \, + \, \rho \, \mathbf{b} \cdot \dot{\mathbf{x}}_{\mathcal{M}} \quad \text{and} \\
\rho \, \boldsymbol{\lambda} \cdot \bar{\mathbf{L}}^T \, &= \, \mathrm{div} \overset{3}{\bar{\mathbf{M}}}{}^d \cdot \bar{\mathbf{L}}^T \, + \, [\, \mathbf{T}^T \, - \, (\mathbf{T}_m)_{\mathcal{B}}^T \,] \cdot \bar{\mathbf{L}}^T \, + \, \rho \boldsymbol{\mathcal{C}} \cdot \bar{\mathbf{L}}^T \, .
\end{aligned} \tag{2.123}$$

Summing up the two parts of (2.123) and integrating over the domain of the continuum body $\mathcal{B}$ by use of the identities (A.6), (A.7), (A.27) and (A.28) yields the balance of

mechanical power in the form

$$\underbrace{\int_{\mathcal{B}} \rho\,(\,\dot{\mathbf{x}}_{\mathcal{M}}\cdot\ddot{\mathbf{x}}_{\mathcal{M}} + \boldsymbol{\lambda}\cdot\bar{\mathbf{L}}^{T}\,)\,\mathrm{d}v}_{\frac{\mathrm{d}}{\mathrm{d}t}\mathcal{K}\,(\,\mathcal{B},\,t\,)} + \underbrace{\int_{\mathcal{B}} [\,\mathbf{T}\cdot(\,\mathbf{L}-\bar{\mathbf{L}}\,) + (\mathbf{T}_m)_{\mathcal{B}}\cdot\bar{\mathbf{L}} + (\overset{3}{\bar{\mathbf{M}}}{}^{d})^{\overset{12}{T}}\cdot\operatorname{grad}\bar{\mathbf{L}}\,]\,\mathrm{d}v}_{\mathcal{L}_i\,(\,\mathcal{B},\,t\,)\,=:\,\int_{\mathcal{B}}\rho\,w_i\,(\,\mathbf{x}_{\mathcal{M}},\,\boldsymbol{\xi},\,t\,)\,\mathrm{d}v}$$

$$= \underbrace{\int_{\partial\mathcal{B}} (\,\dot{\mathbf{x}}_{\mathcal{M}}\cdot\mathbf{t} + \bar{\mathbf{L}}^{T}\cdot\bar{\mathbf{M}}^{d}\,)\,\mathrm{d}a + \int_{\mathcal{B}} (\,\rho\,\mathbf{b}\cdot\dot{\mathbf{x}}_{\mathcal{M}} + \rho\,\mathbf{C}\cdot\bar{\mathbf{L}}^{T}\,)\,\mathrm{d}v}_{\mathcal{L}_a\,(\,\mathcal{B},\,t\,)}\,. \tag{2.124}$$

Again, one can thereby identify the additional contributions in the specific internal stress power w_i due to the kinematic alterations from the Cauchy towards the micromorphic continuum description, viz.:

$$w_i\,(\,\mathbf{x}_{\mathcal{M}},\,\boldsymbol{\xi},\,t\,) = \frac{1}{\rho}\,[\,\mathbf{T}\cdot\overset{\vartriangle}{\bar{\mathbf{A}}} + (\mathbf{T}_m)_{\mathcal{B}}\cdot(\overset{\vartriangle}{\bar{\mathbf{A}}}_m)_{\mathcal{B}} + (\overset{3}{\bar{\mathbf{M}}}{}^{d})^{\overset{12}{T}}\cdot(\overset{3}{\bar{\mathbf{C}}})^{\diamondsuit}\,]$$
$$\text{with}\quad \overset{\diamondsuit}{\bar{\mathbf{A}}} = \mathbf{L}-\bar{\mathbf{L}}\,,\quad (\overset{\vartriangle}{\bar{\mathbf{A}}}_m)_{\mathcal{B}} = \bar{\mathbf{L}}_{\mathrm{sym}}\quad\text{and}\quad (\overset{3}{\bar{\mathbf{C}}})^{\diamondsuit} = \operatorname{grad}\bar{\mathbf{L}} \tag{2.125}$$

from (2.96) and $(\mathbf{T}_m)_{\mathcal{B}}\cdot\bar{\mathbf{L}}_{\mathrm{skw}} = 0$ due to $(\mathbf{T}_m)_{\mathcal{B}} = (\mathbf{T}_m)_{\mathcal{B}}^{T}$. Note that further invariant expressions of w_i with respect to different configurations are possible. However, the derivation of the dual pairs of stresses and strains in a finite strain micromorphic continuum formulation is not straightforward, especially when an intermediate micromorphic configuration is introduced and the micromorphic strains become mixed-variant (see Appendix B.1). In the present work, the focus lies on the averaging of particle interactions and displacements towards micromorphic measures. As this could only be obtained for geometrically linear micromorphic deformation quantities, no further emphasis was laid on a completed finite formulation. On these matters, the interested reader is referred to Grammenoudis & Tsakmakis [99], Hirschberger *et al.* [112] or Regueiro [180]. Nevertheless, (2.125) enables to identify a work-conjugated set of stress and strain/curvature quantities for the extended micromorphic continuum formulation. Specifically, these are

$$\{\,\frac{1}{\rho}\,\mathbf{T}\,,\;\bar{\mathbf{A}}\,\}\,,\quad \{\,\frac{1}{\rho}\,(\mathbf{T}_m)_{\mathcal{B}}\,,\;(\mathbf{A}_m)_{\mathcal{B}}\,\}\quad\text{and}\quad \{\,\frac{1}{\rho}\,(\overset{3}{\bar{\mathbf{M}}}{}^{d})^{\overset{12}{T}}\,,\;\overset{3}{\bar{\mathbf{C}}}\,\}\,. \tag{2.126}$$

In the subsequent section, the kinematic deformation measures will be linearised. In combination with the identifiied work-conjugated pairs, this allows for the separation of the mechanical work of the internal forces into a contribution that can be clearly related to the standard Cauchy part and additional contributions that are associated with the extensions towards the micropolar and the micromorphic formulation.

2.5 Geometrical linearisation

The generally non-linear theory of micromorphic continuum kinematics and, as a subclass, the micropolar continuum kinematics can be reduced to a geometrically linear the-

ory under the assumption of small deformations. For the linearisation of the micropolar strain and curvature tensors, the assumption of small displacement gradients and small total rotations is sufficient to realise the formal transition towards the geometrically linear regime. In the micromorphic case, one additionally has to assume small microdeformations. As will be shown in the subsequent sections, it is convenient to reformulate the strain measures as a function of the macroscopic deformation gradient $\mathbf{F}$, the microstretch tensor $(\mathbf{U}_m)_{\mathcal{B}}$ and the amount of resultant rotation $\bar{\varphi}$ in order to perform the linearisation procedure. A formal geometric linearisation can then be realised for an arbitrary tensor function $\overset{n}{\mathbf{A}} = \overset{n}{\mathbf{A}}(\mathbf{F}, (\mathbf{U}_m)_{\mathcal{B}}, \bar{\varphi})$ of n^{th}-order through a Taylor series expansion around the initial state, characterised by $\mathbf{F} = \mathbf{I}$, $(\mathbf{U}_m)_{\mathcal{B}} = \mathbf{I}$ and $\bar{\varphi} = 0$, followed by a truncation after the linear term. The linearised quantity $\overset{n}{\mathbf{A}}_{\text{lin.}}$ then reads

$$\begin{aligned}\overset{n}{\mathbf{A}}_{\text{lin.}} = \overset{n}{\mathbf{A}}\Big|_{\substack{\mathbf{F}=\mathbf{I}\\(\mathbf{U}_m)_{\mathcal{B}}=\mathbf{I}\\\bar{\varphi}=0}} + \frac{\partial \overset{n}{\mathbf{A}}}{\partial \mathbf{F}}\Big|_{\substack{\mathbf{F}=\mathbf{I}\\(\mathbf{U}_m)_{\mathcal{B}}=\mathbf{I}\\\bar{\varphi}=0}} (\mathbf{F} - \mathbf{I}) + \frac{\partial \overset{n}{\mathbf{A}}}{\partial (\mathbf{U}_m)_{\mathcal{B}}}\Big|_{\substack{\mathbf{F}=\mathbf{I}\\(\mathbf{U}_m)_{\mathcal{B}}=\mathbf{I}\\\bar{\varphi}=0}} [(\mathbf{U}_m)_{\mathcal{B}} - \mathbf{I}] \\ + \frac{\partial \overset{n}{\mathbf{A}}}{\partial \bar{\varphi}}\Big|_{\substack{\mathbf{F}=\mathbf{I}\\(\mathbf{U}_m)_{\mathcal{B}}=\mathbf{I}\\\bar{\varphi}=0}} (\bar{\varphi} - 0)\,.\end{aligned} \tag{2.127}$$

In the geometrically linear case, the deformed state approximately coincides with the initial configuration such that $\operatorname{Grad}(\cdot) \approx \operatorname{grad}(\cdot)$ and the strain and curvature measures approximately coincide, viz.:

$$\begin{aligned}&\mathbf{E} \approx \mathbf{A} \approx: \boldsymbol{\varepsilon}\,, \quad (\mathbf{E}_m)_{\mathcal{B}} \approx (\mathbf{A}_m)_{\mathcal{B}} \approx: (\boldsymbol{\varepsilon}_m)_{\mathcal{B}}\,, \quad \bar{\mathbf{E}} \approx \bar{\mathbf{A}} \approx: \bar{\boldsymbol{\varepsilon}}\,, \\ &{}^{R}\bar{\mathbf{C}} \approx \bar{\mathbf{C}} \approx: \bar{\boldsymbol{\kappa}}\,, \quad {}^{R}\overset{3}{\bar{\mathbf{C}}} \approx \overset{3}{\bar{\mathbf{C}}} \approx: \overset{3}{\bar{\boldsymbol{\kappa}}}\,.\end{aligned} \tag{2.128}$$

Therein, $\boldsymbol{\varepsilon}$, $(\boldsymbol{\varepsilon}_m)_{\mathcal{B}}$, $\bar{\boldsymbol{\varepsilon}}$, $\bar{\boldsymbol{\kappa}}$ and $\overset{3}{\bar{\boldsymbol{\kappa}}}$ denote the linearised quantities to the continuum strain, the microstrain, the extended micropolar/micromorphic continuum strain and the second- and the third-order curvature tensors, respectively.

2.5.1 Linearised Cauchy continuum kinematics

A formal linearisation is exemplarily performed for the Green-Lagrangean strain tensor $\mathbf{E}$ given in (2.12) around the referential state $\mathbf{F} = \mathbf{I}$, which results by use of (2.4) in

$$\begin{aligned}\boldsymbol{\varepsilon} := \mathbf{E}_{\text{lin.}} &= \mathbf{E}\Big|_{\mathbf{F}=\mathbf{I}} + \frac{\partial \mathbf{E}}{\partial \mathbf{F}}\Big|_{\mathbf{F}=\mathbf{I}} (\mathbf{F} - \mathbf{I}) \\ &= (\operatorname{Grad}\mathbf{u})_{\text{sym}} = \tfrac{1}{2}(\operatorname{Grad}\mathbf{u} + \operatorname{Grad}^{T}\mathbf{u})\,.\end{aligned} \tag{2.129}$$

2.5.2 Linearised micropolar continuum kinematics

In the micropolar case, it is convenient to calculate a linearisation $\bar{\mathbf{R}}_{\text{lin.}}$ of the combined micropolar director rotation (2.52), which is only a function of the total rotation $\bar{\boldsymbol{\varphi}}$, when

it is represented in the Euler-Rodrigues notation. The formalism (2.127) results in

$$\bar{\mathbf{R}}_{\text{lin.}} = \mathbf{I} + (\bar{\mathbf{e}} \times \mathbf{I})\,\bar{\varphi} = \mathbf{I} - \overset{3}{\mathbf{E}}\,\bar{\boldsymbol{\varphi}}\,, \tag{2.130}$$

with $(\bar{\mathbf{e}} \times \mathbf{I})\bar{\varphi} = \bar{\boldsymbol{\varphi}} \times \mathbf{I} = -\overset{3}{\mathbf{E}}\bar{\boldsymbol{\varphi}}$, cf. Ehlers [59] and Volk [211]. With (2.130) at hand, the linearised forms of the micropolar strain (2.57) and the micropolar curvature (2.60) can be calculated in a straightforward manner, resulting in

$$\begin{aligned} \bar{\boldsymbol{\varepsilon}} := \bar{\mathbf{E}}_{\text{lin.}} &= \operatorname{Grad}\mathbf{u} + \overset{3}{\mathbf{E}}\,\bar{\boldsymbol{\varphi}} = \bar{\boldsymbol{\varepsilon}}_{\text{sym}} + \bar{\boldsymbol{\varepsilon}}_{\text{skw}} \\ \text{where} \quad &\begin{cases} \bar{\boldsymbol{\varepsilon}}_{\text{sym}} = (\operatorname{Grad}\mathbf{u})_{\text{sym}} = \boldsymbol{\varepsilon} \\ \bar{\boldsymbol{\varepsilon}}_{\text{skw}} = (\operatorname{Grad}\mathbf{u})_{\text{skw}} + \overset{3}{\mathbf{E}}\,\bar{\boldsymbol{\varphi}} = \overset{3}{\mathbf{E}}\,(\bar{\boldsymbol{\varphi}} - \boldsymbol{\varphi}) = \overset{3}{\mathbf{E}}\,(\boldsymbol{\varphi}_m)_{\mathcal{B}}\,. \end{cases} \end{aligned} \tag{2.131}$$

Obviously, the symmetric part $\bar{\boldsymbol{\varepsilon}}_{\text{sym}}$ of $\bar{\boldsymbol{\varepsilon}}$ corresponds to the linearised strain $\boldsymbol{\varepsilon}$ of the standard formulation, while the skew-symmetric part $\bar{\boldsymbol{\varepsilon}}_{\text{skw}}$ stems from the skew-symmetric part of $\operatorname{Grad}\mathbf{u}$ and the linearised contribution of the director rotation, which combine to the permutation of the free rotation $(\boldsymbol{\varphi}_m)_{\mathcal{B}}$. Thereby, the validity of the vector addition theorem for small rotations is used, i. e. $\bar{\boldsymbol{\varphi}} = \boldsymbol{\varphi} + (\boldsymbol{\varphi}_m)_{\mathcal{B}}$. Finally, the linearisation of the curvature tensor $\bar{\mathbf{C}}$ yields

$$\bar{\boldsymbol{\kappa}} := \bar{\mathbf{C}}_{\text{lin.}} = \operatorname{Grad}\bar{\boldsymbol{\varphi}}\,. \tag{2.132}$$

For further details in the formal linearisation procedure of the micropolar formulation, the reader is referred to Ehlers [56].

2.5.3 Linearised micromorphic continuum kinematics

For the present work, it is of interest to investigate how the additional microdeformation mechanism affects the linearised kinematic measures of the micromorphic formulation. Therefore, at first, a geometrically linear microstrain tensor $(\boldsymbol{\varepsilon}_m)_{\mathcal{B}}$ is, for example, calculated by the Taylor-series expansion of $(\mathbf{E}_m)_{\mathcal{B}}$ around $(\mathbf{U}_m)_{\mathcal{B}} = \mathbf{I}$, yielding

$$(\boldsymbol{\varepsilon}_m)_{\mathcal{B}} := (\mathbf{E}_m)_{\mathcal{B}\,\text{lin.}} = (\mathbf{E}_m)_{\mathcal{B}}\Big|_{(\mathbf{U}_m)_{\mathcal{B}}=\mathbf{I}} + \frac{\partial(\mathbf{E}_m)_{\mathcal{B}}}{\partial(\mathbf{U}_m)_{\mathcal{B}}}\Big|_{(\mathbf{U}_m)_{\mathcal{B}}=\mathbf{I}} [\,(\mathbf{U}_m)_{\mathcal{B}} - \mathbf{I}\,] = (\mathbf{U}_m)_{\mathcal{B}} - \mathbf{I}\,. \tag{2.133}$$

Assuming the existence of a microscopic displacement vector $\mathbf{u}_m = \mathbf{x}_m - \mathbf{X}_m$, the linearised microstrain can alternatively be computed analogously to (2.129), which yields

$$(\boldsymbol{\varepsilon}_m)_{\mathcal{B}} = \tfrac{1}{2}\,(\operatorname{Grad}\mathbf{u}_m + \operatorname{Grad}^T\mathbf{u}_m)\,. \tag{2.134}$$

For the computation of the linearised micromorphic strain tensor $\bar{\boldsymbol{\varepsilon}}$, the micromorphic strain tensor $\bar{\mathbf{E}}$, cf. (2.88), is expressed as

$$\bar{\mathbf{E}} = \bar{\mathbf{U}} - \mathbf{I} = (\mathbf{U}_m)_{\mathcal{B}}^{-1}\bar{\mathbf{R}}^T\mathbf{F} - \mathbf{I}\,, \tag{2.135}$$

such that one recognises the combined micropolar director motion $\bar{\mathbf{R}}$, cf. (2.52). Application of the formalism (2.127) leads to

$$\begin{aligned}\bar{\boldsymbol{\varepsilon}} = \bar{\mathbf{E}}_{\text{lin.}} &:= \bar{\mathbf{E}}\Big|_{\substack{\mathbf{F}=\mathbf{I}\\(\mathbf{U}_m)_{\mathcal{B}}=\mathbf{I}\\ \bar{\varphi}=0}} + \frac{\partial\bar{\mathbf{E}}}{\partial\mathbf{F}}\Big|_{\substack{\mathbf{F}=\mathbf{I}\\(\mathbf{U}_m)_{\mathcal{B}}=\mathbf{I}\\ \bar{\varphi}=0}}(\,\mathbf{F}-\mathbf{I}\,) + \frac{\partial\bar{\mathbf{E}}}{\partial(\mathbf{U}_m)_{\mathcal{B}}}\Big|_{\substack{\mathbf{F}=\mathbf{I}\\(\mathbf{U}_m)_{\mathcal{B}}=\mathbf{I}\\ \bar{\varphi}=0}}[\,(\mathbf{U}_m)_{\mathcal{B}}-\mathbf{I}\,] \\ &\quad + \frac{\partial\bar{\mathbf{E}}}{\partial\bar{\varphi}}\Big|_{\substack{\mathbf{F}=\mathbf{I}\\(\mathbf{U}_m)_{\mathcal{B}}=\mathbf{I}\\ \bar{\varphi}=0}}\bar{\varphi} \\ &= \mathbf{0} + (\,\mathbf{F}-\mathbf{I}\,) - (\,(\mathbf{U}_m)_{\mathcal{B}}-\mathbf{I}\,) - (\,\bar{\boldsymbol{\varphi}}\times\mathbf{I}\,) \\ &= \operatorname{Grad}\mathbf{u} - (\boldsymbol{\varepsilon}_m)_{\mathcal{B}} + \overset{3}{\mathbf{E}}\bar{\boldsymbol{\varphi}} = \bar{\boldsymbol{\varepsilon}}_{\text{sym}} + \bar{\boldsymbol{\varepsilon}}_{\text{skw}}\,.\end{aligned} \tag{2.136}$$

As a consequence, the linearised micromorphic strain $\bar{\boldsymbol{\varepsilon}}$ can also be interpreted as being composed of two contributions. The first is its symmetric part and results from the difference of the linearised version $\boldsymbol{\varepsilon}$ of the standard Green-Lagrangean strain, compare (2.129), and the linear microstrain $\boldsymbol{\varepsilon}_m$, compare (2.133). The second is its skew-symmetric part and yields the skew-symmetric part of the linearised micropolar strain, compare (2.131). In particular, one obtains

$$\bar{\boldsymbol{\varepsilon}}_{\text{sym}} = \boldsymbol{\varepsilon} - (\boldsymbol{\varepsilon}_m)_{\mathcal{B}} \quad\text{and}\quad \bar{\boldsymbol{\varepsilon}}_{\text{skw}} = \overset{3}{\mathbf{E}}(\boldsymbol{\varphi}_m)_{\mathcal{B}}\,. \tag{2.137}$$

Comparing the split (2.137) with the linearised micropolar strain given in (2.131) reveals that the additional microdeformation only results in the subtraction of the microstrain contribution $(\boldsymbol{\varepsilon}_m)_{\mathcal{B}}$ from the symmetric part of $\bar{\boldsymbol{\varepsilon}}$.

Finally, the linearised curvature tensor $\bar{\boldsymbol{\kappa}}$ is obtained from the expression of $\overset{3}{\bar{\mathbf{C}}}$ as

$${}^{R}\overset{3}{\bar{\mathbf{C}}} = (\,\bar{\mathbf{F}}^{-1}\operatorname{Grad}\bar{\mathbf{F}}\,)^{\underline{3}} = \big(\,[\,\bar{\mathbf{R}}\,(\mathbf{U}_m)_{\mathcal{B}}\,]^{-1}\operatorname{Grad}[\,\bar{\mathbf{R}}\,(\mathbf{U}_m)_{\mathcal{B}}\,]\,\big)^{\underline{3}} \tag{2.138}$$

such that

$$\begin{aligned}\overset{3}{\bar{\boldsymbol{\kappa}}} := {}^{R}\overset{3}{\bar{\mathbf{C}}}_{\text{lin.}} &= {}^{R}\overset{3}{\bar{\mathbf{C}}}\Big|_{\substack{(\mathbf{U}_m)_{\mathcal{B}}=\mathbf{I}\\ \bar{\varphi}=0}} + \frac{\partial\,{}^{R}\overset{3}{\bar{\mathbf{C}}}}{\partial(\mathbf{U}_m)_{\mathcal{B}}}\Big|_{\substack{(\mathbf{U}_m)_{\mathcal{B}}=\mathbf{I}\\ \bar{\varphi}=0}}[\,(\mathbf{U}_m)_{\mathcal{B}}-\mathbf{I}\,] + \frac{\partial\,{}^{R}\overset{3}{\bar{\mathbf{C}}}}{\partial\bar{\varphi}}\Big|_{\substack{(\mathbf{U}_m)_{\mathcal{B}}=\mathbf{I}\\ \bar{\varphi}=0}}\bar{\varphi} \\ &= \overset{3}{\mathbf{0}} + \operatorname{Grad}(\boldsymbol{\varepsilon}_m)_{\mathcal{B}} - (\,\overset{3}{\mathbf{E}}\operatorname{Grad}\bar{\boldsymbol{\varphi}}\,)^{\underline{3}}.\end{aligned} \tag{2.139}$$

The symmetry characteristics of the components of the linearised curvature tensor of the micromorphic continua read

$$\begin{aligned}(\,\overset{3}{\mathbf{E}}\operatorname{Grad}\bar{\boldsymbol{\varphi}}\,)^{\underline{3}} &= -(\,\overset{3}{\mathbf{E}}\operatorname{Grad}\bar{\boldsymbol{\varphi}}\,)^{\underline{3}\overset{12}{T}} \quad\text{and} \\ \operatorname{Grad}(\boldsymbol{\varepsilon}_m)_{\mathcal{B}} &= [\,\operatorname{Grad}(\boldsymbol{\varepsilon}_m)_{\mathcal{B}}\,]^{\overset{12}{T}},\end{aligned} \tag{2.140}$$

where the first $(2.140)_1$ represents a skew-symmetric condition and $(2.140)_2$ is a symmetry condition. Hence, by use of (A.17), the axial tensor to (2.139) recovers the linearised micropolar curvature (2.131) as a second-order curvature measure, viz.:

$$\bar{\boldsymbol{\kappa}} \;=\; \operatorname{axl} \overset{3}{\bar{\boldsymbol{\kappa}}} \;=\; \overset{a}{\bar{\boldsymbol{\kappa}}} \;=\; \tfrac{1}{2}\,(\,\overset{3}{\mathbf{E}}\,\overset{3}{\bar{\boldsymbol{\kappa}}}^{\,T}\,)^{\underline{2}} \;=\; \tfrac{1}{2}\,(\overset{3}{\mathbf{E}}\,\overset{3}{\mathbf{E}})^{\underline{2}}\operatorname{Grad}\bar{\boldsymbol{\varphi}} \;=\; \operatorname{Grad}\bar{\boldsymbol{\varphi}}\,, \tag{2.141}$$

with $[\,\overset{3}{\mathbf{E}}\operatorname{Grad}(\boldsymbol{\varepsilon}_m)_{\mathcal{B}}\,]^{\underline{2}} \;=\; \operatorname{Grad}[\,\overset{3}{\mathbf{E}}\,(\boldsymbol{\varepsilon}_m)_{\mathcal{B}}\,] \;=\; \mathbf{0}$. For a more detailed derivation of the geometrically linear quantities (2.133), (2.136) and (2.139), compare Appendix B.2.

2.5.4 Consequences for the internal stress power and the internal mechanical work

Additional insight into the internal mechanical work in a geometrically linear framework is gained by reviewing the balance of mechanical power. Thereby note that for linearised kinematics, in addition to the deformation measures, the stresses approximate to

$$\mathbf{T} \;\approx\; \boldsymbol{\mathcal{T}} \;\approx\colon\; \boldsymbol{\sigma}\,, \quad (\mathbf{T}_m)_{\mathcal{B}} \;\approx\colon\; (\boldsymbol{\sigma}_m)_{\mathcal{B}}\,, \quad \bar{\mathbf{M}} \;\approx\; \bar{\boldsymbol{\mathcal{M}}} \;\approx\colon\; \bar{\boldsymbol{\mu}}\,, \quad \overset{3}{\bar{\mathbf{M}}}{}^{d} \;\approx\colon\; \overset{3}{\bar{\boldsymbol{\mu}}}{}^{d}\,, \tag{2.142}$$

where $\boldsymbol{\sigma}$, $(\boldsymbol{\sigma}_m)_{\mathcal{B}}$, $\bar{\boldsymbol{\mu}}$ and $\overset{3}{\bar{\boldsymbol{\mu}}}{}^{d}$ denote the linearised counterparts of the continuum stress, the microstress, the micropolar couple stress and the third-order dyadic stress tensor, respectively. Simplifying the micromorphic stress-energy function, one might proceed from the assumption that local strains and strain rates are small at the macroscopic level compared to the micromotion, meaning that the strains and strain rates included (2.125) can be linearised. In geometrically linear approaches, the transport mechanisms of strain measures between the current and the reference configuration are consequently neglected. Thus,

$$\rho = \rho_0 \det \mathbf{F}^{-1} \quad \longrightarrow \quad \rho \approx \rho_0 \tag{2.143}$$

and

$$\begin{aligned} (\mathbf{A}_m)_{\mathcal{B}} \approx\; (\mathbf{E}_m)_{\mathcal{B}\,\mathrm{lin}} = (\boldsymbol{\varepsilon}_m)_{\mathcal{B}} \quad &\longrightarrow \quad (\overset{\Delta}{\mathbf{A}}_m)_{\mathcal{B}} \approx (\dot{\boldsymbol{\varepsilon}}_m)_{\mathcal{B}} \;=\; (\dot{\mathbf{U}}_m)_{\mathcal{B}}\,, \\ \bar{\mathbf{A}} \approx\; \bar{\mathbf{E}}_{\mathrm{lin}} = \bar{\boldsymbol{\varepsilon}} \quad &\longrightarrow \quad \overset{\diamondsuit}{\mathbf{A}} \;\approx\; \dot{\bar{\boldsymbol{\varepsilon}}} \;=\; \operatorname{Grad}\dot{\mathbf{u}} \;-\; (\dot{\boldsymbol{\varepsilon}}_m)_{\mathcal{B}} \;+\; \overset{3}{\mathbf{E}}\,\dot{\bar{\boldsymbol{\varphi}}}\,, \end{aligned} \tag{2.144}$$

where (2.88), (2.92) and (2.133) have been used. Additionally, the linearised curvature rate reads

$$\overset{3}{\bar{\mathbf{C}}} \;\approx\; {}^{R}\overset{3}{\mathbf{C}}_{\mathrm{lin}} \;=\; \overset{3}{\bar{\boldsymbol{\kappa}}} \quad \longrightarrow \quad (\overset{3}{\bar{\mathbf{C}}})^{\diamondsuit} \approx (\overset{3}{\bar{\boldsymbol{\kappa}}})^{\cdot} \;=\; -\,(\,\overset{3}{\mathbf{E}}\operatorname{Grad}\dot{\bar{\boldsymbol{\varphi}}}\,)^{\underline{3}} \;+\; \operatorname{Grad}(\dot{\boldsymbol{\varepsilon}}_m)_{\mathcal{B}}\,. \tag{2.145}$$

Given (2.125), (2.143) – (2.145) and the stresses and stress moments of the geometrically linear approach (2.142), the stress-energy function (2.125) reads

$$\rho_0\, w_i = \boldsymbol{\sigma} \;\cdot\; \dot{\bar{\boldsymbol{\varepsilon}}} \;+\; (\boldsymbol{\sigma}_m)_{\mathcal{B}} \;\cdot\; (\dot{\boldsymbol{\varepsilon}}_m)_{\mathcal{B}} \;+\; (\overset{3}{\bar{\boldsymbol{\mu}}}{}^{d})^{\overset{12}{T}} \;\cdot\; (\overset{3}{\bar{\boldsymbol{\kappa}}})^{\cdot} \tag{2.146}$$

and can alternatively written as

$$\begin{aligned}\rho_0\, w_i = \boldsymbol{\sigma}_{\mathrm{sym}} \cdot \dot{\boldsymbol{\varepsilon}} \,+\, [\,(\boldsymbol{\sigma}_m)_{\mathcal{B}} - \boldsymbol{\sigma}_{\mathrm{sym}}\,] \cdot (\dot{\boldsymbol{\varepsilon}}_m)_{\mathcal{B}} + \\ +\, \boldsymbol{\sigma}_{\mathrm{skw}} \cdot \overset{3}{\mathbf{E}}\,(\dot{\boldsymbol{\varphi}}_m)_{\mathcal{B}} \,-\, (\overset{3}{\boldsymbol{\mu}}{}^{d})^{\overset{12}{T}} \cdot (\overset{3}{\mathbf{E}}\,\mathrm{Grad}\,\dot{\boldsymbol{\varphi}})^{\underline{3}} \\ +\, (\overset{3}{\boldsymbol{\mu}}{}^{d})^{\overset{12}{T}} \cdot \mathrm{Grad}\,(\dot{\boldsymbol{\varepsilon}}_m)_{\mathcal{B}}\,,\end{aligned} \tag{2.147}$$

where the third-order rate of curvature tensor $(\overset{3}{\boldsymbol{\kappa}})^{\cdot}$ has been split in its symmetric and skew-symmetric parts, viz.:

$$\begin{aligned}&(\overset{3}{\boldsymbol{\kappa}})^{\cdot} = \overset{(12)}{\mathrm{sym}}\,(\overset{3}{\boldsymbol{\kappa}})^{\cdot} + \overset{(12)}{\mathrm{skw}}\,(\overset{3}{\boldsymbol{\kappa}})^{\cdot}\,,\\ &\overset{(12)}{\mathrm{sym}}\,(\overset{3}{\boldsymbol{\kappa}})^{\cdot} = \mathrm{Grad}\,(\dot{\boldsymbol{\varepsilon}}_m)_{\mathcal{B}} = [\,\mathrm{Grad}\,(\dot{\boldsymbol{\varepsilon}}_m)_{\mathcal{B}}]^{\overset{12}{T}}\,,\\ &\overset{(12)}{\mathrm{skw}}\,(\overset{3}{\boldsymbol{\kappa}})^{\cdot} = -(\overset{3}{\mathbf{E}}\,\mathrm{Grad}\,\dot{\boldsymbol{\varphi}})^{\underline{3}} = (\overset{3}{\mathbf{E}}\,\mathrm{Grad}\,\dot{\boldsymbol{\varphi}})^{\underline{3}\overset{12}{T}}\,.\end{aligned} \tag{2.148}$$

Note that the operators $\overset{(12)}{\mathrm{sym}}\,(\,\cdot\,)$ and $\overset{(12)}{\mathrm{skw}}\,(\,\cdot\,)$ denote symmetry or skew-symmetry of the objects $(\,\cdot\,)$ with respect to their first and second basis systems. Given (2.147), the volume-specific stress power or the stress-energy function, respectively, can be split into terms belonging to Cauchy's standard formulation $\rho_0\, w_i^{(sf)}$ and to the micromorphic extension split into micropolar and microstrain contributions, $\rho_0\, w_i^{(mp)}$ and $\rho_0\, w_i^{(ms)}$:

$$\begin{aligned}\rho_0\, w_i^{(sf)} \;&= \boldsymbol{\sigma}_{\mathrm{sym}} \cdot \dot{\boldsymbol{\varepsilon}}\,,\\ \rho_0\, w_i^{(mp)} \;&= \boldsymbol{\sigma}_{\mathrm{skw}} \cdot \overset{3}{\mathbf{E}}\,(\dot{\boldsymbol{\varphi}}_m)_{\mathcal{B}} \,-\, (\overset{3}{\boldsymbol{\mu}}{}^{d})^{\overset{12}{T}} \cdot (\overset{3}{\mathbf{E}}\,\mathrm{Grad}\,\dot{\boldsymbol{\varphi}})^{\underline{3}},\\ \rho_0\, w_i^{(ms)} &= [\,(\boldsymbol{\sigma}_m)_{\mathcal{B}} \,-\, \boldsymbol{\sigma}_{\mathrm{sym}}\,] \cdot (\dot{\boldsymbol{\varepsilon}}_m)_{\mathcal{B}} \,+\, +\,(\overset{3}{\boldsymbol{\mu}}{}^{d})^{\overset{12}{T}} \cdot \mathrm{Grad}\,(\dot{\boldsymbol{\varepsilon}}_m)_{\mathcal{B}}\,.\end{aligned} \tag{2.149}$$

When the dyadic stress moment $\overset{3}{\boldsymbol{\mu}}{}^{d}$ is also split in symmetric and skew-symmetric parts through

$$\begin{aligned}\overset{3}{\boldsymbol{\mu}}{}^{d} \;&=\; \overset{(12)}{\mathrm{sym}}\,\overset{3}{\boldsymbol{\mu}}{}^{d} \,+\, \overset{(12)}{\mathrm{skw}}\,\overset{3}{\boldsymbol{\mu}}{}^{d}\,,\\ \overset{(12)}{\mathrm{sym}}\,\overset{3}{\boldsymbol{\mu}}{}^{d} \;&=\; \tfrac{1}{2}\,[\,\overset{3}{\boldsymbol{\mu}}{}^{d} \,+\, (\overset{3}{\boldsymbol{\mu}}{}^{d})^{\overset{12}{T}}\,] \;=\; (\overset{(12)}{\mathrm{sym}}\,\overset{3}{\boldsymbol{\mu}}{}^{d})^{\overset{12}{T}}\,,\\ \overset{(12)}{\mathrm{skw}}\,\overset{3}{\boldsymbol{\mu}}{}^{d} \;&=\; \tfrac{1}{2}\,[\,\overset{3}{\boldsymbol{\mu}}{}^{d} \,-\, (\overset{3}{\boldsymbol{\mu}}{}^{d})^{\overset{12}{T}}\,] \;=\; -\,(\overset{(12)}{\mathrm{skw}}\,\overset{3}{\boldsymbol{\mu}}{}^{d})^{\overset{12}{T}}\,,\end{aligned} \tag{2.150}$$

the micropolar and microstrain contributions of $\rho_0\, w_i$ can alternatively be expressed as

$$\begin{aligned}\rho_0\, w_i^{(mp)} \;&= \boldsymbol{\sigma}_{\mathrm{skw}} \cdot \overset{3}{\mathbf{E}}\,(\dot{\boldsymbol{\varphi}}_m)_{\mathcal{B}} \,+\, \overset{(12)}{\mathrm{skw}}\,\overset{3}{\boldsymbol{\mu}}{}^{d} \cdot (\overset{3}{\mathbf{E}}\,\mathrm{Grad}\,\dot{\boldsymbol{\varphi}})^{\underline{3}},\\ \rho_0\, w_i^{(ms)} &= [\,(\boldsymbol{\sigma}_m)_{\mathcal{B}} - \boldsymbol{\sigma}_{\mathrm{sym}}\,] \cdot (\dot{\boldsymbol{\varepsilon}}_m)_{\mathcal{B}} \,+\, +\overset{(12)}{\mathrm{sym}}\,\overset{3}{\boldsymbol{\mu}}{}^{d} \cdot \mathrm{Grad}\,(\dot{\boldsymbol{\varepsilon}}_m)_{\mathcal{B}}\,.\end{aligned} \tag{2.151}$$

Using (A.17) and (A.19), the axial tensors of $\overset{3}{\bar{\boldsymbol{\mu}}}{}^{d}$ and $(\overset{3}{\bar{\boldsymbol{\kappa}}})^{\cdot}$ read

$$\begin{aligned} \overset{a}{\bar{\boldsymbol{\mu}}}{}^{d} &:= \operatorname{axl} \overset{3}{\bar{\boldsymbol{\mu}}}{}^{d} = -\tfrac{1}{2}(\overset{3}{\mathbf{E}}\,\overset{3}{\bar{\boldsymbol{\mu}}}{}^{d})^{\underline{2}} = -\tfrac{1}{2}\,\bar{\boldsymbol{\mu}}\,, \\ (\overset{a}{\bar{\boldsymbol{\kappa}}})^{\cdot} &:= \operatorname{axl}(\overset{3}{\bar{\boldsymbol{\kappa}}})^{\cdot} = -\tfrac{1}{2}[\,\overset{3}{\mathbf{E}}\,(\overset{3}{\bar{\boldsymbol{\kappa}}})^{\cdot}\,]^{\underline{2}} = \operatorname{Grad}\dot{\bar{\boldsymbol{\varphi}}}\,. \end{aligned} \tag{2.152}$$

Based on $(2.148)_1$, (A.17) and (2.152), the second term included in $(2.151)_1$ can also be expressed as

$$\begin{aligned} \overset{(12)}{\operatorname{skw}}\overset{3}{\bar{\boldsymbol{\mu}}}{}^{d} \cdot (\overset{3}{\mathbf{E}}\operatorname{Grad}\dot{\bar{\boldsymbol{\varphi}}})^{\underline{3}} &= -(\overset{3}{\mathbf{E}}\,\overset{a}{\bar{\boldsymbol{\mu}}}{}^{d})^{\underline{3}} \cdot [\,\overset{3}{\mathbf{E}}\,(\overset{a}{\bar{\boldsymbol{\kappa}}})^{\cdot}\,]^{\underline{3}} = -(\overset{3\,13}{\mathbf{E}^{T}}\,\overset{3\,12}{\mathbf{E}^{T}})^{\underline{2}} \cdot [\,\overset{a}{\bar{\boldsymbol{\mu}}}{}^{d}\,(\overset{a}{\bar{\boldsymbol{\kappa}}})^{\cdot\,T}] \\ &= -2\,\overset{a}{\bar{\boldsymbol{\mu}}}{}^{d} \cdot (\overset{a}{\bar{\boldsymbol{\kappa}}})^{\cdot}\,, \end{aligned} \tag{2.153}$$

where $\overset{3\,12}{\mathbf{E}^{T}} = -\overset{3}{\mathbf{E}}$, $\overset{3\,13}{\mathbf{E}^{T}} = -\overset{3}{\mathbf{E}}$ together with $(\overset{3}{\mathbf{E}}\,\overset{3}{\mathbf{E}})^{\underline{2}} = 2\,\mathbf{I}$ have been used. As a result of (2.153), $\rho_0\, w_i^{(mp)}$ can finally be expressed as

$$\rho_0\, w_i^{(mp)} = \boldsymbol{\sigma}_{\mathrm{skw}} \cdot \overset{3}{\mathbf{E}}\,(\dot{\boldsymbol{\varphi}}_m)_{\mathcal{B}} - 2\,\overset{a}{\bar{\boldsymbol{\mu}}}{}^{d} \cdot (\overset{a}{\bar{\boldsymbol{\kappa}}})^{\cdot} = \boldsymbol{\sigma}_{\mathrm{skw}} \cdot \overset{3}{\mathbf{E}}\,(\dot{\boldsymbol{\varphi}}_m)_{\mathcal{B}} + \bar{\boldsymbol{\mu}} \cdot (\overset{a}{\bar{\boldsymbol{\kappa}}})^{\cdot}\,, \tag{2.154}$$

where the relation $\bar{\boldsymbol{\mu}} = -2\overset{a}{\bar{\boldsymbol{\mu}}}{}^{d}$ has been used, cf. (2.152). Given the above equations, the local stress power and by means of an appropriate time integration also the mechanical work can be computed by homogenisation methods. Assuming conservative stress measures with a complete integral formulation as in linearised elasticity, the local internal work is obtained by

$$\begin{aligned} W_i &:= W_i^{(sf)} + W_i^{(mp)} + W_i^{(ms)} \quad \text{with} \\ W_i^{(sf)} &= \int_{t_0}^{t} \rho_0\, w_i^{(sf)}\,\mathrm{d}\tilde{t} = \tfrac{1}{2}\,\boldsymbol{\sigma}_{\mathrm{sym}} \cdot \boldsymbol{\varepsilon}\,, \\ W_i^{(mp)} &= \int_{t_0}^{t} \rho_0\, w_i^{(mp)}\,\mathrm{d}\tilde{t} = \tfrac{1}{2}\,[\,\boldsymbol{\sigma}_{\mathrm{skw}} \cdot \overset{3}{\mathbf{E}}\,(\boldsymbol{\varphi}_m)_{\mathcal{B}} - (\overset{3}{\bar{\boldsymbol{\mu}}}{}^{d})^{\overset{12}{T}} \cdot (\overset{3}{\mathbf{E}}\operatorname{Grad}\bar{\boldsymbol{\varphi}})^{\underline{3}}\,] \\ &= \tfrac{1}{2}\,[\,\boldsymbol{\sigma}_{\mathrm{skw}} \cdot \overset{3}{\mathbf{E}}\,(\boldsymbol{\varphi}_m)_{\mathcal{B}} + \bar{\boldsymbol{\mu}} \cdot \overset{a}{\bar{\boldsymbol{\kappa}}}\,], \\ W_i^{(ms)} &= \int_{t_0}^{t} \rho_0\, w_i^{(ms)}\,\mathrm{d}\tilde{t} \\ &= \tfrac{1}{2}\big(\,[\,(\boldsymbol{\sigma}_m)_{\mathcal{B}} - \boldsymbol{\sigma}_{\mathrm{sym}}\,] \cdot (\boldsymbol{\varepsilon}_m)_{\mathcal{B}} + \overset{(12)}{\operatorname{sym}}\overset{3}{\bar{\boldsymbol{\mu}}}{}^{d} \cdot \operatorname{Grad}(\boldsymbol{\varepsilon}_m)_{\mathcal{B}}\,\big)\,. \end{aligned} \tag{2.155}$$

Chapter 3:
From particle-scale information to micromorphic quantities

Granular materials exhibit macroscopic behaviour that is strongly dependent on the microscopic interaction of individual grains, possible concentration of grain rotations or the micro-heterogeneous topology of grain-binder composites. As it is impossible to include all the microstructural information into modelling techniques that aim at engineering applications, the derivation of appropriate substituting models on a larger spatial scale is of great interest. As already mentioned, microcontinuum theories offer such a macroscopic extension to standard continuum theories in order to incorporate some significant micro-effects, such as, for example, free grain rotations as the basis for the micropolar extension. Their physical justification and evaluation in the field of granular material can be obtained by studying granulates from a direct micromechanical approach and a subsequent construction of a homogenisation procedure. This is at the centre of the following chapter. Although specific volume and surface averaging operations were already used to define the micromorphic field quantities, some fundamental issues of homogenisation shall be addressed and reviewed in the following.

3.1 Fundamentals of homogenisation

3.1.1 Representative Elementary Volume

Homogenisation describes the averaging process of quantities from a lower, for example, the microscopic, towards a higher, for example, the mesoscopic or the macroscopic, scale. An averaged quantity is thereby always found by an integration of the respective quantity over a *representative* domain. If the considered domain is a volume V, the volumetric average according to Hill [111] needs to be taken over a *Representative Elementary Volume*, which ensures that the emerging macroscopic quantity is statistically homogeneous for any chosen location of the REV at the microstructural configuration. The continuum-mechanical approach assumes that the averaged quantity is independent of the characteristic size D of the chosen averaging domain, i. e. that the theoretically underlying REV size is chosen large enough to avoid fluctuations emerging from microstructural elements of characteristic size δ, cf. Figure 3.1. However, if this condition is met, an averaging over direct micromechanical models leads to standard Cauchy continua at the macroscopic level, as the extended stresses of microcontinuum theories are only detectable when the interplay of the components of the microstructure is evaluated for a mesoscopic ensemble, cf. Ehlers *et al.* [64]. This motivates the introduction of an REV of size d, which is a characteristic size of the now mesoscopic interpretation of the REV, embedded between the micro- and the macroscale. The assumption of three independent scales is often referred

to as the micro-meso-macro (MMM) principle, firstly introduced by Hashin [107].

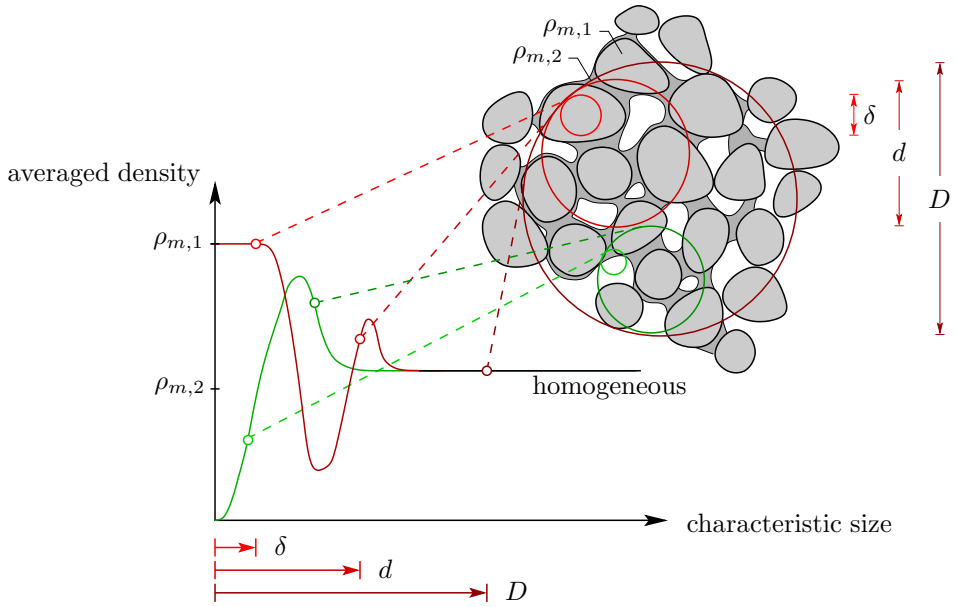

Figure 3.1: *Sketch of the averaged density as a function of the averaging domain after Bachmat & Bear [17] or Hassanizadeh & Gray [108].*

3.1.2 Scale separation

While the continuum approach of assuming an independence of the averaged quantity from variations in the REV size requires the scale of size δ to be separated from the scale of size D, i. e.

$$\delta \ll D\,, \tag{3.1}$$

the MMM principle additionally assumes a scale separation, such that

$$\delta \ll d \ll D\,. \tag{3.2}$$

The scale separation argumentation implies a significant consequence with respect to the balance relations of embedded particles in an REV or in a continuum body, as well as REV embedded into a continuum body. In all three cases, volume-specific quantities of individual particles/REV, like body forces and inertia terms, scale with $(\delta/d)^3$ or $(d/D)^3$, respectively, and can be neglected compared to surface-specific terms like external loads, which scale with $(\delta/D)^2$ or $(d/D)^2$, when large numbers of particles/REV are considered. As a result, volumetric contributions in all balance relations are negligible compared to contributions acting on the respective surfaces of the considered domain.

Table 3.1: *Balance relations for a single particle* $\mathcal{P}^{(i)}$

Balance of linear momentum:	$\int_{\mathcal{P}^{(i)}} \rho_m \, \ddot{\mathbf{x}} \, \mathrm{d}v = \int_{\partial \mathcal{P}^{(i)}} \mathbf{t}_m \, \mathrm{d}a + \int_{\mathcal{P}^{(i)}} \rho_m \, \mathbf{g} \, \mathrm{d}v$
Balance of angular momentum:	$\int_{\mathcal{P}^{(i)}} [\, \mathbf{x} \times (\, \rho \, \ddot{\mathbf{x}} \,) \,] \, \mathrm{d}v = \int_{\partial \mathcal{P}^{(i)}} \mathbf{x} \times \mathbf{t}_m \, \mathrm{d}a + \int_{\mathcal{P}^{(i)}} \mathbf{x} \times (\, \rho_m \, \mathbf{g} \,) \, \mathrm{d}v$
Balance of mechanical power:	$\frac{\mathrm{d}}{\mathrm{d}t} \left(\int_{\mathcal{P}^{(i)}} \frac{1}{2} \rho_m \, \dot{\mathbf{x}} \cdot \dot{\mathbf{x}} \, \mathrm{d}v \right) + \int_{\mathcal{P}^{(i)}} \mathbf{T}_m \cdot \mathbf{D} \, \mathrm{d}v$ $= \int_{\partial \mathcal{P}^{(i)}} \dot{\mathbf{x}} \cdot \mathbf{t}_m \, \mathrm{d}a + \int_{\mathcal{P}^{(i)}} \dot{\mathbf{x}} \cdot (\, \rho_m \, \mathbf{g} \,) \, \mathrm{d}v$

3.2 Single particles as microscopic REV

3.2.1 Governing equations for embedded particles

Generally, if a single particle $\mathcal{P}^{(i)}$ is considered, it is represented as a Cauchy continuum, where the standard forms of the balance equations for linear and angular momentum as well as mechanical power apply. Table 3.1 recapitulates the governing set of equations for $\mathcal{P}^{(i)}$ based on the statements in Section 2.2.3. Thereby, as the scale of the individual particles is considered as the characteristic microscopic scale of the investigated granular materials, the indexation $(\,\cdot\,)_m$ is adopted from the microcontinuum setting. Thus, ρ_m refers to the particle-scale mass density and the microstress vector acting at the particle's boundary is given by $\mathbf{t}_m = \mathbf{T}_m \, \mathbf{n}$ with $\mathbf{T}_m$ as the Cauchy-type microstress tensor of $\mathcal{P}^{(i)}$. When microscopic particles $\mathcal{P}^{(i)}$ are embedded in a macroscopic body $\mathcal{B}$ consisting of a manifold of individual particles, cf. the microcontinuum setting sketched in Figure 2.4, the microscale (of order δ) is separated from the macroscale (of order D) and the arguments of scale separation hold. As a result, volumetric contributions in the particle's balance relations are negligible compared to contributions acting at the particle surface $\partial \mathcal{P}^{(i)}$. Thus, the balance of linear momentum directly reduces to

$$\mathbf{0} = \int_{\partial \mathcal{P}^{(i)}} \mathbf{t}_m \, \mathrm{d}a = \int_{\mathcal{P}^{(i)}} \operatorname{div} \mathbf{T}_m \, \mathrm{d}v \,. \tag{3.3}$$

If, additionally, the microcontinuum setting is assumed to be valid, meaning that either the particle's deformation is assumed as homogeneous (micromorphic case) or the particle is rigid (micropolar case), implies that the additive split of $\mathbf{x}$ into $\mathbf{x}_{\mathcal{M}} + \mathbf{x}_m$, cf. (2.78), holds with $\mathbf{x}_{\mathcal{M}}$ as the position vector pointing to the particle's constant centre of mass $\mathcal{M}$. As a consequence, the position $\mathbf{x}_{\mathcal{M}}$ is independent of the integration over the domain of $\mathcal{P}^{(i)}$ and one additionally obtains

$$\begin{aligned} \mathbf{x}_m &= \mathbf{F}_m \, \mathbf{X}_m \,, \quad \dot{\mathbf{x}}_m = \mathbf{L}_m \, \mathbf{x}_m && \text{for the micromorphic setting, cf. (2.81)} \\ & && \text{and (2.83), and} \\ \mathbf{x}_m &= \mathbf{R}_m \, \mathbf{X}_m \,, \quad \dot{\mathbf{x}}_m = \boldsymbol{\Omega}_m \, \mathbf{x}_m && \text{for the micropolar setting, cf. (2.120).} \end{aligned} \tag{3.4}$$

Moreover, the balance of angular momentum for the embedded particle reduces to

$$\mathbf{0} = \int_{\partial \mathcal{P}^{(i)}} \mathbf{x} \times \mathbf{t}_m \, \mathrm{d}a = \mathbf{x}_{\mathcal{M}} \times \int_{\partial \mathcal{P}^{(i)}} \mathbf{t}_m \, \mathrm{d}a + \int_{\partial \mathcal{P}^{(i)}} \mathbf{x}_m \times \mathbf{t}_m \, \mathrm{d}a = \int_{\mathcal{P}^{(i)}} \operatorname{div} \mathbf{M}_m \, \mathrm{d}v \,, \tag{3.5}$$

where $\mathbf{M}_m = \mathbf{x}_m \times \mathbf{T}_m$ is the tensorial microstress moment with $\mathbf{m}_m = \mathbf{x}_m \times \mathbf{t}_m$ as its corresponding microstress satisfying $\mathbf{m}_m = \mathbf{M}_m\,\mathbf{n}$. Finally, the local forms of (3.3) and (3.5) read

$$\mathbf{0} \,=\, \operatorname{div}\mathbf{T}_m\,, \quad \mathbf{0} \,=\, \operatorname{div}\mathbf{M}_m\,. \tag{3.6}$$

From $(3.6)_1$ and $(3.6)_2$, one easily recovers the symmetry of the microstress from

$$\mathbf{0} \,=\, \operatorname{div}\mathbf{M}_m \,=\, \operatorname{div}\,(\,\mathbf{x}_m \times \mathbf{T}_m\,) \,=\, \mathbf{x}_m \times \operatorname{div}\,\mathbf{T}_m \,+\, \mathbf{I} \times \mathbf{T}_m\,, \tag{3.7}$$

such that $\mathbf{I} \times \mathbf{T}_m \,=\, \overset{3}{\mathbf{E}}\mathbf{T}_m^T \,=\, 2\,\overset{\mathrm{A}}{\mathbf{t}}_m \,=\, \mathbf{0}$, compare Section 2.2.3. As a result, $\mathbf{T}_m \,=\, \mathbf{T}_m^T$. For the case of a homogeneously deformable particle, the relations concerning the homogeneous deformation and the corresponding material time derivatives given (2.83) furthermore hold, such that a scalar multiplication with the velocity field $\dot{\mathbf{x}}$ yields the balance of mechanical power as

$$\begin{aligned}\int_{\mathcal{P}^{(i)}} \dot{\mathbf{x}} \,\cdot\, \operatorname{div}\mathbf{T}_m\,\mathrm{d}v \,&=\, \dot{\mathbf{x}}_{\mathcal{M}} \,\cdot \int_{\mathcal{P}^{(i)}} \operatorname{div}\mathbf{T}_m\,\mathrm{d}v \,+\, \int_{\mathcal{P}^{(i)}} \dot{\mathbf{x}}_m \,\cdot\, \operatorname{div}\mathbf{T}_m\,\mathrm{d}v \\ &=\, \underbrace{\int_{\mathcal{P}^{(i)}} \mathbf{T}_m \,\cdot\, \mathbf{D}_m\,\mathrm{d}v}_{\mathcal{L}_i(\mathcal{P}^{(i)},\,t)} \,-\, \underbrace{\int_{\partial\mathcal{P}^{(i)}} \dot{\mathbf{x}}_m \,\cdot\, \mathbf{t}_m\,\mathrm{d}a}_{\mathcal{L}_a(\mathcal{P}^{(i)},\,t)}\,,\end{aligned} \tag{3.8}$$

where $\mathbf{T}_m \cdot \mathbf{L}_m = \mathbf{T}_m \cdot \mathbf{D}_m$ due to $\mathbf{T}_m \cdot \mathbf{W}_m = 0$, when the local spatial velocity gradient $\mathbf{L}_m$ is additively split into its symmetric part $\mathbf{D}_m$ and its skew-symmetric part $\mathbf{W}_m$. Analogously to the Cauchy continuum in Section 2.2.3, (3.8) states the equivalence of the external stress power $\mathcal{L}_a(\mathcal{P}^{(i)},\,t)$ and the internal stress power $\mathcal{L}_i(\mathcal{P}^{(i)},\,t)$ for the embedded particle.

3.2.2 Homogenisation formalism for particle stresses and stress moments

Volumetric averages of the stress $\mathbf{T}_m$ and the stress moments $\mathbf{M}_m$, taken over individual particles embedded in an ensemble of particles can be derived on the basis of Hill's homogenisation theorem, cf. (2.98). For the homogenisation of the microstresses $\mathbf{T}_m$ of single embedded particles with domain $\mathcal{P}^{(i)}$, the following procedure holds. Based on $(3.6)_1$, a dyadic multiplication of the local momentum balance with $\mathbf{x}_m$ and a subsequent integration over the particle domain leads to

$$\operatorname{div}\mathbf{T}_m \,=\, \mathbf{0} \quad\rightarrow\quad \mathbf{0} \,=\, \int_{\mathcal{P}^{(i)}} (\,\mathbf{x}_m \,\otimes\, \operatorname{div}\mathbf{T}_m\,)\,\mathrm{d}v\,. \tag{3.9}$$

With the aid of the divergence theorem (A.25), (3.9) can be rewritten as

$$\mathbf{0} \,=\, \int_{\mathcal{P}^{(i)}} [\,\operatorname{div}\,(\,\mathbf{x}_m \,\otimes\, \mathbf{T}_m\,) \,-\, (\,\operatorname{grad}\mathbf{x}_m\,)\,\mathbf{T}_m^T\,]\,\mathrm{d}v\,. \tag{3.10}$$

Applying the Gaussian integral theorem to the first term of (3.10) yields

$$\mathbf{0} \,=\, \int_{\partial\mathcal{P}^{(i)}} (\,\mathbf{x}_m \,\otimes\, \mathbf{t}_m\,)\,\mathrm{d}a \,-\, \int_{\mathcal{P}^{(i)}} \mathbf{T}_m^T\,\mathrm{d}v\,, \tag{3.11}$$

where $\operatorname{grad}\mathbf{x}_m = \mathbf{I}$ has been used, such that

$$\int_{\mathcal{P}^{(i)}} \mathbf{T}_m^T \,\mathrm{d}v \;=\; \int_{\partial\mathcal{P}^{(i)}} (\,\mathbf{x}_m \otimes \mathbf{t}_m\,)\,\mathrm{d}a\,. \tag{3.12}$$

Based on (3.12), one obtains the averaged stresses $\langle\mathbf{T}_m\rangle$ acting at the particle centre at position $\mathbf{x}_\mathcal{M}$ in comparison with (2.98) as

$$\langle\mathbf{T}_m\rangle \;:=\; \frac{1}{V_{\mathcal{P}^{(i)}}} \int_{\partial\mathcal{P}^{(i)}} (\,\mathbf{t}_m \otimes \mathbf{x}_m\,)\,\mathrm{d}a\,, \tag{3.13}$$

where $V_{\mathcal{P}^{(i)}}$ is the particle volume, identified as the volumetric homogenisation domain of interest. Note that $\langle\mathbf{T}_m\rangle$ is symmetric as a result of $\mathbf{T}_m = \mathbf{T}_m^T$. Furthermore, note that (3.13) is well known as the average stress of single particles, cf. Christoffersen *et al.* [34] or Bathurst & Rothenburg [20]. However, it is important to recognise that for rigid particles with $|\mathbf{x}_m| = \text{constant}$, variations in $\langle\mathbf{T}_m\rangle$ only originate from variations of external loads $\mathbf{t}_m$, while for homogeneously deformable particles, where the particle size or $\mathbf{x}_m$, respectively, is locally deformed by $\mathbf{F}_m$, the resulting averaged stress additionally also depends on the microdeformation.

Proceeding similarly as before, the local statement of angular momentum $(3.6)_2$ for embedded particles furthermore yields the averaged stress moment $\langle\mathbf{M}_m\rangle$. Thus, one obtains

$$\mathbf{0} \;=\; \int_{\partial\mathcal{P}^{(i)}} (\,\mathbf{x}_m \otimes \mathbf{m}_m\,)\,\mathrm{d}a \;-\; \int_{\mathcal{P}^{(i)}} \mathbf{M}_m^T \,\mathrm{d}v\,, \tag{3.14}$$

such that

$$\langle\mathbf{M}_m\rangle \;:=\; \frac{1}{V_{\mathcal{P}^{(i)}}} \int_{\partial\mathcal{P}^{(i)}} (\,\mathbf{m}_m \otimes \mathbf{x}_m\,)\,\mathrm{d}a \;=\; \frac{1}{V_{\mathcal{P}^{(i)}}} \int_{\partial\mathcal{P}^{(i)}} (\,\mathbf{x}_m \times \mathbf{t}_m\,) \otimes \mathbf{x}_m \,\mathrm{d}a\,. \tag{3.15}$$

When using stress and stress moment averages, the external loads of particles $\mathcal{P}^{(i)}$ are reduced to the particle's mass centre at $\mathbf{x}_\mathcal{M}$ towards homogenised stresses $\langle\mathbf{T}_m\rangle$ and stress couples $\langle\mathbf{M}_m\rangle$, thus allowing for the definition of local values of the corresponding stresses in the body $\mathcal{B}$ or, alternatively, in a mesoscopic REV $\mathcal{R}$.

3.2.3 Homogenisation formalism for particle deformation

In addition to its translational motion, represented by the motion of $\mathbf{x}_\mathcal{M}$, the deformation gradient $\mathbf{F}_m$ is assumed to carry the local deformation of particles. Assuming the existence of a local displacement field $\mathbf{u}_m$ allows to directly determine the volume average $\langle\mathbf{F}_m\rangle$, cf. for example, Schröder [188], as

$$\begin{aligned} &\langle\mathbf{F}_m\rangle \;:=\; \mathbf{I} \,+\, \langle\operatorname{Grad}\mathbf{u}_m\rangle \\ &\text{with}\quad \langle\operatorname{Grad}\mathbf{u}_m\rangle \;:=\; \frac{1}{V_{\mathcal{P}^{(i)}}} \int_{\mathcal{P}} \operatorname{Grad}\mathbf{u}_m \,\mathrm{d}v \;=\; \frac{1}{V_{\mathcal{P}^{(i)}}} \int_{\partial\mathcal{P}^{(i)}} (\,\mathbf{u}_m \otimes \mathbf{n}\,)\,\mathrm{d}a\,. \end{aligned} \tag{3.16}$$

Equivalently, the homogenised spatial velocity gradient $\langle \mathbf{L}_m \rangle$ on the particle level follows as

$$\begin{aligned} \langle \mathbf{L}_m \rangle &:= \langle \operatorname{grad} \dot{\mathbf{x}}_m \rangle \\ \text{with} \quad \langle \operatorname{grad} \dot{\mathbf{x}}_m \rangle &:= \frac{1}{V_{\mathcal{P}^{(i)}}} \int_{\mathcal{P}} \operatorname{grad} \dot{\mathbf{x}}_m \, \mathrm{d}v \;=\; \frac{1}{V_{\mathcal{P}^{(i)}}} \int_{\partial \mathcal{P}^{(i)}} (\dot{\mathbf{x}}_m \otimes \mathbf{n}) \, \mathrm{d}a \,. \end{aligned} \tag{3.17}$$

Analogously to the above introduced averaged particle stresses, which define the local values of the corresponding quantities on the spatially higher scale, the averages $\langle \mathbf{F}_m \rangle$ and $\langle \mathbf{L}_m \rangle$ reduce the deformation state of the particles towards the centre of mass and define the corresponding local values on the continuum or the REV scale.

Note that as the single embedded particle shows the characteristics of a Cauchy continuum, the microstress $\mathbf{T}_m$ is conjugated to $\mathbf{D}_m = \overset{\triangle}{\mathbf{A}}_m$, as can be seen directly from (3.8). With $\langle \mathbf{F}_m \rangle$ at hand, the respective work-conjugated strain measure $\mathbf{A}_m$ can be computed in a straightforward manner. However, for the sake of simplicity, especially with respect to the later discussed ensembles of particles forming an REV, a geometrically linear point of view is taken for all particle-based strain computations. Thus, the primary interest lies in the determination of the average strain $\langle \boldsymbol{\varepsilon}_m \rangle$ to the linearised counterpart $\boldsymbol{\varepsilon}_m$ of the work-conjugated strain $\mathbf{A}_m$. This measure can, again, be computed in a straightforward manner by use of (3.16) as

$$\begin{aligned} \langle \boldsymbol{\varepsilon}_m \rangle &= \tfrac{1}{2} \left(\langle \operatorname{Grad} \mathbf{u}_m \rangle + \langle \operatorname{Grad} \mathbf{u}_m \rangle^T \right) \\ &= \frac{1}{V_{\mathcal{P}^{(i)}}} \int_{\partial \mathcal{P}^{(i)}} \tfrac{1}{2} \left[(\mathbf{u}_m \otimes \mathbf{n}) + (\mathbf{n} \otimes \mathbf{u}_m) \right] \mathrm{d}a \,. \end{aligned} \tag{3.18}$$

3.3 Ensembles of particles as mesoscopic REV

On the microscopic scale, each particle exhibits stresses as a standard continuum in the sense that microscopic stresses $\mathbf{T}_m$ are symmetric, independently of any restrictions to the particle deformation. As was shown in Section 2.4.3, where micromorphic continuum balance relations were principally introduced following the original idea of Eringen & Suhubi [72], an embedded homogeneously deformable microcontinuum forms the basis for the micromorphic continua. Thereby, the characterising higher-order stress moments, the corresponding surface stresses, as well as the microstress average are identified based on averages of microcontinuum quantities defining the field quantities of the macroscopic micromorphic medium. In contrast to this approach, Ehlers *et al.* [64] evaluated the axiomatic balance relations for linear and angular momentum of an REV and thereby identified micropolar stress states on the REV level, concluding that such a particle-centre-based REV needs to be considered as the homogenisation domain when extended micropolar stresses have to be detected. Based on this procedure, the following homogenisation strategy consistently extends this approach by including deformable particles as representatives of deformable components in granular material on the microscopic scale (Ehlers & Bidier [62]). For the detection of micromorphic effects stemming from possible local particle deformation, two different homogenisation procedures are compared and connected to each other. The first one is based on stresses and stress couples taken

from the previously explained homogenisation over single particles as microscopic REV, cf. Section 3.2.2. The second follows the basic argumentation of Ehlers *et al.* [64] on the REV level, thereby directly evaluating the stresses acting on the boundary $\partial\mathcal{R}$ of $\mathcal{R}$.

3.3.1 Balance relations for embedded ensembles of particles

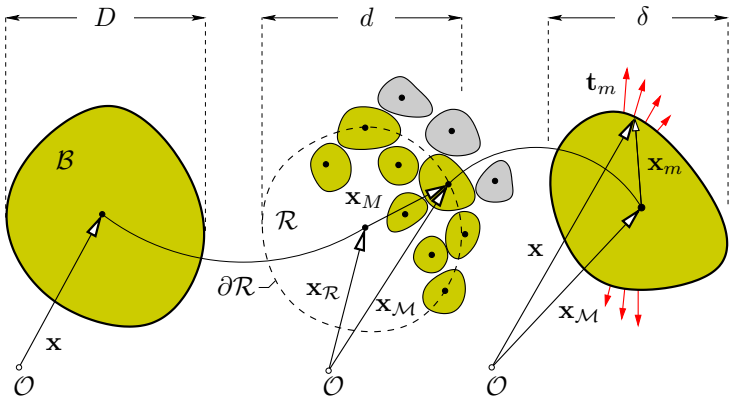

Figure 3.2: *REV $\mathcal{R}$, embedded on the mesoscale between micro- and macroscale.*

An REV $\mathcal{R}$ is considered as an ensemble of rigid particles, where the external REV boundary $\partial\mathcal{R}$ is defined as the connected surface formed by the mass centres of the bounding particles, cf. Figure 3.2 (middle). In the first procedure, the averaged particle stresses (3.13) and (3.15) exist at $\mathbf{x}_M$ and define the local values of stresses $\mathbf{T}_M$ and couple stresses $\bar{\mathbf{M}}_M$ within $\mathcal{R}$ as

$$\mathbf{T}_M(\mathbf{x}_M,\, t) := \langle \mathbf{T}_m \rangle \quad \text{and} \quad \bar{\mathbf{M}}_M(\mathbf{x}_M,\, t) := \langle \mathbf{M}_m \rangle . \tag{3.19}$$

Given (3.19) and the arguments of scale separation, the linear and angular momentum balances of $\mathcal{R}$ reduce to equilibrium conditions of external forces and moments yielding

$$\mathbf{0} = \int_{\partial\mathcal{R}} \mathbf{t}_M \,\mathrm{d}a = \int_{\mathcal{R}} \operatorname{div}_M \mathbf{T}_M \,\mathrm{d}v \tag{3.20}$$

for the linear momentum balance, in which the Gaussian integral theorem has been used, and

$$\mathbf{0} = \int_{\partial\mathcal{R}} (\mathbf{x}_M \times \mathbf{t}_M + \bar{\mathbf{m}}_M)\,\mathrm{d}a = \int_{\mathcal{R}} \operatorname{div}_M (\mathbf{M}_M + \bar{\mathbf{M}}_M)\,\mathrm{d}v \tag{3.21}$$

for the angular momentum balance. Note that the relative positions $\mathbf{x}_M$ of the particle's mass centres are considered as field quantities in $\mathcal{R}$ and $\operatorname{div}_M(\cdot)$, $\operatorname{grad}_M(\cdot)$ are the divergence and gradient operators with respect to the field $\mathbf{x}_M$, respectively. Furthermore, the relations $\mathbf{t}_M = \mathbf{T}_M\mathbf{n}$ and $\bar{\mathbf{m}}_M = \bar{\mathbf{M}}_M\mathbf{n}$ with $\mathbf{n}$ as the outward-oriented surface normal at $\partial\mathcal{R}$ hold, cf. Figure 3.3. The quantity $\mathbf{M}_M := \mathbf{x}_M \times \mathbf{T}_M$ defines the stress moment tensor and $\bar{\mathbf{M}}_M$ is the couple stress tensor at the REV level. With this in mind, (3.21) can be rewritten by use of (3.20) as

$$\mathbf{I} \times \mathbf{T}_M + \operatorname{div}_M \bar{\mathbf{M}}_M = \mathbf{0} . \tag{3.22}$$

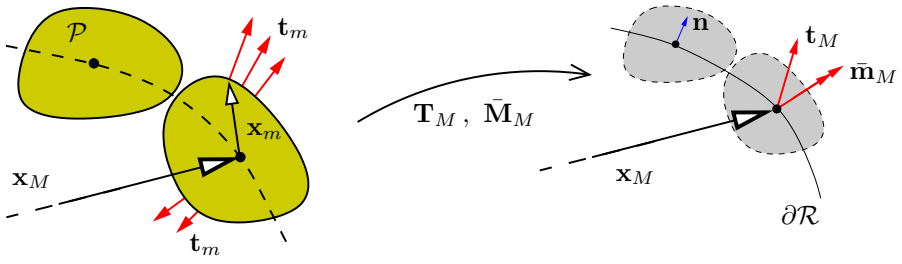

Figure 3.3: Surface stress vectors of the REV based on homogenised particle stresses.

Proceeding from $\mathbf{T}_M = \mathbf{T}_M^T$, one easily concludes to $\mathbf{I} \times \mathbf{T}_M = \mathbf{0}$, such that (3.22) in combination with (3.20) reduces to

$$\operatorname{div}_M \mathbf{T}_M = \mathbf{0} \quad \text{and} \quad \operatorname{div}_M \bar{\mathbf{M}}_M = \mathbf{0}\,, \tag{3.23}$$

thus yielding the same type of result as was obtained for individual particles, cf. (3.6).

In the second procedure for the formulation of REV balances, the loading on the outward-oriented surfaces of the bounding particles $\mathcal{P}^{(i)}$ are considered to formulate the axiomatic balances, cf. Figure 3.4. Therein, $\mathbf{t}$ is the stress resultant and $\bar{\mathbf{m}}$ the resultant couple stress both situated at the particle centre of $\mathcal{P}^{(i)}$ following from the surface-specific average of the microstress $\mathbf{t}_m$ and the first moment of the microstress $\mathbf{x}_m \times \mathbf{t}_m$, respectively, both taken over the external part $\partial\mathcal{P}^{(i)}_{ex}$ of the particle boundary $\partial\mathcal{P}^{(i)}$:

$$\begin{aligned} \mathbf{t} &:= \langle \mathbf{t}_m \rangle_A := \frac{1}{A_{\mathcal{P}^{(i)}_{ex}}} \int_{\partial\mathcal{P}^{(i)}_{ex}} \mathbf{t}_m \,\mathrm{d}a \quad \text{and} \\ \bar{\mathbf{m}} &:= \langle \mathbf{x}_m \times \mathbf{t}_m \rangle_A := \frac{1}{A_{\mathcal{P}^{(i)}_{ex}}} \int_{\partial\mathcal{P}^{(i)}_{ex}} \mathbf{x}_m \times \mathbf{t}_m \,\mathrm{d}a\,. \end{aligned} \tag{3.24}$$

Following this, the global and local statements of momentum and angular momentum equations of $\mathcal{R}$ read

$$\mathbf{0} = \int_{\partial\mathcal{R}} \mathbf{t} \,\mathrm{d}a = \int_{\mathcal{R}} \operatorname{div}_M \mathbf{T} \,\mathrm{d}v \ \rightarrow\ \operatorname{div}_M \mathbf{T} = \mathbf{0}\,, \tag{3.25}$$

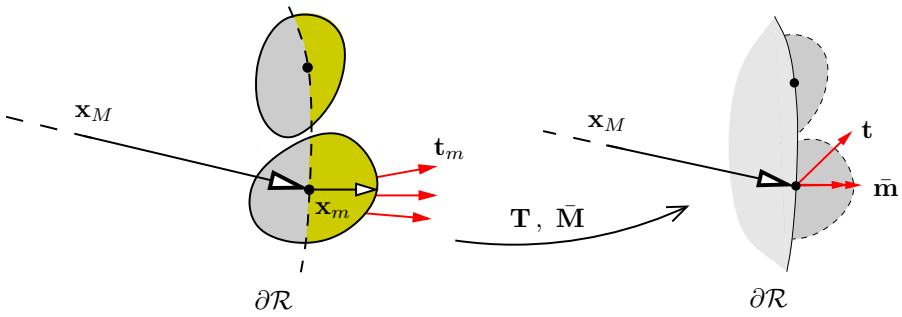

Figure 3.4: Surface stress vectors of the REV based on shifting the boundary stresses to the particle centres.

and

$$\mathbf{0} = \int_{\partial\mathcal{R}} (\,\mathbf{x}_M \times \mathbf{t} + \bar{\mathbf{m}}\,)\,\mathrm{d}a = \int_{\mathcal{R}} \mathrm{div}_M\,(\,\mathbf{M} + \bar{\mathbf{M}}\,)\,\mathrm{d}v \quad \rightarrow \quad \mathrm{div}_M\,(\,\mathbf{M} + \bar{\mathbf{M}}\,) = \mathbf{0}\,, \tag{3.26}$$

where $\mathbf{m} = \mathbf{M}\,\mathbf{n}$ with $\mathbf{M} = \mathbf{x}_M \times \mathbf{T}$ and $\bar{\mathbf{m}} = \bar{\mathbf{M}}\,\mathbf{n}$. Note that

$$\mathrm{div}_M\,\mathbf{M} = \mathbf{x}_M \times \mathrm{div}_M\,\mathbf{T} + \mathbf{I} \times \mathbf{T}\,, \tag{3.27}$$

such that

$$\mathbf{0} = \mathrm{div}_M\,(\mathbf{M} + \bar{\mathbf{M}}) = \mathbf{I} \times \mathbf{T} + \mathrm{div}_M\,\bar{\mathbf{M}}\,, \tag{3.28}$$

where (3.25) has been used. Note that (3.28) is the typical result of the angular momentum balance of micropolar materials stating that $\mathbf{T}$ is only symmetric when there are no couple stresses $\bar{\mathbf{M}}$ or if $\mathrm{div}_M\,\bar{\mathbf{M}} = \mathbf{0}$, cf. Ehlers *et al.* [64]. However, note that in contrast to Ehlers *et al.* [64], $\bar{\mathbf{M}}$ depends on microdeformations, as $\mathbf{x}_m$ and its norm $|\mathbf{x}_m|$ are not constant but depend on the micromotion through $\mathbf{F}_m$, cf. $(3.4)_1$, while in a purely micropolar situation, $\mathbf{x}_m$ is only affected by a rotational micromotion, cf. $(3.4)_2$, such that $|\mathbf{x}_m|$ is constant.

Given the local momentum balances (3.23) and (3.25) based on the equilibrium of $\mathbf{T}_M$ and $\mathbf{T}$, respectively, the dyadic product of the balances with $\mathbf{x}_M$ yields after integration over $\mathcal{R}$

$$\begin{aligned} \mathbf{0} &= \int_{\mathcal{R}} \mathbf{x}_M \otimes \mathrm{div}_M\,\mathbf{T}_M\,\mathrm{d}v = \int_{\mathcal{R}} (\,\mathrm{div}_M\,\overset{3}{\mathbf{M}}{}^d_M - \mathbf{T}^T_M\,)\,\mathrm{d}v\,, \\ \mathbf{0} &= \int_{\mathcal{R}} \mathbf{x}_M \otimes \mathrm{div}_M\,\mathbf{T}\,\mathrm{d}v = \int_{\mathcal{R}} (\,\mathrm{div}_M\,\overset{3}{\mathbf{M}}{}^d - \mathbf{T}^T\,)\,\mathrm{d}v\,, \end{aligned} \tag{3.29}$$

where (A.25) together with the third-order dyadic stress moments $\overset{3}{\mathbf{M}}{}^d_M := \mathbf{x}_M \otimes \mathbf{T}_M$ and $\overset{3}{\mathbf{M}}{}^d := \mathbf{x}_M \otimes \mathbf{T}$ have been used. Combining both equations leads to

$$\mathbf{0} = \int_{\mathcal{R}} [\,\mathrm{div}_M\,(\,\overset{3}{\mathbf{M}}{}^d_M - \overset{3}{\mathbf{M}}{}^d\,) - (\,\mathbf{T}^T_M - \mathbf{T}^T\,)\,]\,\mathrm{d}v. \tag{3.30}$$

Note with respect to the difference between $\mathbf{T}_M$ and $\mathbf{T}$ that $\mathbf{T}_M$ as the stress state homogenised over individual particles depends by definition on $\mathbf{x}_m$, while $\mathbf{T}$ as the stress resultant of the same particle is independent of $\mathbf{x}_m$. As a result, $\mathbf{T}_M$ is affected by microcontinuum deformations, while $\mathbf{T}$ is not. Furthermore, as microcontinuum deformations can be considered as local fluctuations compared to the deformation of the REV or of the whole body itself, it is concluded that a detection of microcontinuum effects such as micromorphic, micropolar or microstrain properties can be obtained from the stress difference $\mathbf{T}_M - \mathbf{T}$ at the REV scale or from $\langle \mathbf{T}_M - \mathbf{T} \rangle$ as the homogenisation of $\mathbf{T}_M - \mathbf{T}$ at the body scale. Note that $\langle \mathbf{T}_M - \mathbf{T} \rangle$ is known as the so-called general micromorphic stress difference. Furthermore, $\overset{3}{\mathbf{M}}{}^d_M$ as $\mathbf{T}_M$ also depends linearly on $\mathbf{x}_m$, while $\overset{3}{\mathbf{M}}{}^d$ and $\mathbf{T}$ are independent of it. In line with the general interpretation of micromorphic continua, the structure of (3.30) as it was obtained from momentum balance equations can formally be compared to a balance relation stating that if a difference between the stresses $\mathbf{T}_M$ and $\mathbf{T}$ exists, $\mathrm{div}_M\,(\overset{3}{\mathbf{M}}{}^d_M - \overset{3}{\mathbf{M}}{}^d)$ balances the REV.

Moreover, (3.30) can be interpreted as a generalised angular momentum balance that contains the micropolar angular momentum balance (3.28) through its axial components. This can be verified by computing the axial vector corresponding to the local statement of (3.30), making use of the symmetry of $\mathbf{T}_M$, such that $\overset{3}{\mathbf{E}}\,\mathbf{T}_M^T$ and, as a result, also $\overset{3}{\mathbf{E}}\,(\mathrm{div}_M\,\overset{3}{\mathbf{M}}{}^d_M) = \mathrm{div}_M\,[(\overset{3}{\mathbf{E}}\,\overset{3}{\mathbf{M}}{}^d_M)^{\underline{2}}]$ vanishes. Note that $\overset{3}{\mathbf{E}}$, as a fundamental tensor which is only constructed by basis vectors, is independent of $\mathbf{x}$ or of $\mathbf{x}_M$, respectively. Furthermore, $\overset{3}{\mathbf{E}}\,(\mathrm{div}_M\,\overset{3}{\mathbf{M}}{}^d) = \mathrm{div}_M\,\big([\overset{3}{\mathbf{E}}\,(\mathbf{x}_M\otimes\mathbf{T})]^{\underline{2}}\big) = \mathrm{div}_M\,(\mathbf{x}_M\times\mathbf{T}) = \mathrm{div}_M\,\mathbf{M} = -\mathrm{div}_M\,\bar{\mathbf{M}}$, where (3.26) has been used. Following this, one obtains

$$\begin{aligned}\mathbf{0} &= \overset{3}{\mathbf{E}}\,[\,\mathrm{div}_M\,(\,\overset{3}{\mathbf{M}}{}^d_M\,-\,\overset{3}{\mathbf{M}}{}^d\,)\,-\,(\,\mathbf{T}_M^T\,-\,\mathbf{T}^T\,)\,]\\ &= -\,\mathrm{div}_M\,\big(\,[\,\overset{3}{\mathbf{E}}\,(\,\mathbf{x}_M\,\otimes\,\mathbf{T}\,)]^{\underline{2}}\big)\,+\,\overset{3}{\mathbf{E}}\,\mathbf{T}^T\,=\,\mathrm{div}_M\,\bar{\mathbf{M}}\,+\,\mathbf{I}\,\times\,\mathbf{T}\,,\end{aligned} \tag{3.31}$$

thus recovering (3.31) as the micropolar angular momentum balance. Therein, the outer tensor product $\mathbf{x}_M\times\mathbf{T} = [\overset{3}{\mathbf{E}}\,(\mathbf{x}_M\otimes\mathbf{T})]^{\underline{2}}$ yields twice the negative tensorial skew-symmetric part of the third-order tensor $\overset{3}{\mathbf{M}}{}^d = \mathbf{x}_M\otimes\mathbf{T}$, where the property of skew symmetry arises between the first two basis systems.

For the determination of the deformational characteristics of the REV, it is of importance to express the position vector $\mathbf{x}$ in a micromorphic or micropolar setting analogously to (2.78) as

$$\mathbf{x}\,=\,\mathbf{x}_{\mathcal{M}}\,(\,\mathbf{X}_{\mathcal{M}}\,,\;t\,)\,+\,\mathbf{x}_m\,(\,\mathbf{X}_{\mathcal{M}}\,,\;t\,)\quad\text{and furthermore}\quad\dot{\mathbf{x}}\,=\,\dot{\mathbf{x}}_{\mathcal{M}}\,+\,\dot{\mathbf{x}}_m\,. \tag{3.32}$$

While the motion of $\mathbf{x}_{\mathcal{M}}$ leads to the existence of a deformation gradient $\mathrm{Grad}_{\mathcal{M}}\,\mathbf{x}_{\mathcal{M}} = \partial\mathbf{x}_{\mathcal{M}}/\partial\mathbf{X}_{\mathcal{M}}$ at the REV level, the local particle position vector $\mathbf{x}_m$ deforms according to (3.4) in a micropolar or a micromorphic setting. Analogously to (3.19), the averaged values of the deformation gradient (3.16) and the spatial velocity gradient (3.17) define the local values of $\mathbf{F}_M$ and $\mathbf{L}_M$ within $\mathcal{R}$ as

$$\mathbf{F}_M\,(\,\mathbf{x}_M,\,t\,)\,:=\,\langle\mathbf{F}_m\rangle\quad\text{and}\quad\mathbf{L}_M\,(\,\mathbf{x}_M,\,t\,)\,:=\,\langle\mathbf{L}_m\rangle\,. \tag{3.33}$$

It is thus concluded that a second averaging of theses local values in $\mathcal{R}$, now with respect to the domain of $\mathcal{R}$ as the homogenisation domain of interest, leads to the micromorphic continuum setting, viz.:

$$\begin{aligned}\mathbf{F}\,&:=\,\langle\mathrm{Grad}_{\mathcal{M}}\,\mathbf{x}_{\mathcal{M}}\rangle\quad\text{and}\quad(\mathbf{F}_m)_{\mathcal{B}}\,:=\,\langle\mathbf{F}_M\rangle\quad\text{as well as}\\ \mathbf{L}\,&:=\,\langle\mathrm{Grad}_{\mathcal{M}}\,\dot{\mathbf{x}}_{\mathcal{M}}\rangle\quad\text{and}\quad(\mathbf{L}_m)_{\mathcal{B}}\,:=\,\langle\mathbf{L}_M\rangle\end{aligned} \tag{3.34}$$

Thereby, $\mathbf{F}$ defines the macroscopic deformation gradient and $(\mathbf{F}_m)_{\mathcal{B}}$ defines the deformation gradient of the micromotion, both valid at the extended material point of the micromorphic body $\mathcal{B}$. Moreover, $\mathbf{L}$ and $(\mathbf{L}_m)_{\mathcal{B}}$ define the corresponding macroscopic and microscopic spatial velocity gradients, respectively. However, although $\mathbf{L}_m$ scales up from the microscale to yield $(\mathbf{L}_m)_{\mathcal{B}}$ as the macroscopic representative of the micro-velocity gradient, a simple integration of the balance of mechanical power (3.8) from the particle level

over the domain of the REV $\mathcal{B}$ would fully neglect the macroscopic deformation velocity $\bar{\mathbf{L}}$. Instead, as in the case of a homogeneously deformable microcontinuum, cf. Section 2.4.3 and especially (2.85), the locally averaged deformation need to be attached at the extended material point of $\mathcal{B}$ via a deformable director $\boldsymbol{\xi}$ such that either

$$\begin{aligned} &\boldsymbol{\xi} = (\mathbf{F}_m)_{\mathcal{B}}\,\boldsymbol{\Xi} \quad \text{and} \quad \dot{\boldsymbol{\xi}} = (\mathbf{L}_m)_{\mathcal{B}}\,\boldsymbol{\xi} \quad \text{or} \\ &\boldsymbol{\xi} = \bar{\mathbf{F}}\,\boldsymbol{\Xi}\,,\ \dot{\boldsymbol{\xi}} = \bar{\mathbf{L}}\,\boldsymbol{\xi} \quad \text{with} \quad \bar{\mathbf{L}} = \dot{\bar{\mathbf{F}}}\,\bar{\mathbf{F}}^{-1}\,,\ \bar{\mathbf{F}} = \mathbf{R}\,(\mathbf{F}_m)_{\mathcal{B}}\,. \end{aligned} \tag{3.35}$$

yields the additional micromorphic motion. Thereby, $(3.35)_2$ again represents the kinematically coupled continuum formulation, cf. Sections 2.4.1 and 2.4.2, while $(3.35)_1$ accounts for completely independent micro- and macromotions. As a consequence, the kinematic derivations concerning the introduction of strain and curvature tensors can directly be adopted from the micromorphic continuum formulation. Furthermore, one concludes that

$$\bar{\mathbf{L}} = \bar{\boldsymbol{\Omega}} + \mathbf{R}\,(\mathbf{L}_m)_{\mathcal{B}}\,\mathbf{R}^T \quad \text{with} \quad \begin{cases} \bar{\boldsymbol{\Omega}} = \dot{\bar{\mathbf{R}}}\,\bar{\mathbf{R}}^T \\ \mathbf{R}\,(\mathbf{L}_m)_{\mathcal{B}}\,\mathbf{R}^T = \bar{\mathbf{R}}\,(\dot{\mathbf{U}}_m)_{\mathcal{B}}\,(\mathbf{U}_m)_{\mathcal{B}}^{-1}\,\bar{\mathbf{R}}^T\,. \end{cases} \tag{3.36}$$

Thus, it is seen that only $\bar{\mathbf{L}}$ includes the total macroscopic deformation velocity by the overall gyration $\bar{\boldsymbol{\Omega}}$ and by the upscaled microscopic deformation gradient $(\mathbf{L}_m)_{\mathcal{B}}$ embedded by the continuum rotation $\mathbf{R}$, alternatively described by $\bar{\mathbf{R}}$ and $(\mathbf{U}_m)_{\mathcal{B}}$ through $(3.36)_3$.

As a result, choosing the balance of mechanical power (3.8) as the starting point is found inappropriate for the construction of the global balance of mechanical power of the REV $\mathcal{R}$. Instead of continuing with an integration of (3.8) over the domain of $\mathcal{R}$, it is straight forward to build the balance of mechanical power on the basis of the balance of linear momentum (2.109) and the micromorphic balance of angular momentum $(2.117)_2$ both directly at the body scale. Consequently, the relations for the balance of mechanical power of $\mathcal{B}$ are valid for the continuum body, which consists of an manifold of mesocopic REV . Furterhmore, proceeding from the assumption that local strains and strain rates are small at the REV level compared to the particle motion, allows the strain and strain rates to be linearised. Thus, the internal stress power $\rho_0\, w_i$ of an REV in $\mathcal{B}$ is given by the (2.149), allowing a split into standard, micropolar and micromorphic contributions.

3.3.2 Homogenisation formalism for REV stresses

In analogy to Section 3.2.2, the local averages of stress quantities can be derived by applying the formalism (3.9) - (3.13) to the REV $\mathcal{R}$, where the averaging domain V is taken as the volume $V_{\mathcal{R}}$ of $\mathcal{R}$. Following this, $(3.29)_1$ and $(3.29)_2$ result in

$$\begin{aligned} \langle \mathbf{T}_M \rangle &:= \frac{1}{V_{\mathcal{R}}} \int_{\partial\mathcal{R}} (\,\mathbf{t}_M \otimes \mathbf{x}_M\,)\,\mathrm{d}a\,, \\ \langle \mathbf{T} \rangle &:= \frac{1}{V_{\mathcal{R}}} \int_{\partial\mathcal{R}} (\,\mathbf{t} \otimes \mathbf{x}_M\,)\,\mathrm{d}a\,, \end{aligned} \tag{3.37}$$

such that the micromorphic stress difference reads

$$\langle \mathbf{T}_M - \mathbf{T} \rangle = \langle \mathbf{T}_M \rangle - \langle \mathbf{T} \rangle = \frac{1}{V_{\mathcal{R}}} \int_{\partial\mathcal{R}} (\,\mathbf{t}_M - \mathbf{t}\,) \otimes \mathbf{x}_M\,\mathrm{d}a\,. \tag{3.38}$$

Note that (3.38) could also have been found by use of (3.30). Proceeding analogously, with the local statement of the angular momentum balance yields

$$\langle \mathbf{M} + \bar{\mathbf{M}} \rangle = \int_{\mathcal{R}} \big([\, (\, \mathbf{x}_M \times \mathbf{t}\,) \otimes \mathbf{x}_M \,] + (\, \bar{\mathbf{m}} \otimes \mathbf{x}_M \,) \big)\, \mathrm{d}a\,. \tag{3.39}$$

Separation by reasons leads to the averaged stress moment $\langle \mathbf{M} \rangle$ and the averaged couple stress $\langle \bar{\mathbf{M}} \rangle$, such that

$$\langle \mathbf{M} \rangle := \frac{1}{V_{\mathcal{R}}} \int_{\partial \mathcal{R}} [\, (\, \mathbf{x}_M \times \mathbf{t}\,) \otimes \mathbf{x}_M \,]\, \mathrm{d}a = \frac{1}{V_{\mathcal{R}}} \int_{\partial \mathcal{R}} [\, \mathbf{x}_M \times (\, \mathbf{t} \otimes \mathbf{x}_M \,) \,]\, \mathrm{d}a \tag{3.40}$$

and

$$\langle \bar{\mathbf{M}} \rangle := \frac{1}{V_{\mathcal{R}}} \int_{\partial \mathcal{R}} (\, \bar{\mathbf{m}} \otimes \mathbf{x}_M \,)\, \mathrm{d}a\,, \tag{3.41}$$

respectively. The identification of an averaged measure related to the difference $\overset{3}{\mathbf{M}}{}^d_M - \overset{3}{\mathbf{M}}{}^d$ given in (3.30) is found on the basis of a dyadic multiplication of the local form of (3.30) with $\mathbf{x}_M$, followed by an integration over the domain of $\mathcal{R}$. Thus,

$$\mathbf{0} = \int_{\mathcal{R}} [\, \mathbf{x}_M \otimes \mathrm{div}_M\, (\, \overset{3}{\mathbf{M}}{}^d_M - \overset{3}{\mathbf{M}}{}^d \,) - (\, \underbrace{\mathbf{x}_M \otimes \mathbf{T}^T_M}_{= (\overset{3}{\mathbf{M}}{}^d_M)^{\overset{23}{T}}} - \underbrace{\mathbf{x}_M \otimes \mathbf{T}^T}_{= (\overset{3}{\mathbf{M}}{}^d)^{\overset{23}{T}}} \,) \,]\, \mathrm{d}v\,. \tag{3.42}$$

Furthermore, reformulation of this expression with the aid of the extended divergence theorem (A.26) finally yields the volume average $\langle \overset{3}{\tilde{\mathbf{M}}} \rangle$, representing twicely the symmetric part of $\overset{3}{\mathbf{M}}{}^d_M - \overset{3}{\mathbf{M}}{}^d$ with respect to the first and third basis systems. In particular, one obtains through comparison with (2.98)

$$\begin{aligned} \langle \overset{3}{\tilde{\mathbf{M}}} \rangle :&= \frac{1}{V_{\mathcal{R}}} \int_{\mathcal{R}} [\, (\, \overset{3}{\mathbf{M}}{}^d_M - \overset{3}{\mathbf{M}}{}^d \,)^{\overset{13}{T}} + (\, \overset{3}{\mathbf{M}}{}^d_M - \overset{3}{\mathbf{M}}{}^d \,) \,]\, \mathrm{d}v \\ &= \frac{1}{V_{\mathcal{R}}} \int_{\partial \mathcal{R}} \mathbf{x}_M \otimes (\, \mathbf{t}_M - \mathbf{t}\,) \otimes \mathbf{x}_M\, \mathrm{d}a\,, \end{aligned}$$

representing the third-order micromorphic stress moment average.

At this point, it should be noted that the local stress state of the extended body $\mathcal{B}$ is defined by the REV-based homogenised quantities $\langle \mathbf{T} \rangle$, $\langle \mathbf{M} \rangle$ and $\langle \bar{\mathbf{M}} \rangle$ as

$$\mathbf{T} := \langle \mathbf{T} \rangle\,, \quad \mathbf{M} := \langle \mathbf{M} \rangle\,, \quad \bar{\mathbf{M}} := \langle \bar{\mathbf{M}} \rangle\,, \tag{3.43}$$

representing the Cauchy stress, the stress moment and the couple stress. In case that $\bar{\mathbf{M}}$ vanishes, $\mathbf{T}$ is symmetric and $\mathcal{B}$ behaves like a Cauchy continuum, either as a result of $|\mathbf{x}_m| \to 0$ or as a result of vanishing eccentricities, such that $\bar{\mathbf{m}} = \mathbf{x}_m \times \mathbf{t}_m \to 0$. With $\bar{\mathbf{M}} \neq 0$, microdeformations are active, yielding non-symmetric Cauchy stresses, mainly proceeding from micropolar effects. In order to detect general micromorphic behaviour, one has to consider $\langle \mathbf{T}_M - \mathbf{T} \rangle$ and/or $\langle \overset{3}{\tilde{\mathbf{M}}} \rangle$ as indicators for the difference between micromorphic and Cauchy continua. Note that the notion micromorphic continuum includes

Table 3.2: *Definition of stress quantities at different scales*

Symbol	Denotation	Volume average with order $\mathcal{O}(\epsilon^n)$	
Single particle of size δ			
$\mathbf{T}_m$	microstress	$\langle \mathbf{T}_m \rangle$	$n=1$
$\mathbf{M}_m = \mathbf{x}_m \times \mathbf{T}_m$	microstress moment	$\langle \mathbf{M}_m \rangle$	$n=2$
$\mathbf{M}_m^d = \mathbf{x}_m \otimes \mathbf{t}_m$	second-order dyadic microstress moment		
$\overset{3}{\mathbf{M}}{}_m^d = \mathbf{x}_m \otimes \mathbf{T}_m$	third-order dyadic microstress moment		
REV scale of size d			
$\mathbf{T}_M := \langle \mathbf{T}_m \rangle$	particle stress average	$\langle \mathbf{T}_M \rangle$	$n=1$
$\mathbf{M}_M = \mathbf{x}_M \times \mathbf{T}_M$	stress moment average		
$\bar{\mathbf{M}}_M := \langle \mathbf{M}_m \rangle$	couple stress average		
$\overset{3}{\mathbf{M}}{}_M^d = \mathbf{x}_M \otimes \mathbf{T}_M$	third-order dyadic stress moment		
$\mathbf{T}$	Cauchy stress	$\langle \mathbf{T} \rangle$	$n=0$
$\mathbf{M} = \mathbf{x}_M \times \mathbf{T}$	Cauchy stress moment	$\langle \mathbf{M} \rangle$	$n=0$
$\bar{\mathbf{M}}$	couple stress	$\langle \bar{\mathbf{M}} \rangle$	$n=1$
$\overset{3}{\mathbf{M}}{}^d = \mathbf{x}_M \otimes \mathbf{T}$	third-order dyadic stress moment		

micropolar and microstrain continua as sub-classes, and that $\langle \mathbf{T}_M - \mathbf{T} \rangle$ is based on the first dyadic moment of $(\mathbf{t}_M - \mathbf{t})$, while $\langle \overset{3}{\tilde{\mathbf{M}}} \rangle$ is based on the second one. In order to summarise the introduced stresses and stress averages, Table 3.2 collects the stress definitions and denotations as well as the derived stress averages with their respective implicit order-dependence on the scale parameter $\epsilon = \delta/d$.

In addition to the above, the relation between the second- and third-order dyadic moments obtained from boundary terms of the REV in combination with their axial vectors and tensors and the corresponding couple terms become apparent in the framework of the exploitation of the balance of mechanical work of micromorphic-media REV. Introducing

$$\bar{\mathbf{M}}_M^d \;:=\; \langle \mathbf{x}_m \otimes \mathbf{t}_m \rangle_A := \frac{1}{A_{\mathcal{P}_{ex}^{(i)}}} \int_{\partial \mathcal{P}_{ex}^{(i)}} \mathbf{x}_m \otimes \mathbf{t}_m \, \mathrm{d}a \tag{3.44}$$

as the resultant dyadic moment at the particle centre of $\mathcal{P}^{(i)}$ stemming from REV-outside oriented external forces, the corresponding couple stress is recovered by

$$\bar{\mathbf{m}} \;=\; \overset{3}{\mathbf{E}}\, \bar{\mathbf{M}}_M^d \;=\; \frac{1}{A_{\mathcal{P}_{ex}^{(i)}}} \int_{\partial \mathcal{P}_{ex}^{(i)}} \overset{3}{\mathbf{E}}\, (\mathbf{x}_m \otimes \mathbf{t}_m) \, \mathrm{d}a \;=\; \frac{1}{A_{\mathcal{P}_{ex}^{(i)}}} \int_{\partial \mathcal{P}_{ex}^{(i)}} (\mathbf{x}_m \times \mathbf{t}_m) \, \mathrm{d}a \,. \tag{3.45}$$

This leads to the following relation between the couple stress $\bar{\mathbf{m}}$ and the axial vector $\overset{A}{\mathbf{m}}{}^{d}_{M}$ of the dyadic stress moment $\bar{\mathbf{M}}^{d}_{M}$:

$$\overset{A}{\mathbf{m}}{}^{d}_{M} \;=\; \operatorname{axl}\bar{\mathbf{M}}^{d}_{M} \;=\; -\tfrac{1}{2}\,\overset{3}{\mathbf{E}}\,\bar{\mathbf{M}}^{d}_{M} \quad\longrightarrow\quad \bar{\mathbf{m}} \;=\; -\,2\,\overset{A}{\mathbf{m}}{}^{d}_{M}\,. \tag{3.46}$$

Based on (3.44) and (3.45), the third-order dyadic moment corresponding to $\bar{\mathbf{M}}^{d}_{M}$ can be identified by use of

$$\begin{aligned}
&\bar{\mathbf{M}}^{d}_{M} = \overset{3}{\bar{\mathbf{M}}}{}^{d}_{M}\,\mathbf{n} \;=\; \frac{1}{A_{\mathcal{P}^{(i)}_{ex}}}\int_{\partial\mathcal{P}^{(i)}_{ex}} (\,\mathbf{x}_m \otimes \mathbf{T}_m\,)\,\mathbf{n}_m\,\mathrm{d}a\,,\\
&\text{where}\quad \overset{3}{\bar{\mathbf{M}}}{}^{d}_{M} \;:=\; \frac{1}{A_{\mathcal{P}^{(i)}_{ex}}}\int_{\partial\mathcal{P}^{(i)}_{ex}} (\,\mathbf{x}_m \otimes \mathbf{T}_m\,)\,\mathrm{d}a\\
&\text{and}\qquad \mathbf{n} \;:=\; \frac{1}{A_{\mathcal{P}^{(i)}_{ex}}}\int_{\partial\mathcal{P}^{(i)}_{ex}} \mathbf{n}_m\,\mathrm{d}a
\end{aligned} \tag{3.47}$$

has been assumed. As a result, one obtains the following relation between the couple-stress tensor $\bar{\mathbf{M}}$ and the third-order dyadic moment $\overset{3}{\bar{\mathbf{M}}}{}^{d}_{M}$:

$$\begin{aligned}
\bar{\mathbf{M}} \;&=\; (\overset{3}{\mathbf{E}}\,\overset{3}{\bar{\mathbf{M}}}{}^{d}_{M})^{\underline{2}} \;=\; \frac{1}{A_{\mathcal{P}^{(i)}_{ex}}}\int_{\partial\mathcal{P}^{(i)}_{ex}} \overset{3}{\mathbf{E}}\,(\,\mathbf{x}_m \otimes \mathbf{T}_m)\,\mathrm{d}a\\
&=\; \frac{1}{A_{\mathcal{P}^{(i)}_{ex}}}\int_{\partial\mathcal{P}^{(i)}_{ex}} (\,\mathbf{x}_m \times \mathbf{T}_m)\,\mathrm{d}a\,.
\end{aligned} \tag{3.48}$$

Given (3.48), one recognises the relation between the couple stress tensor $\bar{\mathbf{M}}$ and the axial tensor $\overset{a}{\bar{\mathbf{M}}}{}^{d}_{M}$ of the dyadic stress moment $\overset{3}{\bar{\mathbf{M}}}{}^{d}_{M}$ as

$$\overset{a}{\bar{\mathbf{M}}}{}^{d}_{M} \;=\; \operatorname{axl}\overset{3}{\bar{\mathbf{M}}}{}^{d}_{M} \;=\; -\,\tfrac{1}{2}(\overset{3}{\mathbf{E}}\,\overset{3}{\bar{\mathbf{M}}}{}^{d}_{M})^{\underline{2}} \quad\longrightarrow\quad \bar{\mathbf{M}} \;=\; -\,2\,\overset{a}{\bar{\mathbf{M}}}{}^{d}_{M}\,. \tag{3.49}$$

As the third-order dyadic moment $(3.47)_2$ directly relates to the dyadic moment $\overset{3}{\bar{\mathbf{M}}}{}^{d}$ of micromorphic continua, cf. (2.115), its average derivation is feasible on the basis of the tensorial angular momentum balance $(2.117)_2$. Applying this equation to the REV $\mathcal{R}$ instead of the body $\mathcal{B}$, an integration over the REV yields

$$0 \;=\; \int_{\partial\mathcal{R}} (\overset{3}{\bar{\mathbf{M}}}{}^{d}_{M})\,\mathbf{n}\,\mathrm{d}a \quad\rightarrow\quad 0 \;=\; \int_{\mathcal{R}} \operatorname{div}\overset{3}{\bar{\mathbf{M}}}{}^{d}_{M}\,\mathrm{d}v \quad\rightarrow\quad 0 \;=\; \operatorname{div}\overset{3}{\bar{\mathbf{M}}}{}^{d}_{M}\,, \tag{3.50}$$

where Hashin's MMM principle has been applied neglecting volume integrals compared with surface integrals. Dyadic multiplication of the above local statement by $\mathbf{x}_M$ and integration over the domain of the REV yields

$$\begin{aligned}
0 \;&=\; \int_{\mathcal{R}} (\,\mathbf{x}_M \otimes \operatorname{div}\overset{3}{\bar{\mathbf{M}}}{}^{d}_{M}\,)\,\mathrm{d}v \;=\; \int_{\mathcal{R}} \{\operatorname{div}(\mathbf{x}_M \otimes \overset{3}{\bar{\mathbf{M}}}{}^{d}_{M}) \;-\; [\,(\overset{3}{\bar{\mathbf{M}}}{}^{d}_{M})^{\overset{13}{T}}\,]^{\overset{23}{T}}\}\,\mathrm{d}v\\
\rightarrow\quad &\int_{\mathcal{R}} [\,(\overset{3}{\bar{\mathbf{M}}}{}^{d}_{M})^{\overset{13}{T}}\,]^{\overset{23}{T}}\,\mathrm{d}v = \int_{\partial\mathcal{R}} (\mathbf{x}_M \otimes \overset{3}{\bar{\mathbf{M}}}{}^{d}_{M})\,\mathbf{n}\,\mathrm{d}a \;=\; \int_{\partial\mathcal{R}} (\mathbf{x}_M \otimes \bar{\mathbf{M}}^{d}_{M})\,\mathrm{d}a\,,
\end{aligned} \tag{3.51}$$

by use of (A.26). As a result, the third-order dyadic stress moment average $\langle \overset{3}{\bar{\mathbf{M}}}{}^{d}_{M} \rangle$ at the REV scale can be identified by use (2.98), such that

$$\langle \overset{3}{\bar{\mathbf{M}}}{}^{d}_{M} \rangle = \frac{1}{V_{\mathcal{R}}} \int_{\partial\mathcal{R}} [\, (\mathbf{x}_M \otimes \bar{\mathbf{M}}^{d}_{M})^{\frac{23}{T}}]^{\frac{13}{T}} \, \mathrm{d}a \;=\; \frac{1}{V_{\mathcal{R}}} \int_{\partial\mathcal{R}} [\, (\bar{\mathbf{M}}^{d}_{M})^{T} \otimes \mathbf{x}_M \,] \, \mathrm{d}a \,. \tag{3.52}$$

3.3.3 Homogenisation of mechanical work of REV

The volume-specific micromorphic mechanical work or the micromorphic potential, respectively, can again be obtained by homogensation methods by use of Hill's basic homogenisation theorem (2.98) in cambination with Hashin's MMM principle [107]. The work locally defined by (2.155) in a geometrically linear setting at each centre of a material micoparticle is thereby obtained through homogenisation over a REV $\mathcal{R}$ as

$$W_i \;=\; \frac{1}{V_{\mathcal{R}}} \int_{\mathcal{R}} \int_{t_0}^{t} \rho_0 \, w_i \, \mathrm{d}\tilde{t} \, \mathrm{d}v \tag{3.53}$$

with the individual work portions $W_i^{(sf)}$, $W_i^{(mp)}$ and $W_i^{(ms)}$. In particular, the portion $W_i^{(sf)}$, which includes the quantities from the standard Cauchy-type formulation, reads

$$W_i^{(sf)} \;=\; \frac{1}{V_{\mathcal{R}}} \int_{\mathcal{R}} \tfrac{1}{2} \, \boldsymbol{\sigma}_{\mathrm{sym}} \cdot \boldsymbol{\varepsilon} \, \mathrm{d}v \;=\; \tfrac{1}{2} \, \langle \boldsymbol{\sigma} \cdot \boldsymbol{\varepsilon} \rangle \;=\; \tfrac{1}{2} \, \langle \boldsymbol{\sigma} \rangle \cdot \langle \boldsymbol{\varepsilon} \rangle, \tag{3.54}$$

where the symmetry of $\boldsymbol{\varepsilon}$ together with the Hill-Mandel condition [111] has been used. In (3.54), the following relations hold:

$$\begin{aligned} \langle \boldsymbol{\sigma} \rangle \;&\approx\; \langle \mathbf{T} \rangle \,, \\ \langle \boldsymbol{\varepsilon} \rangle \;&=\; \tfrac{1}{2} \, (\, \langle \mathrm{Grad}\, \mathbf{u}_{\mathcal{M}} \rangle \;+\; \langle \mathrm{Grad}^{\,T} \mathbf{u}_{\mathcal{M}} \rangle \,) \,, \end{aligned} \tag{3.55}$$

where $\langle \mathbf{T} \rangle$ is given by $(3.37)_2$ and $\langle \mathrm{Grad}\, \mathbf{u}_{\mathcal{M}} \rangle$ follows as

$$\langle \mathrm{Grad}\, \mathbf{u}_{\mathcal{M}} \rangle \;=\; \frac{1}{V_{\mathcal{R}}} \int_{\mathcal{R}} \mathrm{Grad}_{\mathcal{M}}\, \mathbf{u}_{\mathcal{M}} \, \mathrm{d}v \;=\; \frac{1}{V_{\mathcal{R}}} \int_{\partial\mathcal{R}} (\, \mathbf{u}_{\mathcal{M}} \otimes \mathbf{n} \,) \, \mathrm{d}a \,. \tag{3.56}$$

The second part of W_i belongs to the micropolar contribution of the extended formulation and is obtained from $(2.155)_3$ as

$$\begin{aligned} W_i^{(mp)} \;&=\; \frac{1}{V_{\mathcal{R}}} \int_{\mathcal{R}} \tfrac{1}{2} \, [\, \boldsymbol{\sigma}_{\mathrm{skw}} \cdot \overset{3}{\mathbf{E}}(\boldsymbol{\varphi}_m)_{\mathcal{B}} \;-\; 2 \, \overset{a}{\boldsymbol{\mu}}{}^{d} \cdot \overset{a}{\boldsymbol{\kappa}} \,] \, \mathrm{d}v \\ &=\; \tfrac{1}{2} [\, \langle \boldsymbol{\sigma} \rangle \cdot \langle \overset{3}{\mathbf{E}}(\boldsymbol{\varphi}_m)_{\mathcal{B}} \rangle \;-\; 2 \, \langle \, \overset{a}{\boldsymbol{\mu}}{}^{d} \rangle \cdot \langle \overset{a}{\boldsymbol{\kappa}} \rangle \,] \\ &=\; \tfrac{1}{2} [\, \langle \boldsymbol{\sigma} \rangle \cdot \langle \overset{3}{\mathbf{E}}(\boldsymbol{\varphi}_m)_{\mathcal{B}} \rangle \;+\; \langle \, \bar{\boldsymbol{\mu}} \rangle \cdot \langle \overset{a}{\bar{\boldsymbol{\kappa}}} \rangle \,] \,. \end{aligned} \tag{3.57}$$

Therein, the second line proceeds from the fact that $\overset{3}{\mathbf{E}}(\boldsymbol{\varphi}_m)_{\mathcal{B}}$ is skew-symmetric. As a result, only the skew-symmetric part of $\boldsymbol{\sigma}$ matters. Given (3.57), $\langle \boldsymbol{\sigma} \rangle$ is defined by $(3.55)_1$,

while

$$\begin{aligned}
\langle (\boldsymbol{\varphi}_m)_{\mathcal{B}} \rangle &= \frac{1}{V_{\mathcal{R}}} \int_{\mathcal{R}} (\boldsymbol{\varphi}_m)_{\mathcal{B}} \, \mathrm{d}v \,, \\
\langle \bar{\boldsymbol{\mu}} \rangle &\approx \langle \bar{\mathbf{M}} \rangle \,, \\
\langle \overset{a}{\bar{\boldsymbol{\kappa}}} \rangle &= \langle \mathrm{Grad}\, \bar{\boldsymbol{\varphi}} \rangle = \frac{1}{V_{\mathcal{R}}} \int_{\mathcal{R}} \mathrm{Grad}\, \bar{\boldsymbol{\varphi}} \, \mathrm{d}v = \frac{1}{V_{\mathcal{R}}} \int_{\partial \mathcal{R}} \bar{\boldsymbol{\varphi}} \otimes \mathbf{n} \, \mathrm{d}a
\end{aligned} \tag{3.58}$$

with $\langle \bar{\mathbf{M}} \rangle$ from (3.41). Note that, while obtaining the above results, $(\boldsymbol{\varphi}_m)_{\mathcal{B}}$ has been set to the microrotation $\boldsymbol{\varphi}_m$ of the individual particles, while $\bar{\boldsymbol{\varphi}}$ is equal to total particle rotation that, in a geometrical linear setting, is given by $\bar{\boldsymbol{\varphi}} = (\boldsymbol{\varphi}_m)_{\mathcal{B}} + \boldsymbol{\varphi}$.

The mechanical work W_i is completed by the microstrain portion $W_i^{(ms)}$ given by

$$\begin{aligned}
W_i^{(ms)} &= \frac{1}{V_{\mathcal{R}}} \int_{\mathcal{R}} \tfrac{1}{2} \left[\left(\boldsymbol{\sigma}_M - \boldsymbol{\sigma} \right) \cdot (\boldsymbol{\varepsilon}_m)_{\mathcal{B}} + \overset{3}{\bar{\boldsymbol{\mu}}}{}^d \cdot \mathrm{Grad}\, (\boldsymbol{\varepsilon}_m)_{\mathcal{B}} \right] \mathrm{d}v \\
&= \tfrac{1}{2} \left[\left(\langle \boldsymbol{\sigma}_M \rangle - \langle \boldsymbol{\sigma} \rangle \right) \cdot \langle (\boldsymbol{\varepsilon}_m)_{\mathcal{B}} \rangle + \langle \overset{3}{\bar{\boldsymbol{\mu}}}{}^d \rangle \cdot \langle \mathrm{Grad}\, (\boldsymbol{\varepsilon}_m)_{\mathcal{B}} \rangle \right]
\end{aligned} \tag{3.59}$$

where $(\boldsymbol{\sigma}_M)_{sym}$ has been set to $\boldsymbol{\sigma}_M$ as $(\boldsymbol{\varepsilon}_m)_{\mathcal{B}}$ is symmetric. Equivalently, $\overset{(12)}{\mathrm{sym}}\, \overset{3}{\bar{\boldsymbol{\mu}}}{}^d$ has been set to $\overset{3}{\bar{\boldsymbol{\mu}}}{}^d$ as $\mathrm{Grad}\, (\boldsymbol{\varepsilon}_m)_{\mathcal{B}}$ is symmetric in the first two basis systems. In (3.59), $\boldsymbol{\sigma}$ is given by $(3.55)_1$, while

$$\begin{aligned}
\langle \boldsymbol{\sigma}_M \rangle &\approx \langle \mathbf{T}_M \rangle \,, \\
\langle \overset{3}{\bar{\boldsymbol{\mu}}}{}^d \rangle &\approx \langle \overset{3}{\bar{\mathbf{M}}}{}^d_M \rangle \,, \\
\langle (\boldsymbol{\varepsilon}_m)_{\mathcal{B}} \rangle &= \frac{1}{V_{\mathcal{R}}} \int_{\mathcal{R}} \langle \boldsymbol{\varepsilon}_m \rangle \, \mathrm{d}v \,, \\
\langle \mathrm{Grad}\, (\boldsymbol{\varepsilon}_m)_{\mathcal{B}} \rangle &= \frac{1}{V_{\mathcal{R}}} \int_{\mathcal{R}} \mathrm{Grad}\, \langle \boldsymbol{\varepsilon}_m \rangle \, \mathrm{d}v = \frac{1}{V_{\mathcal{R}}} \int_{\partial \mathcal{R}} \left(\langle \boldsymbol{\varepsilon}_m \rangle \otimes \mathbf{n} \right) \mathrm{d}a \,.
\end{aligned} \tag{3.60}$$

Therein, (3.37) has been used for $(3.60)_1$, while $(3.60)_2$ can be considered with $(3.47)_2$ and $(3.60)_{3/4}$ follow with (3.18).

With the above considerations, the internal mechanical work W_i can be computed by homogenisation over local REV at any material point or microcontinuum and can be split in its Cauchy-continuum and its micromorphic parts, where the latter can furthermore be subdivided in a micropolar and a microstrain contribution.

3.4 Transition towards discrete ensembles

In reality, granular media do not consist of an unlimited number or an unspecified manifold of particles, but of a large but limited number of grains. As a result, the REV $\mathcal{R}$ embedded in the body $\mathcal{B}$ exhibits an ensemble of particles that is much smaller than $\mathcal{B}$. Consequently, the scale separation between $\mathcal{R}$ and $\mathcal{B}$ still holds and the continuously

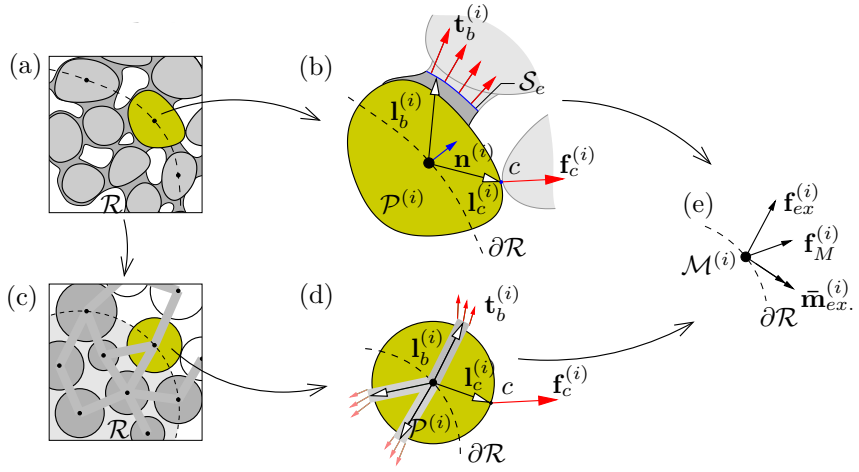

Figure 3.5: *(a) Physical picture of a grain-binder microstructure, (b) discrete representation of a particle $\mathcal{P}^{(i)}$ at $\partial\mathcal{R}$, (c) DE-representation of the microstructure with spherical particles and connecting beams, (d) spherical representation of a particle $\mathcal{P}^{(i)}$ at $\partial\mathcal{R}$, (e) reduced stress vectors at the particle centre $\mathcal{M}^{(i)}$.*

formulated averaged quantities, defined for the stresses in Section 3.3.2 and for the kinematic measures in Section 3.3.3 can be applied. Now, however, they can be transitioned towards a discrete formulation, which accounts for the finite number of particles in an REV, thereby substituting integral with summation operations.

With regard to the homogenisation formalism for REV stresses, the surface integral taken over $\partial\mathcal{R}$ of $\mathcal{R}$ converts to summing up the contact forces of a finite number of boundary particles $\mathcal{P}^{(i)}$ after they have been reduced to stress and couple-stress resultants at the individual particle centres, cf. Figure 3.5 (e). As in Ehlers *et al.* [64], this procedure allows for the application of particle-based simulation techniques, such as the DEM, and to the homogenisation formalism for stress quantities in $\mathcal{R}$.

In the present setting, an ensemble of deformable particles is considered by the assumption of rigid particles embedded in a deformable matrix or in binder material, respectively, such that particle rotations in the sense of micropolar material properties and microstrains of the binder material are easily combined towards micromorphic material properties. Note in passing that the overall homogenisation strategy also applies to microstructures that are totally or partly composed of deformable particles, such as rubber-based or gel-type ones, see e. g. Lu *et al.* [147]. However, as the primary interest in this work lies in the question of whether or not extended stresses and strains of micromorphic and micropolar nature are only active in failure regions of engineering materials triggered by localisation procedures, the subsequent numerical modelling concentrates on bonded and unbonded sand, where shear-banding is experimentally observable and therefore documented in the literature. In particular, the present concept is applied to the microstructural arrangement of bonded sand, as it is exemplarily found as moulding sand in metal-casting sand moulds, cf. for example Iden *et al.* [117], in order to study the evolution of the derived micromorphic stress quantities on the REV level. Additionally, localisation in unbonded sand, see for example the experimental results in Andò *et al.* [11], is modelled enabling a comparison of the

obtained micromorphic characteristics with the established micropolar homogenisation results given in Ehlers *et al.* [64] or Scholz [187].

3.4.1 Discrete representation of stress averages

The derived stress averaging formalisms, which are continuously formulated with respect to a manifold of homogeneously deformable particles forming an REV, need to be linked to the idealised grain-binder microstructure, represented by a discrete number of rigid spherical particles and deformable beam elements connecting the centres of neighbouring particles, thus representing a micropolar or a micromorphic setting, cf. Figure 3.5 (a) and (c). In such a scenario, the contact stresses acting on a single particle $\mathcal{P}^{(i)}$ stem from two different contact possibilities. On the one hand, a particle $\mathcal{P}^{(i)}$ can directly interact with a number of $N^{(i)}$ neighbouring particles (micropolar setting). In this case, the corresponding contact stress $\mathbf{t}_m$ can be identified as a single force $\mathbf{f}_c^{(i)}$ at the contact point c, while $\mathbf{x}_m$ at the contact point is the so-called branch vector $\mathbf{l}_c^{(i)}$ yielding $|\mathbf{l}_c^{(i)}| = \text{constant}$. On the other hand, $\mathcal{P}^{(i)}$ is in contact with neighbouring particles via $M^{(i)}$ deformable binder bridges at contact surfaces $\mathcal{S}_c$ with corresponding stress vectors $\mathbf{t}_b^{(i)} = \mathbf{T}_b^{(i)}\mathbf{n}_b^{(i)}$ and branch vectors $\mathbf{l}_b^{(i)}$ that are not constant over $\mathcal{S}_c$ as a result of the microdeformation (micromorphic setting). Note that the contact surfaces $\mathcal{S}_c$ are introduced by a normal cut with normal $\mathbf{n}_b^{(i)}$ through the binder material between two connected particles $\mathcal{P}^{(i)}$ and $\mathcal{P}^{(j)}$ at the middle of the binder length. As a result, $|\mathbf{l}_b^{(i)}|$ varies through the binder deformation or through the distance between the particle centres, respectively, thereby including the microdeformational character into the modelling approach.

Following this, a transition from a continuous formulation towards a discrete representation of the REV-based averaging quantities $\langle\mathbf{T}\rangle$, $\langle\mathbf{M}\rangle$ and $\langle\bar{\mathbf{M}}\rangle$ defined in (3.37), (3.40) and (3.41) is required. These terms are obtained by use of the discrete counterparts of $\mathbf{t}$ and $\bar{\mathbf{m}}$ of the volume integrals (3.24) and a subsequent consideration of the discrete form of the above averages. Thus, a reduction at the particle centre of the external contact forces acting at the outward-oriented parts of $\partial\mathcal{P}_{ex}^{(i)}$ of $\partial\mathcal{P}^{(i)}$ of the boundary particles yields, cf. Figure 3.5:

$$\begin{aligned} \mathbf{t}^{(i)} \;=\; \int_{\partial\mathcal{P}_{ex}^{(i)}} \mathbf{t}_m \,\mathrm{d}a \;=\; \sum_{c=1}^{N_{ex}^{(i)}} \mathbf{f}_c^{(i)} \;+\; \sum_{b=1}^{M_{ex}^{(i)}} \mathbf{f}_b^{(i)} \;=:\; \mathbf{f}_{ex}^{(i)}\,, \\ \text{where} \quad \mathbf{f}_b^{(i)} \;=\; \int_{\mathcal{S}_c} \mathbf{t}_b^{(i)} \,\mathrm{d}a\,, \end{aligned} \tag{3.61}$$

and

$$\begin{aligned} \bar{\mathbf{m}}^{(i)} \;=\; \int_{\partial\mathcal{P}_{ex}^{(i)}} \mathbf{x}_m \,\times\, \mathbf{t}_m \,\mathrm{d}a \;=\; \sum_{c=1}^{N_{ex}^{(i)}} (\,\mathbf{l}_c^{(i)} \,\times\, \mathbf{f}_c^{(i)}\,) \;+\; \sum_{b=1}^{M_{ex}^{(i)}} \mathbf{m}_b^{(i)} \;=:\; \bar{\mathbf{m}}_{ex}^{(i)}\,, \\ \text{where} \quad \mathbf{m}_b^{(i)} \;=\; \int_{\mathcal{S}_c} (\,\mathbf{l}_b^{(i)} \,\times\, \mathbf{t}_b^{(i)}\,) \,\mathrm{d}a\,. \end{aligned} \tag{3.62}$$

Table 3.3: *Averaged REV stress quantities from discrete contact interactions.*

Cauchy stress	$\langle \mathbf{T} \rangle = \frac{1}{V_{\mathcal{R}}} \sum_{i=1}^{B} (\mathbf{f}_{ex}^{(i)} \otimes \mathbf{x}_M^{(i)})$
Stress moment (torque)	$\langle \mathbf{M} \rangle = \frac{1}{V_{\mathcal{R}}} \sum_{i=1}^{B} [\mathbf{x}_M^{(i)} \times (\mathbf{f}_{ex}^{(i)} \otimes \mathbf{x}_M^{(i)})]$
Micropolar couple stress	$\langle \bar{\mathbf{M}} \rangle = \frac{1}{V_{\mathcal{R}}} \sum_{i=1}^{B} (\bar{\mathbf{m}}_{ex}^{(i)} \otimes \mathbf{x}_M^{(i)})$
Micromorphic stress difference	$\langle \mathbf{T}_M - \mathbf{T} \rangle = \frac{1}{V_{\mathcal{R}}} \sum_{i=1}^{B} [(\mathbf{f}_M^{(i)} - \mathbf{f}_{ex}^{(i)}) \otimes \mathbf{x}_M^{(i)}]$
Micromorphic dyadic stress moment	$\langle \overset{3}{\tilde{\mathbf{M}}} \rangle = \frac{1}{V_{\mathcal{R}}} \sum_{i=1}^{B} [\mathbf{x}_M^{(i)} \otimes (\mathbf{f}_M^{(i)} - \mathbf{f}_{ex}^{(i)}) \otimes \mathbf{x}_M^{(i)}]$

In these equations, $N_{ex}^{(i)}$ and $M_{ex}^{(i)}$ are the numbers of outward-oriented particle-to-particle contacts and bond contacts, respectively.

Furthermore, for the construction of the micromorphic indicators $\langle \mathbf{T}_M - \mathbf{T} \rangle$ and $\langle \overset{3}{\tilde{\mathbf{M}}} \rangle$, the discrete form of $\mathbf{T}_M = \langle \mathbf{T}_m \rangle$ is needed and can be obtained on the basis of (3.13) and $(3.19)_1$, viz.:

$$\begin{aligned} \mathbf{T}_M^{(i)} = \langle \mathbf{T}_m^{(i)} \rangle &= \frac{1}{V_{\mathcal{P}^{(i)}}} \int_{\partial \mathcal{P}^{(i)}} \mathbf{t}_m \otimes \mathbf{x}_m \, \mathrm{d}a \\ &= \frac{1}{V_{\mathcal{P}^{(i)}}} [\sum_{c=1}^{N^{(i)}} (\mathbf{f}_c^{(i)} \otimes \mathbf{l}_c^{(i)}) + \sum_{b=1}^{M^{(i)}} (\int_{\mathcal{S}_c} \mathbf{t}_b^{(i)} \otimes \mathbf{l}_b^{(i)} \, \mathrm{d}a)] \, . \end{aligned} \tag{3.63}$$

Given (3.63), one obtains the discrete force vector $\mathbf{f}_M^{(i)}$ that collects all forces applied to $\mathcal{P}^{(i)}$ as

$$\mathbf{f}_M^{(i)} = \mathbf{T}_M^{(i)} \, \mathbf{n}^{(i)} \, , \tag{3.64}$$

where $\mathbf{n}^{(i)}$ is the outward-oriented surface normal at $\partial \mathcal{R}$ at $\mathbf{x}_M^{(i)}$, cf. Figure 3.5 (b). Given the above discrete terms, the averages $\langle \mathbf{T} \rangle$, $\langle \mathbf{M} \rangle$ and $\langle \bar{\mathbf{M}} \rangle$ as well as the micromorphic indicators $\langle \mathbf{T}_M - \mathbf{T} \rangle$ and $\langle \overset{3}{\tilde{\mathbf{M}}} \rangle$ can easily be computed, compare Table 3.3.

The discrete stress homogenisation formalisms are finally completed with the dyadic boundary-stress moment

$$\bar{\mathbf{M}}_M^{d\,(i)} = \frac{1}{A_{\mathcal{P}_{ex}^{(i)}}} \int_{\partial \mathcal{P}_{ex}^{(i)}} (\mathbf{x}_m \otimes \mathbf{t}_m) \, \mathrm{d}a = \sum_{c=1}^{N_{ex}^{(i)}} (\mathbf{l}_c^{(i)} \otimes \mathbf{f}_c^{(i)}) + \sum_{b=1}^{M_{ex}^{(i)}} [\int_{\mathcal{S}_c} (\mathbf{l}_b^{(i)} \otimes \mathbf{t}_b^{(i)})] \, . \tag{3.65}$$

3.4.2 Discrete representation of deformation averages

Three contributions from the particle-based modelling idealisation of the grain-binder microstructure are of importance for the transition of the averaging formalisms concerning the kinematic measures: The allowed binder deformation between interacting particles, the particle rotation, which is a combination of a continuum-type rigid-body rotation and the additional free rotation, when two interacting particles rotate relative to each other and, finally, the translational displacement of the individual particles, respectively of their mass centres. These particle- and binder specific deformations enter the averaged micromorphic kinematic deformation measures either as a direct average or as the average of their respective spatial gradient.

In particular, the micromorphic strain average $\langle\bar{\boldsymbol{\varepsilon}}\rangle$ is composed of contributions from the averaged gradient $\langle \mathrm{Grad}_{\mathcal{M}}\,\mathbf{u}_{\mathcal{M}}\rangle$, the averaged total rotation $\langle\bar{\boldsymbol{\varphi}}\rangle$ via $\overset{3}{\mathbf{E}}\langle\bar{\boldsymbol{\varphi}}\rangle$ and the microstrain average $\langle(\boldsymbol{\varepsilon}_m)_{\mathcal{B}}\rangle$. Starting with the last, one recognises that, independently of the constitutive description applied to account for the deformable binder, a local displacement vector $\mathbf{u}_b^{(i)}$ can be identified, that accounts for the variation of $|\mathbf{l}_b^{(i)}|$ during deformation. Collecting all attached binders at a single particle $\mathcal{P}^{(i)}$ and recalling the definition of their contact surfaces $\mathcal{S}_c$ allows to identify a discretised formulation of the averaged particle strain $\langle\boldsymbol{\varepsilon}_m^{(i)}\rangle$, cf. (3.18), as

$$\begin{aligned}\langle\boldsymbol{\varepsilon}_m^{(i)}\rangle \;&=\; \frac{1}{V_{\mathcal{P}^{(i)}}}\int_{\partial\mathcal{P}^{(i)}}\tfrac{1}{2}\left[\,(\,\mathbf{u}_m\otimes\mathbf{n}\,)+(\mathbf{n}\otimes\mathbf{u}_m\,)\,\right]\mathrm{d}a\\ &=\; \frac{1}{V_{\mathcal{P}^{(i)}}}\sum_{b=1}^{M^{(i)}}\left[\,\tfrac{1}{2}\left(\,(\int_{\mathcal{S}_c}\mathbf{u}_b^{(i)}\,\mathrm{d}a\,)\otimes\mathbf{n}+\mathbf{n}\otimes(\int_{\mathcal{S}_c}\mathbf{u}_b^{(i)}\,\mathrm{d}a\,)\right)\right].\end{aligned}\tag{3.66}$$

Note that the resulting quantity when calculating $\int_{\mathcal{S}_c}\mathbf{u}_b^{(i)}\,\mathrm{d}a$ isolates the stretching contribution of the binder, when, for example, a linear elastic beam formulation is later chosen within the DE-modelling approach. This is consistent, as potential free microrotations in the sense of resulting rotations of the beam surface at $\mathcal{S}_c$ should not be included into the averaged particle deformation. By use of (3.66), the discrete form of the volumetrically averaged REV microstrain $\langle(\boldsymbol{\varepsilon}_m)_{\mathcal{B}}\rangle$ follows according to $(3.60)_3$ as

$$\langle(\boldsymbol{\varepsilon}_m)_{\mathcal{B}}\rangle \;=\; \frac{1}{V_{\mathcal{R}}}\int_{\mathcal{R}}\langle\boldsymbol{\varepsilon}_m\rangle\,\mathrm{d}v \;=\; \frac{1}{V_{\mathcal{R}}}\sum_{i=1}^{A}V_{\mathcal{P}_{\mathcal{R}}^{(i)}}\,\langle\boldsymbol{\varepsilon}_m^{(i)}\rangle\,,\tag{3.67}$$

where $V_{\mathcal{P}_{\mathcal{R}}^{(i)}}$ is the portion of the volume of the particle $\mathcal{P}^{(i)}$ inside the REV $\mathcal{R}$ and A refers to the total number of particles forming the REV. Given $(3.60)_4$, the average $\langle\mathrm{Grad}\,(\boldsymbol{\varepsilon}_m)_{\mathcal{B}}\rangle$ consequently follows as

$$\langle\mathrm{Grad}\,(\boldsymbol{\varepsilon}_m)_{\mathcal{B}}\rangle \;=\; \frac{1}{V_{\mathcal{R}}}\int_{\mathcal{R}}(\,\langle\boldsymbol{\varepsilon}_m\rangle\otimes\mathbf{n}\,)\,\mathrm{d}v \;=\; \frac{1}{V_{\mathcal{R}}}\sum_{i=1}^{B}A_{\mathcal{P}_{\mathcal{R}}^{(i)}}\,(\,\langle\boldsymbol{\varepsilon}_m^{(i)}\rangle\otimes\mathbf{n}^{(i)}\,)\,,\tag{3.68}$$

where $A_{\mathcal{P}_{\mathcal{R}}^{(i)}}$ is the surface fraction of $\partial\mathcal{R}$ taken up by the boundary particle $\mathcal{P}^{(i)}$ with the outword-oriented unified normal vector $\mathbf{n}^{(i)}$. Next, the averaged gradient $\langle\mathrm{Grad}_{\mathcal{M}}\,\mathbf{u}_{\mathcal{M}}\rangle$,

cf. $(3.55)_2$, follows by a summation over the discrete displacement vectors $\mathbf{u}_{\mathcal{M}}^{(i)}$ of the REV boundary particles leading to

$$\langle \mathrm{Grad}_{\mathcal{M}}\, \mathbf{u}_{\mathcal{M}} \rangle \;=\; \frac{1}{V_{\mathcal{R}}} \int_{\mathcal{R}} (\, \mathbf{u}_{\mathcal{M}} \otimes \mathbf{n}\,)\, \mathrm{d}v \;=\; \frac{1}{V_{\mathcal{R}}} \sum_{i=1}^{B} A_{\mathcal{P}_{\mathcal{R}}^{(i)}}\, (\, \mathbf{u}_{\mathcal{M}}^{(i)} \otimes \mathbf{n}^{(i)}\,)\,, \tag{3.69}$$

. The volume average $\langle (\boldsymbol{\varphi}_m)_{\mathcal{B}} \rangle$ follows for a discrete setting as

$$\langle (\boldsymbol{\varphi}_m)_{\mathcal{B}} \rangle \;=\; \frac{1}{V_{\mathcal{R}}} \int_{\mathcal{R}} (\boldsymbol{\varphi}_m)_{\mathcal{B}}\, \mathrm{d}v \;=\; \frac{1}{V_{\mathcal{R}}} \sum_{i=1}^{A} V_{\mathcal{P}_{\mathcal{R}}^{(i)}}\, \boldsymbol{\varphi}_m^{(i)}\,, \tag{3.70}$$

with $\boldsymbol{\varphi}_m^{(i)}$ as the micro-rotation of the particle $\mathcal{P}^{(i)}$. The averaged micromorphic strain $\langle \bar{\boldsymbol{\varepsilon}} \rangle$ can thus be computed according to (2.136). The averaged second-order curvature tensor $\langle \overset{a}{\bar{\boldsymbol{\kappa}}} \rangle$ for an REV with a discrete number of enclosed particles follows finally, in analogy to the computation of $\langle \mathrm{Grad}_{\mathcal{M}} \mathbf{u}_{\mathcal{M}} \rangle$, as

$$\langle \overset{a}{\bar{\boldsymbol{\kappa}}} \rangle \;=\; \langle \mathrm{Grad}_{M}\, \bar{\boldsymbol{\varphi}} \rangle \;=\; \frac{1}{V_{\mathcal{R}}} \int_{\mathcal{R}} (\, \bar{\boldsymbol{\varphi}} \otimes \mathbf{n}\,)\, \mathrm{d}v \;=\; \frac{1}{V_{\mathcal{R}}} \sum_{i=1}^{B} A_{\mathcal{P}_{\mathcal{R}}^{(i)}}\, (\, \bar{\boldsymbol{\varphi}}^{(i)} \otimes \mathbf{n}^{(i)}\,)\,, \tag{3.71}$$

with $\bar{\boldsymbol{\varphi}}^{(i)}$ as the total particle rotation.

Chapter 4:
Particle model

This chapter is concerned with the DE model that is used to model localisation phenomena in bonded and unbonded granular materials. While the setting combining rigid particles with deformable bonds is suited to detect micromorphic effects after homogenisation, ensembles of unbonded rigid grains are used to treat the encompassed micropolar homogenisation scheme. In the following, the basic fundamentals of the DEM are reviewed, before the applied constitutive material formulations for the contact laws are outlined.

4.1 Fundamentals of the Discrete-Element Method

4.1.1 Discretisation method or direct numerical simulation

In principle, the DEM can be seen as one of the first so-called meshfree particle methods, that circumvent the drawback of the predefined fixed nodal or element wise connectivity of classical mesh-based numerical solution strategies, such as the FEM. In this context, a particle is seen as a discretisation entity, which is not spatially fixed. However, it is still used to solve for the primary variables of the resulting set of partial differential equations that arise, for example, from the continuum-mechanical description of deformable solids or fluid flow. Then, a particle is not related to the physical particle present in the microstructure of the considered material, but is rather seen as being representative in the sense of a homogenised modelling approach. Other meshfree particle methods, such as the so-called smoothed particle hydrodynamics approach have become important and innovative approaches in this regard, see, for example, Liu & Liu [145] or Monaghan [159]. In contrast to this view as a discretisation method, the DEM can also be used as a so-called Direct Numerical Simulation (DNS) tool, where the focus lies on the precise modelling of the microstructure at hand and the discrete element is a direct counterpart to the physical particle. In the present thesis, the latter view is adopted, although many simplifications, for example concerning the actual particle geometry or the number of total particles within a numerical sample, are made.

4.1.2 Balance relations for Discrete Elements

In the framework of the DEM, grains are generally regarded as rigid discrete elements that dynamically move and interact. The starting point in order to describe the state of a single rigid particle, is often the kinetics and kinematics of a material point, which are then extended towards rigid bodies with a distinct volume. The state of the rigid element is then accounted for by the introduction of axiomatic balance equations. However, with the concepts of standard continuum mechanics at hand, it is more convenient to regard the

case of a rigid particle as a the special case of a continuum with negligible deformation, respectively with a very high stiffness. For a detailed derivation of these balance laws starting with the balances of deformable continua, followed by a transition towards their rigid-body counterparts, compare Ehlers *et al.* [64]. The assumption of rigidity can be applied starting with the balance relation for linear and angular momentum of a single Cauchy-type particle as summarised in Table 3.1. The thereby obtained relations are frequently denoted Newton's equations of rigid body translation, referring to the linear momentum balance, and Euler's equation of rotational motion, representing the axiomatic part of the balance of angular momentum with respect to the particle's mass centre $\mathcal{M}^{(i)}$ at position $\mathbf{x}^{(i)}_{\mathcal{M}}$, cf. Jing & Stephansson [127]. With the pre-computed particle's mass $m^{(i)}$ and the mass-moment-of-inertia tensor $\boldsymbol{\Theta}^{(i)}_{\mathcal{M}}$, formulated with respect $\mathcal{M}^{(i)}$, the equations of state (dynamic balance relations) for each particle $\mathcal{P}^{(i)}$ in a many particle system read

$$\begin{aligned} m^{(i)}\,\dot{\mathbf{v}}^{(i)}_{\mathcal{M}} &= \mathbf{f}^{(i)} \\ \text{and} \quad \boldsymbol{\Theta}^{(i)}_{\mathcal{M}}\,\dot{\boldsymbol{\omega}}^{(i)} + \boldsymbol{\omega}^{(i)} \times (\,\boldsymbol{\Theta}^{(i)}_{\mathcal{M}}\,\boldsymbol{\omega}^{(i)}\,) &= \mathbf{m}^{(i)}_{\mathcal{M}}\,, \end{aligned} \tag{4.1}$$

where $\mathbf{v}^{(i)}_{\mathcal{M}} := \dot{\mathbf{x}}^{(i)}_{\mathcal{M}}$ is the particle's translational velocity at $\mathcal{M}^{(i)}$ and $\boldsymbol{\omega}^{(i)} = \dot{\boldsymbol{\varphi}}^{(i)}$ is the particle's angular velocity. Furthermore, recall that the transition from a particle $\mathcal{P}$ which is continuously loaded by stresses $\mathbf{t}_m$ at respective parts of its boundary $\partial\mathcal{P}$ towards a particle in a discrete ensemble, given in Section 3.4, can also be applied here. Thereby, the action on a particle $\mathcal{P}^{(i)}$ are again summarised in a resulting force $\mathbf{f}^{(i)}$ and a resulting moment $\mathbf{m}^{(i)}_{\mathcal{M}}$ with respect to $\mathcal{M}^{(i)}$. These quantities also include possible long range, volume-specific force and torque contributions, such as gravitation or magnetisation effects, as well as external forces and torques induced by application-driven definitions of the respective IBVP. Based on the envisaged material behaviour, different interactions can be accounted for. The present work, for example, makes use of force interactions at contact points, torque interactions in order to account for particle shape as well as a deformable bond-element formulation between interacting particles. A thorough discussion of the interaction laws is given in Section 4.2.

In a DE-modelling approach, the set of equations (4.1) are solved in a coupled manner with respect to the acceleration terms and a numerical time integration scheme is applied to determine the paticles's state, which is given by its position, its translational velocity at $\mathcal{M}^{(i)}$, its rotational orientation and its rotational velocity. The procedure is performed for each rigid particle of an IBVP. Note that the rotational motion representation can easily be solved for the angular acceleration, when the co-rotating frame is chosen in line with the principle directions of the mass-moment-of-inertia tensor of the considered particle. As the discrete elements are generally assumed rigid, the values of $\boldsymbol{\Theta}^{(i)}_{\mathcal{M}}$ are again constant in this frame and the principle directions are pre-computed following standard procedure, cf. e. g. Ehlers [59].

It should finally be noted that not all representations of rotations are suitable for a numerical treatment of finite rigid body rotations in three dimensions. For example, the representation of a rotation using three Euler or Cardano angles leads to a spurious behaviour due to the singularity of the tensor-valued operator relating the angular velocity to the orientation, when the first Euler angle becomes zero, cf. Evans [73]. This drawback

is overcome by applying a four-parameter representation of the rotation, e. g. the Euler-Rodrigues form given in (2.7). In the context of the DEM (and other multibody dynamics applications such as computer animations) the representation of the Euler-Rodrigues form as a so-called unit quaternion has become a common way to treat rotations in an efficient way, compare, for example, Eberly [54] or Evans & Murad [74]. This approach is therefore implemented to describe rotations in the simulation package Pasimodo, cf. Fleissner [78] for details. For the sake of completeness, Appendix C gives a short introduction to quaternions, their application to rotations and their relation to the rotation representation using a second-order rotation tensor $\mathbf{R}$, as it is used throughout this monograph.

4.1.3 Numerical time integration for particle systems

The characteristics of a system of interacting particles with dynamically changing contacts calls for specific numerical time integration schemes. Although it is possible to rewrite the particle system's governing equations for discrete time intervals analogously to a dynamic formulation of a deformable continuum in matrix form, cf. Jing & Stephansson [127], classical implicit integration schemes known from the FEM are generally not suitable for particle systems, as the contact distribution is non-smooth and dissipative. Most particle simulation codes therefore apply explicit time integration schemes, such as the Verlet integrator and its derivatives, denoted after the first application of such an integration for a molecular dynamics problem presented by Verlet [207]. For further applicable methods, the interested reader is referred, for example, to the comparison of different integration schemes in the context of the DEM given in Johnson *et al.* [128] and Rougier *et al.* [181], the latter with special emphasis on the integration of the rotational motion using quaternions. A drawback of strictly explicit integration schemes is their conditional stability, which complicates the choice of suitable time steps that simultaneously ensure a detection of all interactions and a stable integration. As a consequence, Pasimodo employs a semi-implicit integration scheme, denoted the Generalized α - Method, proposed in Chung & Hulbert [35], that ensures unconditional stability and allows for comparatively large time steps due to its implicit approach. As the original method stems from a FEM-based problem setting with displacement DOF only, Fleissner *et al.* [80] extend the method to integrate the rotational motion using a quaternion representation based on the algorithm given in Omelyan [175]. Throughout all following DE simulations, the implemented time integration schemes as well as the automated time step size control in Pasimodo are used with standard values suggested by the developers. Therefore, a detailed description of the integration scheme and its performance is omitted here. Details on these subjects can be found in Fleissner [78], Fleissner & Eberhard [79] or Fleissner *et al.* [80] and citations therein.

4.2 Constitutive contact formulations

4.2.1 Fundamentals

The physical processes active at the collision zone between two particles are very complex. Depending on the constituting materials and the surface quality, local effects occur that generally result in an energy conversion, such that the overall contact is no longer purely elastic. In case of a sphere-sphere collision, for example, the vibration of the spheres caused by the contact, local plastification of fracture at the contact zone as well as energy dissipation due to possible inert viscosity of the materials lead to a relative energy loss, cf. Kuwabara & Kono [135]. In contact dynamics, these effects are generally assign to the material-dependent restitution coefficient allowing for the distinction between elastic, plastic and intermediate contact scenarios.

In a DE approach, one generally aims at capturing only those processes that are assumed to be of major importance for the envisaged behaviour of the overall granulate. Therefore, one firstly assumes that a locally confined deformation takes place in the interaction zones of the particles, while its remaining larger part is still considered as rigid and hence the equations of state (4.1) are still valid. It is important to note that the DEM generally assumes a sufficiently small time step, such that disturbances induced at one particle only propagate to the nearest neighbours (Cundall & Strack [42]). Generally, the constitutive material description in the DEM is not formulated as a relation between the internal stresses with the conjugated deformation of each material point of $\mathcal{P}^{(i)}$, as it is classically done in continuum mechanics. Instead the relevant processes in the constitutive formulation of contact-interaction laws are based on an allowed indentation $\delta^{(ij)}$ (and its rate $\dot{\delta}^{(ij)}$) between two interacting particles $\mathcal{P}^{(i)}$ and $\mathcal{P}^{(j)}$. In principle, $\delta^{(ij)}$ serves as a placeholder for the locally deformed contact zones. This approach is often termed *soft contact* approach as the interpenetration of particles is allowed and penalised. A *hard contact* approach can, for example, be found in *discontinuous deformation analysis* (Shi [193]), strictly enforcing the particle's rigidity and non-penetration. For a wider classification, this approach falls into the group of so-called *discrete contact dynamics models*, where the collision is assumed to be instantaneous and one studies the velocities before and after the collision. Contrary to these methods, the collision approach in the DEM continuously tracks the contact as well as the resulting forces and torques over a finite contact time and is therefore also referred to as a *continuous contact dynamics* model. The character of the contact interaction and therefore the material behaviour is then assigned to the constitutive contact formulations and, more precisely, to the accompanying material or modelling parameters. These coefficients, however, are again in need of experimental determination or other means of identification and calibration. For further insight into collision and contact dynamics with discrete and continuous contact dynamics see Gilardi & Sharf [95], who give an overview and a review of existing strategies. The main advantage of continuously tracking contacts and contact forces is the possibility to have multiple persisting contacts between particles, where then, the ensemble of particles can sustain external loading by storing deformational energy, for example, to address the simplest case, through the combination of indentation and resulting contact force at the local contact points.

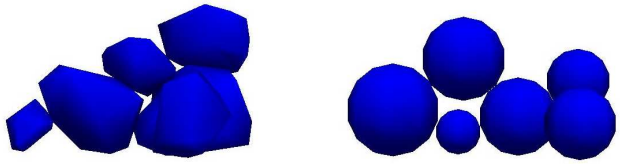

Figure 4.1: *Small piles of six non-convex polyhedrons and six spheres in contact*[1].

4.2.2 Particle shape simplification and contact representation

In reality two colliding particles can have arbitrary shapes with rough or smooth surfaces leading not to a single contact point, but to several contacting points or areas on the surface of each particle, cf. Figure 4.1. The shape of sand grains, which is one of the most frequently investigated granular materials and at the centre of interest of this monograph, can vary in a wide range from angular to spherical, compare Alshibli & Alsaleh [5]. This can even be the case for the same sand, when it is investigated before and after intensive loading that has been accompanied by rounding of the sand grains through inter-particle friction or grain fragmentation (Ma *et al.* [152], Tavares & King [200]). The present work only uses spherical particles for the complete simulation of experimental set-ups. Therefore, the constitutive formulations at the contact point of two spherical particles need to account for the obvious idealisation of the grain shape and the actual stress distribution of colliding grains. These can be found in significantly different forms. Direct contacts of loose granular assemblies can exhibit point-like stress peaks at various contact points, nearly constant stress distributions over flat contact surfaces or Hertzian-type stress distributions for interacting spheres. Inter-particle friction is also likely to occur. If the granular material is embedded in a matrix or if thin films of bounding material enclose and connect individual particles, additional forces and torques might be transmitted, even if the particle surfaces are not in direct contact to each other.

If complex particle-shape representations are chosen, a main task in the DE simulation strategy is the contact detection, meaning the assessment whether particles are in contact and how the geometric details of the individual contacts can be captured accurately during a time step (Hogue [113], Williams & O'Connor [219]). For the case of spherical particles, the contact detection is rather simple, as the (possible) indentation $\delta^{(ij)}$ between two particles can be determined using the positions $\mathbf{x}_{\mathcal{M}}^{(i/j)}$ of the particle's mass centres and their respective radii $r^{(i/j)}$. Specifically, one obtains

$$\delta^{(ij)} = (r^{(i)} + r^{(j)}) - |\mathbf{x}_{\mathcal{M}}^{(i)} - \mathbf{x}_{\mathcal{M}}^{(j)}|\,, \tag{4.2}$$

where the direct contact formulations, i. e. a repulsive contact force $\mathbf{f}_c^{(i)} = -\mathbf{f}_c^{(j)}$ and, if intended a resisting torque $\mathbf{m}_c^{(i)} = -\mathbf{m}_c^{(j)}$, are calculated only for $\delta^{(ij)} > 0$. Thereby, the subscript c refers to the respective contact point at position $\mathbf{x}_c^{(ij)}$, which due to the

[1]The displayed non-convex polyhedrons represent simplified grain geometries of Hostun Sand. The author is grateful to Eward Andò and Cino Viggiani, who willingly supplied imaging data of individual sand grains in the expectation of real time simulations of their experiments, e. g. given in Andò *et al.* [11] or Desrues & Andò [46], an expectation that could unfortunately not be met, but was recently achieved by Kawamoto *et al.* [132].

indentation $\delta^{(ij)}$ is not located at the exact surface of the particles, cf. Figure 4.2. The contact during a time increment is characterised by several geometric quantities. At first, the contact normal $\mathbf{n}_c^{(i)}$ with

$$\mathbf{n}_c^{(i)} = -\,\mathbf{n}_c^{(j)} = \frac{\mathbf{x}_{\mathcal{M}}^{(j)} - \mathbf{x}_{\mathcal{M}}^{(i)}}{|\mathbf{x}_{\mathcal{M}}^{(j)} - \mathbf{x}_{\mathcal{M}}^{(i)}|}\,, \tag{4.3}$$

defines the contact plane. The position $\mathbf{x}_c^{(ij)}$ of the contact point can be expressed either with respect to $\mathcal{P}^{(i)}$ or with respect to $\mathcal{P}^{(j)}$, viz.

$$\mathbf{x}_c^{(ij)} = \mathbf{x}_{\mathcal{M}}^{(i)} + \underbrace{r^{(i)}\,\mathbf{n}_c^{(i)}}_{=\,\bar{\mathbf{x}}_c^{(i)}} = \mathbf{x}_{\mathcal{M}}^{(j)} + \underbrace{r^{(j)}\,\mathbf{n}_c^{(j)}}_{=\,\bar{\mathbf{x}}_c^{(j)}}\,. \tag{4.4}$$

A relative motion of the two particles during one time increment Δt results in a motion of the contact point such that a relative displacement

$$\mathbf{u}_c^{(ij)} = \mathbf{x}_c^{(ij)}(\,t\,) - \mathbf{x}_c^{(ij)}(\,t - \Delta t\,) \tag{4.5}$$

is initiated at the contact point. The relative velocity $\mathbf{v}_c^{(ij)}$ at the contact point reads

$$\mathbf{v}_c^{(ij)} = \mathbf{v}_c^{(i)} - \mathbf{v}_c^{(j)} = \mathbf{v}_{\mathcal{M}}^{(i)} - \mathbf{v}_{\mathcal{M}}^{(j)} + (\,r^{(i)}\,\boldsymbol{\omega}^{(i)} - r^{(j)}\,\boldsymbol{\omega}^{(j)}\,) \times \mathbf{n}_c^{(i)}\,. \tag{4.6}$$

Both quantities are used to formulate constitutive force laws, especially in the tangential

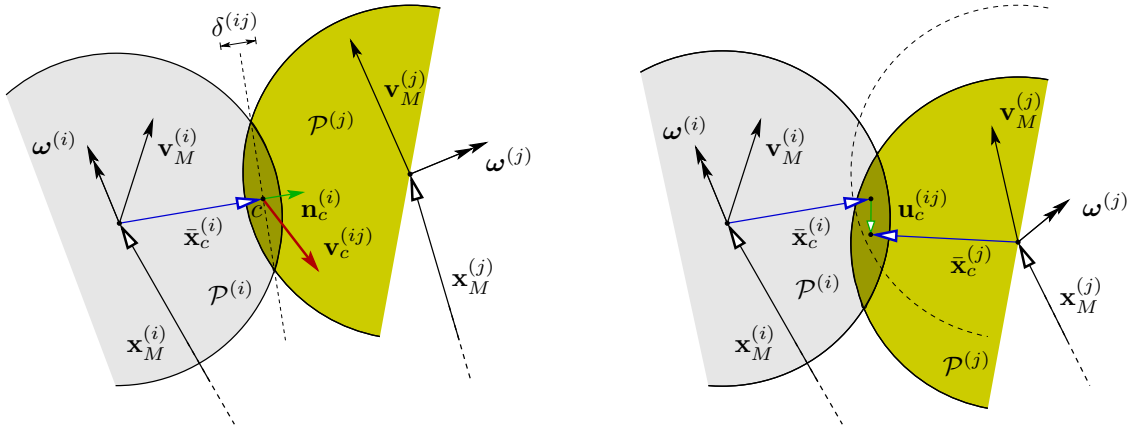

Figure 4.2: *Contact representation and relative displacement of colliding spherical particles.*

direction of the contact. Therefore, their tangential parts, $\mathbf{u}_{c,t}^{(ij)}$ and $\mathbf{v}_{c,t}^{(ij)}$, respectively, are determined by a projection into the contact plane, leading to

$$\mathbf{u}_{c,t}^{(ij)} = \mathbf{u}_c^{(ij)} - (\,\mathbf{u}_c^{(ij)} \cdot \mathbf{n}_c^{(i)}\,)\,\mathbf{n}_c^{(i)} \quad \text{and} \quad \mathbf{v}_{c,t}^{(ij)} = \mathbf{v}_c^{(ij)} - (\,\mathbf{v}_c^{(ij)} \cdot \mathbf{n}_c^{(i)}\,)\,\mathbf{n}_c^{(i)}\,. \tag{4.7}$$

In the same way, a relative rotation $\boldsymbol{\varphi}^{(ij)}$ is given as the change of the relative orientation of two contacting particles. As one can safely assume that the relative rotation during one time increment is small, it is additively decomposed into a rolling part $\boldsymbol{\varphi}_r^{(ij)}$ and a twisting part $\boldsymbol{\varphi}_t^{(ij)}$, yielding

$$\boldsymbol{\varphi}^{(ij)} = \boldsymbol{\varphi}_r^{(ij)} + \boldsymbol{\varphi}_t^{(ij)}\,. \tag{4.8}$$

The decomposition is carried out through the projection of $\boldsymbol{\varphi}^{(ij)}$ onto the contact normal direction:

$$\boldsymbol{\varphi}_t^{(ij)} = (\,\boldsymbol{\varphi}^{(ij)} \cdot \mathbf{n}_c^{(ij)}\,)\,\mathbf{n}_c^{(ij)} \quad \text{and therefore} \quad \boldsymbol{\varphi}_r^{(ij)} = \boldsymbol{\varphi}^{(ij)} - \boldsymbol{\varphi}_t^{(ij)}\,. \tag{4.9}$$

4.2.3 Normal and tangential contact formulations

Generally, the contact force $\mathbf{f}_c^{(i)}$ is additively split into a normal part $\mathbf{f}_{c,n}^{(i)}$ and a tangential part $\mathbf{f}_{c,t}^{(i)}$, viz.:

$$\mathbf{f}_c^{(i)} = \mathbf{f}_{c,n}^{(i)} + \mathbf{f}_{c,t}^{(i)} . \tag{4.10}$$

Physically based constitutive relations are introduced for the force computations in the two directions. The normal force $\mathbf{f}_{c,n}^{(i)}$ is the repulsive force between the contacting particles due to local compression at the contact zone and is generally defined as an explicit function of the indentation $\delta^{(ij)}$ and its rate $\dot{\delta}^{(ij)}$. It can be expressed by use of the contact normal direction $\mathbf{n}_c^{(i)}$ as

$$\mathbf{f}_{c,n}^{(i)} = \mathbf{f}_{c,n}^{(i)} (\delta^{(ij)}, \dot{\delta}^{(ij)}, \mathbf{n}_c^{(i)}) . \tag{4.11}$$

Based on an elasto-static contact investigation, it is possible to derive analytic solutions concerning the local deformation, the local geometry and the local repulsive pressure distribution for specific contact scenarios. In particular, the contact between two spheres can be solved with respect to the repulsive force through integration of the pressure distribution at the deformed contact plane under the assumption of linear elastic material behaviour, no wave propagation and a local deformation only in the vicinity of the contact areas (Hertz [110]). The resulting Hertzian contact formulation is widely used for DE computations and was recently shown to well fit experimental investigations even for natural sand grains (Nardelli *et al.* [162]). By assigning the local deformation to the allowed indentation, the Hertzian contact law for DE implementations reads

$$\mathbf{f}_{c,n}^{(i)} = -[\frac{4}{3} K_n (\frac{r^{(ij)}}{2})^{1/2} (\delta^{(ij)})^{3/2}] \mathbf{n}_c^{(i)} . \tag{4.12}$$

Therein, K_n represents the contact stiffness between the two elastically deformable spheres and can be calculated with respect to the elastic constants, for example Young's modulus $E^{(i/j)}$ and Poisson's ratio $\nu^{(i/j)}$, of the involved materials. If only a single grain material and thus $E^{(i)} = E^{(j)} = E$ and $\nu^{(i)} = \nu^{(j)} = \nu$ is assumed, as it is done throughout the present work, K_n becomes

$$K_n = \frac{E}{2 (1 - \nu)} \tag{4.13}$$

Moreover, the so-called common radius $r^{(ij)}$ is calculated as the harmonic mean of the involved particle's radii,

$$r^{(ij)} = \frac{2 r^{(i)} r^{(j)}}{r^{(i)} + r^{(j)}} . \tag{4.14}$$

The relation (4.12) is fully energy-conserving and is enriched by a damping contribution to include dissipation effects at the contact. Introducing a local damping coefficient D_n, (4.12) extends to

$$\mathbf{f}_{c,n}^{(i)} = -[\frac{4}{3} K_n (\frac{r^{(ij)}}{2})^{1/2} (\delta^{(ij)})^{3/2} + D_n \dot{\delta}^{(ij)}] \mathbf{n}_c^{(i)} . \tag{4.15}$$

Hertzian contact formulations are characterised by a nonlinear elastic relationship between resulting force and indentation, cf. Figure 4.5, top. More complex (hysterectic) formulations that include an internal energy dissipation without additional damping elements

are thoroughly compared and discussed in Džiugys & Peters [53] and Luding [148, 149]. Alternatively, a widely used simple linear force interaction law can be formulated as

$$\mathbf{f}_{c,n}^{(i)} \;=\; -\,(\,K_n^{lin}\,\delta^{(ij)} \;+\; D_n\,\dot{\delta}^{(ij)}\,)\,\mathbf{n}_c^{(i)}\,. \tag{4.16}$$

Therein, K_n^{lin} denotes the linear contact stiffness in normal direction.

If no tangential force law is considered, the collision of two spheres always results in an central impact, such that no rotational motion is induced. Hence, apart from the physical relevance of including a tangential force formulation to account for friction between particles, it is also the only source to invoke a rotational motion of single particles in an IBVP when using a purely spherical discrete element representation. Formulations based on the Coulomb friction model form the basis of most tangential contact laws applied in the DEM (Andersson *et al.* [10], Džiugys & Peters [53]).

Thereby, a frictional force $\mathbf{f}_{c,t}^{(i)}$ hinders a relative tangential displacement at the contact point based on the relation

$$\mathbf{f}_{c,t}^{(i)} \;=\; -\,K_t\,\mathbf{u}_{c,t}^{(ij)} \;-\; D_t\,\mathbf{v}_{c,t}^{(ij)}\,, \tag{4.17}$$

describing the sticking-friction case, where K_t and D_t denote the contact's tangential stiffness and the tangential damping parameter, respectively. After reaching a limit state of the sticking friction force, which is given as a fraction of the amount of resulting normal force, sliding occurs. The material parameter governing the relation between normal and tangential force in the limit case of sticking friction is the so-called sticking (static) friction coefficient μ_s. In order to determine whether the tangential contact is in a sticking or sliding case, a limit state criterion is introduced, comparable to yield-criteria of continuum-based plasticity theories. Summarising, the tangential contact formulation then reads

$$\mathbf{f}_{c,t}^{(i)} \;=\; \begin{cases} -\,K_t\,\mathbf{u}_{c,t}^{(ij)} \;-\; D_t\,\mathbf{v}_{c,t}^{(ij)} & \text{if} \quad |\mathbf{f}_{c,t}^{(i)}| \;\leq\; \mu_s\,|\mathbf{f}_{cn}^{(i)}|\,, \\ -\,\mu_d\,|\mathbf{f}_{cn}^{(i)}|\,\dfrac{\mathbf{v}_{c,t}^{(ij)}}{|\mathbf{v}_{c,t}^{(ij)}|} & \text{else}\,, \end{cases} \tag{4.18}$$

compare Obermayr *et al.* [172]. Therein, μ_d is the sliding (dynamic) friction coefficient, where generally $\mu_d \leq \mu_s$ holds.

4.2.4 Particle-shape modelling through rolling resistance

The grain shape has a significant influence on the microscopic interactions between particles and also manifests itself in macroscopically observable effects. Exemplarily, Desrues & Andò [46] show a correlation between the shear-band width and the roundness of sand grains. This effect is mainly due to the mechanism of co-rotating particles in the shear-band, meaning that, if one angular-shape particle rotates, a contact-force couple might occur due to the possibility of multiple contact points between the particles. Consequently, a contact torque is transmitted and the neighbouring particle rotates unidirectionally. This effect is more pronounced for angular-shaped grains (Desrues & Andò [46]). Contrary to this mechanism, it is obvious that an angular-shaped particle lying, for example, on a

flat surface, needs to overcome a certain amount of rotational resistance, before a rolling mechanism can be initiated. Various publications discuss the importance of including theses effects into DE simulations with spherical particles in order to model natural granular material behaviour more accurately, see especially the first attempts in this regard by Iwashita & Oda [118, 119] and the comparative evaluation of rolling resistance models given in Wensrich & Katterfeld [217]. It should be noted that the above considered effects can not be accounted for by standard normal or tangential friction models. For clarification, one may exemplarily look at a contact with active normal and sliding frictional elements between two particles. Here, the equilibrium $\mathbf{f}_c^{(i)} = -\mathbf{f}_c^{(j)}$ at the contact point stimulates a rotation in contrary directions between the interacting particles, thus having the opposite effect than anticipated. The most common way to include the anticipated behaviour, but still maintaining the spherical discrete element representation, lies in the constitutive formulation of a contact torque initiated at the contact. Rolling resistance is then defined as a manifestation of a resisting torque at the contact area due to a non-symmetric contact pressure distribution. The theoretically assumed contact area is already given by the cutting surface at the contact point c with normal direction $\mathbf{n}_c^{(i)}$, as indicated by the dashed line in Figure 4.2. Ai *et al.* [2] assess different rotational resistance models for spherical discrete elements with regard to their capability to model grain-shape simplification, and conclude that a rheological elasto-plastic spring-damper combination is the most suitable choice for this purpose. Jiang *et al.* [126] propose such a model for 2-d discs, whose idea is generalised to 3-d spheres by the same authors in Jiang *et al.* [124], also including a twisting resistance approach for the transfer of torsional moments between particles. The strength of the model lies in the sole introduction of one additional grain-shape parameter c_s, that relates the common radius, defined in (4.14), to an assumed circular contact area $\mathcal{S}_c$ on which the normal and tangential contact laws are active. Ideally, this approach leads to the possibility that the shape parameter is in direct relation to geometric properties of natural grain materials, such as e. g. statistically determined shape factors for different sands, as presented in Alshibli & Alsaleh [5] using digital microscopy. Following this idea, Wensrich & Katterfeld [217] tried to determine the relation between the shape parameter of a rolling resistance model with averaged contact eccentricities computed from clusters of spherical particles. They, however, state that although rolling resistance is a suitable modelling technique to capture shape simplification for spherical discrete elements, a clear physical identification of the shape parameter is not possible. Hence, the shape parameter should be treated as an additional modelling parameter in need of calibration.

In the present work, the rolling resistance model of Jiang *et al.* [124] is applied, yet without implementation of the twisting resistance contribution. It is assumed that torsional contributions between grains are of negligible importance for localisation phenomena in granular media. This seems reasonable, especially for the case of laboratory test, where the shear zone is generally a flat surface in the 3-d domain and thus relative rotation is predominant in the direction perpendicular to the slope of the shear-zone, cf. Desrues & Andò [46]. In the case of double-curved shear-zones, as they can for example be found in slope failure of natural soils, relative torsional displacement between neighbouring particles might also come into play. In the following section, the rotational resistance model is recapitulated in a nutshell. It is based on the evaluation of the normal contact at an

assumed deformed circular contact area $\mathcal{S}_c$. Thereby, one assumes that the normal contact force $\mathbf{f}_{c,n}^{(i)}$ is evenly distributed over $\mathcal{S}_c$, leading to a constant contact pressure with the amount $\bar{p}$ acting on the contact surface. Note that this assumption only holds for the linear contact model (4.16). In a rheological sense, the contact at $\mathcal{S}_c$ is interpreted as the sum of an infinite number of spring-damper models between the contacting planes, cf. Figure 4.3 (a), with corresponding modelling parameters k_n and d_n given as

$$k_n = \frac{K_n^{lin}}{\mathcal{S}_c} \quad \text{and} \quad d_n = \frac{D_n}{\mathcal{S}_c} . \tag{4.19}$$

The additionally introduced shape parameter c_s connects the radius R of the spherical contact surface $\mathcal{S}_c$ to the common radius $r^{(ij)}$ of the particles in contact via the relation

$$R = c_s \, r^{(ij)} . \tag{4.20}$$

The rheological model implies that an increasing relative rotation $\boldsymbol{\varphi}_r^{(ij)}$ causes a resisting moment $\mathbf{m}_c^{(i)}$. In the case of the contact pressure distribution being non-zero over the whole contact surface, it is a linear function of $\boldsymbol{\varphi}_r^{(ij)}$, see Figure 4.3 (b). Thus, the resisting torque $\mathbf{m}_c^{(i)}$ is determined by reducing the given system with respect to c, yielding

$$\mathbf{m}_c^{(i)} = -\frac{k_n \, R^4 \, \pi}{4} \boldsymbol{\varphi}_r^{(ij)} = -K_\varphi \, \boldsymbol{\varphi}_r^{(ij)} \quad \text{with} \quad K_\varphi := \frac{K_n^{lin} \, (c_s \, r^{(ij)})^2}{4} . \tag{4.21}$$

Therein, K_φ follows by use of (4.19) and (4.20) and can be interpreted as the stiffness of a rotational spring for the linear elastic contact regime. Note that, due to the pressure

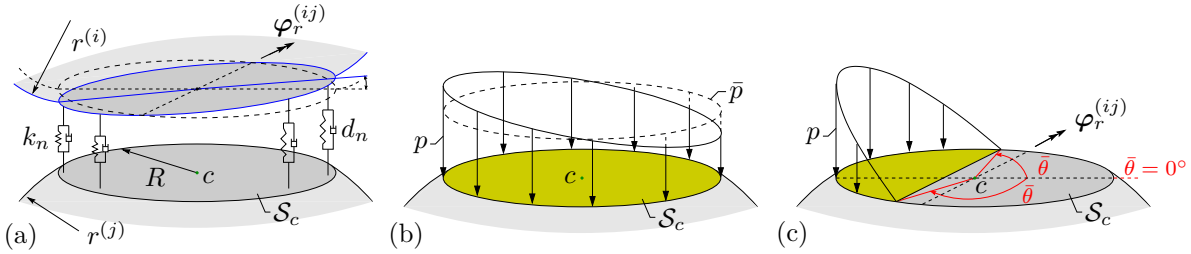

Figure 4.3: *(a) Rheological model of the contact area with relative rotation $\boldsymbol{\varphi}_r^{(ij)}$, (b) and (c) contact-pressure distributions.*

distribution being symmetric and perpendicular to the contact plane, a resisting moment is only initiated against the direction of the rolling part $\boldsymbol{\varphi}_r^{(ij)}$ of the relative rotation $\boldsymbol{\varphi}^{(ij)}$. Analogously to the activation of the distributed spring elements, the damping elements induce a linear viscous stress distribution due to a relative angular velocity $\dot{\boldsymbol{\varphi}}_r^{(ij)}$ in rolling direction. By integration over the contact surface and making use of the relations (4.19) and (4.20), the viscous damping moment $\mathbf{m}_d^{(i)}$ follows as

$$\mathbf{m}_d^{(i)} = \frac{d_n \, \pi \, R^4}{4} \dot{\boldsymbol{\varphi}}_r^{(ij)} = \frac{D_n \, (r^{(ij)})^2}{4} \dot{\boldsymbol{\varphi}}_r^{(ij)} = D_\varphi \, \dot{\boldsymbol{\varphi}}_r^{(ij)} \quad \text{with} \quad D_\varphi := \frac{D_n \, R^2}{4} . \tag{4.22}$$

Regarding the contact stress distribution, the limit case of elastic loading is reached when the pressure distribution becomes zero at one end of the contact surface. From this point

on, the active contact area is reduced with increasing relative rotation. An intermediate contact pressure distribution is shown in Figure 4.3 (c). Therein, an angle $\bar{\theta}$ is introduced to parameterise the active contact area, highlighted in yellow. $\bar{\theta}$ thereby measures the angle between the perpendicular direction to the relative rotation $\boldsymbol{\varphi}_r^{(ij)}$ and the point of zero contact pressure in the contact plane. An increase in $\boldsymbol{\varphi}_r^{(ij)}$ yields a decline of the remaining active contact area with increasing values of $\bar{\theta}$ in the post-elastic case, while $\bar{\theta} = 0°$ defines the limit case of the elastic contact regime. Note that the resisting torque and the amount of normal force are a function of the remaining contact area, i. e. of the angle $\bar{\theta}$. By dropping the dependency on $\bar{\theta}$ for the normal force via enforcing a constant amount of the normal force, Jiang *et al.* [124] derived a non-linear relation between an increasing relative rotation and the resisting moment in the post-elastic regime for a variation of $\bar{\theta}$, as sketched in Figure 4.4. Therein, the relative rotation and the resisting torque are normalised with respect to their values for the limit case of the elastic regime, $\bar{\boldsymbol{\varphi}}_r^{(ij)}$ and $\bar{\mathbf{m}}_c^{(i)}$, respectively, which read

$$\bar{\boldsymbol{\varphi}}_r^{(ij)} = \frac{|\mathbf{f}_{c,n}^{(i)}|}{K_n^{lin}\, R}\, \frac{\boldsymbol{\varphi}_r^{(ij)}}{|\boldsymbol{\varphi}_r^{(ij)}|} \quad \text{and} \quad \bar{\mathbf{m}}_c^{(i)} = -\frac{K_n^{lin}\, R^2}{4}\, \bar{\boldsymbol{\varphi}}_r^{(ij)}\,, \tag{4.23}$$

respectively. In particular, an interpretation of the relation in terms of plasticity at the grain level is proposed. The solid curve in Figure 4.4 represents the case of an uncrushable elastic particle, whereas the dashed line represents a simplified model, where only up to a certain point $\zeta|\bar{\mathbf{m}}_c^{(i)}|$ an elastic behaviour is possible, before stress concentrations on the contact surface lead to local crushing or plastification of the particle. From this point on, an ideal-plastic behaviour is assumed. The value of ζ is determined through the assumption of energy conservation between the elastically stored and the dissipated energy in the originally non-linear part of the relation (grey areas in Figure 4.4). Limiting the admissible relative rotation, for example, to $\varphi_r^{(ij)}/\bar{\varphi}_r^{(ij)} = 5.0$ leads to a value of $\zeta = 2.1$.

The actual benefit of the simplification of the relation lies in the reformulation of the

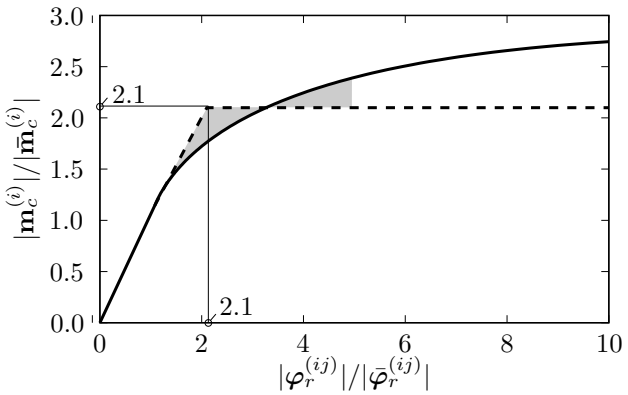

Figure 4.4: *Relation between normalised resisting moment and relative rotation after Jiang et al. [124].*

contact law analogously to (4.18), which allows an effective implementation into DE codes. Summarising this procedure yields

$$\mathbf{m}_c^{(i)} = \begin{cases} -K_\varphi\, \boldsymbol{\varphi}_r^{(ij)} - D_\varphi\, \dot{\boldsymbol{\varphi}}_r^{(ij)} & \text{if} \quad |\mathbf{m}_c^{(i)}| \le \zeta\, |\bar{\mathbf{m}}_c^{(i)}| \\ -\zeta\, \bar{\mathbf{m}}_c^{(i)} & \text{else}\,. \end{cases} \tag{4.24}$$

For the sake of completeness, a detailed derivation of these relations is given in Appendix B.3.

DE contact formulations are rheologically symbolised by combinations of springs, dampers and frictional elements. In this regard, Figure 4.5 summarises a rheological representation of the used formulations and shows their isolated responses in normal, tangential and rotational contact direction. Therefore, a set-up with two interacting particles with radii $r^{(2)} = 2r^{(1)}$ is investigated. Concerning the Hertzian normal contact formulation (top row of Figure 4.5), the particle $\mathcal{P}^{(1)}$ is moved with a constant velocity relative to the spatially fixed particle $\mathcal{P}^{(2)}$ until an overlap of $0.12r^{(1)}$ is reached. The contact force response on $\mathcal{P}^{(1)}$ shows the anticipated non-linear behaviour. For comparison, the response of an equivalent linear contact model is plotted, where the linear contact stiffness is varied to obtain the same contact force in the final simulation step. The tangential frictional contact is validated by enforcing a constant normal force and rotating $\mathcal{P}^{(1)}$ with a constant angular velocity in clockwise direction. The norm of the reaction force $\mathbf{f}_{c,t}^{(1)}$ is plotted with respect to the norm $|\mathbf{u}_{c,t}^{(12)}|$ of relative displacement in tangential direction at the contact point. It can be seen that a variation of the sliding friction coefficient from $\mu_d = \mu_s$ (solid red line) to $\mu_d = 0.8\mu_s$ (dashed blue line) leads to the desired force responses. Furthermore, the particle $\mathcal{P}^{(2)}$ rotates in counter-clockwise direction due to the acceleration by $\mathbf{f}_{c,t}^{(2)}$. Finally, the response of the rotational resistance model is plotted for two values of the shape-coefficient c_s. Here, a constant normal force is again enforced between the particles, and $\mathcal{P}^{(1)}$ is uniformly rotated in clockwise direction. As anticipated, the contact torque response on $\mathcal{P}^{(1)}$ is linear until $|\mathbf{m}_c^{(i)}|$ reaches the limit $\zeta|\bar{\mathbf{m}}_c^{(i)}|$, with $\zeta = 2.1$ in both cases, and is constant afterwards. The initial stiffness, which characterise the linear part of the contact torque, and the limit state, changes with a variation of c_s. Note also that a clockwise rotation of $\mathcal{P}^{(2)}$ is initiated.

4.2.5 Bond-contact formulation

For the additional consideration of micromorphic effects, the possibility of particle deformations has to be included into the numerical scheme. In the present context, this is done by the assumption of deformable bonds of binder material between particles that even allow for local non-homogeneous stress and strain states. When bonds exist, these bonds are represented by geometrically linear Timoshenko beams with circular cross sections connecting the centres of mass of neighbouring particles, cf. Figure 3.5 (d). Furthermore, the radius of the beams is chosen as the mean radius of the connected particles and the beams are assumed to be massless. A relative displacement $\mathbf{u}_r^{(ij)} = \mathbf{x}_{\mathcal{M}}^{(i)} - \mathbf{x}_{\mathcal{M}}^{(j)}$ and a relative rotation $\boldsymbol{\varphi}_r^{(ij)}$ between bonded particles yield a deformation in the beam, that can be accounted for by a displacement vector $\mathbf{u}_b^{(i)}$,

$$\mathbf{u}_b^{(i)} = \mathbf{u}_b^{(i)}\left[\,\mathbf{x}_m,\, \boldsymbol{\varphi}_r^{(ij)}(\mathbf{x}_m)\,\right] = \begin{bmatrix} u_{r1}^{(ij)} + \varphi_{r2}^{(ij)}\, x_{m3} - \varphi_{r3}^{(ij)}\, x_{m2} \\ u_{r2}^{(ij)} - \varphi_{r1}^{(ij)}\, x_{m3} \\ u_{r3}^{(ij)} + \varphi_{r1}^{(ij)}\, x_{m2} \end{bmatrix} \mathbf{e}_{m\,i} \tag{4.25}$$

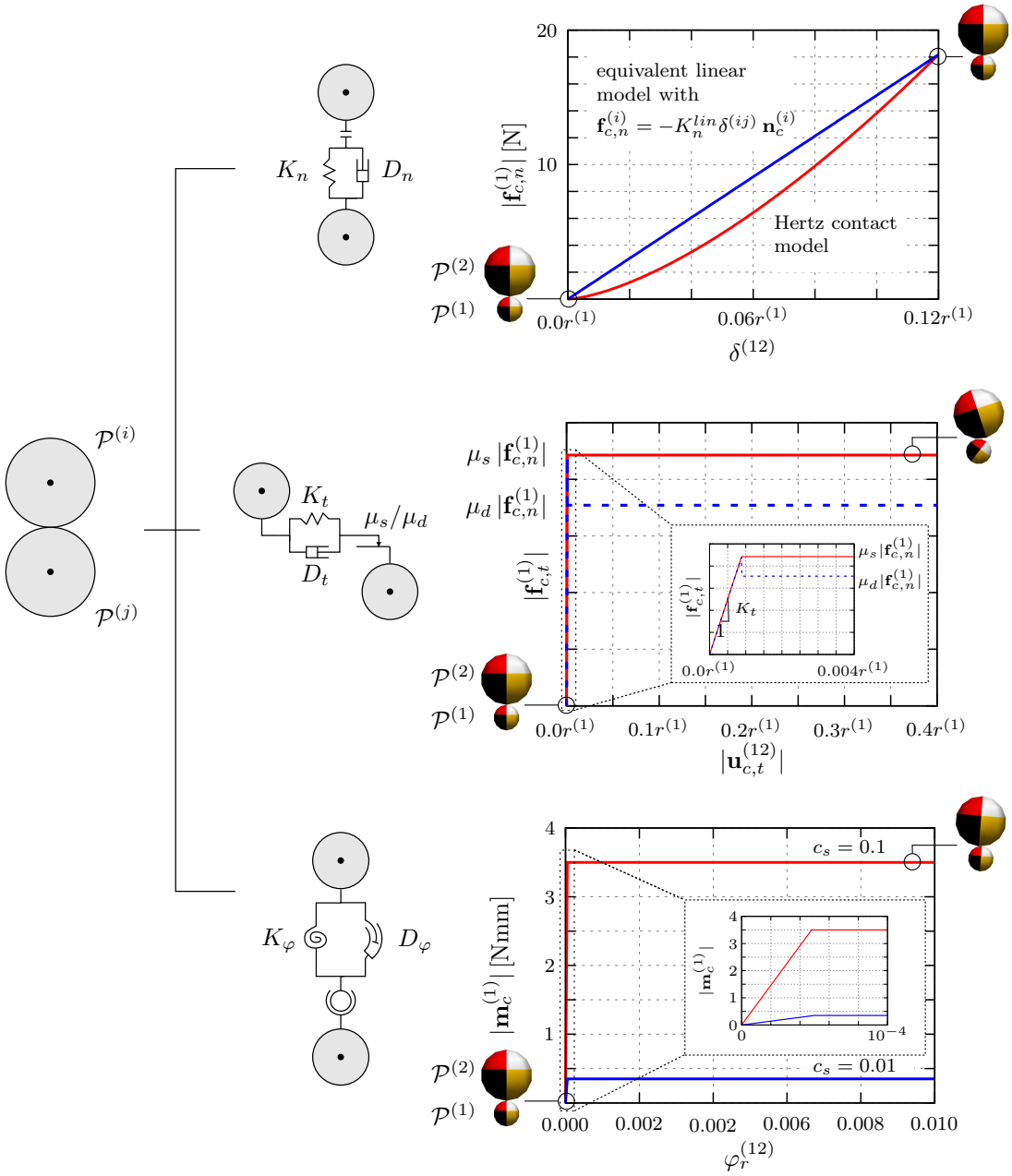

Figure 4.5: *Constitutive contact formulations at the contact point with magnified extractions of the elastic regimes in tangential and rotational directions.*

expressed with respect to a local coordinate system $\mathbf{e}_{m\,i}$, where $\mathbf{e}_{m1} = \mathbf{n}_b^{(i)}$ is aligned with the longitudinal axis of the beam under consideration. Under the assumption of geometric linearity, the strain in the bond element is calculated as

$$\boldsymbol{\varepsilon}_b^{(i)} \;=\; \tfrac{1}{2}\left(\mathrm{Grad}\,\mathbf{u}_b^{(i)} \;+\; \mathrm{Grad}^T\,\mathbf{u}_b^{(i)}\right), \tag{4.26}$$

where derivatives arising in $\mathrm{Grad}\,\mathbf{u}_b^{(i)}$ are linearly approximated over the length of the beam using the discrete values of the relative displacement and rotation of the pair of bonded particles. The material description of the beams follows a Hookean-type elas-

ticity law, where the stress $\mathbf{T}_b^{(i)} \approx \boldsymbol{\sigma}_b^{(i)}$ in the beam with $\boldsymbol{\sigma}_b^{(i)}$ as the Cauchy stress in geometrically linearised approaches is computed as

$$\boldsymbol{\sigma}_b^{(i)} = \begin{bmatrix} E_b\,\varepsilon_{b11}^{(i)} & 2\,\alpha_s\,G_b\,\varepsilon_{b12}^{(i)} & 2\,\alpha_s\,G_b\,\varepsilon_{b13}^{(i)} \\ & 0 & 0 \\ \text{sym.} & & 0 \end{bmatrix} \mathbf{e}_{m\,i} \otimes \mathbf{e}_{mj}\,. \tag{4.27}$$

Therein, E_b and G_b are the elasticity moduli of the considered material and α_s is the Timoshenko shear coefficient. In case that bonds break when a predefined maximum equivalent stress $\sigma_V^{(i)}$ exceeds a threshold value σ_y, such that

$$\sigma_V^{(i)} = \sqrt{(\sigma_{b\,11}^{(i)})^2 + 3\,[\,(\sigma_{b\,21}^{(i)})^2 + (\sigma_{b\,31}^{(i)})^2\,]} > \begin{cases} \alpha_c\,\sigma_y & \text{if } \sigma_{b\,11}^{(i)} < 0\,, \\ \sigma_y & \text{else}\,, \end{cases} \tag{4.28}$$

this is included into the description by deleting the beams between the respective particles. Thereby, the compressive strength of a beam is weighted by a factor α_c in order to account for different resistances to tension and compression generally found in many engineering materials. For a detailed derivation of the model and its performance to compute cemented sand under various loading conditions, the reader is referred to the formulation introduced in Obermayr *et al.* [171] and thoroughly discussed in Obermayr [170].

Chapter 5:
Discrete-element modelling of failure in granular material

This chapter presents numerical simulations of granular material failure. After discussing the general numerical set-up, simulations of uniaxial tension and compression tests on cylindrical specimen are given for bonded granular material. In order to compare bonded and unbonded material behaviour, a biaxial compression test is additionally investigated for the bonded and the unbonded case. The DE simulations supply the necessary microscale information for the intended computational homogenisation towards micromorphic material behaviour on a higher spatial scale.

5.1 General model set-up

For all simulations, the respective specimen is represented by a grain ensemble with a polydisperse particle size distribution. The requirements on such a packing are fairly high, if the modelling of localisation effects should succeed. The packing needs to be in a relatively dense configuration, allowing only for low initial compaction during biaxial compression, cf. the demanding process of experimental sand specimen generation through layer-wise filling and consolidation. Furthermore, a regular contact network and density distribution are necessary, in order to avoid initial weak spots in the packing, which would lead to local failure at a very early stage. One way of fulfilling these requirements, is the generation of the assembly through a constructive algorithm as described in Ergenzinger *et al.* [68], where particles inflate from a predefined configuration without any particle contacts towards a configuration, which exhibits a desired mean number of contacts for all particles and a predefined particle size distribution. Figure 5.1 illustrates the initial particle distribution for a set of 6 700 particles as well as the final assembly of polydisperse particles, which exhibits the size distribution of Hostun quartz sand, as given, for example, in Ezaoui & Benedetto [75]. As the constructed assembly of particles is geometrically restricted by the BVP, overlaps and resulting forces are present in the final particle distribution due to the simple fact that the DEM itself was applied in the construction strategy. It is therefore dynamically relaxed in order to obtain a stress-free reference configuration. This is generally achieved by

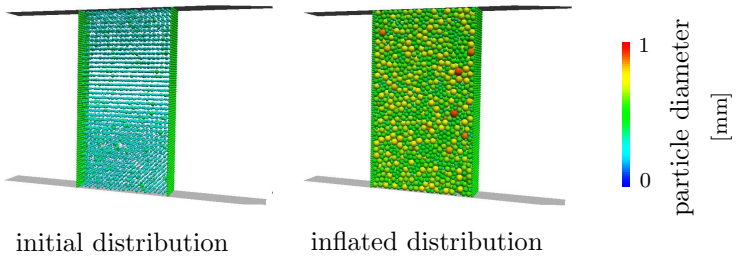

Figure 5.1: Examplary construction of a polydisperse particle-size distribution for the simulation of a biaxial compression test.

allowing an artificial, strongly damped free movement of the particles, such that overlaps between particles are reduced. In the present application, this approach is only directly pursued for the cylindrical specimen used in the simulations of uniaxial compression and tension tests. In the cases of biaxial compression tests, the dynamic relaxation process is combined with the pre-loading of the sample by a lateral confining pressure until a steady state is reached. In particular, the confining pressure is applied as single forces acting on a layer of smaller connected particles, see the left and right columns of particles on the left of Figure 5.1. These particles on both sides of the sample are additionally connected to each other by unbreakable elastic springs, representing the lateral rubber membrane used in the experimental set-up. The application of such a flexible boundary that allows for a local free deformation is essential for the simulation of shear-band phenomena, see e. g. Kawamoto *et al.* [132], Oda & Iwashita [173] or Scholz [187]. Moreover, in the case of biaxial loading, plain strain conditions are ensured by rigid fixed walls in depth direction of the sample. Furthermore, the compressive loading is applied by displacing the rigid top and bottom plates with a constant slow velocity. In combination with local damping at the contacts and the damping formulation of the bond elements, cf. Obermayr *et al.* [171], this approximately ensures quasi-static conditions throughout the simulation, although the fully dynamic simulation method is still applied. The application of the loading boundary conditions slightly differs for the cylindrical specimen used in simulations of uniaxial material tests. Here, no rigid walls are used. Instead, the necessary velocities and positions are directly prescribed to the top and the bottom layer of particles of the respective specimen. This allows for an easy change in loading direction that would not be straightforwardly possible when using rigid platens as surrogates for the loading apparatus of an experimental set-up.

5.2 Localisation in bonded granular media

Unbonded granular material is given, for example, by dry sand, where localisation is well observable in an experimental set-up, see for example the experiments conducted on Hostun quartz sand (Desrues & Andò [46], Desrues & Viggiani [48]). On the other hand, bonded material is found, for example, as moulding material for metal casting cores (Boenisch & Lotz [25], Iden *et al.* [117]) consisting of quartz sand and a polyurethane-based binder material. In the present work, this material is taken as an example for a deformable grain-binder microstructure. In this regard, Caylak & Mahnken [28] investigate the failure on sand-cores through strain localisation in uniaxial compression and tension tests, thus exhibiting qualitatively comparable results to the simulated localisation effects presented in the following. If not explicitly stated otherwise, the set of modelling parameters is used as summarised and commented in Table 5.1. Note thereby, that the rotational resistance model to account for the particle shape simplification is not used in the simulations of bonded granular material. The capability of this modelling feature is addressed in Section 5.3 for the unbonded case. As material parameters for the binder are generally not available at the grain-scale, these values are chosen based on

Table 5.1: Collection of modelling parameters.

Quantity	Value	Unit	Remark/Reference
Grain material (Quartz sand)			
Young's modulus E	94 000	[N/mm^2]	suggested by Nardelli *et al.* [162] based on grain-scale experiments
Poisson's ratio ν	0.1	[-]	suggested by Nardelli *et al.* [162] based on grain-scale experiments
Damping coefficient D_n	100	[Ns/mm]	chosen qualitatively
Tangential contact stiffness K_t	500	[N/mm]	value chosen in the region given in Sandeep & Senetakis [184]
Static friction coefficient μ_s	0.24	[-]	experimental value provided in Senetakis *et al.* [190]
Sliding friction coefficient μ_d	0.166	[-]	experimental value provided in Senetakis *et al.* [190]
Shape coefficient c_s	0.0	[-]	if not stated otherwise
Particle density	1.5	[g/mm^3]	mass is scaled to allow numerical speed-up as inertia effects are negligible under quasi-static conditions
Particle radii	$0.08 - 0.4$	[mm]	according to particle size distributions of Hostun sand
Binder material			
Young's modulus E_b	71 100	[N/mm^2]	as suggested in Schneider *et al.* [186]
Shear modulus G_b	20 385	[N/mm^2]	as suggested in Schneider *et al.* [186]
Shear coefficient α_s	0.87	[-]	computed in reference to Cowper [38]
Compressive strength factor α_c	4	[-]	chosen qualitatively
Failure stress σ_Y	3 500	[N/mm^2]	chosen qualitatively
Gravity $\mathbf{g}$	$\mathbf{0}$	[m/s^2]	gravity is neglected

the parameter region identified by Schneider *et al.* [186] through image-based microstructural computations of a sand-core sample and effective material parameter computations through homogenisation. Parameters for quartz sand grains are based on experimental data provided by Nardelli *et al.* [162], Sandeep & Senetakis [184] and Senetakis *et al.* [190].

Uniaxial compression and tension: A cylindrical specimen with 4 355 particles is simulated under uniaxial compression and tension. Due to the usage of the compressive strength factor α_c in the bond formulation, the so-called strength-differential effect is accounted for, leading to a significantly higher resistance towards compression, compare the global stress-strain relations for uniaxial compression and tension in Figure 5.2, for which the axial stresses, normalised with respect to the maximal tensional stress, are

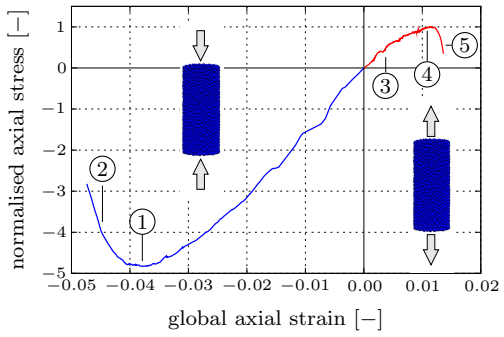

Figure 5.2: *Global stress-strain relations of the simulated uni axial compression test.*

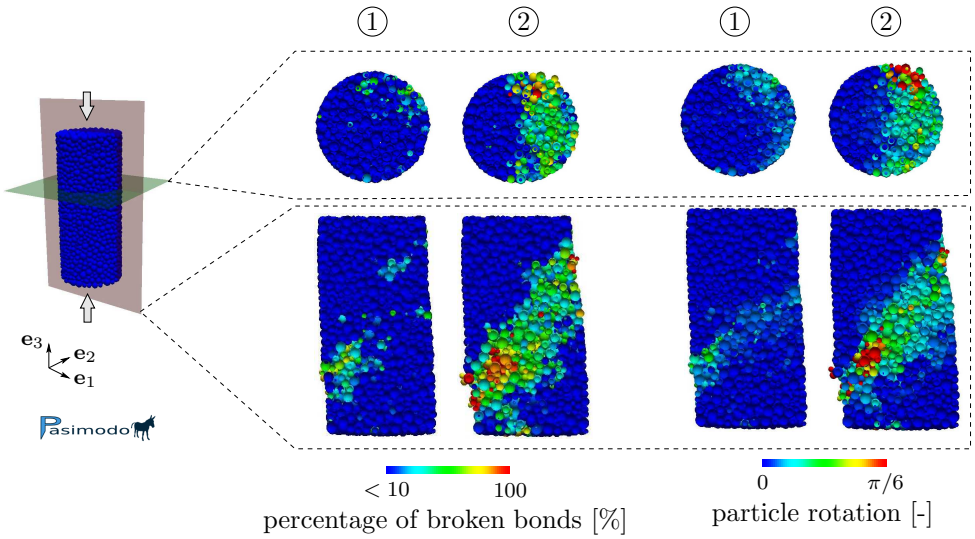

Figure 5.3: *Simulation of an uniaxial compression test on bonded granular material at and after the initiation of the shear band.*

plotted against the global axial strains defined as the reduction, respectively the increase in height, taken over the initial height of the specimen. The choice of $\alpha_c = 4$ results in a simulated compressive strength of the specimen which is 480% the tensile strength. In the case of compressive loading, a primary shear-band under 45° evolves at the peak load (point ① in Figure 5.2) after an initial homogeneous deformation of the sample. The bond elements in the region of the shear band exhibit high stresses and successively fail until the specimen is fully separated (left-hand side of Figure 5.3, corresponding to point ② in Figure 5.2). This state is given when the percentage of broken bonds along the shearing direction is larger than 50% throughout the complete width of the sample. Moreover, accompanying particle rotations accumulate in the region of the localisation, as it is shown on the right-hand side of Figure 5.3. Under tensional loading, a separation of the sample occurs along a primary plane nearly perpendicular to the loading direction, see Figure 5.4.

Biaxial compression: Figure 5.6 illustrates the results of a biaxial compression test of a specimen of initially bonded grains. The polydisperse ensemble contains 6 720 particles. The axial stress response is plotted against the global axial strain in Figure 5.5 (red line). As for the uniaxial compression test, after an initial homogeneous deformation of the sam-

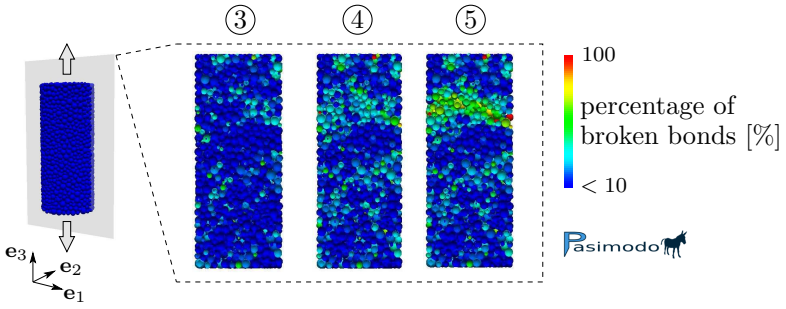

Figure 5.4: *Simulation of an uniaxial tension test on bonded granular material.*

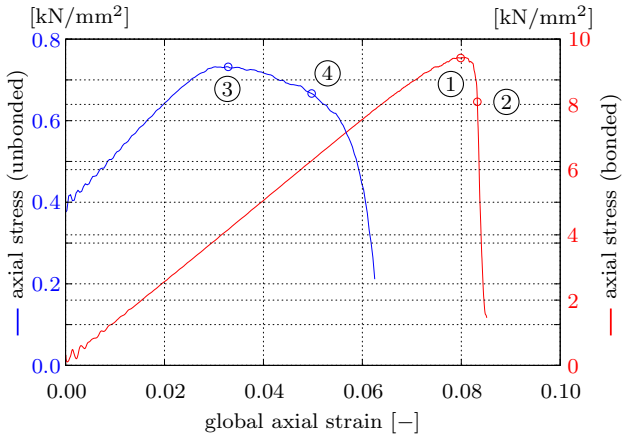

Figure 5.5: *Global stress-strain relations of the simulated biaxial compression test.*

ple, the onset (point ①) with the global peak strength of the sample and the full evolution (point ②) of a primary shear band are observed, indicated by an increasing percentage of broken (deleted) bonds. The evolution of the primary shear band is accompanied by secondary shear bands in opposite direction. The localisation is again accompanied by a concentration of particle rotations, as it is visualised on the right-hand side of Figure 5.6.

5.3 Localisation in unbonded granular media

The simulation of a biaxial compression test enables a direct comparison between initially bonded and unbonded material. In the context of the intended homogenisation this enables a comparison of the results between the complete micromorphic setting and the micropolar setting, cf. Bidier & Ehlers [23]. Therefore, the simulation of the biaxial compression test is repeated, now without consideration of initial bonds between neigh-

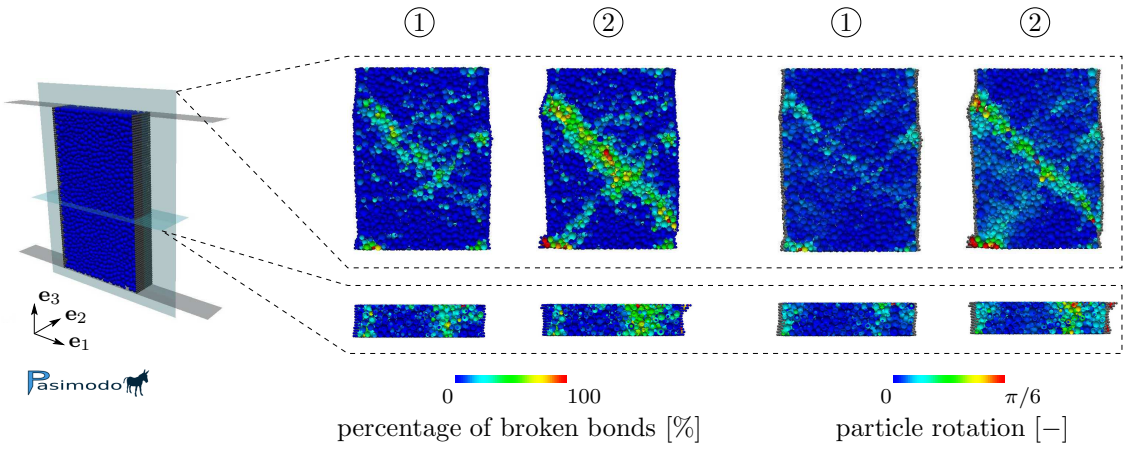

Figure 5.6: Simulation of a biaxial compression test on bonded granular material at and after the initiation of the shear band.

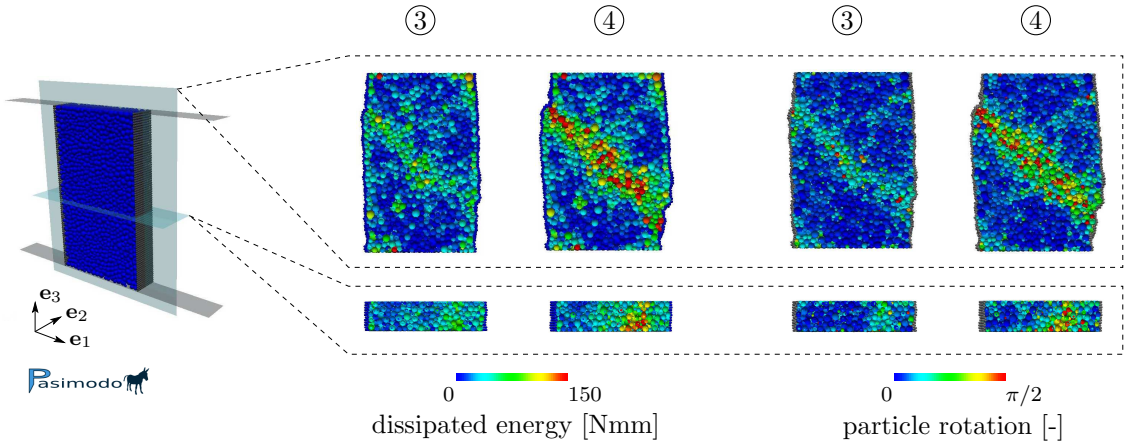

Figure 5.7: *Simulation of a biaxial compression test on unbonded granular material at and after the initiation of the shear band.*

bouring grains. Figure 5.7 displays the results for the biaxial test on unbonded granular material. Again, the initiation of a primary shear band (point ③) is observed, here indicated by the amount of dissipated energy visualised on the left-hand side of Figure 5.7. The loss in energy stems from active frictional elements in the tangential direction of the particle contacts. At the same time, particle rotations accumulate (right-hand side of Figure 5.7) exhibiting a result that is in good qualitative agreement with experiments or computations carried out by Hall *et al.* [104], Ehlers [57], Andò *et al.* [11], Desrues & Andò [46] or Kawamoto *et al.* [132]. The shear-band width is in the order of $5-6\ d_{50}$, when measured by means of rotating particles. Thereby, d_{50} denotes the mean diameter of the particle distribution. As anticipated and experimentally shown in Desrues & Andò [46], the rotations of particles in the shear band show a polarisation, cf. Figure 5.8. Therein, the direction coinciding with 0° is the orientation of the maximum slope of the shear band as displayed in Figure 5.7, point ④. The polar plot collects the number of particles with a certain amount of rotation in combination with the orientation of the rotation axis. It is clearly observed that particles preferably rotate in direction of the slope of the localisation and therefore their rotation axes polarise perpendicular to the shear-band direction, compare also the experimental results given in Desrues & Andò [46] based on the evaluation of a shear band from a triaxial compression test.

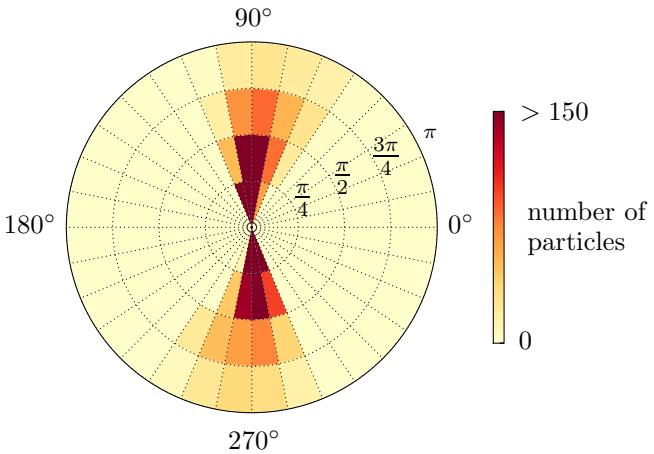

Figure 5.8: Polar plot of particle rotations in the shear band in unbonded material under biaxial compression.

Finally, note that in both simulations of the biaxial compression test, the functionality of the modelled elastic membrane via connected particles can be seen in the free deformation of the sample at both ends of the shear bands. The respective global stress-strain relation for the uniaxial compression test on unbonded material is plotted in Figure 5.5 (blue line). It is seen that the failure stresses at points ① and ③ of bonded and unbonded material differ by a factor of approximately 12.

Influence of the particle shape modelling: In comparison to the measured shear-band width on natural sands given in Andò *et al.* [11], reporting a width of $7 - 8\,d_{50}$ for roundly shaped sand grains and up to $10 - 12\,d_{50}$ for angular shaped grains when measured with respect to particle rotations, the present DE model slightly underestimates the shear-band width. Employing the introduced rolling resistance model leads to an improvement of the model. In this regard, Figure 5.9 displays the amount of particle rotation along a perpendicular cut through the shear band at 0.05 global axial strain (point ④ of Figure 5.5) for three values of the shape parameter c_s. Note in passing that therefore the linear contact model with $K_n^{lin} = 94\,000$ N/mm is applied to guarantee the theoretical consistency with the rotational resistance model. As intended, it is observed that an increase in rolling resistance with higher values of c_s leads to an increase of the shear-band width. For $c_s = 1.5$ the shear-band width is approximately $9\,d_{50}$. For a further increase of c_s, no clear primary shear band could be observed anymore. This might be due to the rather small total size of the numerical specimen and the fact that the shear band hits the upper left corner of the specimen for values of $c_s > 1.5$. It is furthermore observed that for values of $c_s < 1.5$ the peak-stress level does not change significantly, i. e. the initiation of the localisation is dominated by the behaviour of the frictional contacts. Consequently, the rolling resistance model only becomes active in the post-peak domain.

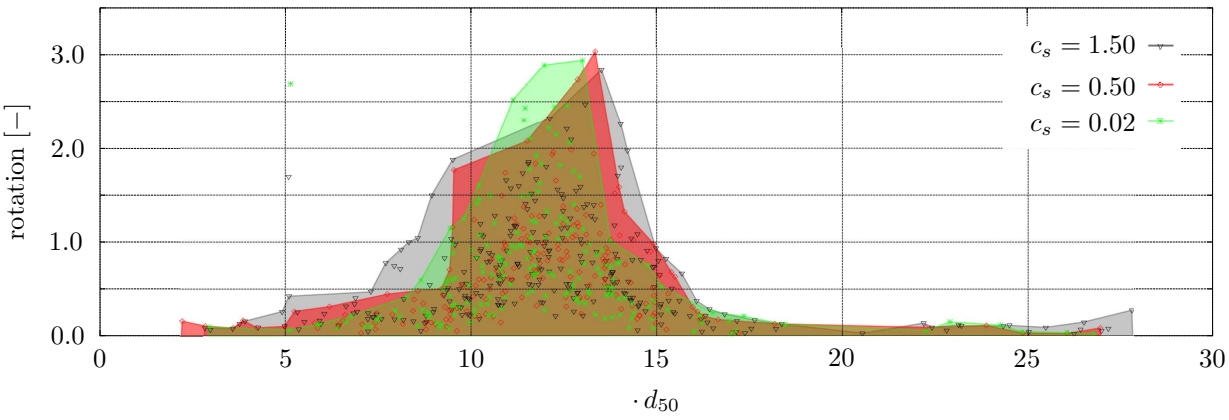

Figure 5.9: *Particle rotations along a perpendicular cut through the shear band for different values of c_s.*

In the subsequent chapter, the focus is on the homogenisation of the obtained particle-based information towards continuum quantities. The rolling resistance model is thereby not applied, as contact torques transmitted between the particles at interacting points

were not considered in the formulation of the homogenisation strategy. Although this is theoretically possible by shifting the location-independent contact torques to the mass centres at the REV boundary, their influence showed to be of minor importance for the detection of micromorphic and micropolar effects.

Chapter 6:
Application of the homogenisation strategy

This chapter applies the homogenisation strategy given in Chapter 3 to the DE simulations presented in the preceding Chapter 5. After addressing some numerical aspect concerning the REV construction, the main focus firstly lies on the detection of micromorphic stress and strain measures. This is primarily done by averaging of the results of the uniaxial compression test simulation on bonded granular material. Additionally, an investigation of the internal mechanical work is carried out to address the significance of the extended continuum mechanical contributions. Secondly, the loss of microstructural information based on an increase of the REV size is investigated. This is based on the results of the biaxial compression test simulations and also allows for a comparison between the micromorphic and the micropolar setting.

6.1 Numerical realisation

The following homogenisation processes proceed from the particle-centre-based strategy (D'Addetta *et al.* [43], Ehlers *et al.* [64], Lin & Wu [144], Wellmann *et al.* [215]), where REV are locally constructed at selected time steps of the simulation by collecting all particles within a spherical region of diameter $d_{\mathcal{R}}$ around each particle of the IBVP. Considering a 3-d ensemble of particles forming such an REV, the necessary calculations of the REV volume $V_{\mathcal{R}}$ requires an approximated determination strategy, which allows a feasible numerical investigation at all desired times of the simulation. This is mainly due to the fact, that the boundary $\partial\mathcal{R}$, i. e. the centres of mass of the particles forming $\partial\mathcal{R}$, is a non-convex 3-d polygon with triangular facets, compare also Wellmann *et al.* [215]. The volume of such a polygon is approximated by determing the volume of the set of particle centres forming its convex hull, cf. Barber *et al.* [18]. Figure 6.1 illustrates an exemplary REV, constructed by selecting particles with centres of mass inside a spherical region with diameter $d_{\mathcal{R}} = 3\,d_{50}$ around a randomly chosen particle from the distribution illustrated in Figure 5.1. The REV boundary itself is defined by all particles of the REV

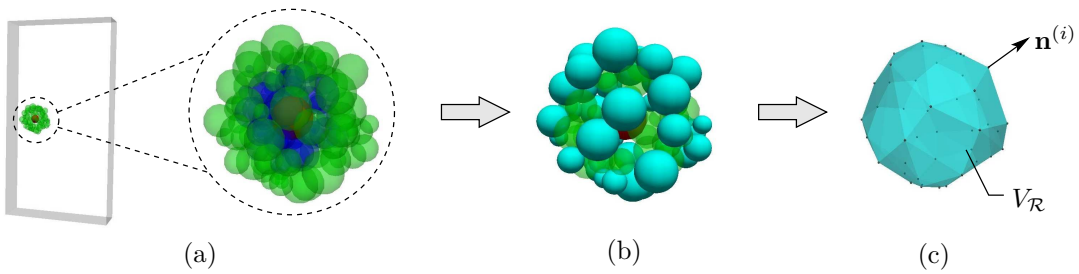

Figure 6.1: *(a) Randomly chosen REV with boundary particles highlighted in green, (b) subset of boundary particles forming the convex hull (cyan), (c) approximated REV-volume $V_{\mathcal{R}}$ via triangulation.*

that have one or more contacts with particles which themselves are not part of the REV. Due to the discrete construction of $\partial\mathcal{R}$, the normal vector $\mathbf{n}^{(i)} = \mathbf{x}_M^{(i)}/|\mathbf{x}_M^{(i)}|$, corresponding to the normal at each centre of mass of a boundary particle, is determined by normalising the relative position $\mathbf{x}_M^{(i)}$. Furthermore, the partial volume $V_{\mathcal{P}_\mathcal{R}^{(i)}}$ of boundary particles, cf. (3.67), which contributes to the homogenised strains, is calculated by a volume calculation of a surface triangulation of a set of evenly distributed points lying on the corresponding partial surface. This is an approximation of the actual volume, which is given as the corresponding volume of several spherical triangles on the particle surface depending on the number of neighbouring particles, compare Figure 6.2.

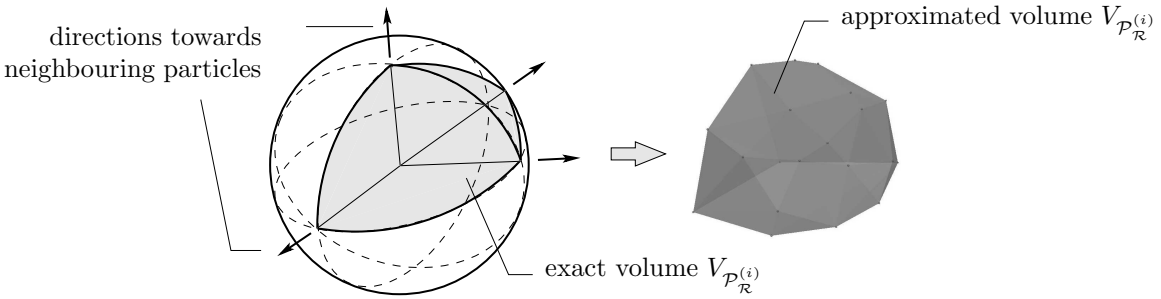

Figure 6.2: *Approximation of the partial volume* $V_{\mathcal{P}_\mathcal{R}^{(i)}}$.

6.2 Micromorphic setting

In the following, the homogenisation procedure is applied to the DE simultions of the uniaxial and the biaxial compression test. The aim thereby firstly lies in the detection of micromorphic effects, when the micromorphic setting with a partly deformable microstructure is chosen in the DE modelling approach. Secondly, the loss of microstructural information is investigated by varying the chosen REV size, thereby clearly pointing at the mesoscopic character of the microstructural ensemble. Throughout the following studies, the ratio between $d_\mathcal{R}$ and the mean particle diameter d_{50} of the particle size distribution is used to address the REV size. The homogenised quantities are visualised at the centre particle of the REV. Furthermore, scalar-valued norms of vector-valued as well as second- and third-order tensor-valued quantities serve as characteristic measures for the visualisations. In particular, $|\mathbf{a}|$ refers to the vector norm of $\mathbf{a}$, $||\mathbf{A}||$ is the spectral norm of $\mathbf{A}$, and $||\overset{3}{\mathbf{A}}||$ is is the largest spectral norm of the sub-coefficient matrices A_{1jk}, A_{2jk} and A_{3jk} of $\overset{3}{\mathbf{A}}$.

6.2.1 Detection of micromorphic effects

The complete averaging procedure is firstly undertaken for the uniaxial compression test simulation for the points ① and ② addressed in Figures 5.2 and 5.3. The overall results are given in Figure 6.3.

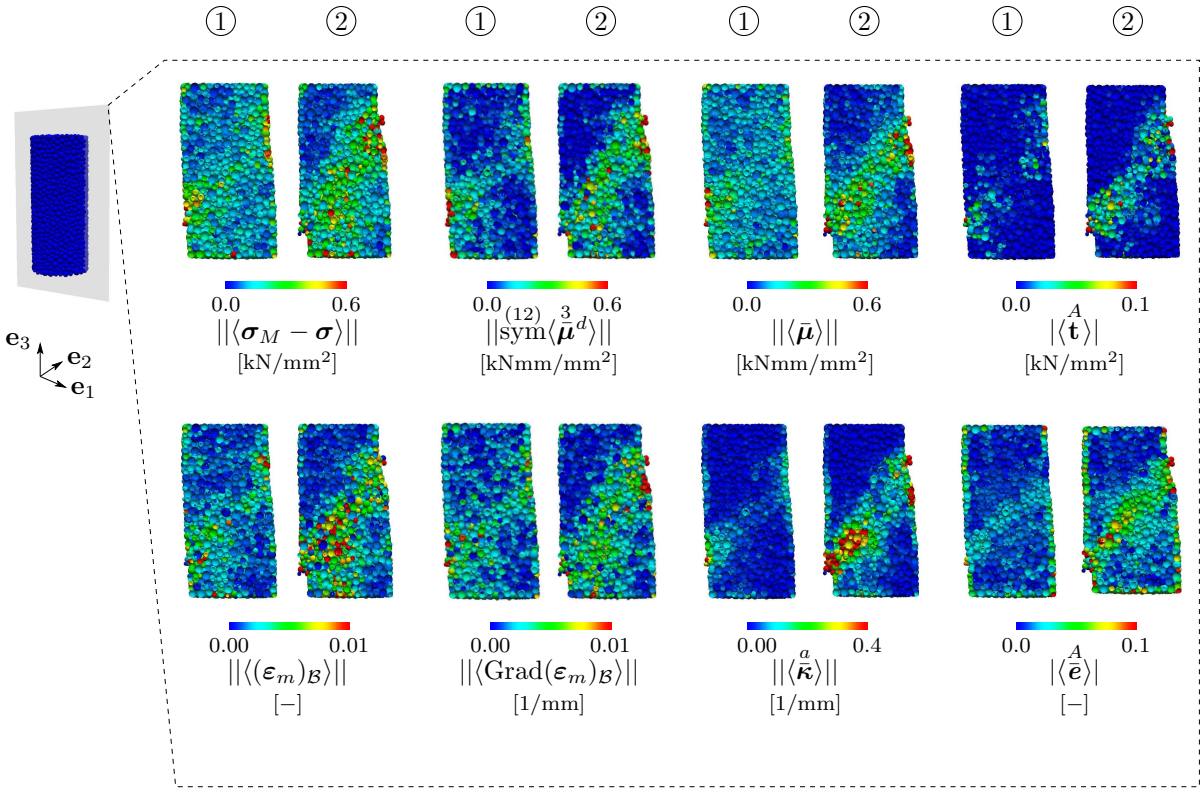

Figure 6.3: *Initially bonded material under uniaxial compression: Results of the homogenisation procedure for* $d_{\mathcal{R}}/d_{50} = 2.5$.

It is seen from the norm $||\langle(\boldsymbol{\sigma}_M - \boldsymbol{\sigma}\rangle|| \approx ||\langle \mathbf{T}_M - \mathbf{T} \rangle||$ as the micromorphic stress indicator (top left of Figure 6.3) that mircromorphic effects concentrate in the localisation zone. This result is obtained from a concentration of both norms, $||\langle(\boldsymbol{\sigma}_M\rangle||$ and $||\langle \boldsymbol{\sigma} \rangle||$, however, with different values at the onset and the evolution of the shear band. This can in particular be seen from the additional plot of the evolution of the norms $||\langle \boldsymbol{\sigma} \rangle||$ and $||\langle \boldsymbol{\sigma}_M \rangle||$ of selected REV over the complete simulation time, given on the left of Figure 6.4. Therein, the arithmetic means of the respective quantities of 30 REV, centred in the region of the shear band, are plotted and show the concentration with the onset of the shear band at around 0.04 global axial strain. Note furthermore that the second micromorphic stress indicator, the third-order dyadic stress moment $\langle \overset{3}{\tilde{\mathbf{M}}} \rangle$, as it incorporates the dyadic moment of the micromorphic stress difference, shows the same behaviour (right-hand side of Figure 6.4).

In addition to the stress difference, the avergaes of the symmetric part $\overset{(12)}{\text{sym}}\langle \overset{3}{\bar{\boldsymbol{\mu}}}^{d} \rangle$ of the 3-rd order dyadic stress moment and the couple stress $\langle \bar{\boldsymbol{\mu}} \rangle$ are also predominant in the localisation zone (top middle of Figure 6.3), where $||\overset{(12)}{\text{sym}}\langle \overset{3}{\bar{\boldsymbol{\mu}}}^{d} \rangle||$ and $||\langle \bar{\boldsymbol{\mu}} \rangle||$ address the microstrain and the micropolar contributions of the overall micromorphic behaviour in an additive manner. In agreement with the angular momentum balance, the occurrence of couple stresses coincides with the evolution of skew-symmetric stresses visualised via the norm of the averaged axial stress vector $\overset{A}{\langle \mathbf{t} \rangle}$ on the top right of Figure 6.3. However,

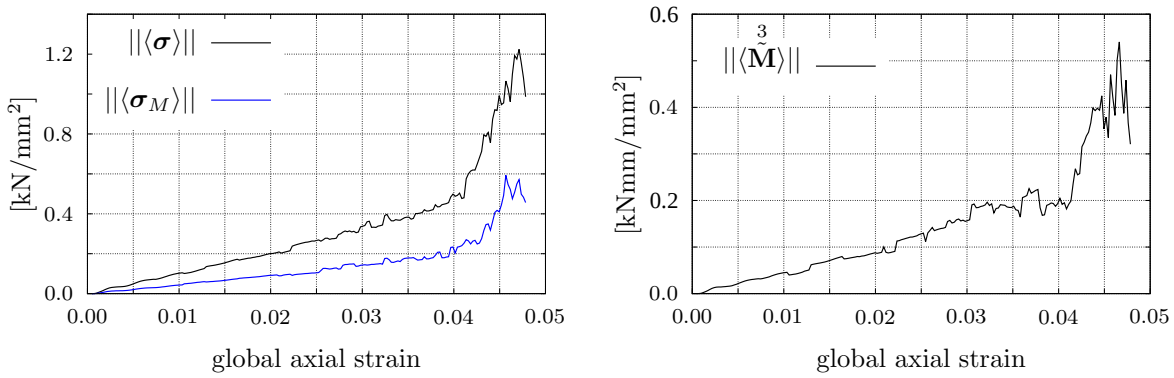

Figure 6.4: *Initially bonded material under uniaxial compression: Evolution of mean values of homogenised stress norms of 30 REV inside the shear band for* $d_{\mathcal{R}}/d_{50} = 2.5$.

the concentration of $|\langle\overset{A}{\mathbf{t}}\rangle|$ is not as smoothly distributed over the complete domain of the shearing zone, as this is the case for $||\langle\bar{\boldsymbol{\mu}}\rangle||$ and $||\langle\boldsymbol{\sigma}_M - \boldsymbol{\sigma}\rangle||$.

The second row of Figure 6.3 displays the norms of the significant corresponding averages of the kinematic measures, namely the microstrain average $\langle(\boldsymbol{\varepsilon}_m)_{\mathcal{B}}\rangle$ and its gradient, the averaged curvature $\langle\overset{a}{\bar{\boldsymbol{\kappa}}}\rangle$ and the axial vector $\langle\overset{A}{\bar{\boldsymbol{e}}}\rangle$ corresponding to the micromorphic strain average $\langle\bar{\boldsymbol{\varepsilon}}\rangle$. From these visualisations, the concentration of the respective quantities with the onset and the evolution is again clearly recognised.

A further insight into the role of the micromorphic extension of standard continua can be gained from the evaluation of the individual portions $W_i^{(sf)}$, $W_i^{(mp)}$ and $W_i^{(ms)}$ of the mechanical work W_i stemming from the internal forces according to (3.54), (3.57) and (3.59). In this regard, Figure 6.5 shows the internal mechanical work of 36 different REV at at the loading stage ① outside (top left) and inside (top right) the localised zone. Note that in Figure 6.5, the individual 36 REV samples have been arranged according to increasing values of $W_i^{(sf)}$.

It is obvious that higher total amounts of internal mechanical work are performed in the localised domain. However, the decomposition of the overall mechanical work W_i into its individual contributions, especially regarding the portions $W_i^{(mp)}$ and $W_i^{(ms)}$ as parts of the micromorphic setting, shows that the former plays a significant role, while the latter is of negligible size, especially, compared to the standard portion $W_i^{(sf)}$. A percentage-based segmentation of the different work contributions emerging additionally to the standard work $W_i^{(sf)}$, compare bottom right of Figure 6.5, shows that the largest portions stem from the mechanical work of the conjugated pair of couple stress and curvature.

6.2.2 Loss of microstructural information

In the preceding section, REV are evaluated for the size $d_{\mathcal{R}}/d_{50} = 2.5$, which results in approximately 10 particles collected in a REV. For the homogenisation of the uniaxial compression test on initially bonded material, this generally yields the most significant results concerning the detection of micromorphic effects. As these effects are of microstructural character, it is not astonishing that they are only detectable at a reasonable size,

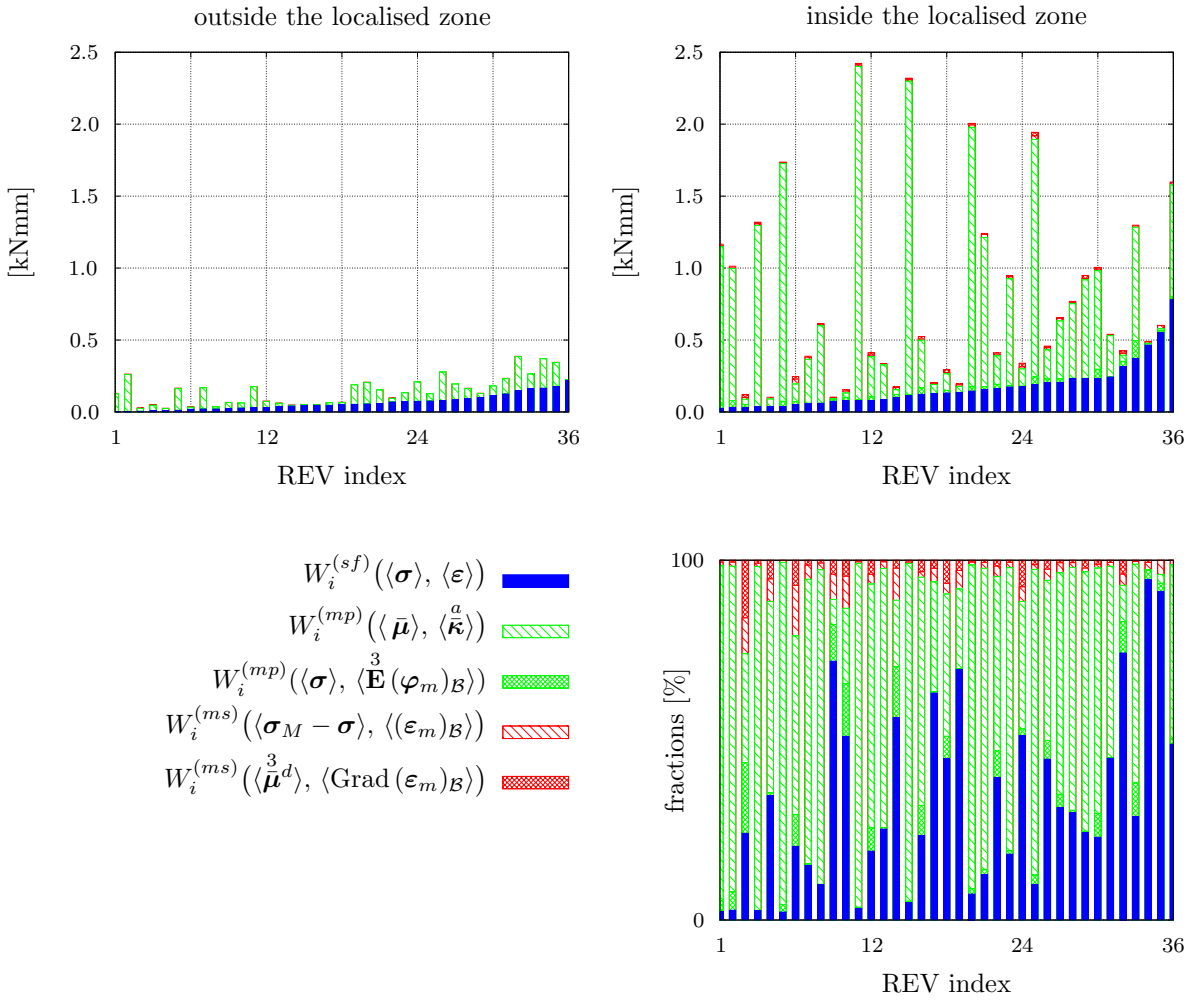

Figure 6.5: *Initially bonded material under uniaxial compression: Evaluation of the internal mechanical work at point ①, cf. Figure 5.2, of 36 REV in- and outside the localised zone for* $d_{\mathcal{R}}/d_{50} = 2.5$.

when they are obtained by homogenisation over reasonably small REV. For a detailed investigation on the role of the REV size, the averaging process is carried out for initially bonded material under biaxial compression (points ① and ② of Figure 5.5) for three different REV sizes: $d_{\mathcal{R}}/d_{50} = 2.2$ as the minimal size for geometrically reasonable REV with an average of 6 particles, $d_{\mathcal{R}}/d_{50} = 3.0$ with an average of 16 particles, and $d_{\mathcal{R}}/d_{50} = 3.7$ with an average of 30 particles, respectively. For simplicity, the investigation is restricted to the averaging of stress quantities. Figure 6.6 shows the evolution of micromorphic stress moments and stress differences at points ① and ② of Figure 5.5 for the different ratios of $d_{\mathcal{R}}/d_{50}$ for initially bonded material, exhibiting the onset and the evolution of the shear band. As can be seen from Figure 6.6, the identification of micromorphic effects is given in the regions of shear zones and shrinks with the increase of the homogenisation domain. The loss of the mircrostructural information is also seen in Figure 6.7, where the homogenisation over increasing REV sizes from $d_{\mathcal{R}}/d_{50} = 2$ up to values of $d_{\mathcal{R}}/d_{50} = 12$ is

displayed. Given Figure 6.7, a comparison of the plots of the homogenised micromorphic stress difference and the homogenised axial vector corresponding to $\langle \mathbf{T} \rangle$ both again taken as the arithmetic mean, now over a number of 15 REV centred in the shear zone, yields that the homogenisation results are rapidly shrinking from $d_{\mathcal{R}}/d_{50} = 2$ to $d_{\mathcal{R}}/d_{50} = 8$ and are then approximately constant at small values. This is not astonishing, as REV

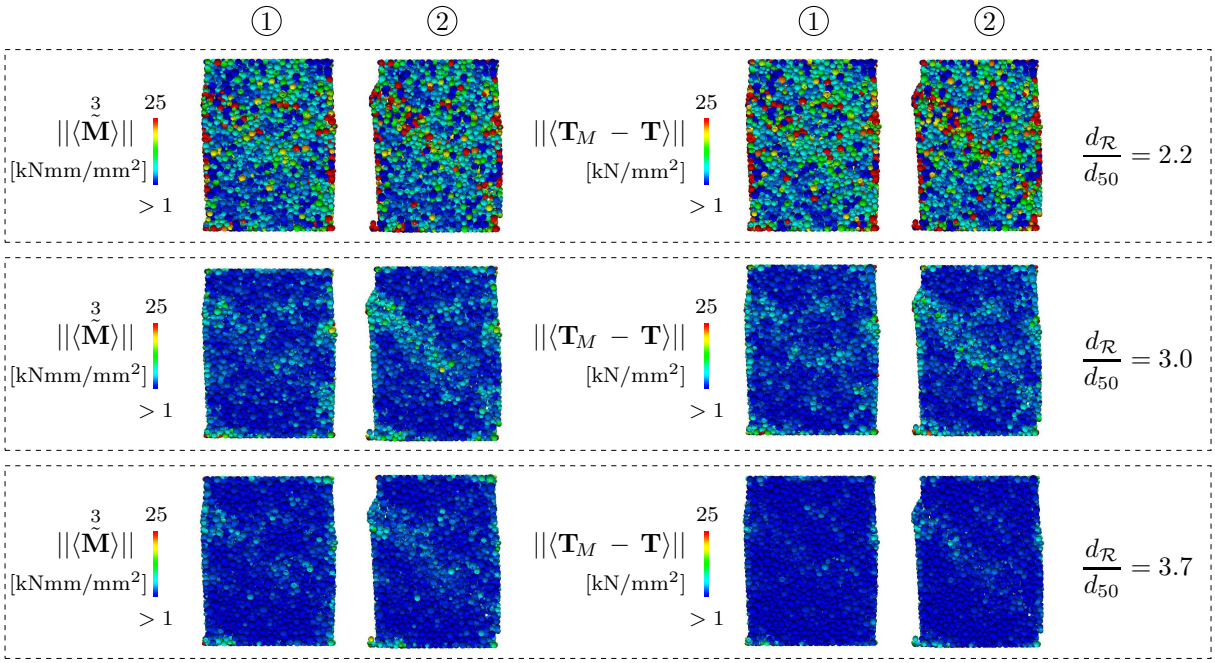

Figure 6.6: *Initially bonded material under biaxial compression: Norms of homogenised micromorphic stress moments and stress differences for varying REV sizes at the initiation of and in a fully evolved shear band (cf. points ① and ② of Figure 5.5).*

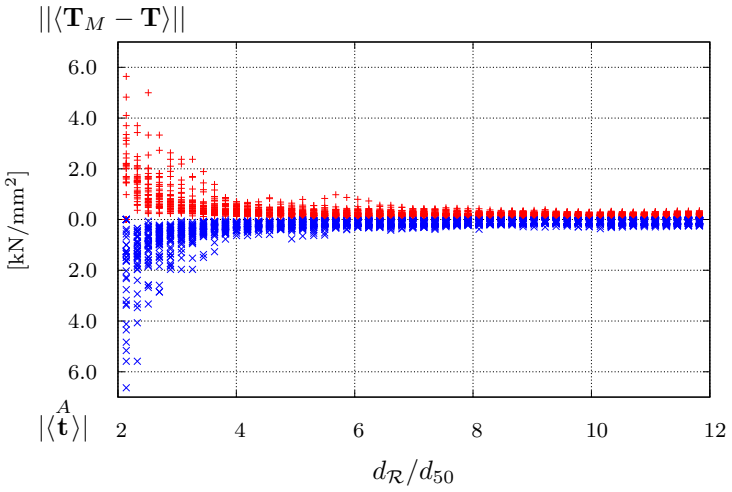

Figure 6.7: *Initially bonded material under biaxial compression: Loss of microstructural information with increasing REV size displayed for the amount of averaged micromorphic stress differences and axial stress vectors from the initially bonded particle model at point ②, cf. Figure 5.5, for a number of 15 REV inside the shear zone.*

with REV sizes larger than approximately $d_{\mathcal{R}}/d_{50} = 4$ not only collect particles inside the shear zone but also from outside, such that microstructural effects are, on the one hand, still noticeable but, on the other hand, nearly smeared out. From the evolution of the homogenised micromorphic stress moments, the micropolar couple stresses $\langle \bar{\mathbf{M}} \rangle$, the Cauchy stresses $\langle \mathbf{T} \rangle$, the particle stress averages $\langle \mathbf{T}_M \rangle$, and the axial vectors of $\langle \mathbf{T} \rangle$ and $\langle \mathbf{T}_M \rangle$, respectively, further effects are visible, when these values are displayed for the three considered REV sizes during the complete simulation time, cf. Figures 6.8 - 6.10. Results are thereby again plotted as mean values of 15 REV inside the primary region and 15 REV outside the primary and further secondary shear-zones. From these figures and especially from Figure 6.8, it is again clearly recognised that micromorphic effects

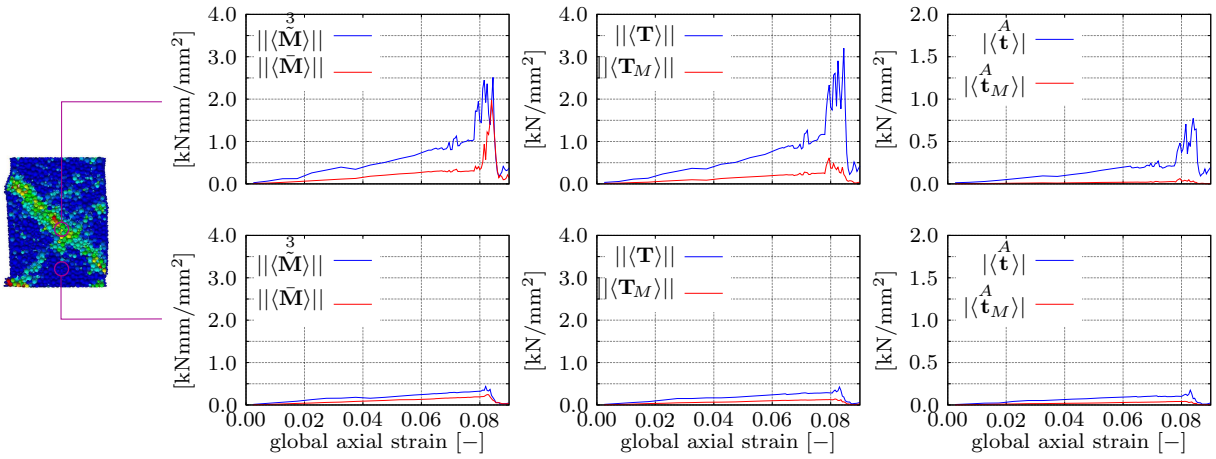

Figure 6.8: *Initially bonded material under biaxial compression: Evolution of mean values of homogenised stress quantities for a number of 15 REV in the marked regions in- and outside the localised zone for* $d_{\mathcal{R}}/d_{50} = 2.2$.

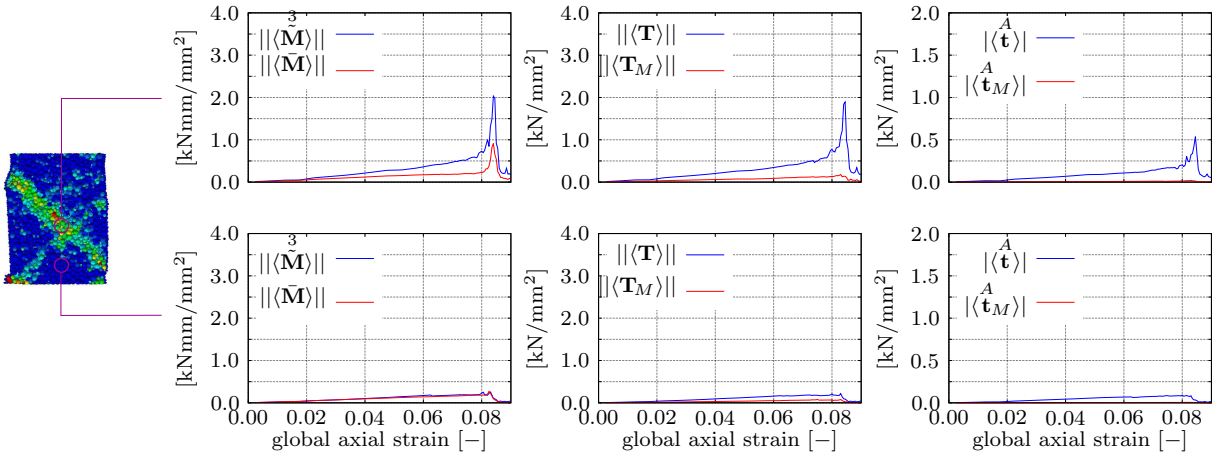

Figure 6.9: *Initially bonded material under biaxial compression: Evolution of mean values of homogenised stress quantities for a number of 15 REV in the marked regions in- and outside the localised zone for* $d_{\mathcal{R}}/d_{50} = 3.0$.

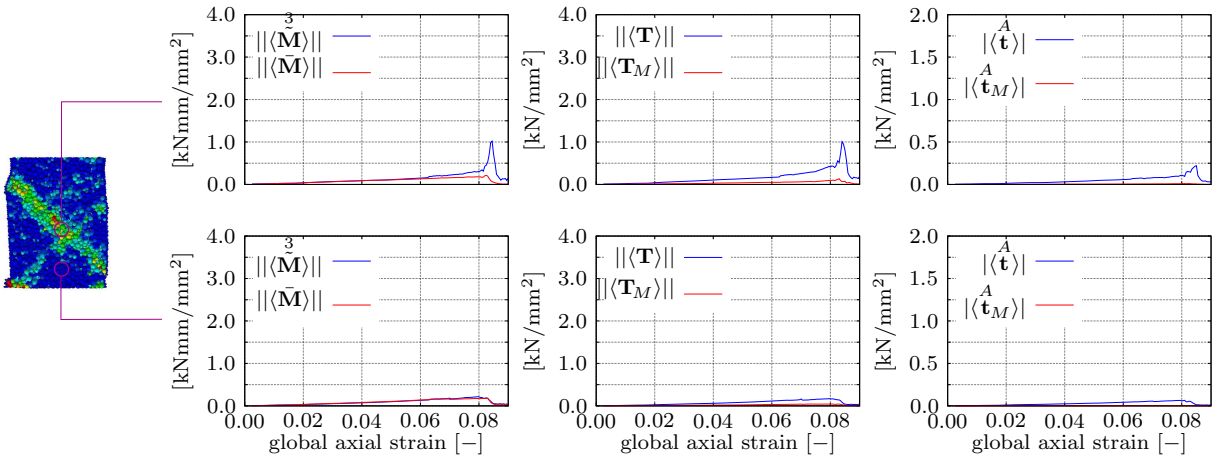

Figure 6.10: *Initially bonded material under biaxial compression: Evolution of mean values of homogenised stress quantities for a number of 15 REV in the marked regions in- and outside the localised zone for* $d_{\mathcal{R}}/d_{50} = 3.7$.

represented by the micromorphic stress moments and the micromorphic stress differences are dominant in the fully evolved shear band at a global axial strain of approximately 0.075, while their values are between very small and negligible outside the localisation domain. It is furthermore seen that micropolar effects displayed by $\langle \bar{\mathbf{M}} \rangle$ and the axial vector of $\langle \mathbf{T} \rangle$ are active at the same values of the global axial strain as are the micromorphic terms. Finally it is found that the axial vector of $\langle \mathbf{T}_M \rangle$ also vanishes numerically as $\mathbf{T}_M$ was theoretically found symmetric. Also note that all the effects described above are shrinking with increasing REV size, cf. Figures 6.9 and 6.10.

The above investigations clearly exhibit the mesoscopic character of micromorphic continua, where the microstructural information is only observed at higher spatial scales, when the REV size, or the respective number of particles summarised in a REV, is small enough to capture these fluctuations from the standard Cauchy continuum. This behaviour is typical for material with microstructural character as, for example, for micropolar and micromorphic material.

6.3 Micropolar setting

If the microstructural arrangement is restricted to rigid particles, the homogenisation strategy yields characteristic micropolar quantities on the REV scale, cf. Ehlers *et al.* [64]. These results can be reviewed by applying the averaging formalisms to the DE simulation of the biaxial compression test on initially unbonded material (micropolar setting). As in the preceding section, the same overall significant properties of microstructure-dependent materials are again found. Figure 6.11 shows the occurrence of micropolar couple stresses $\langle \bar{\mathbf{M}} \rangle$ in the shear zone and the accompanying skew-symmetric stress state of $\langle \mathbf{T} \rangle$. The effects are most clearly present for the smallest REV size $d_{\mathcal{R}}/d_{50} = 2.2$ and significantly decrease for the larger REV sizes $d_{\mathcal{R}}/d_{50} = 3.0$ and $d_{\mathcal{R}}/d_{50} = 3.7$. The corresponding

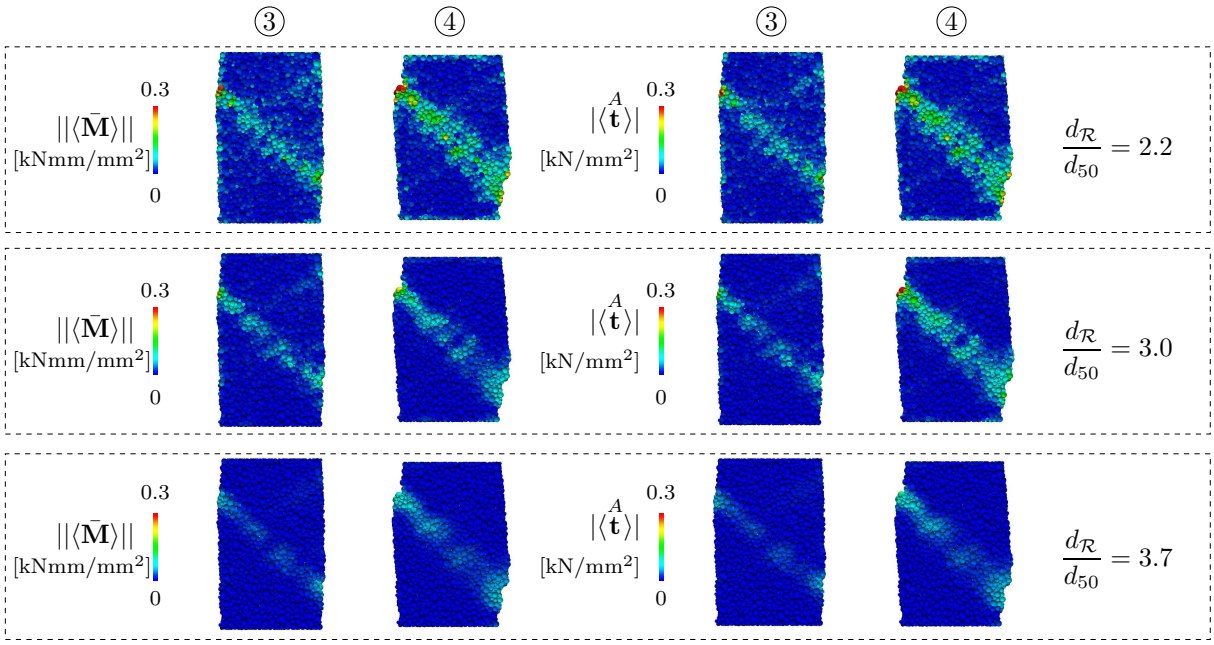

Figure 6.11: *Unbonded material under biaxial compression: Norms of homogenised micropolar couple stress and axial stress vector of the Cauchy stress for varying REV sizes at the initiation of and in a fully evolved shear band (cf. points ③ and ④ of Figure 5.5).*

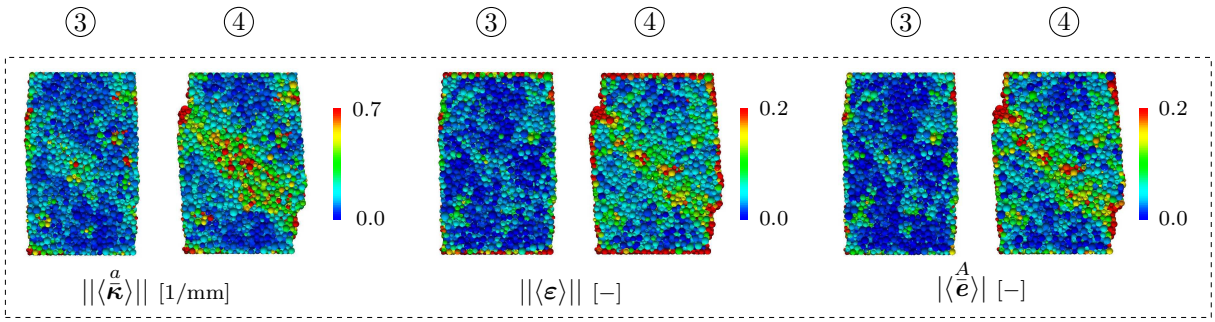

Figure 6.12: *Unbonded material under biaxial compression: Norms of the homogenised micropolar curvature, the symmetric part of the micropolar strain and the axial vector of the micropolar strain for $d_\mathcal{R}/d_{50} = 2.2$ at the initiation of and in a fully evolved shear band (cf. points ③ and ④ of Figure 5.5).*

averages of the deformation measures are displayed for $d_\mathcal{R}/d_{50} = 2.2$ for the onset (point ③) and for a fully evolved shear band (point ④) in Figure 6.12. Visualised on the left of Figure 6.12 is the norm of the micropolar curvature $\langle\overset{a}{\bar{\boldsymbol{\kappa}}}\rangle$. Here, a clear concentration is observed in the shear band, where the particles rotate, compare Figure 5.7. Due to higher relative displacements of the particles contained in a REV within the region of the shear band, the norm of the symmetric part of the micropolar strain, $\langle\bar{\boldsymbol{\varepsilon}}\rangle_{\text{sym}} = \langle\boldsymbol{\varepsilon}\rangle$ also shows higher values in the localising areas (Figure 6.12, middle). Moreover, the averaged micropolar strain $\langle\bar{\boldsymbol{\varepsilon}}\rangle$ also becomes skew-symmetric in these domains, as it is displayed

on the right of Figure 6.12, again by means of the norm of the axial vector $\langle \overset{A}{\bar{\boldsymbol{e}}} \rangle$ containing the skew-symmetric information of $\langle \bar{\boldsymbol{\varepsilon}} \rangle$.

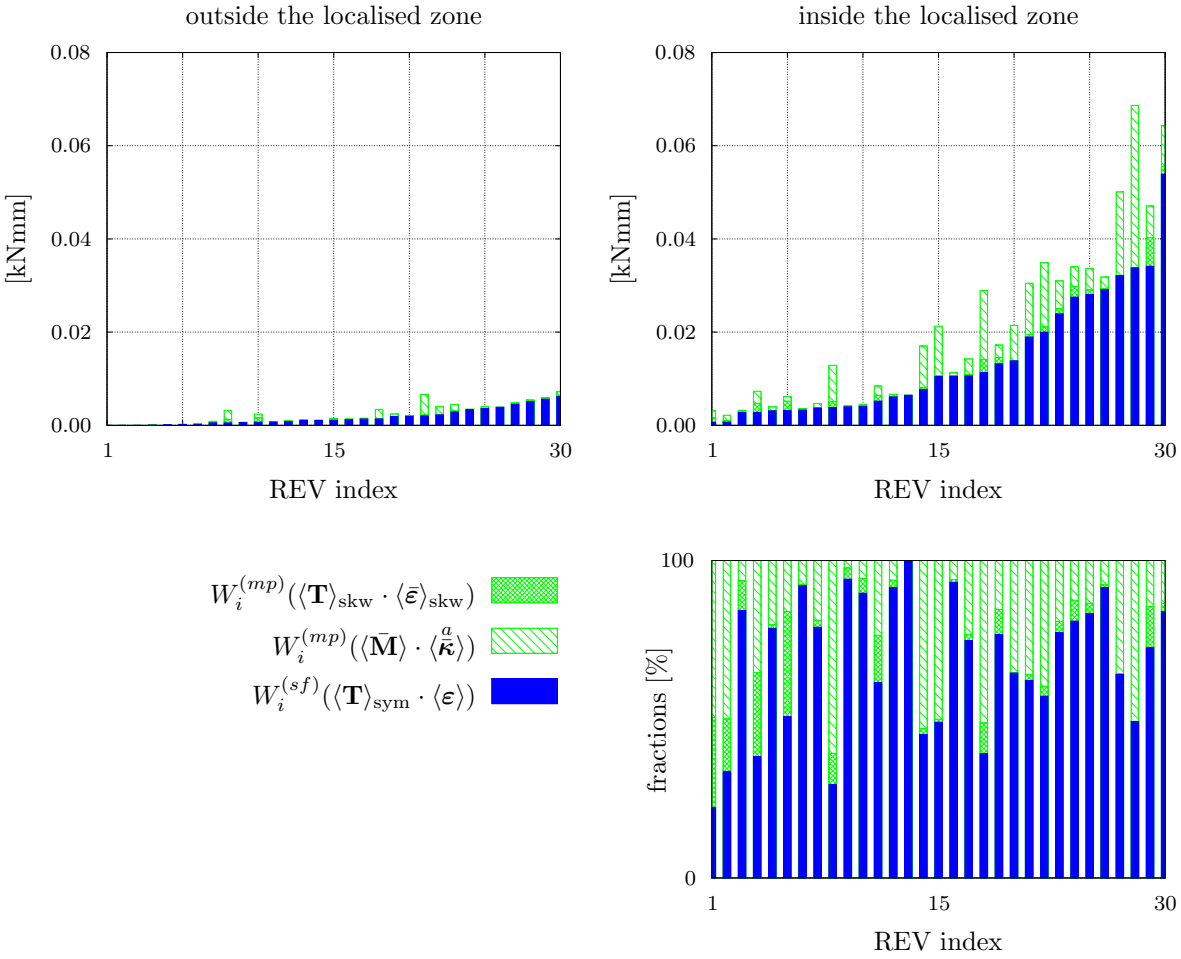

Figure 6.13: *Initially unbonded material under biaxial compression: Evaluation of the internal mechanical work of 30 REV in- and outside the localised zone for $d_{\mathcal{R}}/d_{50} = 3.0$ in a fully evolved shear band (cf. point ④ of Figure 5.5).*

An evaluation of the mechanical power of the internal forces of 30 REV centred in the shear zone and 30 REV selected outside the domain of the shear band is given in Figure 6.13. In the micropolar setting, a division into the standard Cauchy continuum part $W_i^{(sf)}$ and the extended micropolar part $W_i^{(mp)}$ is performed, where the latter is again split into a part stemming from the skew-symmetric stress-strain contribution and a part stemming from the pair of couple stress and micropolar curvature. Once more the differences between localising and non-localising domains are evident. Concerning the absolute amount of internal mechanical work, displayed in the top row of Figure 6.13, high total values are found inside the shear band, where stresses and strains concentrate, while significantly lower values are found outside the shear band. Moreover, as already recognised for the micromorphic setting, the extended micropolar parts of W_i significantly contribute to the overall internal mechanical work. This can clearly be observed from the proportional

representation of the different fractions of W_i given on the bottom right-hand side of Figure 6.13, showing that in some REV in the localisation zone up to 50% of the internal mechanical work is performed by the extended micropolar quantities.

Chapter 7:
Summary and conclusion

The main goal of this monograph was the development of a homogenisation strategy that links particle-based information with macroscopic quantities within the framework of microcontinuum theories. Therefore, it was firstly necessary to foster the continuum-mechanical understanding of kinematically extended theories. This was done by deriving the basic relations for the kinematic description, the stress state and the governing balance relations in a structured way. The starting point was a short introduction of the standard Cauchy continuum description, followed by the micropolar extension and finally giving a more detailed review of the micromorphic continuum formulation in the sense of Eringen [71]. Thereby, the application of micromorphic-continuum properties generally allows for the consideration of microstructural effects in continuum-based modelling approaches through the introduction of a microcontinuum with an associated length scale. The distinction between the micropolar and the micromorphic case lies in the assumption whether the attached microcontinuum is rigid (micropolar) or homogeneously deformable (micromorphic). However, it should be stressed that the micromorphic and the micropolar continuum are still purely macroscopic continuum-mechanical approaches, where, for example, the micro- and the macrodeformation gradient are still averaged quantities and the resulting model remains a phenomenological one.

In what followed, the focus was thus on how to directly compute these averaged quantities based on the introduction of a mesoscopic particle-centre-based REV description, introduced between the microscale of the individual grain and the macroscale of the overall continuum body. The application of the MMM principle and the assumption of scale separation between the three considered scales thereby simplified the balance relations for embedded REV and particles. This ultimately lead to the possibility of deriving direct averaging formalisms between the microstructural particle-based information and micromorphic quantities on the mesoscopic REV scale. The physical link between the granular microstructure and the micromorphic continuum was thereby established between two levels: Firstly, forces and stresses at the particle-scale are linked to the extended stress states of micromorphic type, and, secondly, local particle deformation, displacement and rotation at the particle-scale are linked to the extended deformation measures of micromorphic continua. In the latter case, the multiscale connection is given in a rather straightforward manner, when a particle, theoretically assumed as being homogeneously deformable, is embedded into a mesoscopic REV, and the thereby obtained coupled kinematic relations are derived. Adopting a geometrically linear point of view thereby enabled an additive decomposition of the micromorphic strain into standard and extended micropolar and micromorphic contributions. On the interaction-stress level, a stress homogenisation was possible due to the formulation of averaged stress measures for the REV that are linearly depending on a homogeneous particle deformation at the microscale. In particular, these are the particle stress average $\mathbf{T}_M$, the couple stress $\bar{\mathbf{M}}$ and the third-order dyadic stress

moment $\overset{3}{\mathbf{M}}{}^{d}_{M}$, which serve as indicators for the detection of micromorphic and micropolar quantities.

In order to verify the established strategy, particle-based simulations of material failure in granular media were necessary, in order to provide the microstructural information, which can then be processed towards the REV scale. A DE model using a spherical particle representation was therefore set up. While the usage of unbonded grains in combination with constitutive contact formulations for normal and tangential contact forces represented a suitable setting to detect micropolar effects, the consideration of deformable binder or matrix material, modelled via deformable beam elements connecting neighbouring particles, was additionally incorporated in order to extend the setting towards micromorphic material behaviour. The idealised model allowed for the transition of the continuously formulated averages towards discrete forms of the stress and strain averages, where only a finite number of particles forming an REV need evaluation. Concerning the deformation homogenisation, the gradient of relative displacement of the REV-boundary particles contributes to the strain on the REV scale, while the gradient of the particle rotation averages towards an REV curvature measure. Furthermore, a so-called microstrain average can be found from a two-step averaging process. First, the average of the homogeneous local deformation of the particles, given by the deformation of the connecting beam elements, yields the homogeneous particle strain. Second, this strain is again be averaged volumetrically within the REV in order to obtain a micromorphic-type microstrain average on the REV level. In a similar way, the microstress average is found based on the particle stress average and a subsequent second average with respect to all particles in the REV. Overall, the homogenisation enabled to identify micromorphic indicators on the stress and the deformation level.

As it is well known that micropolar effects play an important role in localising granular material, the main focus of the DE computations was on the simulation of shear-banding phenomena. As exemplarily materials, unbonded and bonded Quartz sand were chosen, the latter being a frequently used material for sand-based moulds in metal casting applications. The clear initiation and the full evolution of shear-bands was successfully simulated for both settings. In particular, simulations of uniaxial compression and tension tests on initially bonded material and biaxial compression tests on initially bonded and unbonded material were performed.

The application of the homogenisation strategy to the results of the DE simulations revealed the following key points: As in the case of micropolar continua, the extended stress and kinematic states of micromorphic material are predominant in localised zones, while the REV size correlates to the intrinsic length scale. The size of a locally constructed REV is furthermore the critical quantity for the evaluation and the existence of micromorphic and micropolar stresses at a higher spatial scale. A study with different REV sizes revealed a loss of microstructural information with increasing REV sizes.

By means of the balance of mechanical power of an REV, it was furthermore possible to identify the work-conjugated pairs of averaged stress and deformation quantities. The evaluation of the performed mechanical work of REV in the shear zone provided an additional important insight into the necessities of considering microcontinuum extensions when choosing a macroscopic modelling approach: While the micropolar extension

significantly contributes to the overall mechanical work, the same is not true for the additional microstrain contribution that extends the description towards a fully micromorphic model. Whether these effects are more pronounced for other granular materials, for example mixtures of rigid grains and highly deformable particles, such as gel-type ones, would be one interesting question to be further investigated for the future application of the derived homogenisation approach. In addition to the micromorphic setting, where parts of the microstructure are considered as deformable, the established homogenisation strategy incorporates the special case of the micropolar continuum, when the microstructure consists solely of rigid particles. In this regard, it should be recognised that a clear additive decomposition of the micromorphic contributions into micropolar and microstrain contributions, where the first incorporates only particle-scale rotations and the latter only particle-scale stretches, is not fully possible, as the micropolar couple stresses $\bar{\mathbf{M}}$ are immediately dependent on the particle deformation, if these are allowed in the modelling approach.

A significant drawback of the presented work lies in the necessity of particle-based computations of complete IBVP. In combination with the requirement of quasi-static simulations of material tests, where the loading rate in the simulation needs to correspond to the rate of loading used in the experiment, this leads to a significantly high total number of computational time steps, even if the number of considered discrete elements is quiet small. Note that in this regard full-scale simulations of the small-scale triaxial compression tests with approximately 50 000 particles, given in Desrues & Andò [46], were also performed. However, no further significant findings were obtained in comparison to the smaller biaxial compression test simulations. The results are therefore not documented within this monograph. In particular, the wish to step from a qualitative simulation towards quantitative results could not be met without further parameter calibration, as the global stress-strain path could not be directly reproduced. This might be due to the simplified usage of a spherical particle representation, where the influence of the grain shape on the macroscopic strength of the material is ignored. Although a rotational resistance model was investigated to overcome the shape simplification, the results were not satisfactory in this regard. The shear-band width of angular-shaped granular material, such as Hostun sand, could not be reproduced by a variation of the shape parameter of the rotational resistance model. As pointed out by Wensrich & Katterfeld [217], this might be due to the fact that rolling resistance always initially hinders a rotational motion and only causes co-rotations once a rotational motion is active. In this regard, Kawamoto *et al.* [132] achieved a direct numerical representation of the small-scale triaxial test of Desrues & Andò [46] using arbitrarily shaped particles based on a level-set DE representation.

Alternatively to this DNS approach, a challenging future task lies in the application of the proposed homogenisation technique within an embedded FEM $\times$ DEM strategy in order to be able to simulate unscaled experimental tests and even application-scale problems. Thereby, the macroscale continuum body would exhibit the micromorphic character, while the microscale DE model would still be of Cauchy-continuum type. Although such strategies are generally available and can be found in the literature, see, for example, Biswas & Poh [24] or Jänicke *et al.* [120], many technical aspects of such a combined multiscale strategy are yet not accounted for, if a DE model is chosen as the microscale

model. Among these are the question whether non-periodic REV, such as the here used particle-centre-based REV, can be treated and the issue how to consistently prescribe the extended boundary and volumetric deformation mechanisms from the application scale onto the mesoscale of the particle-based REV and onto the individual particles. In this field, first promising attempts to consider a DE-model in combination with an extended continuum description on the macroscale are underway, cf. Desrues *et al.* [47].

Appendix A:
Selected tensor calculus

Without going into the detailed derivations, the following Appendix gives a collection of selected tensor algebra and analysis that are necessary for the handling of the operations conducted throughout this monograph. A more detailed and completed introduction can be found in Ehlers [59].

A.1 Tensor algebra

Arbitrary placeholders are introduced, where

$$\begin{array}{lll} \{\,\alpha\,,\ \beta\,\} & \in \mathbb{R} & \text{are rational scalars (zeroth-order tensors),} \\ \{\,\mathbf{u},\,\mathbf{v},\,\mathbf{w},\,\mathbf{y}\,\} & \in \mathcal{V}^3 & \text{are vectors (first-order tensors) of the proper} \\ & & \text{Euklidian 3-d vector space } \mathcal{V}^3 \\ \{\,\mathbf{A}\,,\ \mathbf{B}\,,\ \mathbf{C}\,\} & \in \mathcal{V}^3 \otimes \mathcal{V}^3 & \text{are second-order tensors of the corresponding} \\ & & \text{dyadic product space } \mathcal{V}^3 \otimes \mathcal{V}^3, \\ \{\,\overset{3}{\mathbf{A}}\,\} & \in \mathcal{V}^3 \otimes \mathcal{V}^3 \otimes \mathcal{V}^3 & \text{is a third-order tensor of the corresponding} \\ & & \text{dyadic product space } \mathcal{V}^3 \otimes \mathcal{V}^3 \otimes \mathcal{V}^3. \end{array} \tag{A.1}$$

Selected rules for second-order tensors are given for products of tensors with scalars or vectors via associated and distributive laws as

$$\begin{aligned} \alpha\,(\,\beta\,\mathbf{A}\,) &= (\,\alpha\,\beta\,)\,\mathbf{A} \\ \mathbf{A}\,(\,\alpha\,\mathbf{u}\,) &= \alpha\,(\,\mathbf{A}\,\mathbf{u}\,) = (\,\alpha\,\mathbf{A}\,)\,\mathbf{u} \\ (\,\alpha\,+\,\beta\,)\,\mathbf{A} &= \alpha\,\mathbf{A} + \beta\,\mathbf{B} \\ \mathbf{A}\,(\,\mathbf{u}+\mathbf{v}\,) &= \mathbf{A}\,\mathbf{u} + \mathbf{A}\,\mathbf{v} \\ (\,\mathbf{A}+\mathbf{B}\,)\,\mathbf{u} &= \mathbf{A}\,\mathbf{u} + \mathbf{B}\,\mathbf{u} \\ \alpha\,\mathbf{A} &= \mathbf{A}\,\alpha \\ \mathbf{u} &= \mathbf{A}\,\mathbf{v}\,. \end{aligned} \tag{A.2}$$

The expansion theorem for vectors reads

$$\mathbf{u} \times (\,\mathbf{v} \times \mathbf{w}\,) = (\mathbf{u}\cdot\mathbf{w}\,)\,\mathbf{v} - (\,\mathbf{u}\cdot\mathbf{v}\,)\,\mathbf{w}\,. \tag{A.3}$$

Scalar (inner) products of tensors read

$$\begin{aligned} (\,\alpha\,\mathbf{A}\,)\cdot\mathbf{B} &= \mathbf{A}\cdot(\,\alpha\,\mathbf{B}\,) = \alpha\,(\,\mathbf{A}\cdot\mathbf{B}\,) \\ \mathbf{A}\cdot(\,\mathbf{B}+\mathbf{C}\,) &= \mathbf{A}\cdot\mathbf{B} + \mathbf{A}\cdot\mathbf{C} \\ \mathbf{A}\cdot\mathbf{B} &= \mathbf{B}\cdot\mathbf{A} \\ \mathbf{A}\cdot\mathbf{B} &= 0 \quad \forall\,\mathbf{A}\,,\ \text{if } \mathbf{B}\equiv\mathbf{0} \\ \mathbf{A}\cdot(\,\mathbf{u}\otimes\mathbf{v}\,) &= \mathbf{u}\cdot\mathbf{A}\,\mathbf{v}\,. \end{aligned} \tag{A.4}$$

The tensor product of tensors shows associated, distributive and non-commutative relations, viz.:

$$\begin{aligned}
\alpha\,(\,\mathbf{A}\,\mathbf{B}\,) &= (\,\alpha\,\mathbf{A}\,)\,\mathbf{B} = \mathbf{A}\,(\,\alpha\,\mathbf{B}\,)\\
(\,\mathbf{A}\,\mathbf{B}\,)\,\mathbf{u} &= \mathbf{A}\,(\,\mathbf{B}\,\mathbf{u}\,)\\
(\,\mathbf{A}\,\mathbf{B}\,)\,\mathbf{C} &= \mathbf{A}\,(\,\mathbf{B}\,\mathbf{C}\,)\\
\mathbf{A}\,(\,\mathbf{B}+\mathbf{C}\,) &= \mathbf{A}\,\mathbf{B}+\mathbf{A}\,\mathbf{C}\\
\mathbf{A}\,\mathbf{B} &\neq \mathbf{B}\,\mathbf{A}\\
\mathbf{I}\,\mathbf{A} &= \mathbf{A}\,\mathbf{I} = \mathbf{A}\\
\mathbf{0}\,\mathbf{A} &= \mathbf{A}\,\mathbf{0} = \mathbf{0}\\
(\,\mathbf{u}\otimes\mathbf{v}\,)\,(\,\mathbf{w}\otimes\mathbf{y}\,) &= (\,\mathbf{v}\cdot\mathbf{w}\,)\,(\,\mathbf{u}\otimes\mathbf{y}\,)\,.
\end{aligned} \tag{A.5}$$

The transposed tensors follow the relations

$$\mathbf{u}\cdot(\,\mathbf{A}\,\mathbf{v}\,) = (\,\mathbf{A}^T\,\mathbf{u}\,)\cdot\mathbf{v} \tag{A.6}$$

$$\mathbf{B}\cdot(\,\overset{3}{\mathbf{A}}\,\mathbf{u}\,) = (\,\overset{3\;13}{\mathbf{A}^T}\,\mathbf{B}^T\,)\cdot\mathbf{u} \tag{A.7}$$

and furthermore

$$\begin{aligned}
(\,\mathbf{u}\otimes\mathbf{v}\,)^T &= (\,\mathbf{v}\otimes\mathbf{u}\,)\\
(\,\alpha\,\mathbf{A}\,)^T &= \alpha\,\mathbf{A}^T\\
(\,\mathbf{A}\,\mathbf{B}\,)^T &= \mathbf{B}^T\,\mathbf{A}^T\\
\mathbf{A}\cdot(\mathbf{B}\,\mathbf{C}\,) &= (\,\mathbf{A}^T\,\mathbf{B}\,)\cdot\mathbf{C}\\
(\,\mathbf{A}+\mathbf{B}\,)^T &= \mathbf{A}^T+\mathbf{B}^T\,.
\end{aligned} \tag{A.8}$$

A second-order tensor is symmetric, if $\mathbf{A}=\mathbf{A}^T$, and skew-symmetric, if $\mathbf{A}=-\mathbf{A}^T$, and can be split into a symmetric part $\mathbf{A}_{\mathrm{sym}}$ and a skew-symmetric part $\mathbf{A}_{\mathrm{skw}}$, where

$$\mathbf{A}_{\mathrm{sym}} = \tfrac{1}{2}(\,\mathbf{A}+\mathbf{A}^T\,) \quad\text{and}\quad \mathbf{A}_{\mathrm{skw}} = \tfrac{1}{2}(\,\mathbf{A}-\mathbf{A}^T\,) \quad\text{with}\quad \mathbf{A} = \mathbf{A}_{\mathrm{sym}}+\mathbf{A}_{\mathrm{skw}}\,. \tag{A.9}$$

The inverse tensor is given by

$$\mathbf{A}^{-1} = (\det\mathbf{A}\,)^{-1}\operatorname{cof}\mathbf{A} \quad\rightarrow\quad \mathbf{A}^{-1}\text{ exists if }\det\mathbf{A}\neq\mathbf{0}\,, \tag{A.10}$$

where $\operatorname{cof}\mathbf{A}$ is the cofactor of $\mathbf{A}$. The inverse tensor obeys to the rules

$$\begin{aligned}
\mathbf{A}\,\mathbf{A}^{-1} &= \mathbf{A}^{-1}\,\mathbf{A} = \mathbf{I}\\
(\,\mathbf{A}^{-1}\,)^T &= (\,\mathbf{A}^T\,)^{-1} =: \mathbf{A}^{T-1}\\
(\,\mathbf{A}\,\mathbf{B}\,)^{-1} &= \mathbf{B}^{-1}\,\mathbf{A}^{-1}\,.
\end{aligned} \tag{A.11}$$

The **second-order fundamental tensor**, or identity tensor, $\mathbf{I}$ represents an identical map, if applied to an arbitrary vector $\mathbf{u}$ or an arbitrary tensor $\mathbf{A}$:

$$\mathbf{u} = \mathbf{I}\,\mathbf{u}\,, \quad \mathbf{A} = \mathbf{I}\,\mathbf{A} \quad\text{with}\quad \mathbf{I} := \delta_{ij}\,\mathbf{e}_i\otimes\mathbf{e}_j\,, \tag{A.12}$$

where δ_{ij} is the Kronecker symbol, which takes the value 1 for $i = j$ and the value 0 for $i \neq j$.

The **third-order fundamental tensor** (Ricci tensor) and the **axial vector** follow the relations

$$\begin{aligned} \mathbf{u} \times \mathbf{v} &= \overset{3}{\mathbf{E}}(\mathbf{u} \otimes \mathbf{v}) && \text{where } \overset{3}{\mathbf{E}} \text{ is the Ricci permutation tensor cf. (A.14),} \\ \mathbf{A} \times \mathbf{B} &= \overset{3}{\mathbf{E}}(\mathbf{A}\,\mathbf{B}^T) && \text{with the special case } \mathbf{I} \times \mathbf{B} = \overset{3}{\mathbf{E}}\,\mathbf{B}^T = 2\overset{A}{\mathbf{b}} \text{ and} \\ \operatorname{axl}\mathbf{B} = \overset{A}{\mathbf{b}} &= \tfrac{1}{2}\overset{3}{\mathbf{E}}\,\mathbf{B}^T && \text{as the axial vector of } \mathbf{B}. \end{aligned} \tag{A.13}$$

In index notation, the properties of the permutation tensor are given as

$$\begin{aligned} &\overset{3}{\mathbf{E}} = e_{ijk}(\mathbf{e}_i \otimes \mathbf{e}_j \otimes \mathbf{e}_k) \quad \text{with the permutation symbol } e_{ijk}, \\ &\text{where } e_{ijk} = \begin{cases} 1 & : \text{ even permutation} \\ -1 & : \text{ odd permutation} \\ 0 & : \text{ double indexing.} \end{cases} \quad \begin{aligned} &e_{123} = e_{231} = e_{312} = 1 \\ &e_{321} = e_{213} = e_{132} = -1 \end{aligned} \end{aligned} \tag{A.14}$$

Second-order axial tensors $\overset{A}{\mathbf{A}}$ to arbitrary third-order tensors $\overset{3}{\mathbf{A}}$ are given by

$$\overset{A}{\mathbf{A}} = -\tfrac{1}{2}(\overset{3}{\mathbf{E}}\overset{3}{\mathbf{A}})^{\underline{2}}, \tag{A.15}$$

where $\overset{A}{\mathbf{A}}$ corresponds to the skew-symmetric tensor part $\overset{3}{\mathbf{A}}_{\text{sym}} = -\overset{3}{\mathbf{A}}^{\overset{12}{T}}$ and $\overset{A}{\mathbf{A}}$ uniquely reduces $\overset{3}{\mathbf{A}}_{\text{sym}}$ towards a second-order tensor. Finally, for the case of $\mathbf{u}$ being an axial vector, the relation $\mathbf{u} \times \mathbf{I} = -\overset{3}{\mathbf{E}}\mathbf{u}$ leads to

$$\overset{3}{\mathbf{E}}(\mathbf{u} \times \mathbf{I}) = -\overset{3}{\mathbf{E}}(\overset{3}{\mathbf{E}}\,\mathbf{u}) = -(\overset{3}{\mathbf{E}}\overset{3}{\mathbf{E}})^{\underline{2}}\mathbf{u} \overset{!}{=} -2\,\mathbf{u} \quad \rightarrow \quad (\overset{3}{\mathbf{E}}\overset{3}{\mathbf{E}})^{\underline{2}} = 2\,\mathbf{I}. \tag{A.16}$$

Each third-order tensor $\overset{3}{\mathbf{A}}$ with a skew-symmetric part $\overset{(12)}{\operatorname{skw}}\overset{3}{\mathbf{A}}$ has an associated axial tensor $\overset{a}{\mathbf{A}}$ of second order and the following rules hold:

$$\begin{aligned} &\overset{a}{\mathbf{A}} := \operatorname{axl}\overset{3}{\mathbf{A}} = \tfrac{1}{2}(\overset{3}{\mathbf{E}}\overset{3}{\mathbf{A}}^{\overset{12}{T}})^{\underline{2}} = -\tfrac{1}{2}(\overset{3}{\mathbf{E}}\overset{3}{\mathbf{A}})^{\underline{2}}, \\ &\overset{(12)}{\operatorname{skw}}\overset{3}{\mathbf{A}} = -(\overset{3}{\mathbf{E}}\overset{a}{\mathbf{A}})^{\underline{3}} = \tfrac{1}{2}[\,\overset{3}{\mathbf{E}}(\overset{3}{\mathbf{E}}\overset{3}{\mathbf{A}})^{\underline{2}}\,]^{\underline{3}} = \tfrac{1}{2}[\,(\overset{3}{\mathbf{E}}\overset{3}{\mathbf{E}})^{\underline{4}}\overset{3}{\mathbf{A}})\,]^{\underline{3}} = \tfrac{1}{2}(\overset{3}{\mathbf{A}} - \overset{3}{\mathbf{A}}^{\overset{12}{T}}), \end{aligned} \tag{A.17}$$

where (A.19) has been used

Fourth-order fundamental tensors are constructed from dyadic products of second-order fundamental tensors. By additional transpositions $(\cdot)^{\overset{ij}{T}}$, representing an exchange of the i-th and j-th basis systems, three fourth-order fundamental tensors are given by

$$\begin{aligned} (\mathbf{I} \otimes \mathbf{I})^{\overset{23}{T}}\mathbf{A} &= \overset{4}{\mathbf{I}}\,\mathbf{A} = \mathbf{A}, && \text{the identical map,} \\ (\mathbf{I} \otimes \mathbf{I})^{\overset{24}{T}}\mathbf{A} &= \mathbf{A}^T, && \text{the transposing map and} \\ (\mathbf{I} \otimes \mathbf{I})\,\mathbf{A} = (\mathbf{A} \cdot \mathbf{I})\,\mathbf{I} &= (\operatorname{tr}\mathbf{A})\,\mathbf{I}, && \text{the tracing map.} \end{aligned} \tag{A.18}$$

Furthermore, a map of the third-oder fundamental tensor towards a fourth-order tensor results in

$$(\overset{3}{\mathbf{E}}\overset{3}{\mathbf{E}})^{\underline{4}} = (\mathbf{I}\otimes\mathbf{I})^{\overset{23}{T}} - (\mathbf{I}\otimes\mathbf{I})^{\overset{24}{T}}. \tag{A.19}$$

A.2 Tensor analysis

The spatial derivative of a field function with respect to the position $\mathbf{x}$ yields its gradient $\operatorname{grad}(\bullet)$. The gradient of scalar-valued functions $\alpha(\mathbf{x})$, vector-valued functions $\mathbf{u}(\mathbf{x})$ and tensor-valued functions $\mathbf{A}(\mathbf{x})$ read

$$\operatorname{grad}\alpha(\mathbf{x}) = \frac{\mathrm{d}\alpha(\mathbf{x})}{\mathrm{d}\mathbf{x}}, \quad \operatorname{grad}\mathbf{u}(\mathbf{x}) = \frac{\mathrm{d}\mathbf{u}(\mathbf{x})}{\mathrm{d}\mathbf{x}} \quad \text{and} \quad \operatorname{grad}\mathbf{A}(\mathbf{x}) = \frac{\mathrm{d}\mathbf{A}(\mathbf{x})}{\mathrm{d}\mathbf{x}}. \tag{A.20}$$

respectively. The divergence $\operatorname{div}(\bullet)$ of a vector-valued and a tensor-valued field function follows as

$$\operatorname{div}\mathbf{u}(\mathbf{x}) = \operatorname{grad}\mathbf{u}(\mathbf{x}) \cdot \mathbf{I} \quad \text{and} \quad \operatorname{div}\mathbf{A}(\mathbf{x}) = [\operatorname{grad}\mathbf{A}(\mathbf{x})]\,\mathbf{I}. \tag{A.21}$$

Selected identities for gradient and divergence operations are

$$\operatorname{grad}(\mathbf{A}\,\mathbf{v}) = (\operatorname{grad}\mathbf{A})^{\overset{23}{T}}\,\mathbf{v} + \mathbf{A}\operatorname{grad}\mathbf{v} \tag{A.22}$$

$$\operatorname{grad}(\mathbf{A}\,\mathbf{B}) = [(\operatorname{grad}\mathbf{A})^{\overset{23}{T}}\,\mathbf{B}]^{\underline{3}\overset{23}{T}} + (\mathbf{A}\operatorname{grad}\mathbf{B})^{\underline{3}} \tag{A.23}$$

$$\operatorname{div}(\mathbf{v}\times\mathbf{A}) = \mathbf{v}\times\operatorname{div}\mathbf{A} + \operatorname{grad}\mathbf{v}\times\mathbf{A} \tag{A.24}$$

$$\operatorname{div}(\mathbf{v}\otimes\mathbf{A}) = \mathbf{v}\otimes\operatorname{div}\mathbf{A} + (\operatorname{grad}\mathbf{v})\,\mathbf{A}^T \tag{A.25}$$

$$\operatorname{div}(\mathbf{v}\otimes\overset{3}{\mathbf{A}}) = \mathbf{v}\otimes\operatorname{div}\overset{3}{\mathbf{A}} + [(\operatorname{grad}\mathbf{v})(\overset{3}{\mathbf{A}}^{\overset{13}{T}})^{\overset{23}{T}}]^{\underline{3}} \tag{A.26}$$

$$\operatorname{div}(\mathbf{A}\,\mathbf{v}) = \operatorname{div}\mathbf{A}^T\cdot\mathbf{v} + \mathbf{A}^T\cdot\operatorname{grad}\mathbf{v} \tag{A.27}$$

$$\operatorname{div}(\overset{3}{\mathbf{A}}\,\mathbf{B}) = \operatorname{div}(\overset{3}{\mathbf{A}}^{\overset{13}{T}})\cdot\mathbf{B}^T + \overset{3}{\mathbf{A}}^{\overset{13}{T}}\cdot\operatorname{grad}\mathbf{B}^T. \tag{A.28}$$

Product rules for material time derivatives of vector- and tensor-valued functions are given as

$$\begin{aligned}(\mathbf{u}\otimes\mathbf{v})^{\cdot} &= \dot{\mathbf{u}}\otimes\mathbf{v} + \mathbf{u}\otimes\dot{\mathbf{v}}\\ (\mathbf{A}\,\mathbf{B})^{\cdot} &= \dot{\mathbf{A}}\,\mathbf{B} + \mathbf{A}\,\dot{\mathbf{B}}\\ (\mathbf{A}^{-1})^{\cdot} &= -\mathbf{A}^{-1}\,\dot{\mathbf{A}}\,\mathbf{A}^{-1}.\end{aligned} \tag{A.29}$$

Selected derivatives of arbitrary vectorial and tensorial functions are

$$\frac{\partial\mathbf{A}}{\partial\mathbf{A}} = (\mathbf{I}\otimes\mathbf{I})^{\overset{23}{T}} = \overset{4}{\mathbf{I}} \tag{A.30}$$

$$\frac{\partial\mathbf{A}^T}{\partial\mathbf{A}} = (\mathbf{I}\otimes\mathbf{I})^{\overset{24}{T}} \tag{A.31}$$

$$\frac{\partial \mathbf{A}^{-1}}{\partial \mathbf{A}} = -(\mathbf{A}^{-1} \otimes \mathbf{A}^{T-1})^{\overset{23}{T}} \tag{A.32}$$

$$\frac{\partial \mathbf{A}^{T-1}}{\partial \mathbf{A}} = -(\mathbf{A}^{T-1} \otimes \mathbf{A}^{T-1})^{\overset{24}{T}} \tag{A.33}$$

$$\frac{\partial \mathbf{A}^{T}\mathbf{A}}{\partial \mathbf{A}} = (\mathbf{A}^{T} \otimes \mathbf{I})^{\overset{23}{T}} + (\mathbf{I} \otimes \mathbf{A})^{\overset{24}{T}} \tag{A.34}$$

$$\frac{\partial \mathbf{A}\mathbf{A}}{\partial \mathbf{A}} = (\mathbf{A} \otimes \mathbf{I})^{\overset{23}{T}} + (\mathbf{I} \otimes \mathbf{A}^{T})^{\overset{23}{T}} \tag{A.35}$$

$$\frac{\partial \mathbf{A}\mathbf{B}}{\partial \mathbf{B}} = (\mathbf{A} \otimes \mathbf{I})^{\overset{23}{T}} \tag{A.36}$$

$$\frac{\partial \mathbf{A}\mathbf{B}}{\partial \mathbf{A}} = (\mathbf{I} \otimes \mathbf{B}^{T})^{\overset{23}{T}} \tag{A.37}$$

$$\frac{\partial \mathbf{A}\mathbf{B}}{\partial \mathbf{C}} = \big([(\frac{\partial \mathbf{A}}{\partial \mathbf{C}})^{\overset{24}{T}}\mathbf{B}]^{\underline{4}}\big)^{\overset{24}{T}} + \big([(\frac{\partial \mathbf{B}}{\partial \mathbf{C}})^{\overset{24}{T}}\mathbf{A}^{T}]^{\underline{4}}\big)^{\overset{14}{T}} \tag{A.38}$$

$$\frac{\partial([\mathbf{A}\,\mathrm{Grad}\,\mathbf{B}]^{\underline{3}})}{\partial \mathbf{C}} = \big[\big([(\frac{\partial \mathbf{A}}{\partial \mathbf{C}})^{\overset{24}{T}}(\mathrm{Grad}\,\mathbf{B})^{\overset{23}{T}}]^{\underline{5}}\big)^{\overset{25}{T}}\big]^{\overset{34}{T}} + [\mathbf{A}\,\frac{\partial(\mathrm{Grad}\,\mathbf{B})}{\mathbf{C}}]^{\underline{5}}. \tag{A.39}$$

Appendix B: Mechanical supplements

B.1 Natural basis representation of deformation and strain measures

The deformation and strain measures introduced in Sections 2.2.1 for the standard Cauchy continuum and in Section 2.4.2 for the extended micromorphic formulation are derived using a direct notation without reference to a particular coordinate system. Additionally, the representation of deformation and strain measures with respect to convective coordinates, representing material lines that continuously follow the deformation of the body $\mathcal{B}$, offers a possibility to understand the configurational characteristics of the investigated tensors. In the following, this so-called natural basis representation is given for the Cauchy continuum and the micromorphic continuum.

B.1.1 Cauchy continuum

Contravariant convective curvilinear coordinate lines θ^i are defined at each material point P and follow the deformation of the body over time. Thus, the deforming material lines can be expressed with respect to reference and actual configuration as

$$\theta^i = \theta^i(\mathbf{X},\, t_0) \quad \text{and} \quad \theta^i = \theta^i(\mathbf{x},\, t) \tag{B.1}$$

and inversely

$$\mathbf{X} = \mathbf{X}(\theta^i,\, t_0) \quad \text{and} \quad \mathbf{x} = \mathbf{x}(\theta^i,\, t)\,. \tag{B.2}$$

Covariant tangent vectors follow from the derivation of the position vectors (B.2) with respect to the contravariant coordinates and define the local natural basis vectors in the referential and in the actual configuration as

$$\mathbf{h}_i = \frac{\partial \mathbf{X}}{\partial \theta^i} \quad \text{and} \quad \mathbf{a}_i = \frac{\partial \mathbf{x}}{\partial \theta^i}\,, \tag{B.3}$$

respectively. The local contravariant dual basis vectors follow by derivation of (B.1) with respect to the position vectors as

$$\mathbf{h}^i = \frac{\partial \theta^i}{\partial \mathbf{X}} \quad \text{and} \quad \mathbf{a}^i = \frac{\partial \theta^i}{\partial \mathbf{x}}\,. \tag{B.4}$$

Covariant and contravariant basis vectors span the tangent and the cotangent space, respectively, where a contravariant basis vector $(\,\cdot\,)^i$ is orthogonal to two covariant basis vectors $(\,\cdot\,)_k$ for $k \neq l$. This leads to

$$\mathbf{h}^i \cdot \mathbf{h}_k = \delta^i_k \quad \text{and} \quad \mathbf{a}^i \cdot \mathbf{a}_k = \delta^i_k\,, \tag{B.5}$$

where δ^i_k is the Kronecker delta. The deformation and the inverse deformation gradient (2.4) follow in natural basis representation as

$$\begin{aligned} \mathbf{F} &= \frac{\partial \mathbf{x}}{\partial \mathbf{X}} = \frac{\partial \mathbf{x}}{\partial \theta^i} \otimes \frac{\partial \theta^i}{\partial \mathbf{X}} = \mathbf{a}_i \otimes \mathbf{h}^i \\ \mathbf{F}^{-1} &= \frac{\partial \mathbf{X}}{\partial \mathbf{x}} = \frac{\partial \mathbf{X}}{\partial \theta^i} \otimes \frac{\partial \theta^i}{\partial \mathbf{x}} = \mathbf{h}_i \otimes \mathbf{a}^i \,. \end{aligned} \tag{B.6}$$

It can be seen that the deformation gradient is a mixed-variant two-field tensor and that $\mathbf{F}$ maps covariant vectors from the reference to the actual configuration (covariant push-forward operation), while $\mathbf{F}^{-1}$ maps covariant vectors from the actual to the reference configuration (covariant pull-back operation). The contravariant push-forward and pull-back operations are consequently performed with $\mathbf{F}^{T-1}$ and $\mathbf{F}^T$, respectively. The right and left Cauchy-Green deformation tensors (2.10) and (2.11) as well as their inverses in natural basis representation consequently read

$$\begin{aligned} \mathbf{C} &= a_{ik} \, (\, \mathbf{h}^i \otimes \mathbf{h}^k \,) \,, & \mathbf{B} &= h^{kl} \, (\, \mathbf{a}_i \otimes \mathbf{a}_k \,) \,, \\ \mathbf{C}^{-1} &= a^{kl} \, (\, \mathbf{h}_i \otimes \mathbf{h}_k \,) \,, & \mathbf{B}^{-1} &= h_{ik} \, (\, \mathbf{a}^i \otimes \mathbf{a}^k \,) \,. \end{aligned} \tag{B.7}$$

Herein, a_{ik}, h_{ik} and a^{kl}, h^{kl} are the respective co- and contravariant metric coefficients derived from the scalar products of two sets of basis vectors and thereby describe their geometry. It is evident that the right Cauchy-Green deformation tensor (and hence the Green-Langrangean strain tensor) is a quantity of the referential state, while the left Cauchy-Green deformation tensor (and hence the Almansi strain tensor) is a quantity of the actual configuration. Finally, the natural basis representation of $\mathbf{E}$ and $\mathbf{A}$ follow as

$$\mathbf{E} = \tfrac{1}{2} \, (\, a_{ik} - h_{ik} \,) \, (\, \mathbf{h}^i \otimes \mathbf{h}^k \,) \quad \text{and} \quad \mathbf{A} = \tfrac{1}{2} \, (\, a_{ik} - h_{ik} \,) \, (\, \mathbf{a}^i \otimes \mathbf{a}^k \,) \,. \tag{B.8}$$

B.1.2 Micromorphic continuum

The micromotion $\bar{\mathbf{F}} \, (\, \mathbf{X}, t \,)$ transports the covariant vector-valued director between configurations and is thus also a two-field tensor, which can be written in analogy to $\mathbf{F}$ as

$$\bar{\mathbf{F}} = \bar{F}^i_{\ k} \, (\, \mathbf{a}_i \otimes \mathbf{h}^k \,) \,, \tag{B.9}$$

cf. Diebels [49]. By use of Einstein's summation convention, two alternative natural basis vectors and consequently two formulations for the micromotion arise, viz.:

$$\begin{aligned} \bar{\mathbf{a}}_k &:= \bar{F}^i_{\ k} \, \mathbf{a}_i \quad \longrightarrow \quad \bar{\mathbf{F}} = \bar{\mathbf{a}}_k \otimes \mathbf{h}^k, \quad \bar{\mathbf{F}}^{-1} = \mathbf{h}_k \otimes \bar{\mathbf{a}}^k \\ \bar{\mathbf{h}}^i &:= \bar{F}^i_{\ k} \, \mathbf{h}^i \quad \longrightarrow \quad \bar{\mathbf{F}} = \mathbf{a}_i \otimes \bar{\mathbf{h}}^i, \quad \bar{\mathbf{F}}^{-1} = \bar{\mathbf{h}}_i \otimes \mathbf{a}^i \,. \end{aligned} \tag{B.10}$$

Assuming the dualities

$$\bar{\mathbf{a}}^i \cdot \bar{\mathbf{a}}_k = \delta^i_k \quad \text{and} \quad \bar{\mathbf{h}}^i \cdot \bar{\mathbf{h}}_k = \delta^i_k \tag{B.11}$$

defines the covariant basis vectors $\bar{\mathbf{h}}_k$ and the contravariant basis vectors $\bar{\mathbf{a}}^k$. The newly introduced basis vectors define configurations embedded between the referential and the

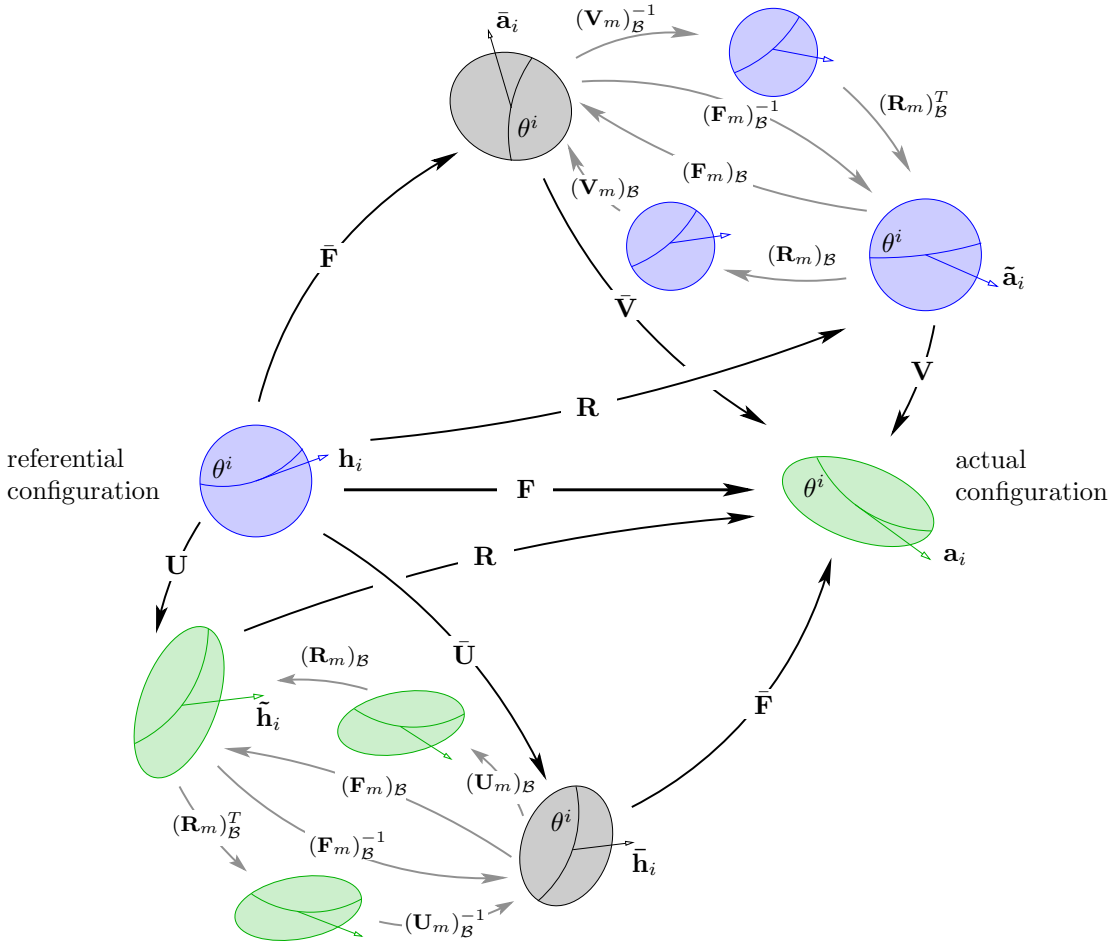

Figure B.1: *Micromorphic configurations.*

actual configuration, however, these basis vectors are no longer tangents to the material lines, cf. Figure B.1, as they characterise the microdeformation consisting of an additional stretching and a free rotation. The two formulations of $\bar{\mathbf{F}}$ in (B.10) lead to two transport mechanism of the micromotion in a natural basis representation

$$\mathbf{a}_i = \bar{\mathbf{F}}\,\bar{\mathbf{h}}_i \quad \text{and} \quad \bar{\mathbf{a}}_i = \bar{\mathbf{F}}\,\mathbf{h}_i\,. \tag{B.12}$$

Combined and compared with (2.86), the split of the microdeformation gradient and the complete motion of the director (Figure 2.5) allows several conclusions and interpretations. At first, regarding the alternative right polar decomposition of $\mathbf{F}$: If the director $\boldsymbol{\xi}$ in the actual frame is identified with $\mathbf{a}_i$, the basis vector $\bar{\mathbf{h}}_i$ is identified as the referential director $\boldsymbol{\Xi}$. Compared to a micropolar formulation, this intermediate configuration does not have the geometric properties of the actual configuration, which is established by additional mapping with $(\mathbf{U}_m)_{\mathcal{B}}$ due to the orthogonality of $(\mathbf{R}_m)_{\mathcal{B}}$ and $\mathbf{R}$. The second possibility is the choice following from the left micromorphic decomposition of $\mathbf{F}$, identifying the referential directors $\boldsymbol{\Xi}$ with the referential basis $\mathbf{h}_i$. Then, the referential geometry is retained through the combined map of $\bar{\mathbf{F}}$ and $(\mathbf{V}_m)_{\mathcal{B}}^{-1}$. $\bar{\mathbf{U}}$ and $\bar{\mathbf{V}}$ remain two-field tensors with respect to the referential and the actual configuration, respectively.

However, in comparison to the standard formulation of the deformation tensors $\mathbf{U}$ and $\mathbf{V}$, the micromorphic deformation tensors are mixed-variant, viz.:

$$\begin{aligned} \bar{\mathbf{U}} &= \bar{\mathbf{F}}^{-1}\,\mathbf{F} = \bar{\mathbf{F}}^{-1}\,\bar{\mathbf{V}}\,\bar{\mathbf{F}} = \bar{\mathbf{h}}_i \otimes \mathbf{h}^i \\ \bar{\mathbf{V}} &= \mathbf{F}\bar{\mathbf{F}}^{-1} = \bar{\mathbf{F}}\,\bar{\mathbf{U}}\,\bar{\mathbf{F}}^{-1} = \mathbf{a}_i \otimes \bar{\mathbf{a}}^i\,. \end{aligned} \tag{B.13}$$

The micromorphic strain tensors follow with respect to the introduced natural basis systems accordingly as

$$\begin{aligned} \bar{\mathbf{E}} &= \bar{\mathbf{U}} - \mathbf{I} = (\,\delta^i_k - \bar{\mathbf{h}}^i \cdot \mathbf{h}_k\,)\,(\,\bar{\mathbf{h}}_i \otimes \mathbf{h}^k\,) \\ \bar{\mathbf{A}} &= \mathbf{I} - \bar{\mathbf{V}}^{-1} = (\,\bar{\mathbf{a}}^i \cdot \mathbf{a}_k - \delta^i_k\,)\,(\,\bar{\mathbf{a}}_i \otimes \mathbf{a}^k\,)\,. \end{aligned} \tag{B.14}$$

This justifies the transport mechanism given in (2.88) and the geometric derivation based on the combination of a covariant macro- and a contravariant microelement. With the two alternative formulations of $\bar{\mathbf{F}}$ in (B.10) and the corresponding intermediate configurations, the curvature tensors ${}^{R}\overset{3}{\bar{\mathbf{C}}}$ and $\overset{3}{\bar{\mathbf{C}}}$, given in (2.10), can be written with respect to various combinations of natural basis vectors. All notations are presented in Volk [211] for the micropolar case, which formally only differs from the micromorphic case by use of the orthogonality of $\bar{\mathbf{F}}$. Exemplarily, the formulations written with respect to referential and actual basis systems read

$$\begin{aligned} {}^{R}\overset{3}{\bar{\mathbf{C}}} &= (\,\bar{\mathbf{F}}^{-1}\,\mathrm{Grad}\,\bar{\mathbf{F}})^{\underline{3}} = (\,\bar{\gamma}^i_{jk} - \Gamma^i_{\ jk}\,)\,\mathbf{h}_i \otimes \mathbf{h}^j \otimes \mathbf{h}^k\,, \\ \overset{3}{\bar{\mathbf{C}}} &= [\,(\,\mathrm{grad}\,\bar{\mathbf{F}})^{\overset{23}{T}}\,\bar{\mathbf{F}}^{-1}\,]^{\underline{3}} = (\,\gamma^i_{jk} - \bar{\Gamma}^i_{\ jk}\,)\,\mathbf{a}_i \otimes \mathbf{a}^j \otimes \mathbf{a}^k\,, \end{aligned} \tag{B.15}$$

respectively. Herein, use is made of the so-called Christoffel symbols $\gamma^i_{jk}, \Gamma^i_{\ jk}$ and $\bar{\gamma}^i_{jk}, \bar{\Gamma}^i_{\ jk}$, that stem from the spatial derivative of the natural basis vectors, viz.:

$$\begin{aligned} \frac{\partial \mathbf{h}_i}{\partial \theta^j} &= \Gamma_{ij}^{\ \ k}\,\mathbf{h}_k\,, & \frac{\partial \mathbf{h}^i}{\partial \theta^j} &= \Gamma^i_{\ jk}\,\mathbf{h}^k = -\Gamma_{kj}^{\ \ i}\,\mathbf{h}^k\,, \\ \frac{\partial \mathbf{a}_i}{\partial \theta^j} &= \gamma_{ij}^{\ \ k}\,\mathbf{a}_k & \frac{\partial \mathbf{a}^i}{\partial \theta^j} &= \gamma^i_{\ jk}\,\mathbf{a}^k = -\gamma_{kj}^{\ \ i}\,\mathbf{a}^k\,, \\ \frac{\partial \bar{\mathbf{h}}_i}{\partial \theta^j} &= \bar{\Gamma}_{ij}^{\ \ k}\,\bar{\mathbf{h}}_k\,, & \frac{\partial \bar{\mathbf{h}}^i}{\partial \theta^j} &= \bar{\Gamma}^i_{\ jk}\,\bar{\mathbf{h}}^k = -\bar{\Gamma}_{kj}^{\ \ i}\,\bar{\mathbf{h}}^k \\ \frac{\partial \bar{\mathbf{a}}_i}{\partial \theta^j} &= \bar{\gamma}_{ij}^{\ \ k}\,\bar{\mathbf{a}}_k & \frac{\partial \bar{\mathbf{a}}^i}{\partial \theta^j} &= \bar{\gamma}^i_{\ jk}\,\bar{\mathbf{a}}^k = -\bar{\gamma}_{kj}^{\ \ i}\,\bar{\mathbf{a}}^k\,. \end{aligned} \tag{B.16}$$

The Christoffel symbols are computed from the scalar product of the respective spatial derivative of a basis vector with its dual counterpart, e. g. $\gamma_{ij}^{\ \ k} = \partial \mathbf{a}_i / \partial \theta^j \cdot \mathbf{a}^k$, see Diebels [49] for more details. Note that in the expressions (B.15) of the curvature tensor, the reference to the micromotion is only present in the Christoffel symbols $\bar{\Gamma}^i_{\ jk}$ and $\bar{\gamma}^i_{\ jk}$, respectively.

B.2 Linearisation of micromorphic strain and curvature

In this section, the formal linearisation procedure is given for the micromorphic kinematic deformation and curvature tensors in Section 2.5. The linearisation is thereby obtained from a Taylor-series expansion around the natural state, characterised by $\mathbf{F}=\mathbf{I}$, $(\mathbf{U}_m)_{\mathcal{B}}=\mathbf{I}$ and $\bar{\varphi}=0$. For a detailed derivation of the linearised micropolar strain and curvature, see Ehlers [56], Scholz [187] or Volk [211].

Linearised micromorphic microstrain: The microstrain tensor $(\mathbf{E}_m)_{\mathcal{B}}$ is a local measure of the homogeneous microdeformation of the underlying microcontinuum. Its geometrically linearised counterpart $(\boldsymbol{\varepsilon}_m)_{\mathcal{B}}$ follows by use of (A.18) and (A.35) as

$$\begin{aligned}(\boldsymbol{\varepsilon}_m)_{\mathcal{B}} := (\mathbf{E}_m)_{\mathcal{B}\,\text{lin.}} &= (\mathbf{E}_m)_{\mathcal{B}}\Big|_{(\mathbf{U}_m)_{\mathcal{B}}=\mathbf{I}} + \frac{\partial(\mathbf{E}_m)_{\mathcal{B}}}{\partial(\mathbf{U}_m)_{\mathcal{B}}}\Big|_{(\mathbf{U}_m)_{\mathcal{B}}=\mathbf{I}}[\,(\mathbf{U}_m)_{\mathcal{B}}-\mathbf{I}\,]\\ &= \mathbf{0}+\tfrac{1}{2}[\,(\mathbf{I}\otimes\mathbf{I})^{\overset{23}{T}}+(\mathbf{I}\otimes\mathbf{I})^{\overset{23}{T}}\,][\,(\mathbf{U}_m)_{\mathcal{B}}-\mathbf{I}\,]\\ &= (\mathbf{U}_m)_{\mathcal{B}}-\mathbf{I}\,.\end{aligned} \tag{B.17}$$

Linearised micromorphic strain: The micromorphic strain tensor

$$\bar{\mathbf{E}}=\bar{\mathbf{E}}[\,\mathbf{F},\,(\mathbf{U}_m)_{\mathcal{B}},\,\bar{\varphi}\,]=(\mathbf{U}_m)_{\mathcal{B}}^{-1}\bar{\mathbf{R}}^T\mathbf{F}-\mathbf{I}\,, \tag{B.18}$$

cf. (2.135), is a combined measure of the homogeneous microdeformation and the macroscopic deformation. Its geometrically linearised counterpart $\bar{\boldsymbol{\varepsilon}}$ follows by use of (2.7), (A.18), (A.36) and (A.38) as

$$\begin{aligned}\bar{\boldsymbol{\varepsilon}} := \bar{\mathbf{E}}_{\text{lin.}} &= \bar{\mathbf{E}}\Big|_{\substack{\mathbf{F}=\mathbf{I}\\(\mathbf{U}_m)_{\mathcal{B}}=\mathbf{I}\\\bar{\varphi}=0}} + \frac{\partial\bar{\mathbf{E}}}{\partial\mathbf{F}}\Big|_{\substack{\mathbf{F}=\mathbf{I}\\(\mathbf{U}_m)_{\mathcal{B}}=\mathbf{I}\\\bar{\varphi}=0}}(\mathbf{F}-\mathbf{I}) + \frac{\partial\bar{\mathbf{E}}}{\partial\mathbf{U}_m}\Big|_{\substack{\mathbf{F}=\mathbf{I}\\(\mathbf{U}_m)_{\mathcal{B}}=\mathbf{I}\\\bar{\varphi}=0}}[(\mathbf{U}_m)_{\mathcal{B}}-\mathbf{I}]\\ &\quad+\frac{\partial\bar{\mathbf{E}}}{\partial\bar{\varphi}}\Big|_{\substack{\mathbf{F}=\mathbf{I}\\(\mathbf{U}_m)_{\mathcal{B}}=\mathbf{I}\\\bar{\varphi}=0}}\bar{\varphi} = \operatorname{Grad}\mathbf{u}-(\boldsymbol{\varepsilon}_m)_{\mathcal{B}}+\overset{3}{\mathbf{E}}\,\bar{\boldsymbol{\varphi}}\,.\end{aligned} \tag{B.19}$$

with

$$\begin{aligned}\frac{\partial\bar{\mathbf{E}}}{\partial\mathbf{F}}\Big|_{\substack{\mathbf{F}=\mathbf{I}\\(\mathbf{U}_m)_{\mathcal{B}}=\mathbf{I}\\\bar{\varphi}=0}}(\mathbf{F}-\mathbf{I}) &= \Big([(\mathbf{U}_m)_{\mathcal{B}}^{-1}\,\bar{\mathbf{R}}^T]\otimes\mathbf{I}\Big)^{\overset{23}{T}}\Big|_{\substack{\mathbf{F}=\mathbf{I}\\(\mathbf{U}_m)_{\mathcal{B}}=\mathbf{I}\\\bar{\varphi}=0}}(\mathbf{F}-\mathbf{I})\\ &= (\mathbf{I}\otimes\mathbf{I})^{\overset{23}{T}}(\mathbf{F}-\mathbf{I}) = \mathbf{F}-\mathbf{I} = \operatorname{Grad}\mathbf{u}\,,\end{aligned} \tag{B.20}$$

$$
\begin{aligned}
\frac{\partial \bar{\mathbf{E}}}{\partial (\mathbf{U}_m)_{\mathcal{B}}}\bigg|_{\substack{\mathbf{F}=\mathbf{I}\\(\mathbf{U}_m)_{\mathcal{B}}=\mathbf{I}\\ \bar{\varphi}=0}} ((\mathbf{U}_m)_{\mathcal{B}} - \mathbf{I}) &= \big[\,\big(\big[\,\big(\frac{\partial (\mathbf{U}_m)_{\mathcal{B}}{}^{-1}}{\partial (\mathbf{U}_m)_{\mathcal{B}}}\big)^{\overset{24}{T}} \bar{\mathbf{R}}^T\,\mathbf{F}\,\big]^{\underline{4}}\big)^{\overset{24}{T}} \\
&\quad + \big(\big[\,\big(\underbrace{\frac{\partial (\bar{\mathbf{R}}^T\,\mathbf{F})}{\partial (\mathbf{U}_m)_{\mathcal{B}}}}_{\overset{4}{\mathbf{0}}}\big)\,(\mathbf{U}_m)_{\mathcal{B}}{}^{-1}\,\big]^{\underline{4}}\big)^{\overset{14}{T}}\big]\Big|_{\substack{\mathbf{F}=\mathbf{I}\\(\mathbf{U}_m)_{\mathcal{B}}=\mathbf{I}\\ \bar{\varphi}=0}} ((\mathbf{U}_m)_{\mathcal{B}} - \mathbf{I}) \\
&= -\Big(\big[\big(\big(\,(\mathbf{U}_m)_{\mathcal{B}}{}^{-1} \otimes (\mathbf{U}_m)_{\mathcal{B}}^{T-1}\,\big)^{\overset{23}{T}}\big)^{\overset{24}{T}} \bar{\mathbf{R}}^T\,\mathbf{F}\,\big]^{\underline{4}}\Big)^{\overset{24}{T}}\Big|_{\substack{\mathbf{F}=\mathbf{I}\\(\mathbf{U}_m)_{\mathcal{B}}=\mathbf{I}\\ \bar{\varphi}=0}} ((\mathbf{U}_m)_{\mathcal{B}} - \mathbf{I}) \\
&= -\,(\,\mathbf{I}\otimes\mathbf{I}\,)^{\overset{23}{T}}\,[\,(\mathbf{U}_m)_{\mathcal{B}} - \mathbf{I}\,] = -\,[\,(\mathbf{U}_m)_{\mathcal{B}} - \mathbf{I}\,] = -\,(\boldsymbol{\varepsilon}_m)_{\mathcal{B}}\,,
\end{aligned}
\tag{B.21}
$$

$$
\begin{aligned}
\frac{\partial \bar{\mathbf{E}}}{\partial \bar{\varphi}}\bigg|_{\substack{\mathbf{F}=\mathbf{I}\\(\mathbf{U}_m)_{\mathcal{B}}=\mathbf{I}\\ \bar{\varphi}=0}} \bar{\varphi} &= \big[\,\underbrace{\frac{\partial (\mathbf{U}_m)_{\mathcal{B}}^{-1}}{\partial \bar{\varphi}}}_{\mathbf{0}}\,\bar{\mathbf{R}}^T\mathbf{F} + (\mathbf{U}_m)_{\mathcal{B}}^{-1}\frac{\partial \bar{\mathbf{R}}^T}{\partial \bar{\varphi}}\,\mathbf{F} + (\mathbf{U}_m)_{\mathcal{B}}{}^{-1}\bar{\mathbf{R}}^T\,\underbrace{\frac{\partial \mathbf{F}}{\partial \bar{\varphi}}}_{\mathbf{0}}\,\big]\Big|_{\substack{\mathbf{F}=\mathbf{I}\\(\mathbf{U}_m)_{\mathcal{B}}=\mathbf{I}\\ \bar{\varphi}=0}} \bar{\varphi} \\
&= \big(\,(\mathbf{U}_m)_{\mathcal{B}}^{-1}\,[\,(\,\mathbf{I} - \bar{\mathbf{e}}\otimes\bar{\mathbf{e}}\,)\,(-\sin\bar{\varphi}) - (\,\bar{\mathbf{e}}\times\mathbf{I}\,)\cos\bar{\varphi})\,]\,\mathbf{F}\,\big)\Big|_{\substack{\mathbf{F}=\mathbf{I}\\(\mathbf{U}_m)_{\mathcal{B}}=\mathbf{I}\\ \bar{\varphi}=0}} \bar{\varphi} \\
&= \mathbf{I}\,[\,-(\bar{\mathbf{e}}\times\mathbf{I})]\,\bar{\varphi} = -\,(\,\bar{\boldsymbol{\varphi}}\times\mathbf{I}\,) = \overset{3}{\mathbf{E}}\,\bar{\boldsymbol{\varphi}}\,.
\end{aligned}
\tag{B.22}
$$

Linearised micromorphic curvature: The formal linearisation of the micromorphic curvature is examplarily performed for

$$
{}^{R}\overset{3}{\mathbf{C}} = {}^{R}\overset{3}{\bar{\mathbf{C}}}((\mathbf{U}_m)_{\mathcal{B}},\,\bar{\varphi}) = [(\mathbf{U}_m)_{\mathcal{B}}^{-1}\bar{\mathbf{R}}^T\,\mathrm{Grad}\,(\bar{\mathbf{R}}(\mathbf{U}_m)_{\mathcal{B}})]^{\underline{3}}, \tag{B.23}
$$

cf. (2.138), by a Taylor-series expansion around the initial state $(\mathbf{U}_m)_{\mathcal{B}} = \mathbf{I}$ and $\bar{\varphi} = 0$. In particular, one obtains for $\overset{3}{\boldsymbol{\kappa}}$ by use of (A.23), (A.31), (A.32) and (A.39)

$$
\begin{aligned}
\overset{3}{\boldsymbol{\kappa}} = {}^{R}\overset{3}{\bar{\mathbf{C}}}_{\text{lin.}} &= {}^{R}\overset{3}{\mathbf{C}}\bigg|_{\substack{(\mathbf{U}_m)_{\mathcal{B}}=\mathbf{I}\\ \bar{\varphi}=0}} + \frac{\partial\,{}^{R}\overset{3}{\bar{\mathbf{C}}}}{\partial (\mathbf{U}_m)_{\mathcal{B}}}\bigg|_{\substack{(\mathbf{U}_m)_{\mathcal{B}}=\mathbf{I}\\ \bar{\varphi}=0}} [\,(\mathbf{U}_m)_{\mathcal{B}} - \mathbf{I}\,] + \frac{\partial\,{}^{R}\overset{3}{\bar{\mathbf{C}}}}{\partial \bar{\varphi}}\bigg|_{\substack{(\mathbf{U}_m)_{\mathcal{B}}=\mathbf{I}\\ \bar{\varphi}=0}} \bar{\varphi} \\
&= \overset{3}{\mathbf{0}} + \mathrm{Grad}(\boldsymbol{\varepsilon}_m)_{\mathcal{B}} - [\,\overset{3}{\mathbf{E}}\,\mathrm{Grad}\,\bar{\boldsymbol{\varphi}}\,]^{\underline{3}}
\end{aligned}
\tag{B.24}
$$

with

$$
\begin{aligned}
\frac{\partial\, {}^{R}\overset{3}{\bar{\mathbf{C}}}}{\partial(\mathbf{U}_m)_{\mathcal{B}}}\Big|_{\substack{(\mathbf{U}_m)_{\mathcal{B}}=\mathbf{I}\\ \bar{\varphi}=0}}[\,(\mathbf{U}_m)_{\mathcal{B}}\,-\,\mathbf{I}\,] \;=\;& \\
&\Big(\frac{\partial[(\mathbf{U}_m)_{\mathcal{B}}^{(-1)}\,\bar{\mathbf{R}}^T]}{\partial(\mathbf{U}_m)_{\mathcal{B}}}\,\mathrm{Grad}[\,\bar{\mathbf{R}}(\mathbf{U}_m)_{\mathcal{B}}\,]\Big)^{\underline{5}}\Big|_{\substack{(\mathbf{U}_m)_{\mathcal{B}}=\mathbf{I}\\ \bar{\varphi}=0}}[\,(\mathbf{U}_m)_{\mathcal{B}}\,-\,\mathbf{I}\,] \\
&+\,\Big([(\mathbf{U}_m)_{\mathcal{B}}^{-1}\,\bar{\mathbf{R}}^T]\,\frac{\partial\mathrm{Grad}(\mathbf{U}_m)_{\mathcal{B}}}{\partial(\mathbf{U}_m)_{\mathcal{B}}}\Big)^{\underline{5}}\Big|_{\substack{(\mathbf{U}_m)_{\mathcal{B}}=\mathbf{I}\\ \bar{\varphi}=0}}[\,(\mathbf{U}_m)_{\mathcal{B}}\,-\,\mathbf{I}\,] \\
=\;&-\Big([\,(\mathbf{U}_m)_{\mathcal{B}}^{-1}\otimes\bar{\mathbf{R}}\,(\mathbf{U}_m)_{\mathcal{B}}^{T-1}\,]^{\underline{23}}_{\underline{T}}\,^{\underline{24}}_{\underline{T}}\,(\mathrm{Grad}[\bar{\mathbf{R}}\,(\mathbf{U}_m)_{\mathcal{B}}\,]^{\underline{23}}_{\underline{T}})^{\underline{5}}\,^{\underline{25}}_{\underline{T}}\,^{\underline{34}}_{\underline{T}}\Big|_{\substack{(\mathbf{U}_m)_{\mathcal{B}}=\mathbf{I}\\ \bar{\varphi}=0}}[\,(\mathbf{U}_m)_{\mathcal{B}}\,-\,\mathbf{I}\,] \\
&+\Big((\,\mathrm{Grad}\,\bar{\mathbf{R}}\otimes\mathbf{I}\,)\,+\,[\,\bar{\mathbf{R}}\,\frac{\partial\mathrm{Grad}(\mathbf{U}_m)_{\mathcal{B}}}{\partial(\mathbf{U}_m)_{\mathcal{B}}}]^{\underline{5}}\Big)\Big|_{\substack{(\mathbf{U}_m)_{\mathcal{B}}=\mathbf{I}\\ \bar{\varphi}=0}}[\,(\mathbf{U}_m)_{\mathcal{B}}\,-\,\mathbf{I}\,] \\
=\;&\overset{3}{\mathbf{0}}\,+\,\Big(\overset{5}{\mathbf{0}}\,+\,[\,\mathbf{I}\,\frac{\mathrm{Grad}(\mathbf{U}_m)\mathcal{B}}{\partial(\mathbf{U}_m)_{\mathcal{B}}}\,]^{\underline{5}}\Big|_{\substack{(\mathbf{U}_m)_{\mathcal{B}}=\mathbf{I}\\ \bar{\varphi}=0}}\Big)\,[\,(\mathbf{U}_m)_{\mathcal{B}}\,-\,\mathbf{I}\,] \\
=\;&\overset{3}{\mathbf{0}}\,+\,\mathrm{Grad}\,(\mathbf{U}_m)_{\mathcal{B}}\,.
\end{aligned}
\tag{B.25}
$$

and

$$
\begin{aligned}
\frac{\partial\, {}^{R}\overset{3}{\bar{\mathbf{C}}}}{\partial\bar{\varphi}}\Big|_{\substack{(\mathbf{U}_m)_{\mathcal{B}}=\mathbf{I}\\ \bar{\varphi}=0}}\bar{\varphi} \;=\;&\Big((\mathbf{U}_m)_{\mathcal{B}}^{-1}\,\frac{\partial[(\,\bar{\mathbf{R}})^T]}{\partial\bar{\varphi}}\,\mathrm{Grad}\,(\bar{\mathbf{R}}\,(\mathbf{U}_m)_{\mathcal{B}}) \\
&+\,(\mathbf{U}_m)_{\mathcal{B}}^{-1}\,\bar{\mathbf{R}}^T\,\frac{\partial\mathrm{Grad}\,(\,\bar{\mathbf{R}}\,(\mathbf{U}_m)_{\mathcal{B}})}{\partial\bar{\varphi}}\Big)^{\underline{3}}\Big|_{\substack{(\mathbf{U}_m)_{\mathcal{B}}=\mathbf{I}\\ \bar{\varphi}=0}}\bar{\varphi} \\
=\;&\Big(\big([\,(\mathbf{U}_m)_{\mathcal{B}}^{-1}\,\bar{\mathbf{R}}_{\mathrm{lin.}}^T\,\mathrm{Grad}\,(\,\bar{\mathbf{R}}\,(\mathbf{U}_m)_{\mathcal{B}}\,)\,]^{\underline{3}} \\
&+\,[\,(\mathbf{U}_m)_{\mathcal{B}}^{-1}\,\bar{\mathbf{R}}^T\,(\mathrm{Grad}\,(\,\frac{\partial\bar{\mathbf{R}}}{\partial\bar{\varphi}}\,(\mathbf{U}_m)_{\mathcal{B}}\,)\,]^{\underline{3}}\big)\Big|_{\substack{(\mathbf{U}_m)_{\mathcal{B}}=\mathbf{I}\\ \bar{\varphi}=0}}\Big)\,\bar{\varphi} \\
=\;&-[\,\overset{3}{\mathbf{E}}\,\mathrm{Grad}\,\bar{\boldsymbol{\varphi}}\,]^{\underline{3}}.
\end{aligned}
\tag{B.26}
$$

B.3 Derivation of the rolling resistance model

A short derivation of the rolling resistance relations (4.19) - (4.24) shall be given. The model is nearly identical to the rolling resistance model presented in Jiang *et al.* [124]. The basic assumptions are: Two interacting spheres, which have a common small circular contact area $\mathcal{S}_c$. The normal contact force $\mathbf{f}_{c,n}^{(i)}$ is assumed to be evenly distributed over $\mathcal{S}_c$,

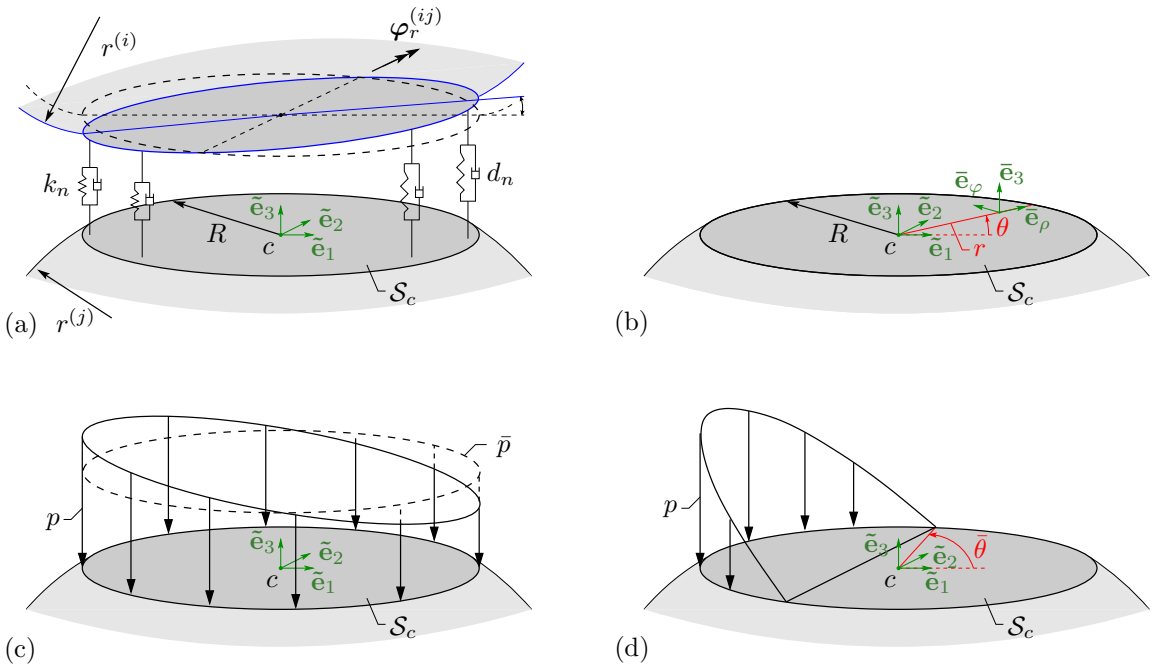

Figure B.2: *(a) Rheological model of the contact area with relative rotation $\boldsymbol{\varphi}_r^{(ij)}$, (b) definitions of basis systems on $\mathcal{S}_c$, (c) and (d) contact-pressure distributions.*

leading to a constant contact pressure of an amount $\bar{p}$ acting on the contact surface. In a rheological sense, the contact is represented by the sum of an infinite number of spring-damper models between the contacting planes, cf. Figure 4.3 (a), with corresponding modelling parameters k_n and d_n, given in (4.19), as $k_n = K_n^{lin}/\mathcal{S}_c$ and $d_n = D_n/\mathcal{S}_c$. The shape parameter c_s connects the radius R of the spherical contact surface $\mathcal{S}_c$ to the common radius $r^{(ij)}$ of the particles in contact via $R = c_s\, r$. The rheological model implies that an increasing relative rotation $\boldsymbol{\varphi}_r^{(ij)}$ causes a resisting moment $\mathbf{m}_c^{(ij)}$. In the case of the contact pressure distribution $\mathbf{p}^{(i)}$ being non-zero over the whole contact surface $\mathbf{p}^{(i)}$ is a linear function of $\boldsymbol{\varphi}_r^{(ij)}$, see Figure B.2 (c). By use of cylinder coordinates $\{r,\, \theta,\, x_3\}$ that relate the co-rotating basis system $\bar{\mathbf{e}}_i$ with $\tilde{\mathbf{e}}_i$, compare Figure B.2 (b), $\mathbf{p}^{(i)}$ follows as

$$\mathbf{p}^{(i)} \;=\; -(\,\bar{p} \;-\; \varphi_r\, k_n\, r\cos\theta\,)\,\bar{\mathbf{e}}_3 \quad \text{with} \quad \bar{p} \;=\; -\,\frac{|\mathbf{f}_{c,n}^{(i)}|}{\pi R^2}\,, \tag{B.27}$$

where the basis system $\tilde{\mathbf{e}}_i$ is fixed at the contact point c and includes $\tilde{\mathbf{e}}_2 = \boldsymbol{\varphi}_r^{(ij)}/|\boldsymbol{\varphi}_r^{(ij)}|$. Furthermore, $\tilde{\mathbf{e}}_3 = \bar{\mathbf{e}}_3$. A lever arm $\mathbf{r}$ located in the contact plane, can be expressed with respect to c as

$$\mathbf{r} \;=\; r\,\bar{\mathbf{e}}_\rho \;=\; r\,\cos\theta\,\tilde{\mathbf{e}}_1 \;+\; r\,\sin\theta\,\tilde{\mathbf{e}}_2\,. \tag{B.28}$$

Thus, the resisting moment $\mathbf{m}_c^{(i)}$ is determined by reducing the given system with respect to c, which results by use of (4.19) and (4.20) in the moment

$$\begin{aligned}\mathbf{m}_c^{(i)} \;=\; -\int_{\mathcal{S}_c} \mathbf{r} \,\times\, \mathbf{p}^{(i)}\, \mathrm{d}\mathbf{a} \;&=\; -\int_0^{2\pi}\int_0^{R} -\left(\bar{p} \,-\, \varphi_r\, K_n^{lin}\, r\cos\theta\,\right) r^2\, \cos\,\theta\, \mathrm{d}r\, \mathrm{d}\theta\, \tilde{\mathbf{e}}_2 \\ &=\; -\,\frac{k_n\, R^4\, \pi}{4}\, \varphi_r\, \tilde{\mathbf{e}}_2 \;=\; -\,\underbrace{\frac{K_n^{lin}\, c_s^2\, r^2}{4}}_{=:\, K_\varphi}\, \boldsymbol{\varphi}_r^{(ij)}\,.\end{aligned} \tag{B.29}$$

In the same way, the viscous damping moment $\mathbf{m}_d^{(i)}$ follows as

$$\mathbf{m}_d^{(i)} \;=\; \frac{d_n\, \pi\, R^4}{4}\, \dot{\boldsymbol{\varphi}}_r^{(ij)} \;=\; \frac{D_n\, r^2}{4}\, \dot{\boldsymbol{\varphi}}_r^{(ij)} \;=\; D_\varphi\, \dot{\boldsymbol{\varphi}}_r^{(ij)} \quad \text{with} \quad D_\varphi \;:=\; \frac{D_n\, R^2}{4}\,. \tag{B.30}$$

Regarding the contact stress distribution, the limit case of elastic loading is reached, when the pressure distribution reaches zero at one end of the contact surface. From this point on, the active contact area is reduced with increasing relative rotation. An intermediate contact pressure distribution is obtained as it is shown in Figure B.2 (d). Herein, the angle $\bar{\theta}$ is introduced in the contact plane to parameterise the remaining active contact area and increases with relative rotation in the post-elastic case. $\bar{\theta}$ measures the angle between the perpendicular direction to the relative rotation $\boldsymbol{\varphi}_r^{(ij)}$, which coincides with $\tilde{\mathbf{e}}_1$, and the point of zero contact pressure in the contact plane. An increase in $\boldsymbol{\varphi}_r^{(ij)}$ yields a decline of the remaining active contact area with increasing values of $\bar{\theta}$ in the post-elastic case, while $\bar{\theta} = 0°$ defines the limit case of the elastic contact regime. The resisting moment in the post-elastic case is obtained as

$$\begin{aligned}\mathbf{m}_c^{(i)} \;&=\; -\int_{\mathcal{S}_c} \mathbf{r} \,\times\, \mathbf{p}\, \mathrm{d}\mathbf{a} \\ &=\; -\Big(\int_{\bar{\theta}}^{2\pi-\bar{\theta}} \int_0^{R} -\varphi_r\, k_n\, (R\,\cos\bar{\theta} \,-\, r\,\cos\theta\,)\, r^2\, \cos\theta\, \mathrm{d}r\, \mathrm{d}\theta \\ &\quad +\, \int_{-\bar{\theta}}^{\bar{\theta}} \int_{\frac{R\,\cos\bar{\theta}}{\cos\theta}}^{R} -\varphi_r\, k_n\, (R\,\cos\bar{\theta} \,-\, r\,\cos\theta\,)\, r^2\, \cos\theta\, \mathrm{d}r\, \mathrm{d}\theta \Big)\, \tilde{\mathbf{e}}_2 \\ &=\; -\,\frac{k_n\, R^4}{4}\Big(\,\pi \,-\, \bar{\theta} \,+\, \frac{5}{3}\,\sin\bar{\theta}\,\cos\bar{\theta} \,-\, \frac{2}{3}\,\cos^3\bar{\theta}\,\sin\bar{\theta}\Big)\, \varphi_r\, \tilde{\mathbf{e}}_2\,.\end{aligned}$$

Consequently, the elastic limit case is obtained for $\bar{\theta} \,=\, 0$,

$$\bar{\mathbf{m}}_c \;=\; -\,\frac{K_n^{lin}\, R^2}{4}\, \bar{\boldsymbol{\varphi}}_r^{(ij)}\,, \tag{B.31}$$

where $\boldsymbol{\varphi}_r^{(ij)} \,=\, \bar{\boldsymbol{\varphi}}_r^{(ij)}$ denotes the (unknown) relative rotation for $\theta = \bar{\theta}$. Reducing the force system with respect to c implies that the resulting force from the pressure distribution

equals the amount of normal contact, which yields

$$\begin{aligned} |\mathbf{f}_{c,n}^{(i)}| &= \int_{\mathcal{S}_c} \mathbf{p}\,\mathrm{d}\mathbf{a} \\ &= \int_{\bar{\theta}}^{2\pi-\bar{\theta}} \int_0^R -\varphi_r\, k_n\,(R\,\cos\bar{\theta}\,-\,r\,\cos\theta\,)\,r\,\mathrm{d}r\,\mathrm{d}\theta \\ &\quad + \int_{-\bar{\theta}}^{\bar{\theta}} \int_{\frac{R\,\cos\bar{\theta}}{\cos\theta}}^R -\varphi_r\, k_n\,(R\,\cos\bar{\theta}\,-\,r\,\cos\theta\,)\,r\,\mathrm{d}r\,\mathrm{d}\theta \\ &= \varphi_r\, k_n\, R^3 \left((\pi\,-\,\bar{\theta})\,\cos\bar{\theta}\,+\,\frac{2}{3}\sin\bar{\theta}\,+\,\frac{1}{3}\,\cos^2\bar{\theta}\,\sin\bar{\theta}\,\right) \end{aligned} \tag{B.32}$$

and allows to determine $\bar{\varphi}^{(ij)}$ in the elastic limit case as

$$\bar{\varphi}^{(ij)} \;=\; \frac{|\mathbf{f}_{cn}|}{K_n^{lin}\,R}\,. \tag{B.33}$$

Inserting into (B.31) yields the final form of the resisting moment for the elastic limit as

$$\bar{\mathbf{m}}_c^{(i)} \;=\; -\frac{|\mathbf{f}_{c,n}^{(i)}|\,R}{4}\;\tilde{\mathbf{e}}_2 \;=\; -\frac{|\mathbf{f}_{c,n}^{(i)}|\,c_s\,r}{4}\;\tilde{\mathbf{e}}_2\,. \tag{B.34}$$

A normalisation of (B.32) and (B.31) with respect to the elastic limit case using equations (B.33) and (B.34) reveals

$$\frac{|\mathbf{m}_c^{(i)}|}{|\bar{\mathbf{m}}_c^{(i)}|} \;=\; \frac{\pi\,-\,\bar{\theta}\,+\frac{5}{3}\,\sin\bar{\theta}\,\cos\bar{\theta}\,-\,\frac{2}{3}\,\cos^3\bar{\theta}\,\sin\bar{\theta}}{(\pi\,-\,\bar{\theta})\,\cos\bar{\theta}\,+\,\frac{2}{3}\sin\bar{\theta}\,+\,\frac{1}{3}\,\cos^2\bar{\theta}\,\sin\bar{\theta}} \tag{B.35}$$

and

$$\frac{\varphi_r^{(ij)}}{\bar{\varphi}_r^{(ij)}} \;=\; \frac{\pi}{(\pi\,-\,\bar{\theta})\,\cos\bar{\theta}\,+\,\frac{2}{3}\sin\bar{\theta}\,+\,\frac{1}{3}\,\cos^2\bar{\theta}\,\sin\bar{\theta}}\,. \tag{B.36}$$

The evualation of (B.35) and (B.36) after Jiang *et al.* [124] for a variation of $\bar{\theta}$ is plotted in Figure 4.4 and ultimately leads to the implemented version of the contact relation as given in (4.24).

Appendix C:
Quaternion representation of rotations

A short introduction to the usage of quaternions as representation of rotations shall be given here to clarify how the computed rotational states in Pasimodo are related to the general proper-orthogonal rotation tensors $\mathbf{R}$, commonly used in continuum mechanics. For further information on quaternions and their advantages and performance for representing rotating objects in three dimensions, the interested reader is referred to Eberly [54], Evans [73], Evans & Murad [74], Johnson *et al.* [128], Shoemake [194] or Van Waveren [206].

Fundamentals: An arbitrary quaternion $\mathbf{q}$ is an entity with one real and three complex components, firstly introduced by Hamilton [105] in the mid 19$^{\text{th}}$ century, and can be written in the form

$$\begin{aligned} \mathbf{q} \;&=\; \mathsf{q}_0 + \mathsf{q}_1\, i + \mathsf{q}_2\, j + \mathsf{q}_3\, k \\ &\text{with} \quad \begin{cases} i, j, k & : \text{ imaginary unit} \\ \mathsf{q}_0,\, \mathsf{q}_1,\, \mathsf{q}_2,\, \mathsf{q}_3 & : \text{ real components}\,. \end{cases} \end{aligned} \tag{C.1}$$

Frequently, the components q_1, q_2 and q_3 are also summarised as the components q_i with $i = \{1, 2, 3\}$ of a vector $\mathbf{q}$ with respect to an orthonormal basis $\mathbf{e}_i$. This allows for the representation of a vector as a so-called pure quaternion, where $\mathsf{q}_0 = 0$. The imaginary units follow a cyclic calculation rule, the so-called Hamilton rule, reading

$$\begin{aligned} i^2 \;=\; j^2 \;=\; k^2 \;&=\; -1 \\ i\, j \;&=\; -j\, i \;=\; k \\ j\, k \;&=\; -k\, j \;=\; i \\ k\, i \;&=\; -i\, k \;=\; j\,. \end{aligned} \tag{C.2}$$

A quaternion multiplication of two quaternions $\mathbf{q}_A$ and $\mathbf{q}_B$ is not commutative, but follows with (C.2) as

$$\begin{aligned} \mathbf{q}_A\, \mathbf{q}_B \;=\; &(\mathsf{q}_{A0}\, \mathsf{q}_{B0} - \mathsf{q}_{A1}\, \mathsf{q}_{B1} - \mathsf{q}_{A2}\, \mathsf{q}_{B2} - \mathsf{q}_{A3}\, \mathsf{q}_{B3}) + \\ &+ (\mathsf{q}_{A0}\, \mathsf{q}_{B1} + \mathsf{q}_{A1}\, \mathsf{q}_{B0} + \mathsf{q}_{A2}\, \mathsf{q}_{B3} - \mathsf{q}_{A3}\, \mathsf{q}_{B2})\, i + \\ &+ (\mathsf{q}_{A0}\, \mathsf{q}_{B2} - \mathsf{q}_{A1}\, \mathsf{q}_{B3} + \mathsf{q}_{A2}\, \mathsf{q}_{B0} + \mathsf{q}_{A3}\, \mathsf{q}_{B1})\, j + \\ &+ (\mathsf{q}_{A0}\, \mathsf{q}_{B3} + \mathsf{q}_{A1}\, \mathsf{q}_{B2} - \mathsf{q}_{A2}\, \mathsf{q}_{B1} + \mathsf{q}_{A3}\, \mathsf{q}_{B0})\, k\,. \end{aligned} \tag{C.3}$$

The complex conjugated quaternion $\overset{*}{\mathbf{q}}$ is given by

$$\overset{*}{\mathbf{q}} \;=\; \mathsf{q}_0 - \mathsf{q}_1\, i - \mathsf{q}_2\, j - \mathsf{q}_3\, k\,. \tag{C.4}$$

The norm $|\mathbf{q}|$ of a quaternion is defined as

$$|\mathbf{q}| \;=\; \sqrt{\mathsf{q}_0^2 \,+\, \mathsf{q}_1^2 \,+\, \mathsf{q}_2^2 \,+\, \mathsf{q}_3^2}\,. \tag{C.5}$$

A unit quaternion $\mathbf{q}_e$ with $|\mathbf{q}_e| = 1$ thus follows by normalisation of (C.1) as

$$\mathsf{q}_e \;=\; \frac{\mathbf{q}}{|\mathbf{q}|} \;=\; \frac{\mathsf{q}_0}{|\mathbf{q}|} \,+\, \frac{\mathsf{q}_1}{|\mathbf{q}|}\, i \,+\, \frac{\mathsf{q}_2}{|\mathbf{q}|}\, j \,+\, \frac{\mathsf{q}_3}{|\mathbf{q}|}\, k\,. \tag{C.6}$$

Fortunately, one concludes that for a unit quaternion, the relation

$$\mathbf{q}_e \overset{*}{\mathbf{q}}_e \;=\; \overset{*}{\mathbf{q}}_e \mathbf{q}_e \;=\; 1 \tag{C.7}$$

holds and the imaginary part vanishes. $\overset{*}{\mathbf{q}}_e$ is the inverse quaternion.

Quaternion representation of rotations: Given is a rotation of a vector $\mathbf{x}$ by the angle φ around the rotation axes $\mathbf{r}$ with $|\mathbf{r}| = 1$. Thus, the rotation is characterised by $\boldsymbol{\varphi} = \varphi\,\mathbf{r}$. With respect to a fixed, orthonormal basis $\mathbf{e}_i$, $\mathbf{r}$ can be written as

$$\mathbf{r} \;=\; r_1\,\mathbf{e}_1 \,+\, r_2\,\mathbf{e}_2 \,+\, r_3\,\mathbf{e}_3\,. \tag{C.8}$$

Through substitution of

$$\begin{aligned} \mathsf{q}_{R0} \;&=\; \cos\,(\frac{\varphi}{2}) \\ \mathsf{q}_{R1} \;&=\; r_1 \sin\,(\frac{\varphi}{2}) \\ \mathsf{q}_{R2} \;&=\; r_2 \sin\,(\frac{\varphi}{2}) \\ \mathsf{q}_{R3} \;&=\; r_3 \sin\,(\frac{\varphi}{2}) \end{aligned} \tag{C.9}$$

the rotation quaternion $\mathbf{q}_R$ follows as

$$\mathbf{q}_R \;=\; \underbrace{\cos\,(\frac{\varphi}{2})}_{\mathsf{q}_{R0}} \,+\, \underbrace{r_1 \sin\,(\frac{\varphi}{2})}_{\mathsf{q}_{R1}}\, i \,+\, \underbrace{r_2 \sin\,(\frac{\varphi}{2})}_{\mathsf{q}_{R2}}\, j \,+\, \underbrace{r_3 \sin\,(\frac{\varphi}{2})}_{\mathsf{q}_{R3}}\, k\,. \tag{C.10}$$

The rotation quaternion $\mathbf{q}_R$ is a unit quaternion, since

$$\begin{aligned} |\mathbf{q}_R| \;&=\; \sqrt{\cos^2(\frac{\varphi}{2}) \,+\, r_1^2 \sin^2\,(\frac{\varphi}{2}) \,+\, r_2^2 \sin^2\,(\frac{\varphi}{2}) \,+\, r_3^2 \sin^2\,(\frac{\varphi}{2})} \\ &=\; \sqrt{\cos^2(\frac{\varphi}{2}) \,+\, (r_1^2 \,+\, r_2^2 \,+\, r_3^2) \sin^2\,(\frac{\varphi}{2})} \;=\; 1\,. \end{aligned} \tag{C.11}$$

Expressing $\mathbf{x}$ as a pure quaternion, viz.

$$\mathbf{x} \;=\; 0 \,+ \mathsf{x}_1\, i \,+\, \mathsf{x}_2\, j \,+\, \mathsf{x}_2\, k\,, \tag{C.12}$$

allows to express the rotation of $\mathbf{x}$ into its rotated configuration $\tilde{\mathbf{x}}$ as the corresponding series of the quaternion multiplication

$$\tilde{\mathbf{x}} \;=\; \mathbf{q}_R\, \mathbf{x}\, \overset{*}{\mathbf{q}}_R\,. \tag{C.13}$$

A short example shall be given. Suppose

$$\begin{aligned} \mathbf{x} &= \mathbf{e}_1 \\ \boldsymbol{\varphi} &= \varphi_3\,\mathbf{r} \\ \mathbf{r} &= \mathbf{e}_3\,. \end{aligned} \tag{C.14}$$

The rotation quaternions consequently follow as

$$\begin{aligned} \mathbf{q}_R &= \cos\left(\frac{\varphi_3}{2}\right) + r_3 \sin\left(\frac{\varphi_3}{2}\right) k \;=\; \cos\left(\frac{\varphi_3}{2}\right) + \sin\left(\frac{\varphi_3}{2}\right) k \\ \overset{*}{\mathbf{q}}_R &= \cos\left(\frac{\varphi_3}{2}\right) - \sin\left(\frac{\varphi_3}{2}\right) k\,. \end{aligned} \tag{C.15}$$

The rotated state $\tilde{\mathbf{e}}_1$ follows by expressing $\mathbf{e}_1$ as a pure quaternion $\mathbf{e}_1 = 1\,i$ via

$$\begin{aligned} \tilde{\mathbf{e}}_1 \;=\; \mathbf{q}_R\,\mathbf{e}_1\,\overset{*}{\mathbf{q}}_R \;&=\; [\underbrace{\cos^2\left(\frac{\varphi_3}{2}\right) - \sin^2\left(\frac{\varphi_3}{2}\right)}_{=2\,\cos^2\left(\frac{\varphi_3}{2}\right)-1\,=\,\cos(\varphi_3)}]\,i \;+\; [\underbrace{\cos\left(\frac{\varphi_3}{2}\right)\,\sin\left(\frac{\varphi_3}{2}\right) + \sin\left(\frac{\varphi_3}{2}\right)\,\cos\left(\frac{\varphi_3}{2}\right)}_{=2\,\sin\left(\frac{\varphi_3}{2}\right)\,\cos\left(\frac{\varphi_3}{2}\right)\,=\,\sin(\varphi_3)}]\,j \\ &=\; \cos(\varphi_3)\,i \;+\; \sin(\varphi_3)\,j\,. \\ \longrightarrow \qquad \tilde{\mathbf{e}}_1 \;&=\; \cos(\varphi_3)\,\mathbf{e}_1 \;+\; \sin(\varphi_3)\,\mathbf{e}_2 \quad \checkmark \end{aligned} \tag{C.16}$$

Linking Quaternion and Euler-Rodrigues representations of rotations: The corresponding rotation tensor $\mathbf{R}$ to the above described rotation around a central axis is given by the Euler-Rodrigues representation

$$\mathbf{R} \;=\; \mathbf{r} \otimes \mathbf{r} \;+\; \cos\varphi\,(\mathbf{I} \;-\; \mathbf{r} \otimes \mathbf{r}) \;+\; \sin\varphi\,(\mathbf{r} \;\times\; \mathbf{I})\,. \tag{C.17}$$

With respect to $\mathbf{e}_i$, $\mathbf{R}$ can be expressed using a coefficient matrix R_{ik}, yielding

$$\mathbf{R} \;=\; R_{ik}\,\mathbf{e}_i \otimes \mathbf{e}_k \quad \text{with} \tag{C.18}$$

$$R_{ik} = \begin{bmatrix} \cos\varphi + r_1^2\,(1-\cos\varphi) & r_1 r_2(1-\cos\varphi) - r_3\sin\varphi & r_1 r_3(1-\cos\varphi) + r_2\sin\varphi \\ r_2 r_1(1-\cos\varphi) + r_3\sin\varphi & \cos\varphi + r_2^2(1-\cos\varphi) & r_2 r_3(1-\cos\varphi) - r_1\sin\varphi \\ r_3 r_1(1-\cos\varphi) - r_2\sin\varphi & r_3 r_2(1-\cos\varphi) + r_1\sin\varphi & \cos\varphi + r_3^2(1-\cos\varphi) \end{bmatrix}.$$

For arbitrary rotations of a vector $\mathbf{x}$, one thus has

$$\tilde{\mathbf{x}} \;=\; \mathbf{R}\,\mathbf{x}\,. \tag{C.19}$$

Through comparison of the coefficients in R_{ik} with a quaternion rotation, it is possible to construct R_{ik} as a function of quaternion operations yielding

$$\mathsf{R}_{ik} \;=\; \begin{bmatrix} 1 - 2(\mathsf{q}_{R2}^2 + \mathsf{q}_{R3}^2) & 2(\mathsf{q}_{R1}\,\mathsf{q}_{R2} + \mathsf{q}_{R0}\,\mathsf{q}_{R3}) & 2(\mathsf{q}_{R1}\,\mathsf{q}_{R3} - \mathsf{q}_{R0}\,\mathsf{q}_{R2}) \\ 2(\mathsf{q}_{R1}\,\mathsf{q}_{R2} - \mathsf{q}_{R0}\,\mathsf{q}_{R3}) & 1 - 2(\mathsf{q}_{R1}^2 + \mathsf{q}_{R3}^2) & 2(\mathsf{q}_{R2}\,\mathsf{q}_{R3} + \mathsf{q}_{R0}\,\mathsf{q}_{R1}) \\ 2(\mathsf{q}_{R1}\,\mathsf{q}_{R3} + \mathsf{q}_{R0}\,\mathsf{q}_{R2}) & 2(\mathsf{q}_{R2}\,\mathsf{q}_{R3} - \mathsf{q}_{R0}\,\mathsf{q}_{R1}) & 1 - 2(\mathsf{q}_{R1}^2 + \mathsf{q}_{R2}^2) \end{bmatrix}. \tag{C.20}$$

The equivalence between (C.18) and (C.20) can be seen by evaluation of the coefficients. For example R_{11} yields

$$\begin{aligned}
\mathsf{R}_{11} &= 1 - 2\,(\mathsf{q}_{R2}^2 + \mathsf{q}_{R3}^2) \;=\; 1 - 2\,[\,\sin^2(\frac{\varphi}{2})\,r_2^2 \;+\; \sin^2(\frac{\varphi}{2})\,r_3^2\,] \\
&= 1 \;-\; 2\,\sin^2(\frac{\varphi}{2})\,(r_2^2 \;+\; r_3^2) \\
&= 1 \;-\; (1 \;-\; \cos\varphi)\,(1 \;-\; r_1^2) \\
&= \cos\varphi \;+\; r_1^2\,(1 \;-\; \cos\varphi) \;=\; R_{11}
\end{aligned}$$

using $\sin^2(\frac{\varphi}{2}) \;=\; 1 \;-\; \cos\varphi$ and $r_2^2 \;+\; r_3^2 \;=\; 1 \;-\; r_1^2$.

Orientation, angular velocity and angular acceleration: If the orientational state of a rigid particle $\mathcal{P}^{(i)}$ is captured by a quaternion $\mathbf{q}^{(i)}$, the need of its time derivatives arises in order to account for the angular velocity and the angular acceleration of the rigid body rotation. By use of the orthogonal quaternion matrix $\mathbf{Q}\,(\,\mathbf{q}^{(i)}\,)$,

$$\mathbf{Q}\,(\mathbf{q}\,) \;=\; \begin{bmatrix} \mathsf{q}_0 & -\,\mathsf{q}_1 & -\,\mathsf{q}_2 & -\,\mathsf{q}_3 \\ \mathsf{q}_1 & \mathsf{q}_0 & -\,\mathsf{q}_3 & \mathsf{q}_2 \\ \mathsf{q}_2 & \mathsf{q}_3 & \mathsf{q}_3 & -\,\mathsf{q}_1 \\ \mathsf{q}_3 & -\,\mathsf{q}_2 & \mathsf{q}_1 & \mathsf{q}_0 \end{bmatrix}\,, \tag{C.21}$$

cf. Omelyan [175], the time derivative $\dot{\mathbf{q}}$ follows through the linear map

$$\dot{\mathbf{q}}^{(i)} \;=\; \mathbf{Q}\,(\,\mathbf{q}^{(i)}\,)\,\mathbf{w}^{(i)} \tag{C.22}$$

with $\mathbf{w}^{(i)}$ as an expansion of the angular velocity $\boldsymbol{\omega}^{(i)}$ towards a pure quaternion. Consequently the angular acceleration follows as

$$\ddot{\mathbf{q}}^{(i)} \;=\; \frac{1}{2}\,[\,\mathbf{Q}\,(\,\dot{\mathbf{q}}^{(i)}\,)\,\mathbf{w}^{(i)} \;+\; \mathbf{Q}\,(\,\mathbf{q}^{(i)}\,)\,\dot{\mathbf{w}}^{(i)}\,]\,. \tag{C.23}$$

Bibliography

[1] Adam, J.; Urai, J.; Wieneke, B.; Oncken, O.; Pfeiffer, K.; Kukowski, N.; Lohrmann, J.; Hoth, S.; Van Der Zee, W. & Schmatz, J.: Shear localisation and strain distribution during tectonic faulting – new insights from granular-flow experiments and high-resolution optical image correlation techniques. *Journal of Structural Geology* **27** (2005), 283–301.

[2] Ai, J.; Chen, J.-F.; Rotter, J. M. & Ooi, J. Y.: Assessment of rolling resistance models in discrete element simulations. *Powder Technology* **206** (2011), 269–282.

[3] Aifantis, E. C.: On the microstructural origin of certain inelastic models. *ASME Journal of Engineering Material Technology* **106** (1984), 326–330.

[4] Al-Raoush, R.: Microstructure characterization of granular materials. *Physica A: Statistical mechanics and its Applications* **377** (2007), 545–558.

[5] Alshibli, K. A. & Alsaleh, M. I.: Characterizing surface roughness and shape of sands using digital microscopy. *Journal of Computing in Civil Engineering* **18** (2004), 36–45.

[6] Alshibli, K. A.; Batiste, S. N. & Sture, S.: Strain localization in sand: plane strain versus triaxial compression. *Journal of Geotechnical and Geoenvironmental Engineering* **129** (2003), 483–494.

[7] Alshibli, K. A.; Lankton, M.; Frank, M.; Costes, N.; Swanson, R.; Sture, S. & Batiste, S. N.: Assessment of localized deformations in sand using x-ray computed tomography. *Geotechnical Testing Journal* **23** (2000), 274–299.

[8] Altenbach, H. & Eremeyev, V. A.: Cosserat media. In *Generalized Continua from the Theory to Engineering Applications*. Springer 2013, pp. 65–130.

[9] Anand, L. & Gu, C.: Granular materials: constitutive equations and strain localization. *Journal of the Mechanics and Physics of Solids* **48** (2000), 1701–1733.

[10] Andersson, S.; Söderberg, A. & Björklund, S.: Friction models for sliding dry, boundary and mixed lubricated contacts. *Tribology International* **40** (2007), 580–587.

[11] Andò, E.; Hall, S. A.; Viggiani, G.; Desrues, J. & Bésuelle, P.: Grain-scale experimental investigation of localised deformation in sand: A discrete particle tracking approach. *Acta Geotechnica* **7** (2012), 1–13.

[12] Andrade, J.; Avila, C.; Hall, S.; Lenoir, N. & Viggiani, G.: Multiscale modeling and characterization of granular matter: From grain kinematics to continuum mechanics. *Journal of the Mechanics and Physics of Solids* **59** (2011), 237–250.

[13] Andrade, J. E. & Borja, R. I.: Capturing strain localization in dense sands with random density. *International Journal for Numerical Methods in Engineering* **67** (2006), 1531–1564.

[14] Andrade, J. E.; Lim, K.-W.; Avila, C. F. & Vlahinić, I.: Granular element method for computational particle mechanics. *Computer Methods in Applied Mechanics and Engineering* **241** (2012), 262–274.

[15] Argilaga, A.; Desrues, J.; Dal Pont, S.; Combe, G. & Caillerie, D.: FEM × DEM multiscale modeling: Model performance enhancement from Newton strategy to element loop parallelization. *International Journal for Numerical Methods in Engineering* **114** (2018), 47–65.

[16] Åström, J.; Herrmann, H. & Timonen, J.: Granular packings and fault zones. *Physical Review Letters* **84** (2000), 638.

[17] Bachmat, Y. & Bear, J.: Macroscopic modelling of transport phenomena in porous media. 1: The continuum approach. *Transport in Porous Media* **1** (1986), 213–240.

[18] Barber, C. B.; Dobkin, D. P. & Huhdanpaa, H.: The Qbachuickhull algorithm for convex hulls. *ACM Transactions on Mathematical Software (TOMS)* **22** (1996), 469–483.

[19] Bardet, J. & Proubet, J.: Numerical investigation of the structure of persistent shear bands in granular media. *Geotechnique* **41** (1991), 599–613.

[20] Bathurst, R. & Rothenburg, L.: Micromechanical aspects of isotropic granular assemblies with linear contact interactions. *Journal of Applied Mechanics* **55** (1988), 17–23.

[21] Bauman, P. T.; Dhia, H. B.; Elkhodja, N.; Oden, J. T. & Prudhomme, S.: On the application of the Arlequin method to the coupling of particle and continuum models. *Computational Mechanics* **42** (2008), 511–530.

[22] Behraftar, S.; Torres, S. G.; Scheuermann, A.; Williams, D.; Marques, E. & Avarzaman, H. J.: A calibration methodology to obtain material parameters for the representation of fracture mechanics based on discrete element simulations. *Computers and Geotechnics* **81** (2017), 274–283.

[23] Bidier, S. & Ehlers, W.: Micromorphic and micropolar continua: A comparative study based on homogenisation of particle simulations. *Proceedings in Applied Mathematics and Mechanics* **18** (2018), doi.org/10.1002/pamm.201800390.

[24] Biswas, R. & Poh, L.: A micromorphic computational homogenization framework for heterogeneous materials. *Journal of the Mechanics and Physics of Solids* **102** (2017), 187–208.

[25] Boenisch, D. & Lotz, W.: Mechanical strength of cold-box mold components. *Giesserei* **71** (1984), 187–196.

[26] Boenisch, D. & Lotz, W.: Causes for unexpected losses of strengths of cold box cores. *Giesserei* **72** (1985), 83–88.

[27] de Borst, R.: Simulation of strain localization: A reappraisal of the Cosserat continuum. *Engineering Computations* **8** (1991), 317 – 332.

[28] Caylak, I. & Mahnken, R.: Thermomechanical characterisation of cold box sand including optical measurements. *International Journal of Cast Metals Research* **23** (2010), 176–184.

[29] Chen, K.-C.: Microcontinuum balance equations revisited: The mesoscopic approach. *Journal of Non-Equilibrium Thermodynamics* **32** (2007), 435–458.

[30] Chen, Y. & Lee, J. D.: Connecting molecular dynamics to micromorphic theory (I). Instantaneous and averaged mechanical variables. *Physica A: Statistical Mechanics and its Applications* **322** (2003), 359–376.

[31] Chen, Y. & Lee, J. D.: Connecting molecular dynamics to micromorphic theory (II). Balance laws. *Physica A: Statistical Mechanics and its Applications* **322** (2003), 377–392.

[32] Chen, Y.; Zimmerman, J.; Krivtsov, A. & McDowell, D. L.: Assessment of atomistic coarse-graining methods. *International Journal of Engineering Science* **49** (2011), 1337–1349.

[33] Cheng, H.; Shuku, T.; Thoeni, K. & Yamamoto, H.: Probabilistic calibration of discrete element simulations using the sequential quasi-monte carlo filter. *Granular matter* **20** (2018), doi.org/10.1007/s10035-017-0781-y.

[34] Christoffersen, J.; Mehrabadi, M. & Nemat-Nasser, S.: A micromechanical description of granular material behavior. *Journal of Applied Mechanics* **48** (1981), 339–344.

[35] Chung, J. & Hulbert, G.: A time integration algorithm for structural dynamics with improved numerical dissipation: The Generalized α-Method. *Journal of Applied Mechanics* **60** (1993), 371–375.

[36] Cleary, P. W.: Large scale industrial DEM modelling. *Engineering Computations* **21** (2004), 169–204.

[37] Cosserat, E. & Cosserat, F.: Théorie des corps déformables. *Herman et Fils, Paris* (1909).

[38] Cowper, G.: The shear coefficient in Timoshenko's beam theory. *Journal of Applied Mechanics* **33** (1966), 335–340.

[39] Cramer, H.; Findeiss, R.; Steinl, G. & Wunderlich, W.: An approach to the adaptive finite element analysis in associated and non-associated plasticity considering localization phenomena. *Computer Methods in Applied Mechanics and Engineering* **176** (1999), 187–202.

[40] Cundall, P. A.: Formulation of a three-dimensional distinct element model - Part I. A scheme to detect and represent contacts in a system composed of many polyhedral blocks. *International Journal of Rock Mechanics and Mining Sciences & Geomechanics Abstracts* **25** (1988), 107–116.

[41] Cundall, P. A.: Numerical experiments on localization in frictional materials. *Archive of Applied Mechanics* **59** (1989), 148–159.

[42] Cundall, P. A. & Strack, O. D.: A discrete numerical model for granular assemblies. *Geotechnique* **29** (1979), 47–65.

[43] D'Addetta, G.; Ramm, E.; Diebels, S. & Ehlers, W.: A particle center based homogenization strategy for granular assemblies. *Engineering Computations* **21** (2004), 360–383.

[44] D'Addetta, G. A. & Ramm, E.: A microstructure-based simulation environment on the basis of an interface enhanced particle model. *Granular Matter* **8** (2006), 159–174.

[45] Daphalapurkar, N.; Wang, F.; Fu, B.; Lu, H. & Komanduri, R.: Determination of mechanical properties of sand grains by nanoindentation. *Experimental Mechanics* **51** (2011), 719–728.

[46] Desrues, J. & Andò, E.: Strain localisation in granular media. *Comptes Rendus Physique* **16** (2015), 26–36.

[47] Desrues, J.; Argilaga, A.; Dal Pont, S.; Combe, G.; Caillerie, D. & kein Nguyen, T.: Restoring mesh independency in FEM-DEM multi-scale modelling of strain localization using second gradient regularization. In *International Workshop on Bifurcation and Degradation in Geomaterials*, Springer 2017, pp. 453–457.

[48] Desrues, J. & Viggiani, G.: Strain localization in sand: an overview of the experimental results obtained in Grenoble using stereophotogrammetry. *International Journal for Numerical and Analytical Methods in Geomechanics* **28** (2004), 279–321.

[49] Diebels, S.: *Mikropolare Zweiphasenmodelle: Formulierung auf der Basis der Theorie Poröser Medien*. Habilitation, Report No. II-4 of the Institute of Applied Mechanics (CE), University of Stuttgart 2000.

[50] Diebels, S. & Ehlers, W.: Dynamic analysis of a fully saturated porous medium accouting for gemoetrical and material non-linearities. *International Journal for Numerical Methods in Engineering* **39** (1996), 81–97.

[51] Diebels, S. & Steeb, H.: Stress and couple stress in foams. *Computational Materials Science* **28** (2003), 714–722.

[52] Dietsche, A.; Steinmann, P. & Willam, K.: Micropolar elastoplasticity and its role in localization. *International Journal of Plasticity* **9** (1993), 813–831.

[53] Džiugys, A. & Peters, B.: An approach to simulate the motion of spherical and non-spherical fuel particles in combustion chambers. *Granular Matter* **3** (2001), 231–266.

[54] Eberly, D.: Rotation representations and performance issues. *Magic Software, Inc., Chapel Hill, NC* (2002).

[55] Ebinger, T.; Steeb, H. & Diebels, S.: Modeling macroscopic extended continua with the aid of numerical homogenization schemes. *Computational Materials Science* **32** (2005), 337–347.

[56] Ehlers, W.: Foundations of multiphasic and porous materials. In Ehlers, W. & Bluhm, J. (eds.): *Porous media: Theory, Experiments and Numerical Applications*. Springer 2002, pp. 3–86.

[57] Ehlers, W.: Recovering micropolar continua from particle mechanics by use of homogenisation strategies. In Müller-Hoeppe, D.; Löhnert, S. & Reese, S. (eds.): *Recent Developments and Innovative Applications in Computational Mechanics*. Springer, Berlin 2011, pp. 179–189.

[58] Ehlers, W.: *Poröse Medien – ein kontinuumsmechanisches Modell auf der Basis der Mischungstheorie*. Reprint of the habilitation treatise of 1989 (Forschungsberichte aus dem Fachbereich Bauwesen der Universität-GH-Essen **47**, Essen 1989), Report No. II-22 of the Institute of Applied Mechanics (CE), University of Stuttgart 2012.

[59] Ehlers, W.: Vector and Tensor Calculus: A Supplement to Continuum Mechanics Research. University of Stuttgart 2018, URL http://www.mechbau.uni-stuttgart.de/ls2/Downloads/vektortensorskript_eng_ws1314.pdf.

[60] Ehlers, W. & Avci, O.: Stress-dependent hardening and failure surfaces of dry sand. *International Journal for Numerical and Analytical Methods in Geomechanics* **37** (2013), 787–809.

[61] Ehlers, W. & Bidier, S.: Cosserat media. In Altenbach, H. & Öchsner, A. (eds.): *Encyclopedia of Continuum Mechanics*. Springer, Berlin, Heidelberg 2018, pp. 101–115.

[62] Ehlers, W. & Bidier, S.: From particle mechanics to micromorphic media. Part I: Homogenisation of discrete interactions towards stress quantities. *International Journal of Solids and Structures* (2018), doi.org/10.1016/j.ijsolstr.2018.08.013.

[63] Ehlers, W.; Graf, T. & Ammann, M.: Deformation and localization analysis of partially saturated soil. *Computer Methods in Applied Mechanics and Engineering* **193** (2004), 2885–2910.

[64] Ehlers, W.; Ramm, E.; Diebels, S. & D'Addetta, G. A.: From particle ensembles to Cosserat continua: Homogenization of contact forces towards stresses and couple stresses. *International Journal of Solids and Structures* **40** (2003), 6681–6702.

[65] Ehlers, W. & Scholz, B.: An inverse algorithm for the identification and the sensitivity analysis of the parameters governing micropolar elasto-plastic granular material. *Archive of Applied Mechanics* **77** (2007), 911–931.

[66] Ehlers, W. & Volk, W.: On shear band localization phenomena of liquid-saturated granular elastoplastic porous solid materials accounting for fluid viscosity and micropolar solid rotations. *Mechanics of Cohesive-frictional Materials* **2** (1997), 301–320.

[67] Ehlers, W. & Volk, W.: Localization Phenomena in Liquid-saturated and Empty Porous Solids. In *Porous Media: Theory and Experiments*. Springer 1999, pp. 159–177.

[68] Ergenzinger, C.; Seifried, R. & Eberhard, P.: A discrete element model to describe failure of strong rock in uniaxial compression. *Granular Matter* **13** (2011), 341–364.

[69] Eringen, A. C.: Balance laws of micromorphic mechanics. *International Journal of Engineering Science* **8** (1970), 819–828.

[70] Eringen, A. C.: Theory of thermo-microstretch elastic solids. *International Journal of Engineering Science* **28** (1990), 1291–1301.

[71] Eringen, A. C.: *Microcontinuum field theories: I: Foundations and Solids*. Springer Science & Business Media, New York 1999.

[72] Eringen, A. C. & Suhubi, E.: Nonlinear theory of simple micro-elastic solids. *International Journal of Engineering Science* **2** (1964), 189–203.

[73] Evans, D. J.: On the representatation of orientation space. *Molecular Physics* **34** (1977), 317–325.

[74] Evans, D. J. & Murad, S.: Singularity free algorithm for molecular dynamics simulation of rigid polyatomics. *Molecular Physics* **34** (1977), 327–331.

[75] Ezaoui, A. & Benedetto, H. D.: Experimental measurements of the global anisotropic elastic behaviour of dry Hostun sand during triaxial tests, and effect of sample preparation. *Géotechnique* **59** (2009), 621–635.

[76] Ferellec, J. & McDowell, G.: Modelling realistic shape and particle inertia in DEM. *Géotechnique* **60** (2010), 227–232.

[77] Finno, R. J.; Harris, W. W.; Mooney, M. A. & Viggiani, G.: Strain localization and undrained steady state of sand. *Journal of Geotechnical Engineering* **122** (1996), 462–473.

[78] Fleissner, F.: *Parallel object oriented simulation with Lagrangian particle methods*. Shaker, Aachen 2010.

[79] Fleissner, F. & Eberhard, P.: Parallel load-balanced simulation for short-range interaction particle methods with hierarchical particle grouping based on orthogonal recursive bisection. *International Journal for Numerical Methods in Engineering* **74** (2008), 531–553.

[80] Fleissner, F.; Gaugele, T. & Eberhard, P.: Applications of the discrete element method in mechanical engineering. *Multibody System Dynamics* **18** (2007), 81–94.

[81] Fleissner, F.; Lehnart, A. & Eberhard, P.: Dynamic simulation of sloshing fluid and granular cargo in transport vehicles. *Vehicle System Dynamics* **48** (2010), 3–15.

[82] Foerster, S. F.; Louge, M. Y.; Chang, H. & Allia, K.: Measurements of the collision properties of small spheres. *Physics of Fluids* **6** (1994), 1108–1115.

[83] Fonseca, J.; O`Sullivan, C.; Coop, M. R. & Lee, P.: Non-invasive characterization of particle morphology of natural sands. *Soils and Foundations* **52** (2012), 712–722.

[84] Forest, S.: Cosserat media. *Encyclopedia of Materials: Science and Technology* (2001), 1715–1718.

[85] Forest, S.: Homogenization methods and the mechanics of generalized continua - Part 2. *Theoretical and Applied Mechanics* **28** (2002), 113–144.

[86] Forest, S.: Micromorphic approach for gradient elasticity, viscoplasticity, and damage. *Journal of Engineering Mechanics* **135** (2009), 117–131.

[87] Forest, S.: Micromorphic media. In Altenbach, H. & Eremeyev, V. (eds.): *Generalized Continua - from the Theory to Engineering Applications*. Springer 2012, vol. 541 of *Courses and Lectures*, pp. 249–300.

[88] Forest, S.; Barbe, F. & Cailletaud, G.: Cosserat modelling of size effects in the mechanical behaviour of polycrystals and multi-phase materials. *International Journal of Solids and Structures* **37** (2000), 7105 – 7126.

[89] Forest, S. & Sab, K.: Cosserat overall modeling of heterogeneous materials. *Mechanics Research Communications* **25** (1998), 449–454.

[90] Forest, S. & Sievert, R.: Elastoviscoplastic constitutive frameworks for generalized continua. *Acta Mechanica* **160** (2003), 71–111.

[91] Forest, S. & Sievert, R.: Nonlinear microstrain theories. *International Journal of Solids and Structures* **43** (2006), 7224–7245.

[92] Froiio, F.; Tomassetti, G. & Vardoulakis, I.: Mechanics of granular materials: The discrete and the continuum descriptions juxtaposed. *International Journal of Solids and Structures* **43** (2006), 7684–7720.

[93] Galindo-Torres, S. & Pedroso, D.: Molecular dynamics simulations of complex-shaped particles using Voronoi-based spheropolyhedra. *Physical Review E* **81** (2010), 061303.

[94] Galindo-Torres, S.; Pedroso, D.; Williams, D. & Li, L.: Breaking processes in three-dimensional bonded granular materials with general shapes. *Computer Physics Communications* **183** (2012), 266–277.

[95] Gilardi, G. & Sharf, I.: Literature survey of contact dynamics modelling. *Mechanism and Machine Theory* **37** (2002), 1213–1239.

[96] Goddard, J.: A general micromorphic theory of kinematics and stress in granular media. *Powder and Grains* **1** (2007), 129–134.

[97] Goddard, J.: From granular matter to generalized continuum. *Lecture Notes in Mathematics* **1937** (2008), 1–22.

[98] Goldhirsch, I.: Stress, stress asymmetry and couple stress: From discrete particles to continuous fields. *Granular Matter* **12** (2010), 239–252.

[99] Grammenoudis, P. & Tsakmakis, C.: Micromorphic continuum. Part I: Strain and stress tensors and their associated rates. *International Journal of Non-Linear Mechanics* **44** (2009), 943–956.

[100] Grammenoudis, P.; Tsakmakis, C. & Hofer, D.: Micromorphic continuum. Part II: Finite deformation plasticity coupled with damage. *International Journal of Non-Linear Mechanics* **44** (2009), 957–974.

[101] Grammenoudis, P.; Tsakmakis, C. & Hofer, D.: Micromorphic continuum. Part III: Small deformation plasticity coupled with damage. *International Journal of Non-Linear Mechanics* **45** (2010), 140 – 148.

[102] Guo, N. & Zhao, J.: A coupled FEM/DEM approach for hierarchical multiscale modelling of granular media. *International Journal for Numerical Methods in Engineering* **99** (2014), 789–818.

[103] Gupta, R.; Salager, S.; Wang, K. & Sun, W.: Open-source support toward validating and falsifying discrete mechanics models using synthetic granular materials – Part I: Experimental tests with particles manufactured by a 3D printer. *Acta Geotechnica* (2018), 1–15.

[104] Hall, S.; Bornert, M.; Desrues, J.; Pannier, Y.; Lenoir, N.; Viggiani, G. & Bésuelle, P.: Discrete and continuum analysis of localised deformation in sand using x-ray μCT and volumetric digital image correlation. *Géotechnique* **60** (2010), 315–322.

[105] Hamilton, W. R.: On quaternions; or on a new system of imaginaries in algebra. *Philosophical Magazine Series 3* **25** (1844), 10–13.

[106] Hart, R.; Cundall, P. & Lemos, J.: Formulation of a three-dimensional distinct element model - Part II. Mechanical calculations for motion and interaction of a system composed of many polyhedral blocks. *International Journal of Rock Mechanics and Mining Sciences & Geomechanics Abstracts* **25** (1988), 117–125.

[107] Hashin, Z.: Analysis of composite materials: A survey. *Journal of Applied Mechanics* **50** (1983), 481–505.

[108] Hassanizadeh, M. & Gray, W. G.: General conservation equations for multi-phase systems: 1. Averaging procedure. *Advances in Water Resources* **2** (1979), 131–144.

[109] Herrmann, H.; Astrøm, J. & Baram, R. M.: Rotations in shear bands and polydisperse packings. *Physica A: Statistical Mechanics and its Applications* **344** (2004), 516–522.

[110] Hertz, H.: Über die Berührung fester elastischer Körper. *Journal für die reine und angewandte Mathemathik* **92** (1882).

[111] Hill, R.: Elastic properties of reinforced solids: some theoretical principles. *Journal of the Mechanics and Physics of Solids* **11** (1963), 357–372.

[112] Hirschberger, C. B.; Kuhl, E. & Steinmann, P.: On deformational and configurational mechanics of micromorphic hyperelasticity–theory and computation. *Computer Methods in Applied Mechanics and Engineering* **196** (2007), 4027–4044.

[113] Hogue, C.: Shape representation and contact detection for discrete element simulations of arbitrary geometries. *Engineering Computations* **15** (1998), 374–390.

[114] Hu, N. & Molinari, J.: Shear bands in dense metallic granular materials. *Journal of the Mechanics and Physics of Solids* **52** (2004), 499–531.

[115] Hütter, G.: Application of a microstrain continuum to size effects in bending and torsion of foams. *International Journal of Engineering Science* **101** (2016), 81 – 91.

[116] Hütter, G.: Homogenization of a Cauchy continuum towards a micromorphic continuum. *Journal of the Mechanics and Physics of Solids* **99** (2017), 394–408.

[117] Iden, F.; Pohlmann, U.; Tilch, W. & Wojtas, H.-J.: Structures of cold box binder systems and the possibility of influencing them. *Giesserei* **98** (2011), 3–8.

[118] Iwashita, K. & Oda, M.: Rolling resistance at contacts in simulation of shear band development by DEM. *Journal of Engineering Mechanics* **124** (1998), 285–292.

[119] Iwashita, K. & Oda, M.: Micro-deformation mechanism of shear banding process based on modified distinct element method. *Powder Technology* **109** (2000), 192–205.

[120] Jänicke, R.; Diebels, S.; Sehlhorst, H.-G. & Düster, A.: Two-scale modelling of micromorphic continua. *Continuum Mechanics and Thermodynamics* **21** (2009), 297–315.

[121] Jänicke, R. & Steeb, H.: Minimal loading conditions for higher-order numerical homogenisation schemes. *Archive of Applied Mechanics* **82** (2012), 1075–1088.

[122] Jänicke, R. & Steeb, H.: Wave propagation in periodic microstructures by homogenisation of extended continua. *Computational Materials Science* **52** (2012), 209–211.

[123] Janis, R.: Cold box method (1972), US Patent 3,702,316.

[124] Jiang, M.; Shen, Z. & Wang, J.: A novel three-dimensional contact model for granulates incorporating rolling and twisting resistances. *Computers and Geotechnics* **65** (2015), 147–163.

[125] Jiang, M.; Yan, H.; Zhu, H. & Utili, S.: Modeling shear behavior and strain localization in cemented sands by two-dimensional distinct element method analyses. *Computers and Geotechnics* **38** (2011), 14–29.

[126] Jiang, M.; Yu, H.-S. & Harris, D.: A novel discrete model for granular material incorporating rolling resistance. *Computers and Geotechnics* **32** (2005), 340–357.

[127] Jing, L. & Stephansson, O.: *Fundamentals of Discrete Element Methods for Rock Engineering: Theory and Applications*, vol. 85 of *Developments in Geotechnical Engineering*. Elsevier Sciences 2007.

[128] Johnson, S. M.; Williams, J. R. & Cook, B. K.: Quaternion-based rigid body rotation integration algorithms for use in particle methods. *International Journal for Numerical Methods in Engineering* **74** (2008), 1303–1313.

[129] Ju, X. & Mahnken, R.: Goal-oriented adaptivity for linear elastic micromorphic continua based on primal and adjoint consistency analysis. *International Journal for Numerical Methods in Engineering* **112** (2017), 1017–1039.

[130] Kafadar, C. B. & Eringen, A. C.: Micropolar media – I the classical theory. *International Journal of Engineering Science* **9** (1971), 271 – 305.

[131] Kawamoto, R.; Andò, E.; Viggiani, G. & Andrade, J. E.: Level set discrete element method for three-dimensional computations with triaxial case study. *Journal of the Mechanics and Physics of Solids* **91** (2016), 1–13.

[132] Kawamoto, R.; Andò, E.; Viggiani, G. & Andrade, J. E.: All you need is shape: Predicting shear banding in sand with LS-DEM. *Journal of the Mechanics and Physics of Solids* **111** (2018), 375–392.

[133] Kotera, H.; Sawada, M. & Shima, S.: Cosserat continuum theory to simulate microscopic rotation of magnetic powder in applied magnetic field. *International Journal of Mechanical Sciences* **42** (2000), 129–145.

[134] Kruyt, N. P.: Statics and kinematics of discrete Cosserat-type granular materials. *International Journal of Solids and Structures* **40** (2003), 511–534.

[135] Kuwabara, G. & Kono, K.: Restitution coefficient in a collision between two spheres. *Japanese Journal of Applied Physics* **26** (1987), 1230.

[136] Labous, L.; Rosato, A. D. & Dave, R. N.: Measurements of collisional properties of spheres using high-speed video analysis. *Physical review E* **56** (1997), 5717.

[137] Lakes, R. S.: Size effects and micromechanics of a porous solid. *Journal of materials science* **18** (1983), 2572–2580.

[138] Leismann, T. & Mahnken, R.: Comparison of hyperelastic micromorphic, micropolar and microstrain continua. *International Journal of Non-Linear Mechanics* **77** (2015), 115–127.

[139] Lenoir, N.; Bornert, M.; Desrues, J.; Bésuelle, P. & Viggiani, G.: Volumetric digital image correlation applied to x-ray microtomography images from triaxial compression tests on argillaceous rock. *Strain* **43** (2007), 193–205.

[140] Leroy, Y. & Ortiz, M.: Finite element analysis of strain localization in frictional materials. *International Journal for Numerical and Analytical Methods in Geomechanics* **13** (1989), 53–74.

[141] Li, S.; Marshall, J. S.; Liu, G. & Yao, Q.: Adhesive particulate flow: The Discrete-Element Method and its application in energy and environmental engineering. *Progress in Energy and Combustion Science* **37** (2011), 633–668.

[142] Li, X.; Liu, Q. & Zhang, J.: A micro - macro homogenization approach for discrete particle assembly - Cosserat continuum modeling of granular materials. *International Journal of Solids and Structures* **47** (2010), 291–303.

[143] Lim, K.-W.; Kawamoto, R.; Andò, E.; Viggiani, G. & Andrade, J. E.: Multiscale characterization and modeling of granular materials through a computational mechanics avatar: A case study with experiment. *Acta Geotechnica* **11** (2015), 243–253.

[144] Lin, J. & Wu, W.: A general rotation averaging method for granular materials. *Granular Matter* **19** (2017), 44.

[145] Liu, M. & Liu, G.: Smoothed particle hydrodynamics (SPH): An overview and recent developments. *Archives of Computational Methods in Engineering* **17** (2010), 25–76.

[146] Lorenz, A.; Tuozzolo, C. & Louge, M.: Measurements of impact properties of small, nearly spherical particles. *Experimental Mechanics* **37** (1997), 292–298.

[147] Lu, W.-M.; Tung, K.-L.; Hung, S.-M.; Shiau, J.-S. & Hwang, K.-J.: Compression of deformable gel particles. *Powder Technology* **116** (2001), 1–12.

[148] Luding, S.: Collisions & contacts between two particles. *NATO ASI Series E Applied Sciences-Advanced Study Institute* **350** (1998), 285–304.

[149] Luding, S.: Contact models for very loose granular materials. In Eberhard, P. (ed.): *IUTAM Symposium on Multiscale Problems in Multibody System Contacts*. Springer Netherlands 2007, vol. 1 of *IUTAM Bookseries*, pp. 135–150.

[150] Luding, S.: Cohesive, frictional powders: contact models for tension. *Granular Matter* **10** (2008), 235–246.

[151] Luding, S.; Lätzel, M.; Volk, W.; Diebels, S. & Herrmann, H.: From discrete element simulations to a continuum model. *Computer Methods in Applied Mechanics and Engineering* **191** (2001), 21–28.

[152] Ma, G.; Regueiro, R. A.; Zhou, W.; Wang, Q. & Liu, J.: Role of particle crushing on particle kinematics and shear banding in granular materials. *Acta Geotechnica* **13** (2018), 601–618.

[153] Mahnken, R. & Stein, E.: A unified approach for parameter identification of inelastic material models in the frame of the finite element method. *Computer Methods in Applied Mechanics and Engineering* **136** (1996), 225–258.

[154] Mayeur, J. & McDowell, D.: A comparison of Gurtin type and micropolar theories of generalized single crystal plasticity. *International Journal of Plasticity* **57** (2014), 29–51.

[155] Mayeur, J. R.; McDowell, D. L. & Bammann, D. J.: Dislocation-based micropolar single crystal plasticity: Comparison of multi- and single criterion theories. *Journal of the Mechanics and Physics of Solids* **59** (2011), 398–422.

[156] Miehe, C. & Dettmar, J.: A framework for micro–macro transitions in periodic particle aggregates of granular materials. *Computer Methods in Applied Mechanics and Engineering* **193** (2004), 225–256.

[157] Miehe, C.; Dettmar, J. & Zäh, D.: Homogenization and two-scale simulations of granular materials for different microstructural constraints. *International Journal for Numerical Methods in Engineering* **83** (2010), 1206–1236.

[158] Mindlin, R. D.: Second gradient of strain and surface-tension in linear elasticity. *International Journal of Solids and Structures* **1** (1965), 417–438.

[159] Monaghan, J. J.: Smoothed particle hydrodynamics. *Reports on Progress in Physics* **68** (2005), 1703.

[160] Mühlhaus, H. & Vardoulakis, I.: The thickness of shear bands in granular materials. *Geotechnique* **37** (1987), 271–283.

[161] Munjiza, A. A.: *The combined Finite-Discrete Element Method*. John Wiley & Sons 2004.

[162] Nardelli, V.; Coop, M.; Andrade, J. & Paccagnella, F.: An experimental investigation of the micromechanics of Eglin sand. *Powder Technology* **312** (2017), 166–174.

[163] Neff, P.: On material constants for micromorphic continua. *Trends in Applications of Mathematics to Mechanics, STAMM Proceedings, Seeheim* (2004), 337–348.

[164] Neff, P.: A finite-strain elastic-plastic Cosserat theory for polycrystals with grain rotations. *International Journal of Engineering Science* **44** (2006), 574 – 594.

[165] Neff, P. & Forest, S.: A geometrically exact micromorphic model for elastic metallic foams accounting for affine microstructure. Modelling, existence of minimizers, identification of moduli and computational results. *Journal of Elasticity* **87** (2007), 239–276.

[166] Nguyen, T.; Combe, G.; Caillerie, D. & Desrues, J.: FEM × DEM modelling of cohesive granular materials: Numerical homogenisation and multi-scale simulations. *Acta Geophysica* **62** (2014), 1109–1126.

[167] Niedostatkiewicz, M.; Lesniewska, D. & Tejchman, J.: Experimental analysis of shear zone patterns in cohesionless for earth pressure problems using particle image velocimetry. *Strain* **47** (2011), 218–231.

[168] Noll, W.: A mathematical theory of the mechanical behavior of continuous media. *Archive for Rational Mechanics and Analysis* **2** (1958), 197–226.

[169] Nübel, K. & Huang, W.: A study of localized deformation pattern in granular media. *Computer Methods in Applied Mechanics and Engineering* **193** (2004), 2719–2743.

[170] Obermayr, M.: *Prediction of Load Data for Construction Equipment using the Discrete Element Method*. Shaker 2013.

[171] Obermayr, M.; Dressler, K.; Vrettos, C. & Eberhard, P.: A bonded-particle model for cemented sand. *Computers and Geotechnics* **49** (2013), 299–313.

[172] Obermayr, M.; Vrettos, C.; Eberhard, P. & Däuwel, T.: A discrete element model and its experimental validation for the prediction of draft forces in cohesive soil. *Journal of Terramechanics* **53** (2014), 93–104.

[173] Oda, M. & Iwashita, K.: Study on couple stress and shear band development in granular media based on numerical simulation analyses. *International Journal of Engineering Science* **38** (2000), 1713–1740.

[174] Oda, M.; Takemura, T. & Takahashi, M.: Microstructure in shear band observed by microfocus x-ray computed tomography. *Geotechnique* **54** (2004), 539–542.

[175] Omelyan, I. P.: On the numerical integration of motion for rigid polyatomics: The modified quaternion approach. *Computers in Physics* **12** (1998), 97–103.

[176] Onck, P. R.: Cosserat modeling of cellular solids. *Comptes Rendus Mecanique* **330** (2002), 717–722.

[177] Potyondy, D. & Cundall, P.: A bonded-particle model for rock. *International Journal of Rock Mechanics and Mining Sciences* **41** (2004), 1329–1364.

[178] Rechenmacher, A. L.: Grain-scale processes governing shear band initiation and evolution in sands. *Journal of the Mechanics and Physics of Solids* **54** (2006), 22–45.

[179] Regueiro, R.; Zhang, B.; Shahabi, F. & Soga, K.: Micromorphic continuum stress measures calculated from three-dimensional ellipsoidal discrete element simulations on granular media. In Soga, K.; Kumar, K.; Biscontin, G. & Kuo, M. (eds.): *Geomechanics from Micro to Macro*. CRC Press 2014, vol. 1, pp. 195–200.

[180] Regueiro, R. A.: On finite strain micromorphic elastoplasticity. *International Journal of Solids and Structures* **47** (2010), 786–800.

[181] Rougier, E.; Munjiza, A. & John, N.: Numerical comparison of some explicit time integration schemes used in DEM, FEM/DEM and molecular dynamics. *International Journal for Numerical Methods in Engineering* **61** (2004), 856–879.

[182] Rueger, Z. & Lakes, R. S.: Experimental cosserat elasticity in open-cell polymer foam. *Philosophical Magazine* **96** (2016), 93–111.

[183] Salot, C.; Gotteland, P. & Villard, P.: Influence of relative density on granular materials behavior: DEM simulations of triaxial tests. *Granular matter* **11** (2009), 221–236.

[184] Sandeep, C. & Senetakis, K.: Grain-scale mechanics of quartz sand under normal and tangential loading. *Tribology International* **117** (2018), 261–271.

[185] Schnaid, F.; Prietto, P. D. & Consoli, N. C.: Characterization of cemented sand in triaxial compression. *Journal of Geotechnical and Geoenvironmental Engineering* **127** (2001), 857–868.

[186] Schneider, M.; Hofmann, T.; Andrä, H.; Lechner, P.; Ettemeyer, F.; Volk, W. & Steeb, H.: Modelling the microstructure and computing effective elastic properties of sand core materials. *International Journal of Solids and Structures* **143** (2018), 1–17.

[187] Scholz, B.: *Application of a Micropolar Model to the Localization Phenomena in Granular Materials: General Model, Sensitivity Analysis and Parameter Optimization*. Dissertation, Report No. II-15 of the Institute of Applied Mechanics (CE), University of Stuttgart 2007.

[188] Schröder, J.: *Homogenisierungsmethoden der nichtlinearen Kontinuumsmechanik unter Beachtung von Stabilitätsproblemen*. Habilitation, Report No. I-7 of the Institute of Applied Mechanics (CE), University of Stuttgart 2000.

[189] Schröder, J.: A numerical two-scale homogenization scheme: The FE^2-method. In *Plasticity and Beyond*. Springer 2014, pp. 1–64.

[190] Senetakis, K.; Coop, M. R. & Todisco, M. C.: The inter-particle coefficient of friction at the contacts of Leighton Buzzard sand quartz minerals. *Soils and Foundations* **53** (2013), 746–755.

[191] Senetakis, K. & Sandeep, C.: Experimental study of sand grains behavior at their contacts with force-and displacement-controlled sliding tests. *Underground Space* **2** (2017), 38–44.

[192] Shahin, G.; Desrues, J.; Dal Pont, S.; Combe, G. & Argilaga, A.: A study of the influence of REV variability in double scale FEM × DEM analysis. *International Journal for Numerical Methods in Engineering* (2016).

[193] Shi, G.-H.: Discontinuous deformation analysis: a new numerical model for the statics and dynamics of deformable block structures. *Engineering Computations* **9** (1992), 157–168.

[194] Shoemake, K.: Animating rotation with quaternion curves. In *ACM SIGGRAPH Computer Graphics*, ACM 1985, vol. 19, pp. 245–254.

[195] Shriver, H. R.; Dunnayant, W. R. & Gruber, B. A.: Cold box process for preparing foundry shapes which use acrylated epoxy resins (1990), US Patent 4,974,659.

[196] Sorg, A. & Bischoff, M.: Adaptive discrete-continuous modeling of evolving discontinuities. *Engineering Computations* **31** (2014), 1305–1320.

[197] Stefanou, I.; Sulem, J. & Rattez, H.: Cosserat approach to localization in geomaterials. In Voyiadjis, G. (ed.): *Handbook of Nonlocal Continuum Mechanics for Materials and Structure*. Springer 2017, pp. 1–25.

[198] Steinmann, P.: Theory and numerics of ductile micropolar elastoplastic damage. *International Journal for Numerical Methods in Engineering* **38** (1995), 583–606.

[199] Stühler, S.; Fleissner, F. & Eberhard, P.: A contact detection algorithm for deformable tetrahedral geometries based on a novel approach for general simplices used in the Discrete Element Method. *Computational Particle Mechanics* **5** (2018), 35–47.

[200] Tavares, L. & King, R.: Single-particle fracture under impact loading. *International Journal of Mineral Processing* **54** (1998), 1–28.

[201] Tekoğlu, C. & Onck, P. R.: Size effects in two-dimensional Voronoi foams: A comparison between generalized continua and discrete models. *Journal of the Mechanics and Physics of Solids* **56** (2008), 3541–3564.

[202] Tijskens, E.; Ramon, H. & De Baerdemaeker, J.: Discrete element modelling for process simulation in agriculture. *Journal of Sound and Vibration* **266** (2003), 493–514.

[203] Tordesillas, A.; Peters, J. & Gardiner, B.: Shear band evolution and accumulated microstructural development in Cosserat media. *International Journal for Numerical and Analytical Methods in Geomechanics* **28** (2004), 981–1010.

[204] Tordesillas, A.; Walsh, S. & Gardiner, B.: Bridging the length scales: Micromechanics of granular media. *BIT Numerical Mathematics* **44** (2004), 539–556.

[205] Utili, S. & Nova, R.: DEM analysis of bonded granular geomaterials. *International Journal for Numerical and Analytical Methods in Geomechanics* **32** (2008), 1997–2031.

[206] Van Waveren, J.: From quaternion to matrix and back. *ID Software, Inc* (2005).

[207] Verlet, L.: Computer ‘‘experiments” on classical fluids. I. Thermodynamical properties of Lennard-Jones molecules. *Physical Review* **159** (1967), 98.

[208] Vernerey, F.; Liu, W. K. & Moran, B.: Multi-scale micromorphic theory for hierarchical materials. *Journal of the Mechanics and Physics of Solids* **55** (2007), 2603–2651.

[209] Vernerey, F. J.; Liu, W. K.; Moran, B. & Olson, G.: A micromorphic model for the multiple scale failure of heterogeneous materials. *Journal of the Mechanics and Physics of Solids* **56** (2008), 1320–1347.

[210] Viggiani, G.; Lenoir, N.; Bésuelle, P.; Di Michiel, M.; Marello, S.; Desrues, J. & Kretzschmer, M.: X-ray microtomography for studying localized deformation in fine-grained geomaterials under triaxial compression. *Comptes Rendus Mécanique* **332** (2004), 819–826.

[211] Volk, W.: *Untersuchung des Lokalisierungsverhaltens mikropolarer poröser Medien mit Hilfe der Cosserat-Theorie*. Dissertation, Report No. II-2 of the Institute of Applied Mechanics (CE), University of Stuttgart 1999.

[212] Walsh, S. D.; Tordesillas, A. & Peters, J. F.: Development of micromechanical models for granular media. *Granular Matter* **9** (2007), 337–352.

[213] Wang, Y. & Leung, S.: Characterization of cemented sand by experimental and numerical investigations. *Journal of Geotechnical and Geoenvironmental Engineering* **134** (2008), 992–1004.

[214] Wang, Y. & Tonon, F.: Calibration of a discrete element model for intact rock up to its peak strength. *International Journal for Numerical and Analytical Methods in Geomechanics* **34** (2010), 447–469.

[215] Wellmann, C.; Lillie, C. & Wriggers, P.: Homogenization of granular material modeled by a three-dimensional discrete element method. *Computers and Geotechnics* **35** (2008), 394–405.

[216] Wellmann, C. & Wriggers, P.: A two-scale model of granular materials. *Computer Methods in Applied Mechanics and Engineering* **205** (2012), 46–58.

[217] Wensrich, C. & Katterfeld, A.: Rolling friction as a technique for modelling particle shape in DEM. *Powder Technology* **217** (2012), 409–417.

[218] Widuliński, Ł.; Tejchman, J.; Kozicki, J. & Leśniewska, D.: Discrete simulations of shear zone patterning in sand in earth pressure problems of a retaining wall. *International Journal of Solids and Structures* **48** (2011), 1191–1209.

[219] Williams, J. R. & O'Connor, R.: Discrete element simulation and the contact problem. *Archives of Computational Methods in Engineering* **6** (1999), 279–304.

[220] Wolf, H.; König, D. & Triantafyllidis, T.: Experimental investigation of shear band patterns in granular material. *Journal of Structural Geology* **25** (2003), 1229–1240.

[221] Yamakawa, Y.; Ikeda, K.; Saiki, I.; Desrues, J. & Tanaka, R. J.: Diffuse bifurcations engraving diverse shear bands in granular materials. *International Journal for Numerical and Analytical Methods in Geomechanics* **42** (2018), 3–33.

[222] Yan, B.; Regueiro, R. A. & Sture, S.: Three-dimensional ellipsoidal discrete element modeling of granular materials and its coupling with finite element facets. *Engineering Computations* **27** (2010), 519–550.

[223] Zhu, H. & Yu, A.: Averaging method of granular materials. *Physical Review E* **66** (2002), 021302.

[224] Zhu, H.; Zhou, Z.; Yang, R. & Yu, A.: Discrete particle simulation of particulate systems: Theoretical developments. *Chemical Engineering Science* **62** (2007), 3378–3396.

[225] Zhu, H.; Zhou, Z.; Yang, R. & Yu, A.: Discrete particle simulation of particulate systems: A review of major applications and findings. *Chemical Engineering Science* **63** (2008), 5728–5770.

[226] Zimmerman, J. A.; Jones, R. E. & Templeton, J. A.: A material frame approach for evaluating continuum variables in atomistic simulations. *Journal of Computational Physics* **229** (2010), 2364–2389.

List of Figures

List of Tables

Curriculum Vitae

Personal data:

Name:	Sami Ismail Wilhelm Bidier
Date of birth:	July 30, 1985
Place of birth:	Filderstadt, Germany
Nationality:	German

Education:

09/1991 – 06/1995	elementary school in Grunbach, Germany
09/1995 – 06/2004	secondary school "Georg-Büchner-Gymnasium", Winnenden, Germany
06/2004	degree: "Allgemeine Hochschulreife" (high-school diploma)
10/2005 – 04/2011	studies in civil engineering at the University of Stuttgart, Germany, major subject: "Konstruktiver Ingenieurbau"
09/2008 – 06/2009	studies in civil engineering at the Ecole Spéciale des Travaux Publics in Paris, France
04/2011	degree: "Diplom-Ingenieur (Dipl.-Ing.) Bauingenieurwesen", passed with distinction

Civilian service:

09/2004 – 06/2005	civilian service at the "Berufsbildungswerk Paulinenpflege", Winnenden, Germany

Professional occupation:

06/2011 – 12/2018	teaching assistant and research associate at the Institute of Applied Mechanics (Civil Engineering) at the University of Stuttgart, Germany
04/2019	structural engineer at str.ucture GmbH, Stuttgart, Germany

Presently published contributions in this report series

II-1 Gernot Eipper: *Theorie und Numerik finiter elastischer Deformationen in fluidgesättigten porösen Festkörpern*, 1998.

II-2 Wolfram Volk: *Untersuchung des Lokalisierungsverhaltens mikropolarer poröser Medien mit Hilfe der Cosserat-Theorie*, 1999.

II-3 Peter Ellsiepen: *Zeit- und ortsadaptive Verfahren angewandt auf Mehrphasenprobleme poröser Medien*, 1999.

II-4 Stefan Diebels: *Mikropolare Zweiphasenmodelle: Formulierung auf der Basis der Theorie Poröser Medien*, 2000.

II-5 Dirk Mahnkopf: *Lokalisierung fluidgesättigter poröser Festkörper bei finiten elastoplastischen Deformationen*, 2000.

II-6 Heiner Müllerschön: *Spannungs-Verformungsverhalten granularer Materialien am Beispiel von Berliner Sand*, 2000.

II-7 Stefan Diebels (Ed.): *Zur Beschreibung komplexen Materialverhaltens: Beiträge anläßlich des 50. Geburtstages von Herrn Prof. Dr.-Ing. Wolfgang Ehlers*, 2001.

II-8 Jack Widjajakusuma: *Quantitative Prediction of Effective Material Parameters of Heterogeneous Materials*, 2002.

II-9 Alexander Droste: *Beschreibung und Anwendung eines elastisch-plastischen Materialmodells mit Schädigung für hochporöse Metallschäume*, 2002.

II-10 Peter Blome: *Ein Mehrphasen-Stoffmodell für Böden mit Übergang auf Interface-Gesetze*, 2003.

II-11 Martin Ammann: *Parallel Finite Element Simulations of Localization Phenomena in Porous Media*, 2005.

II-12 Bernd Markert: *Porous Media Viscoelasticity with Application to Polymeric Foams*, 2005.

II-13 Saeed Reza Ghadiani: *A Multiphasic Continuum Mechanical Model for Design Investigations of an Effusion-Cooled Rocket Thrust Chamber*, 2005.

II-14 Wolfgang Ehlers & Bernd Markert (Eds.): *Proceedings of the 1st GAMM Seminar on Continuum Biomechanics*, 2005.

II-15 Bernd Scholz: *Application of a Micropolar Model to the Localization Phenomena in Granular Materials: General Model, Sensitivity Analysis and Parameter Optimization*, 2007.

II-16 Wolfgang Ehlers & Nils Karajan (Eds.): *Proceedings of the 2nd GAMM Seminar on Continuum Biomechanics*, 2007.

II-17 Tobias Graf: *Multiphasic Flow Processes in Deformable Porous Media under Consideration of Fluid Phase Transitions*, 2008.

II-18 Ayhan Acartürk: *Simulation of Charged Hydrated Porous Materials*, 2009.

II-19 Nils Karajan: *An Extended Biphasic Description of the Inhomogeneous and Anisotropic Intervertebral Disc*, 2009.

II-20 Bernd Markert: *Weak or Strong – On Coupled Problems In Continuum Mechanics*, 2010.

II-21 Wolfgang Ehlers & Bernd Markert (Eds.): *Proceedings of the 3rd GAMM Seminar on Continuum Biomechanics*, 2012.

II-22 Wolfgang Ehlers: *Poröse Medien – ein kontinuumsmechanisches Modell auf der Basis der Mischungstheorie*, 2012. Nachdruck der Habilitationsschrift aus dem Jahr 1989 (Forschungsberichte aus dem Fachbereich Bauwesen der Universität-GH-Essen **47**, Essen 1989).

II-23 Hans-Uwe Rempler: *Damage in multi-phasic Materials Computed with the Extended Finite-Element Method*, 2012.

II-24 Irina Komarova: *Carbon-Dioxide Storage in the Subsurface: A Fully Coupled Analysis of Transport Phenomena and Solid Deformation*, 2012.

II-25 Yousef Heider: *Saturated Porous Media Dynamics with Application to Earthquake Engineering*, 2012.

II-26 Okan Avci: *Coupled Deformation and Flow Processes of Partial Saturated Soil: Experiments, Model Validation and Numerical Investigations*, 2013.

II-27 Arndt Wagner: *Extended Modelling of the Multiphasic Human Brain Tissue with Application to Drug-Infusion Processes*, 2014.

II-28 Joffrey Mabuma: *Multi-Field Modelling and Simulation of the Human Hip Joint*, 2014.

II-29 Robert Krause: *Growth, Modelling and Remodelling of Biological Tissue*, 2014.

II-30 Seyedmohammad Zinatbakhsh: *Coupled Problems in the Mechanics of Multi-Physics and Multi-Phase Materials*, 2015.

II-31 David Koch: *Thermomechanical Modelling of Non-isothermal Porous Materials with Application to Enhanced Geothermal Systems*, 2016.

II-32 Maik Schenke: *Parallel Simulation of Volume-coupled Multi-field Problems with Special Application to Soil Dynamics*, 2017.

II-33 Steffen Mauthe: *Variational Multiphysics Modeling of Diffusion in Elastic Solids and Hydraulic Fracturing in Porous Media*, 2017.

II-34 Kai Häberle: *Fluid-Phase Transitions in a Multiphasic Model of CO_2 Sequestration into Deep Aquifers: A fully coupled analysis of transport phenomena and solid deformation*, 2017.

II-35 Cheny Luo: *A Phase-field Model Embedded in the Theory of Porous Media with Application to Hydraulic Fracturing*, 2019.

II-36 Sami Bidier: *From Particle Mechanics to Micromorphic Continua*, 2019.